EFFECTIVE ANALYTIC AND ASYMPTOTIC PROCEDURES FOR WAVE DIFFRACTION BY PERFECT AND PENETRABLE WEDGES

A thesis submitted to the University of Manchester
for the degree of Doctor of Philosophy
in the Faculty of Science and Engineering

2019

Matthew Allan Nethercote
School of Mathematics

Contents

Word count 64732

List of Figures

The University of Manchester

Matthew Allan Nethercote
Doctor of Philosophy
Effective analytic and asymptotic procedures for wave diffraction by perfect and penetrable wedges
October 21, 2019

In this thesis, various canonical problems of plane wave diffraction by infinite two-dimensional wedges are studied in both acoustic and electromagnetic physical settings. The thesis is divided into two main parts. The first, which is essentially an extensive review of extant methods, focuses on wedge diffraction with homogeneous Dirichlet or Neumann boundary conditions. It involves studying the well-known solution to Sommerfeld's half-plane diffraction problem and provides an extensive review of the literature on the perfect wedge problem, including analytic methods such as the Sommerfeld-Malyuzhinets and Wiener-Hopf techniques, as well as asymptotic techniques such as Keller's geometrical theory of diffraction.

The second part of the thesis is dedicated to the problem of diffraction by a penetrable wedge. To this day, there is no clear analytical solution to this important canonical problem, but there have been numerous attempts at computational and asymptotic solutions by many reputable authors using extensions of techniques applied to perfect wedge diffraction.

Because it is penetrable, the material properties between the wedge scatterer and the exterior host differ. It is hence possible to define the so-called contrast parameter as the ratio of specific material properties (depending on the physical context) between the host and the scatterer. Throughout the thesis, this parameter is considered to be small and the contrast is said to be high. This assumption allows construction of an asymptotic iterative scheme, which enables the penetrable wedge problem to be written as an infinite sequence of impenetrable wedge problems.

All but the first of these impenetrable wedge problems are solved using a combination of the Sommerfeld-Malyuzhinets and Wiener-Hopf techniques. The result is a sequence of complex nested integrals which are evaluated using a subtle interplay of interpolation, asymptotic expansions and advanced complex analysis. For several test cases, including those illustrated in this thesis (that were chosen for mathematical convenience and consistency with the literature), the numerical results were in good agreement with alternative approaches.

Declaration

No portion of the work referred to in the thesis has been submitted in support of an application for another degree or qualification of this or any other university or other institute of learning.

Copyright Statement

i. The author of this thesis (including any appendices and/or schedules to this thesis) owns certain copyright or related rights in it (the "Copyright") and s/he has given The University of Manchester certain rights to use such Copyright, including for administrative purposes.

ii. Copies of this thesis, either in full or in extracts and whether in hard or electronic copy, may be made **only** in accordance with the Copyright, Designs and Patents Act 1988 (as amended) and regulations issued under it or, where appropriate, in accordance with licensing agreements which the University has from time to time. This page must form part of any such copies made.

iii. The ownership of certain Copyright, patents, designs, trade marks and other intellectual property (the "Intellectual Property") and any reproductions of copyright works in the thesis, for example graphs and tables ("Reproductions"), which may be described in this thesis, may not be owned by the author and may be owned by third parties. Such Intellectual Property and Reproductions cannot and must not be made available for use without the prior written permission of the owner(s) of the relevant Intellectual Property and/or Reproductions.

iv. Further information on the conditions under which disclosure, publication and commercialisation of this thesis, the Copyright and any Intellectual Property

Acknowledgements

I would like to thank my PhD supervisors Dr Raphaël Assier and Professor Ian David Abrahams for their expertise and being immensely patient with me over the past few years. I truly would not have got this far without them.

I also thank all of the staff at the university especially Professor William Parnell for their support throughout this PhD. I have made many great friends during my time here and I could not possibly name them all. I thank all of them for providing much needed distractions/rants as well as joyous laughter in times of crisis and for feeding me when I forget to eat my lunch.

Thank you to Chris for always providing a friendly escape from the PhD life when I needed it. I would like to thank my parents most of all for their infinite love and support, for fattening me up and making sure I always had a roof over my head. I thank them for always being there for me.

Chapter 1

Introduction

Research on the subject of wave motion is a topic of significant importance in the engineering and physical sciences, and various aspects can be traced back through the centuries by many exceptional scholars including, but by no means limited to, Lord Rayleigh, Poincaré, Newton, Kepler and even Da Vinci (the latter three actually studied optics before the wave theory of light was generally accepted). Waves can take many different forms (mechanical, acoustic, electromagnetic, water and gravitational for example) and have an enormous amount of applications such as non-destructive testing, seismology, noise management, sonar, electromagnetic propagation, oceanography, traffic flow (Billingham and King, 2001) and even Einstein's theory of general relativity (Einstein and Rosen, 1937).

There are plenty of active research topics on wave motion, for example, the interaction of waves with multiple finite bodies is a well established topic (see Martin (2006) and references within), which has been studied in periodic and random arrangements (for instance, see recent developments by Andrew (2014); Gower et al. (2019)). These studies have been combined with machine learning to train micro-sized robots to detect faults or blockages in underground pipes with sonar. Another example, is the design of metamaterials (a class of materials with a

special microstructure not found in nature) for noise control using transformation acoustics (Rowley, 2018). There is also the development of active cloaking which involves finding the configuration of point sources required to nullify the scattered field and create a 'quiet-zone' (Norris et al., 2012).

In this thesis, we shall study some canonical scattering problems to investigate the diffraction of waves by sharp edges or corners. The first accurate observations of diffraction is credited to Grimaldi, as well as the invention of the word itself (Cajori, 1899), and the theory was popularised by the work of Huygens, Fresnel and Kirchhoff as well as the double slit experiments of Young. It is believed that the mathematical theory of diffraction became an important field of research when Sommerfeld solved his famous half-plane problem in 1896 (see the original paper (Sommerfeld, 1896) as well as the English translation (Sommerfeld, 2003)).

Since Grimaldi's observations, there has been a large number of advancements such as Huygens-Fresnel principle and a wide variety of methods and formulas developed in order to model this phenomenon including, Kirchhoff's diffraction formula, the Sommerfeld-Malyuzhinets (S-M) technique (Babich et al., 2007) and the Wiener-Hopf (W-H) technique (Noble, 1958) as well as the geometrical theory of diffraction (GTD) (Keller, 1962).

The investigation of diffraction by sharp edges and corners can be used as a component in modelling the scattering of waves by polygons and prisms (Groth et al., 2015, 2018). As an example, take Figure 1.1 (left) which is a COMSOL numerical simulation of an incident plane wave being scattered by an equilateral penetrable triangle. This is useful to model acoustics in single rooms and urban environments as well as for noise management in aircraft engines and the development of acoustic noise barriers. It is also useful to model the propagation of electromagnetic waves for antenna theory and the scattering of solar radiation by high-altitude clouds formed by microscopic ice crystals (see Figure 1.1 (right) for

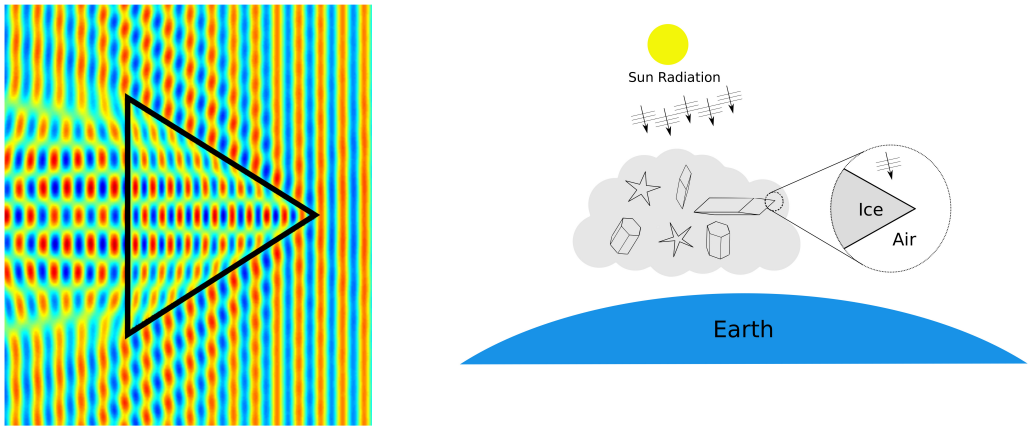

Figure 1.1: Example of convex polygon diffraction (with an equilateral triangle where the side length is 2π and the wavenumbers 10 (outside) and 13.1 (inside)) numerically simulated using COMSOL (left). Diagram outlining the application to ice crystal diffraction and illustrating how a crystal edge is approximated as an infinite penetrable wedge (right). Note that the left image is courtesy of my supervisor Assier.

an illustration of the latter application).

Despite the progress in the field, some diffraction problems remain open to this day. These include the quarter-plane, the plane sector, the penetrable cone and the penetrable wedge. In this thesis, we shall study perfect and penetrable wedge diffraction problems.

Sommerfeld would be the first to conceive a solution to model wave diffraction by perfect wedges (Sommerfeld, 1901) using the method of images. His solution was restricted, however, to wedges with a rational interior angle (meaning of the form $m\pi/n$ with integers m and n). For wedges with an arbitrary angle, Macdonald was the first to obtain a solution using separation of variables (Macdonald, 1902).

Since then, a wide range of techniques have been derived to solve wedge diffraction problems with perfect boundary conditions (homogeneous Dirichlet or Neumann) and they work very well in doing so. A thorough review of these techniques is the first main objective of this thesis.

For diffraction by penetrable wedges, there have been several attempts to construct numerical and asymptotic solutions. The second main objective is to review this literature on penetrable wedge diffraction and to present a new method to obtain an efficient and accurate solution.

The content of the thesis is as follows. We start by defining the perfect and penetrable wedge diffraction problems in acoustic and electromagnetic physical settings and show that, under certain electromagnetic polarizations, both settings are equivalent mathematically. The rest of this thesis consists of four chapters discussing increasingly difficult wedge diffraction problems.

In the next chapter (2), we shall study a fundamental problem in diffraction theory that is the Sommerfeld half-plane problem. This serves as the ideal introductory problem because a half-plane is simply a wedge with zero interior angle. We use this chapter to present the W-H technique, which will prove to be a crucial method in later chapters, and rewrite the classic solution in terms of Fresnel integrals.

Chapter 3 features a review on the wide range of analytical and asymptotic techniques that have been applied to perfect wedge diffraction problems. This will include introducing the S-M technique as well as demonstrating the versatility of the W-H technique and briefly considering the Kontorovich-Lebedev (K-L) transform approach and Macdonald's separation of variables method. We will also discuss some unfamiliar methods such as the embedding formula, the random walk method and the Sobolev-Smirnoff method (also known as the method of functionally invariant solutions). References to these various methods are contained within this chapter. Additionally, we perform a numerical comparison between the exact solution and asymptotic approximations such as GTD.

Although we do not study it in detail, we will acknowledge (in the first part of the thesis) the important work undertaken for diffraction by impedance wedges,

including the original Malyuzhinets solution (Malyuzhinets, 1958) as well as recent developments (Daniele and Lombardi, 2006) and treatises (Osipov and Norris, 1999; Lyalinov and Zhu, 2013). Similarly, we also acknowledge the work on diffraction by elastic wedges (Knopoff, 1969; Budaev and Bogy, 1998; Croisille and Lebeau, 1999).

Before we attempt the penetrable wedge problem, we will look over some of the different formulations of the penetrable wedge diffraction problem in Chapter 4. Focusing on four papers, (Rawlins, 1999; Lyalinov, 1999; Shanin, 1998) and (Daniele and Lombardi, 2011), we shall briefly review the various asymptotic and numerical methods and critically analyse the advantages and disadvantages. Many of these methods will extend from the ones featured in Chapter 3.

Following the literature review, we tackle the penetrable wedge problem in Chapter 5. We will attempt to construct a solution by assuming that the material parameters differ significantly between the wedge scatterer and the host it is immersed in. By creating a high-contrast asymptotic approximation, the penetrable wedge problem is split into a series of impenetrable wedge problems. These problems will all be solved using a combination of the S-M and W-H techniques which will lead to solutions in integral form. These integral solutions can then be numerically evaluated using interpolation, asymptotic and complex integration techniques. Lastly, we will discuss some possible avenues for extending the methodology of Chapter 5 in Chapter 6.

1.1 Physical context

Here we will describe two physical settings (acoustic and electromagnetic) and show that each setting creates equivalent mathematical problems. Each of our problems will be set in a two-dimensional environment which consists of two infinite domains:

the host Ω_1 and the scatterer Ω_2 as well as their common boundary $\partial\Omega$.

1.1.1 Acoustic setting

Governing equations. For acoustics, we have domains that are considered to be inviscid, compressible fluids without any body forces. The wave quantities satisfy the continuity equation (for conservation of mass),

$$\frac{\partial \rho}{\partial t} + \nabla \cdot (\rho \boldsymbol{u}) = 0, \tag{1.1}$$

and the Euler equations (for conservation of momentum),

$$\rho \left(\frac{\partial \boldsymbol{u}}{\partial t} + \boldsymbol{u} \cdot \nabla \boldsymbol{u} \right) + \nabla p = \mathbf{0}, \tag{1.2}$$

with density ρ, velocity $\boldsymbol{u}$ and pressure p. When the fluid is at rest, these quantities have the constant values, $\rho = \rho_0$, $\boldsymbol{u} = \mathbf{0}$ and $p = p_0$, say. Assuming that we are dealing with small fluctuations in the fluid, then we can define the following linear approximations:

$$\begin{aligned} \rho(\boldsymbol{r}, t) &= \rho_0 + \hat{\rho}(\boldsymbol{r}, t) + ..., \\ \boldsymbol{u}(\boldsymbol{r}, t) &= \hat{\boldsymbol{u}}(\boldsymbol{r}, t) + ..., \\ p(\boldsymbol{r}, t) &= p_0 + \hat{p}(\boldsymbol{r}, t) + ..., \end{aligned} \tag{1.3}$$

where any higher order terms or products of the fluctuations $\hat{\rho}, \hat{\boldsymbol{u}}$ and $\hat{p}$ are neglected. We use (1.3) to linearise (1.1) and (1.2), yielding

$$\frac{\partial \hat{\rho}}{\partial t} + \rho_0 \nabla \cdot \hat{\boldsymbol{u}} = 0, \tag{1.4}$$

$$\rho_0 \frac{\partial \hat{\boldsymbol{u}}}{\partial t} + \nabla \hat{p} = \mathbf{0}. \tag{1.5}$$

We combine the governing equations by the relationship $\frac{\partial}{\partial t}(1.4) - \nabla \cdot (1.5)$ to obtain

$$\frac{\partial^2 \hat{\rho}}{\partial t^2} - \nabla^2 \hat{p} = 0. \tag{1.6}$$

Assuming that the fluid media is barotropic, i.e. the pressure is a function only of density, $p = p(\rho)$, we Taylor expand this relationship in order to get

$$\hat{p} = \frac{\partial p}{\partial \rho}(\rho_0)\hat{\rho}. \tag{1.7}$$

Upon writing $c^2 = \frac{\partial p}{\partial \rho}(\rho_0)$, applying (1.7) to (1.6) gives us the homogeneous wave equation,

$$\frac{1}{c^2}\frac{\partial^2 \hat{p}}{\partial t^2} - \nabla^2 \hat{p} = 0, \tag{1.8}$$

hence c can be taken as the speed of sound. Note that in an adiabatic process, we have the following equation of state for a gas,

$$\frac{p}{p_0} = \left(\frac{\rho}{\rho_0}\right)^{\gamma_c} \tag{1.9}$$

where γ_c is the heat capacity ratio. This implies that

$$\frac{\partial p}{\partial \rho}(\rho_0) = \frac{\gamma_c p_0}{\rho_0} \tag{1.10}$$

hence $c = \sqrt{\frac{\gamma_c p_0}{\rho_0}}$. We can determine that the density and the velocity potential (in an irrotational flow) also satisfies the wave equation but we will prioritise finding the acoustic pressure field in future chapters.

Throughout this thesis, we will be looking for steady time-harmonic solutions to (1.8). Therefore, we assume that $\hat{p}(\boldsymbol{r}, t) = \mathrm{Re}\{P(\boldsymbol{r})e^{-i\omega t}\}$ (we also assume $\hat{\boldsymbol{u}}(\boldsymbol{r}, t) = \mathrm{Re}\{\boldsymbol{U}(\boldsymbol{r})e^{-i\omega t}\}$) with frequency ω and then $P(\boldsymbol{r})$ satisfies the homogeneous Helmholtz equation with wavenumber k,

$$\nabla^2 P + k^2 P = 0. \tag{1.11}$$

Perfect boundary conditions. The first problems we consider will have perfect boundary conditions. In an acoustic setting, the scatterer Ω_2 will be unable to support an acoustic pressure field and hence is known as a perfectly soft or perfectly

rigid scatterer; hence, on $\partial\Omega$, there are two types of boundary conditions: sound-soft and sound-hard.

Sound-soft boundary conditions have zero acoustic pressure $P = 0$ at the boundary $\partial\Omega$, which are homogeneous Dirichlet boundary conditions. Sound-hard or rigid boundary conditions means that the velocity normal to the boundary is zero ($\boldsymbol{U} \cdot \boldsymbol{n} = 0$). Here $\boldsymbol{n}$ is the outward pointing (with respect to Ω_1) normal to the boundary $\partial\Omega$. Noting the linearised relationship (1.5), we find that $\nabla P \cdot \boldsymbol{n} = 0$ on the boundary $\partial\Omega$, which are referred to as homogeneous Neumann boundary conditions.

Interface conditions. The other problems we consider are when the domain Ω_2 can support an acoustic pressure field but has a different set of material parameters to Ω_1 (density, for example). Note that for penetrable bodies we relabel ρ_0 to ρ_1 (resp. ρ_2) in Ω_1 (resp. Ω_2). In this case, the boundary $\partial\Omega$ becomes an interface where we will require continuity of pressure and normal velocity,

$$(P_2 - P_1)|_{\partial\Omega} = 0, \tag{1.12}$$

$$((\boldsymbol{U}_2 - \boldsymbol{U}_1) \cdot \boldsymbol{n})|_{\partial\Omega} = 0, \tag{1.13}$$

where the subscripts 1 and 2 correspond to the domains Ω_1 and Ω_2 respectively. We use the linearised momentum equation (1.5) to rewrite (1.13) in terms of the pressure gradient,

$$\left(\left(\frac{1}{\rho_2} \nabla P_2 - \frac{1}{\rho_1} \nabla P_1 \right) \cdot \boldsymbol{n} \right) \Bigg|_{\partial\Omega} = 0. \tag{1.14}$$

The continuity conditions (1.12) and (1.14) are hereby called the acoustic interface conditions.

1.1.2 Electromagnetic setting

Governing equations. In the electromagnetic setting, we start with the source-free Maxwell's equations

$$\begin{aligned} \nabla \times \boldsymbol{E} + \frac{\partial \boldsymbol{B}}{\partial t} &= \boldsymbol{0}, \qquad \nabla \cdot \boldsymbol{B} = 0, \\ \nabla \times \boldsymbol{H} - \frac{\partial \boldsymbol{D}}{\partial t} &= \boldsymbol{0}, \qquad \nabla \cdot \boldsymbol{D} = 0, \end{aligned} \tag{1.15}$$

where $\boldsymbol{E}$ is called the electric intensity, $\boldsymbol{D}$ is the electric flux density, $\boldsymbol{H}$ is the magnetic intensity and $\boldsymbol{B}$ is the magnetic flux density. We say that the media governed by (1.15) are linear, isotropic and homogeneous, so we can use the following constitutive equations,

$$\boldsymbol{D} = \epsilon \boldsymbol{E}, \qquad \boldsymbol{B} = \mu \boldsymbol{H}, \tag{1.16}$$

where ϵ and μ are the electric permittivity and magnetic permeability respectively (which are both constant scalar quantities). We also look for time-harmonic solutions, hence we propose that,

$$\boldsymbol{E} = \mathrm{Re}\left\{\hat{\boldsymbol{E}}(\boldsymbol{r})e^{-i\omega t}\right\}, \quad \boldsymbol{H} = \mathrm{Re}\left\{\hat{\boldsymbol{H}}(\boldsymbol{r})e^{-i\omega t}\right\}, \tag{1.17}$$

where ω is the angular frequency of the waves. Applying (1.16) and (1.17) to Maxwell's equations gives the equations for the electric and magnetic intensities,

$$\begin{aligned} \nabla \times \hat{\boldsymbol{E}} - i\omega\mu \hat{\boldsymbol{H}} &= \boldsymbol{0}, \qquad \nabla \cdot \hat{\boldsymbol{H}} = 0, \\ \nabla \times \hat{\boldsymbol{H}} + i\omega\epsilon \hat{\boldsymbol{E}} &= \boldsymbol{0}, \qquad \nabla \cdot \hat{\boldsymbol{E}} = 0. \end{aligned} \tag{1.18}$$

The problems we examine will be formulated such that they are invariant in the z coordinate. In the case of an infinite wedge scatterer, this means that the wedge edge will be parallel to the z-axis and the incoming wave will be normally incident to the wedge (i.e. no skew incidence). For brevity and simplicity, we consider two types of problems: electric-polarised (E-pol) and magnetic-polarised

(H-pol) waves. In these cases, either $\hat{\boldsymbol{E}}$ or $\hat{\boldsymbol{H}}$ has only one component in the z direction, hence

$$\text{E-pol:} \quad \hat{\boldsymbol{E}} = E_z \boldsymbol{e}_z, \quad \hat{\boldsymbol{H}} = \frac{1}{i\omega\mu}\nabla \times \hat{\boldsymbol{E}} = \frac{1}{i\omega\mu r}\frac{\partial E_z}{\partial \theta}\boldsymbol{e}_r - \frac{1}{i\omega\mu}\frac{\partial E_z}{\partial r}\boldsymbol{e}_\theta, \tag{1.19}$$

$$\text{H-pol:} \quad \hat{\boldsymbol{H}} = H_z \boldsymbol{e}_z, \quad \hat{\boldsymbol{E}} = -\frac{1}{i\omega\epsilon}\nabla \times \hat{\boldsymbol{H}} = -\frac{1}{i\omega\epsilon r}\frac{\partial H_z}{\partial \theta}\boldsymbol{e}_r + \frac{1}{i\omega\epsilon}\frac{\partial H_z}{\partial r}\boldsymbol{e}_\theta, \tag{1.20}$$

where $\{\boldsymbol{e}_r, \boldsymbol{e}_\theta, \boldsymbol{e}_z\}$ are the basis vectors for a cylindrical coordinate system. It is straightforward to show that Maxwell's equations (1.18) will be satisfied provided that E_z or H_z, respectively, satisfy the two-dimensional homogeneous Helmholtz equation

$$\nabla^2 \Phi + k^2 \Phi = 0, \tag{1.21}$$

where $k = \omega\sqrt{\mu\epsilon}$.

Perfect electric conducting boundary conditions. At first, the scatterer Ω_2 will be a perfect electric conductor (PEC). Physically, this means that the scatterer has infinite conductivity and offers zero electrical resistance. Therefore, it cannot support an electric field ($\hat{\boldsymbol{E}} = 0$ in Ω_2) and any magnetic field must be constant in time ($\frac{\partial \hat{\boldsymbol{H}}}{\partial t} = 0$ in Ω_2). In the absence of sources, we can state further that $\hat{\boldsymbol{H}} = 0$ in Ω_2. It follows from Maxwell's equations that the electric tangential and magnetic normal field components are continuous across the boundary $\partial\Omega$. With zero electromagnetic field in Ω_2, we obtain the PEC boundary conditions,

$$\text{PEC boundary conditions:} \; = \begin{cases} \left(\hat{\boldsymbol{E}} \times \boldsymbol{n}\right)\Big|_{\partial\Omega} = \boldsymbol{0}, & \text{(1.22a)} \\ \left(\hat{\boldsymbol{H}} \cdot \boldsymbol{n}\right)\Big|_{\partial\Omega} = 0, & \text{(1.22b)} \end{cases}$$

where $\boldsymbol{n}$ is the outward pointing (with respect to Ω_1) normal to the boundary $\partial\Omega$.

We apply the PEC boundary conditions to the E-pol case (1.19), to give

$$\left(\hat{\boldsymbol{E}} \times \boldsymbol{n}\right)\Big|_{\partial\Omega} = (E_z \boldsymbol{t})|_{\partial\Omega} = \boldsymbol{0}, \tag{1.23}$$

$$\left(\hat{\boldsymbol{H}} \cdot \boldsymbol{n}\right)\Big|_{\partial\Omega} = \left(\frac{1}{i\omega\mu}\nabla E_z \cdot \boldsymbol{t}\right)\Big|_{\partial\Omega} = 0, \tag{1.24}$$

where $\boldsymbol{t}$ is the tangent of the boundary $\partial\Omega$ defined such that $\boldsymbol{n} \times \boldsymbol{t} = \boldsymbol{e}_z$. Here (1.23) is equivalent to homogeneous Dirichlet boundary conditions and the dot product of (1.24) represents the tangent derivative which is automatically zero due to (1.23). This means that the E-pol case has Dirichlet boundary conditions for E_z.

Applying the PEC boundary conditions to the H-pol case (1.20) will automatically satisfy (1.22b) and

$$\left(\hat{\boldsymbol{E}} \times \boldsymbol{n}\right)\Big|_{\partial\Omega} = \left(-\frac{1}{i\omega\epsilon}\nabla H_z \cdot \boldsymbol{n}\right)\Big|_{\partial\Omega} \boldsymbol{e}_z = \boldsymbol{0}. \tag{1.25}$$

The dot product of (1.25) is the normal derivative hence the H-pol case has homogeneous Neumann boundary conditions for H_z.

Interface conditions. After the problems with perfect boundary conditions, we say that the domain Ω_2 is able to support an electromagnetic field but with a different set of material parameters to Ω_1. In this case, the boundary $\partial\Omega$ becomes an interface with the following continuity conditions (again a consequence of Maxwell's equations),

$$\text{Interface conditions: } = \begin{cases} \left(\left(\hat{\boldsymbol{E}}_2 - \hat{\boldsymbol{E}}_1\right) \times \boldsymbol{n}\right)\Big|_{\partial\Omega} = \boldsymbol{0}, & \text{(1.26a)} \\ \left(\left(\epsilon_2\hat{\boldsymbol{E}}_2 - \epsilon_1\hat{\boldsymbol{E}}_1\right) \cdot \boldsymbol{n}\right)\Big|_{\partial\Omega} = 0, & \text{(1.26b)} \\ \left(\left(\hat{\boldsymbol{H}}_2 - \hat{\boldsymbol{H}}_1\right) \times \boldsymbol{n}\right)\Big|_{\partial\Omega} = \boldsymbol{0}, & \text{(1.26c)} \\ \left(\left(\mu_2\hat{\boldsymbol{H}}_2 - \mu_1\hat{\boldsymbol{H}}_1\right) \cdot \boldsymbol{n}\right)\Big|_{\partial\Omega} = 0, & \text{(1.26d)} \end{cases}$$

where the subscripts 1 and 2 correspond to the domains Ω_1 and Ω_2 respectively.

If we apply (1.26) to the E-pol case (1.19), then we find (1.26b) is automatically

satisfied and the others become,

$$(1.26a) \longrightarrow (E_{z2} - E_{z1})|_{\partial\Omega} = 0, \tag{1.27}$$

$$(1.26c) \longrightarrow \left(\left(\frac{1}{\mu_2} \nabla E_{z2} - \frac{1}{\mu_1} \nabla E_{z1} \right) \cdot \boldsymbol{n} \right) \Big|_{\partial\Omega} = 0, \tag{1.28}$$

$$(1.26d) \longrightarrow ((\nabla E_{z2} - \nabla E_{z1}) \cdot \boldsymbol{t})|_{\partial\Omega} = 0. \tag{1.29}$$

Note that if (1.27) is satisfied, then (1.29) is also satisfied as a consequence. This means that the E-pol case has the interface conditions (1.27) and (1.28).

Similarly, for the H-pol case (1.20), then we find (1.26d) is automatically satisfied and the others become,

$$(1.26a) \longrightarrow \left(\left(\frac{1}{\epsilon_2} \nabla H_{z2} - \frac{1}{\epsilon_1} \nabla H_{z1} \right) \cdot \boldsymbol{n} \right) \Big|_{\partial\Omega} = 0, \tag{1.30}$$

$$(1.26b) \longrightarrow ((\nabla H_{z2} - \nabla H_{z1}) \cdot \boldsymbol{t})|_{\partial\Omega} = 0, \tag{1.31}$$

$$(1.26c) \longrightarrow (H_{z2} - H_{z1})|_{\partial\Omega} = 0, \tag{1.32}$$

where we see that (1.31) is satisfied if (1.32) is satisfied. This means that the H-pol case has the interface conditions (1.30) and (1.32).

1.2 Mathematical formulation

In this section, we shall formally define the two types of wedge diffraction problems to be considered in this thesis from a mathematical point of view. The domain Ω_2 is an infinite wedge region and the boundary $\partial\Omega$ consists of the two wedge faces. Therefore, $\Omega_{1,2}$ and $\partial\Omega$ take the following definitions,

$$\begin{aligned}
\Omega_1 &= \{(r,\theta) : 0 \le r < \infty,\ -\theta_{\mathrm{w}} < \theta < \theta_{\mathrm{w}}\}, \\
\Omega_2 &= \{(r,\theta) : 0 \le r < \infty,\ \theta_{\mathrm{w}} < \theta < 2\pi - \theta_{\mathrm{w}}\}, \\
\partial\Omega &= \{(r,\theta) : 0 \le r < \infty,\ \theta = -\theta_{\mathrm{w}}\} \cup \{(r,\theta) : 0 \le r < \infty,\ \theta = \theta_{\mathrm{w}}\}
\end{aligned} \tag{1.33}$$

where $0 < \theta_{\rm w} < \pi$. Defining $\bar{\theta}_{\rm w} = \pi - \theta_{\rm w}$, the interior angle of the wedge scatterer is $2\bar{\theta}_{\rm w}$. This setup is illustrated in Figure 1.2. Here the boundary normal vector is $\boldsymbol{n} = \pm\boldsymbol{e}_\theta$ on $\theta = \pm\theta_{\rm w}$; hence $\nabla\Phi \cdot \boldsymbol{n} = \pm\frac{1}{r}\frac{\partial\Phi}{\partial\theta}$.

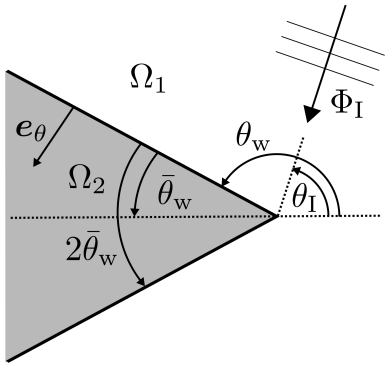

Figure 1.2: The geometry of the wedge diffraction problem where the grey region is the wedge scatterer (Ω_2) and $\Phi_{\rm I}$ is the incident plane wave.

Perfect wedge problems. In this scenario, the total wave field Φ in the host Ω_1 satisfies the homogeneous Helmholtz equation,

$$\nabla^2\Phi + k^2\Phi = 0, \tag{1.34}$$

with wavenumber k. For physical context, $\Phi = P$ in an acoustic setting (with $k = \omega/c$) and $\Phi = E_z$ or H_z in an electromagnetic setting (with $k = \omega\sqrt{\mu\epsilon}$) for the E-pol and H-pol cases respectively. There are two cases of boundary conditions for the perfect wedge problem; Dirichlet (representing sound-soft or E-pol) and Neumann (representing sound-hard or H-pol),

$$\text{Dirichlet boundary conditions:} \quad \Phi(\theta = \pm\theta_{\rm w}) = 0, \tag{1.35}$$

$$\text{Neumann boundary conditions:} \quad \frac{1}{r}\frac{\partial\Phi}{\partial\theta}(\theta = \pm\theta_{\rm w}) = 0. \tag{1.36}$$

The incident wave (illustrated in Figure 1.2) is a unit-amplitude plane wave with wavenumber k and incident angle θ_{I},

$$\Phi_{\mathrm{I}} = e^{-ikr\cos(\theta-\theta_{\mathrm{I}})}. \tag{1.37}$$

Due to the symmetry of the problem, we restrict the incident angle to $\theta_{\mathrm{I}} \in [0, \theta_{\mathrm{w}}]$. Using Geometrical Optics (GO), we can gather the incident wave and all the reflected waves to create the GO component of the total field (Φ_{GO}). The diffracted component, Φ_{Diff}, is considered to be the difference between the total field and the GO component, $\Phi_{\mathrm{Diff}} = \Phi - \Phi_{\mathrm{GO}}$ and is required to satisfy a two-dimensional radiation condition (see the review paper Schot (1992)) which we write in integral form:

$$\lim_{r\to\infty} \int_{-\theta_{\mathrm{w}}}^{\theta_{\mathrm{w}}} \left| \frac{\partial \Phi_{\mathrm{Diff}}}{\partial r} - ik\Phi_{\mathrm{Diff}} \right|^2 r \mathrm{d}\theta = 0. \tag{1.38}$$

Lastly, we will have edge conditions at the origin which are obtained by asymptotically approximating Φ as $r \to 0$. Generally, we can derive the edge conditions using the Frobenius method (see Bender and Orszag (1999) for a good treatise on the method). To start, we pose and substitute the following into (1.34),

$$\Phi = \sum_{n=0}^{\infty} a_n(\theta) r^{\alpha_n}, \quad \text{where} \quad \alpha_0 < \alpha_1 < \alpha_2 < \ldots. \tag{1.39}$$

This results in a series of ordinary differential equations to solve, for which the first two solutions are,

$$a_0(\theta) = \mathcal{B}_1 \cos(\alpha_0\theta) + \mathcal{B}_2 \sin(\alpha_0\theta), \tag{1.40}$$

$$a_1(\theta) = \mathcal{C}_1 \cos(\alpha_1\theta) + \mathcal{C}_2 \sin(\alpha_1\theta) - \frac{k^2}{4(1+\alpha_0)}(\mathcal{B}_1 \cos(\alpha_0\theta) + \mathcal{B}_2 \sin(\alpha_0\theta)), \tag{1.41}$$

where $\alpha_1 = \alpha_0 + 2$. To ensure that the energy remains finite in a small area around the wedge edge, we require $\alpha_0 \geq 0$. This can be shown by approximating $\Phi \sim a_0(\theta) r^{\alpha_0}$ and using the energy integral (with $0 < \epsilon \ll 1$),

$$\int_{-\theta_{\mathrm{w}}}^{\theta_{\mathrm{w}}} \int_0^{\epsilon} r \left|\nabla\Phi\right|^2 \mathrm{d}r\mathrm{d}\theta \quad \text{where,} \quad \left|\nabla\Phi\right|^2 = \left(\frac{\partial\Phi}{\partial r}\right)^2 + \frac{1}{r^2}\left(\frac{\partial\Phi}{\partial\theta}\right)^2. \tag{1.42}$$

Consider the Dirichlet case for now and apply the relevant boundary conditions to (1.40). For a non-trivial solution, we find that either $\mathcal{B}_1 = 0$ and $\alpha_0 = 2N\delta$ or $\mathcal{B}_2 = 0$ and $\alpha_0 = (2N+1)\delta$ where $\delta = \frac{\pi}{2\theta_\mathrm{w}}$ and $N = 0, 1, 2....$ Applying (1.35) to (1.41) will conclude that $\mathcal{C}_1 = \mathcal{C}_2 = 0$, hence the Dirichlet edge condition is

$$\Phi \underset{r\to 0}{\sim} \mathcal{B} r^{\delta} \cos(\delta\theta) + ... \tag{1.43}$$

Similarly, for the Neumann case, we find that after applying the Neumann boundary conditions to (1.40), either $\mathcal{B}_1 = 0$ and $\alpha_0 = (2N+1)\delta$ or $\mathcal{B}_2 = 0$ and $\alpha_0 = 2N\delta$ where $\delta = \frac{\pi}{2\theta_\mathrm{w}}$ and $N = 0, 1, 2....$ Applying (1.36) to (1.41) will also conclude that $\mathcal{C}_1 = \mathcal{C}_2 = 0$. Hence the Neumann edge condition is

$$\Phi \underset{r\to 0}{\sim} \mathcal{A} + \mathcal{B} r^{\delta} \sin(\delta\theta) - \frac{\mathcal{A}}{4}(kr)^2 + ... \tag{1.44}$$

Penetrable wedge problem. For this problem, the total wave solutions in Ω_1 and Ω_2 are called Φ and Ψ respectively. This means that in an acoustic setting, $\Phi = P_1$ and $\Psi = P_2$ whereas in an electromagnetic setting, $\Phi = E_{z1}$ or H_{z1} and $\Psi = E_{z2}$ or H_{z2} (depending on the choice of polarisation). These two solutions satisfy the homogeneous Helmholtz equation with wavenumbers k_1 and k_2 respectively,

$$\nabla^2\Phi + k_1^2\Phi = 0, \quad \text{in} \quad \Omega_1, \tag{1.45}$$

$$\nabla^2\Psi + k_2^2\Psi = 0, \quad \text{in} \quad \Omega_2. \tag{1.46}$$

At the two wedge faces $\theta = \pm\theta_\mathrm{w}$, we will connect Φ and Ψ by the interface conditions,

$$\Phi|_{\theta=\pm\theta_\mathrm{w}} = \Psi|_{\theta=\pi\mp\bar{\theta}_\mathrm{w}}, \quad \left.\frac{\partial\Phi}{\partial\theta}\right|_{\theta=\pm\theta_\mathrm{w}} = \lambda \left.\frac{\partial\Psi}{\partial\theta}\right|_{\theta=\pi\mp\bar{\theta}_\mathrm{w}}. \tag{1.47}$$

where the contrast parameter λ is defined as,

$$\lambda = \frac{\rho_1}{\rho_2}, \ \frac{\mu_1}{\mu_2} \ \text{ or } \ \frac{\epsilon_1}{\epsilon_2} \tag{1.48}$$

in the acoustic, E-pol or H-pol cases respectively. It was stated earlier that Chapter 5 will involve the creation of a high-contrast asymptotic approximation. By high-contrast, we are implying that the denominators in (1.48) are much larger than the numerators, hence λ is a small parameter.

The incident wave is defined the same as (1.37) but with wavenumber k_1 and only satisfies (1.45), hence it is only present in Ω_1,

$$\Phi_{\mathrm{I}} = \begin{cases} e^{-ik_1 r\cos(\theta-\theta_{\mathrm{I}})} & \text{in } \Omega_1, \\ 0 & \text{in } \Omega_2, \end{cases} \tag{1.49}$$

with $\theta_{\mathrm{I}} \geq 0$ due to the problem's symmetry. Both the total wave fields can be decomposed into GO and diffracted components. This time, the GO component (Φ_{GO} and Ψ_{GO}) includes all transmitted waves as well as the incident and reflected ones. The two diffracted components (Φ_{Diff} and Ψ_{Diff}) satisfy different radiation conditions depending on the relevant wavenumber,

$$\begin{aligned} \lim_{r\to\infty} \int_{-\theta_{\mathrm{w}}}^{\theta_{\mathrm{w}}} \left| \frac{\partial \Phi_{\mathrm{Diff}}}{\partial r} - ik_1 \Phi_{\mathrm{Diff}} \right|^2 r \mathrm{d}\theta = 0, \\ \lim_{r\to\infty} \int_{\pi-\bar{\theta}_{\mathrm{w}}}^{\pi+\bar{\theta}_{\mathrm{w}}} \left| \frac{\partial \Psi_{\mathrm{Diff}}}{\partial r} - ik_2 \Psi_{\mathrm{Diff}} \right|^2 r \mathrm{d}\theta = 0. \end{aligned} \tag{1.50}$$

Finally, we have edge conditions for both total wave fields at the origin. Following the same procedure as before, we use the following total wave approximations,

$$\Phi = \sum_{n=0}^{\infty} a_n(\theta) r^{\alpha_n}, \quad \Psi = \sum_{n=0}^{\infty} b_n(\theta-\pi) r^{\alpha_n}, \tag{1.51}$$

where $\alpha_0 < \alpha_1 < \ldots$. Continuing with the Frobenius method and considering the energy integral, we find that $\alpha_0 \geq 0$, $\alpha_1 = \alpha_0 + 2$ and we obtain the following

solutions for $a_{0,1}$ and $b_{0,1}$,

$$a_0(\theta) = \mathcal{B}_1 \cos(\alpha_0\theta) + \mathcal{B}_2 \sin(\alpha_0\theta), \tag{1.52}$$

$$b_0(\theta) = \mathcal{B}_3 \cos(\alpha_0\theta) + \mathcal{B}_4 \sin(\alpha_0\theta), \tag{1.53}$$

$$a_1(\theta) = \mathcal{C}_1 \cos(\alpha_1\theta) + \mathcal{C}_2 \sin(\alpha_1\theta) - \frac{k_1^2 a_0(\theta)}{4(1+\alpha_0)}, \tag{1.54}$$

$$b_1(\theta) = \mathcal{C}_3 \cos(\alpha_1\theta) + \mathcal{C}_4 \sin(\alpha_1\theta) - \frac{k_2^2 b_0(\theta)}{4(1+\alpha_0)}, \tag{1.55}$$

Take the case where $\alpha_0 = 0$, then after applying the boundary conditions (1.47), we determine that $\mathcal{B}_1 = \mathcal{B}_3$ (which we relabel to $\mathcal{A}$) and $\mathcal{C}_{1,2,3,4} = 0$. To find the coefficients $\mathcal{B}_{1,2,3,4}$ for the case where $\alpha_0 > 0$, we must solve the matrix equation

$$\begin{pmatrix} \cos(\alpha_0\theta_w) & 0 & -\cos(\alpha_0\bar{\theta}_w) & 0 \\ 0 & \sin(\alpha_0\theta_w) & 0 & \sin(\alpha_0\bar{\theta}_w) \\ \sin(\alpha_0\theta_w) & 0 & \lambda\sin(\alpha_0\bar{\theta}_w) & 0 \\ 0 & \cos(\alpha_0\theta_w) & 0 & -\lambda\cos(\alpha_0\bar{\theta}_w) \end{pmatrix} \begin{pmatrix} \mathcal{B}_1 \\ \mathcal{B}_2 \\ \mathcal{B}_3 \\ \mathcal{B}_4 \end{pmatrix} = \begin{pmatrix} 0 \\ 0 \\ 0 \\ 0 \end{pmatrix}. \tag{1.56}$$

A non-trivial solution is only possible provided that the determinant of the matrix is zero. This means that we need to find a value for α_0 that satisfies,

$$\left(\cot(\alpha_0\theta_w) + \lambda\cot(\alpha_0\bar{\theta}_w)\right)\left(\cot(\alpha_0\bar{\theta}_w) + \lambda\cot(\alpha_0\theta_w)\right) = 0 \tag{1.57}$$

for all given λ and θ_w. We call $\hat{\delta}$ the smallest positive solution of (1.57), then the edge conditions take the form,

$$\Phi(r,\theta) \underset{r\to 0}{\sim} \mathcal{A} + \left[\mathcal{B}_1 \cos(\widehat{\delta}\theta) + \mathcal{B}_2 \sin(\widehat{\delta}\theta)\right] r^{\widehat{\delta}} - \frac{\mathcal{A}}{4}(k_1 r)^2 + ..., \tag{1.58}$$

$$\Psi(r,\theta) \underset{r\to 0}{\sim} \mathcal{A} + \left[\mathcal{B}_3 \cos(\widehat{\delta}\theta) + \mathcal{B}_4 \sin(\widehat{\delta}\theta)\right] r^{\widehat{\delta}} - \frac{\mathcal{A}}{4}(k_2 r)^2 + ... \tag{1.59}$$

Chapter 2

Sommerfeld's half-plane problem

In this chapter, we shall introduce a core procedure for diffraction: the Wiener-Hopf (W-H) technique (Wiener and Hopf, 1931). For this introduction, we shall apply it to Sommerfeld's half-plane problem which will allow us to outline the key aspects of its implementation. This will be useful because we will use the technique in later chapters and it is important to understand the procedure. For more thorough explanation, there is an abundance of literature that applies the W-H technique to the half-plane problem (see Noble (1958), Carrier et al. (1966), Jones (1986), Crighton et al. (1992), Billingham and King (2001), Ablowitz and Fokas (2003) for example). For a historical overview as well as alternative applications of the technique, see Lawrie and Abrahams (2007).

2.1 Initialisation

In a Cartesian coordinate system, we position the half-plane on the negative x-axis where the edge of the half-plane is located at the origin (see Section 1.2 with $\theta_{\mathrm{w}} = \pi$). This half-plane is forced by a plane wave of the form (1.37), which we

rewrite in cartesian coordinates,

$$\Phi_{\mathrm{I}} = e^{-ik(x\cos(\theta_{\mathrm{I}})+y\sin(\theta_{\mathrm{I}}))}. \tag{2.1}$$

The total wave field Φ, including this incident wave, satisfies the homogeneous Helmholtz equation (1.34) and satisfies homogeneous Dirichlet (1.35) or Neumann (1.36) boundary conditions at the half-plane. See Figure 2.1 for an illustration to this problem.

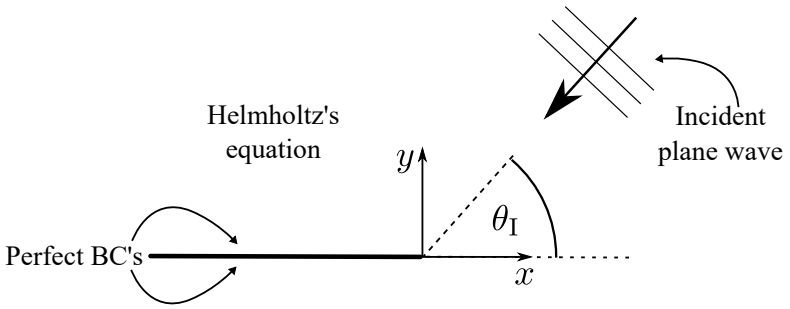

Figure 2.1: Diagram of Sommerfeld's half-plane problem including the governing equation, the plane wave forcing and the perfect (Dirichlet or Neumann) boundary conditions.

Since this problem is linear, we can decompose Φ into incident and scattered parts,

$$\Phi = \Phi_{\mathrm{I}} + \Phi_{\mathrm{S}}, \tag{2.2}$$

where the scattered wave Φ_{S} satisfies (1.34) and two cases of boundary conditions,

$$\text{Dirichlet:} \quad \Phi_{\mathrm{S}}(x<0, y=0^{\pm}) = -e^{-ikx\cos(\theta_{\mathrm{I}})}, \tag{2.3}$$

$$\text{Neumann:} \quad \frac{\partial \Phi_{\mathrm{S}}}{\partial y}(x<0, y=0^{\pm}) = ik\sin(\theta_{\mathrm{I}})e^{-ikx\cos(\theta_{\mathrm{I}})}. \tag{2.4}$$

In the Dirichlet (resp. Neumann) case, the scattered wave will be symmetric (resp. antisymmetric) with respect to y. Noting that the total wave (and hence the scattered wave) is continuously differentiable in the entire domain except across

the half-plane itself, we can use this symmetry to show that,

$$\text{Dirichlet:} \quad \frac{\partial \Phi_{\mathrm{S}}}{\partial y}(x > 0, y = 0) = 0, \tag{2.5}$$

$$\text{Neumann:} \quad \Phi_{\mathrm{S}}(x > 0, y = 0) = 0. \tag{2.6}$$

Using Geometric-Optics and polar coordinates (r, θ) can give us an impression on how the total wave (and the scattered wave) behaves in different regions of the domain. This means that we can also decompose Φ in terms of the Geometrical-Optic (GO) part Φ_{GO} and the diffracted wave Φ_{Diff},

$$\Phi = \Phi_{\mathrm{GO}} + \Phi_{\mathrm{Diff}}. \tag{2.7}$$

The GO component comprises of the incident wave and the reflection from the half-plane (which we call Φ_{R}),

$$\Phi_{\mathrm{R}} = e^{-ik(x\cos(\theta_{\mathrm{I}}) - y\sin(\theta_{\mathrm{I}}))}, \tag{2.8}$$

and is given below:

$$\Phi_{\mathrm{GO}} = \begin{cases} \Phi_{\mathrm{I}} \mp \Phi_{\mathrm{R}} & \pi - \theta_{\mathrm{I}} \leq \theta \leq \pi, \\ \Phi_{\mathrm{I}} & \theta_{\mathrm{I}} - \pi \leq \theta < \pi - \theta_{\mathrm{I}}, \\ 0 & -\pi \leq \theta < \theta_{\mathrm{I}} - \pi, \end{cases} \tag{2.9}$$

where the upper and lower signs indicate the Dirichlet and Neumann cases respectively. Figure 2.2 visualises the different geometrical regions of (2.9). To prevent incoming radiation, the diffracted wave must satisfy the two-dimensional Sommerfeld-Radiation condition defined by (1.38) (with $\theta_{\mathrm{w}} = \pi$). This radiation condition means that the diffracted wave has the following behaviour as $kr \to \infty$:

$$\Phi_{\mathrm{Diff}} = O\left(\frac{e^{ikr}}{\sqrt{kr}}\right). \tag{2.10}$$

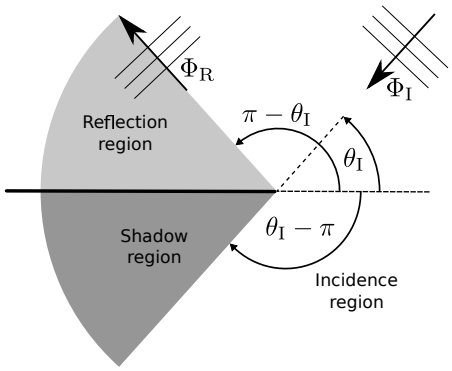

Figure 2.2: Diagram of the different geometrical regions. Here the solid black line is the half-plane scatterer, the dark-grey sector is where the half-plane has created a shadow from the incident wave and the light grey sector indicates the region that includes the reflection from the half-plane.

(2.2), (2.7) and (2.9) can be used to decompose the scattered wave in terms of the GO components and the diffracted wave,

$$\Phi_S = \Phi_{Diff} + \begin{cases} \mp\Phi_R & \pi - \theta_I \leq \theta \leq \pi, \\ 0 & \theta_I - \pi \leq \theta < \pi - \theta_I, \\ -\Phi_I & -\pi \leq \theta < \theta_I - \pi, \end{cases} \tag{2.11}$$

where the upper and lower signs indicate the Dirichlet and Neumann cases respectively.

As $r \to 0$, the total wave field has edge conditions defined by the Frobenius method (see (1.43) and (1.44) with $\theta_w = \pi$),

$$\text{Dirichlet:} \quad \Phi = O\left(r^{\frac{1}{2}} \cos\left(\theta/2\right)\right), \tag{2.12}$$

$$\text{Neumann:} \quad \Phi = \mathcal{A} + O\left(r^{\frac{1}{2}} \sin\left(\theta/2\right)\right), \tag{2.13}$$

where $\mathcal{A}$ is constant. Considering that the asymptotic behaviour of Φ_I as $r \to 0$ is $\Phi_I = 1 + O(r)$, the edge conditions for the scattered wave are

$$\text{Dirichlet:} \quad \Phi_S = -1 + O\left(r^{\frac{1}{2}} \cos\left(\theta/2\right)\right), \tag{2.14}$$

$$\text{Neumann:} \quad \Phi_S = \mathcal{A} - 1 + O\left(r^{\frac{1}{2}} \sin\left(\theta/2\right)\right). \tag{2.15}$$

2.2 Wiener-Hopf (W-H) technique

For the implementation of this technique, we replace all occurrences of k with $\hat{k}$. This is the same wavenumber but with a tiny positive imaginary increment (i.e. $\hat{k} = k + 0i$). To proceed, we Fourier transform[1] the x coordinate by the following definition and associated inverse,

$$U(\eta, y) = \int_{-\infty}^{\infty} \Phi_{\mathrm{S}}(x, y) e^{i\hat{k}\eta x} \mathrm{d}x, \quad \Phi_{\mathrm{S}}(x, y) = \frac{\hat{k}}{2\pi} \int_{-\infty+0i}^{\infty-0i} U(\eta, y) e^{-i\hat{k}\eta x} \mathrm{d}\eta, \tag{2.16}$$

where the inverse contour runs above the negative real axis and below the positive real axis. We also define the half-range Fourier transforms by the identity $U(\eta, y) = U_+(\eta, y) + U_-(\eta, y)$,

$$U_+(\eta, y) = \int_0^{\infty} \Phi_{\mathrm{S}}(x, y) e^{i\hat{k}\eta x} \mathrm{d}x, \quad U_-(\eta, y) = \int_{-\infty}^{0} \Phi_{\mathrm{S}}(x, y) e^{i\hat{k}\eta x} \mathrm{d}x. \tag{2.17}$$

Note (2.11) implies that as $|x| \to \infty$ (regardless of the sign of y),

$$\Phi_{\mathrm{S}} = \begin{cases} O\left(\frac{e^{i\hat{k}x}}{(\hat{k}x)^{\frac{1}{2}}}\right) & x \to \infty, \\ O\left(e^{-i\hat{k}x\cos(\theta_{\mathrm{I}})}\right) & x \to -\infty, \end{cases} \tag{2.18}$$

By considering the imaginary increment of $\hat{k}$ and (2.18), we can determine that,

$$\Phi_{\mathrm{S}} e^{i\hat{k}\eta x} = O\left(\frac{e^{i\hat{k}x(\eta+1)}}{(\hat{k}x)^{\frac{1}{2}}}\right)$$

as $x \to \infty$. This is bounded if $\arg(\eta + 1) \in [0, \pi)$. This means that U_+ is analytic for all y on the domain $\eta \in \mathcal{R}_+$. where $\mathcal{R}_+$ is the upper half-plane (UHP) domain

$$\mathcal{R}_+ = \{\eta : \mathrm{Im}\{\eta\} > 0\} \cup \{\eta : \mathrm{Re}\{\eta\} > -1, \mathrm{Im}\{\eta\} = 0\}. \tag{2.19}$$

Similarly as $x \to -\infty$, we have

$$\Phi_{\mathrm{S}} e^{i\hat{k}\eta x} = O\left(e^{i\hat{k}x(\eta - \cos(\theta_{\mathrm{I}}))}\right)$$

[1]Note that this is not the classic definition of the Fourier transform. We include $\hat{k}$ in the exponential to stay consistent with what is done in later chapters and make the algebra easier.

which is bounded if η is in the lower half-plane (LHP) domain,

$$\mathcal{R}_- = \{\eta : \mathrm{Im}\{\eta\} < 0\} \cup \{\eta : \mathrm{Re}\{\eta\} < \cos(\theta_\mathrm{I}), \mathrm{Im}\{\eta\} = 0\}, \tag{2.20}$$

hence U_- is analytic on the domain $\eta \in \mathcal{R}_-$. This means that the full-range Fourier Transform U is analytic on the intersection $\eta \in \mathcal{R}_+ \cap \mathcal{R}_-$ where,

$$\mathcal{R}_+ \cap \mathcal{R}_- = \{\eta : -1 < \mathrm{Re}\{\eta\} < \cos(\theta_\mathrm{I}), \mathrm{Im}\{\eta\} = 0\}, \tag{2.21}$$

Figure 2.3 contains diagrams of the two half-planes $\mathcal{R}_+$ and $\mathcal{R}_-$.

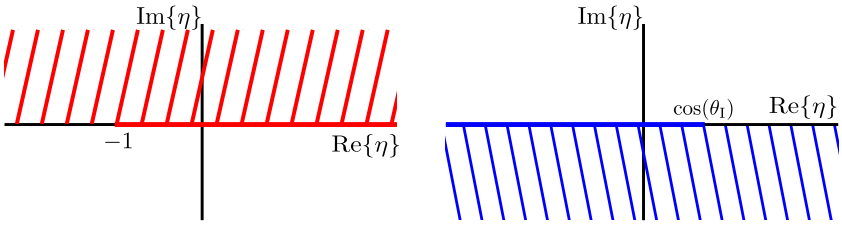

Figure 2.3: Illustration of the upper half-plane $\mathcal{R}_+$ (left) and the lower half-plane $\mathcal{R}_-$ (right) given by (2.19) and (2.20) respectively.

We can also use (2.18) to show that

$$\lim_{x\to\pm\infty}\left[\left(\frac{\partial\Phi_\mathrm{S}}{\partial x} - i\hat{k}\eta\Phi_\mathrm{S}\right)e^{i\hat{k}\eta x}\right] = 0, \tag{2.22}$$

when $\eta \in \mathcal{R}_+ \cap \mathcal{R}_-$, because $\mathrm{Im}\left\{\hat{k}\right\} > 0$. Then the transformed Helmholtz equation is

$$\frac{\partial^2 U}{\partial y^2} + \hat{k}^2\left(1-\eta^2\right)U = 0, \tag{2.23}$$

which has the following general solution:

$$U(\eta, y) = F_1(\eta)e^{i\hat{k}\left(1-\eta^2\right)^{\frac{1}{2}}y} + F_2(\eta)e^{-i\hat{k}\left(1-\eta^2\right)^{\frac{1}{2}}y}. \tag{2.24}$$

We define the branch cuts of the kernel components $(1\mp\eta)^{\frac{1}{2}}$ to be from $\eta = \pm 1$ to $\eta = \pm\infty$ respectively (see Figure 2.4) such that $\arg\left((1\mp\eta)^{\frac{1}{2}}\right) = 0$ for all η on $\mathcal{R}_+ \cap \mathcal{R}_-$.

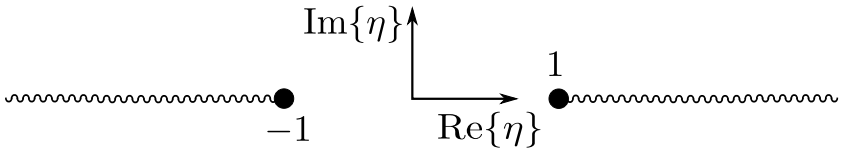

Figure 2.4: Branch cuts of the kernel components $(1 \mp \eta)^{\frac{1}{2}}$ starting from $\eta = \pm 1$.

Inspired by Wegert (2012), a colourful way to illustrate the chosen branch of the kernel is to use programs such as MATLAB to create phase portraits. These portraits assign the complex argument of a function to a HSV colour model. Figure 2.5 (left) demonstrates these phase portraits by plotting the function $f(z) = z$. To program the kernel correctly, we need to type the square root parts separately. Figure 2.5 (right) is a phase portrait of the kernel written as separate square roots, $(1-\eta)^{\frac{1}{2}}(1+\eta)^{\frac{1}{2}}$. Using phase portraits has been very useful throughout the PhD and more portraits will appear later in the thesis.

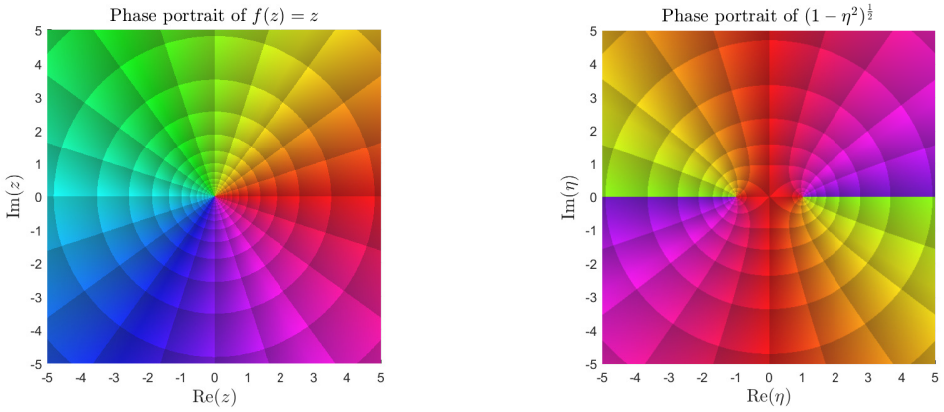

Figure 2.5: A demonstration of phase portraits via the function $f(z) = z$ (left). The second phase portrait is of the kernel written as separate square root functions, $(1-\eta)^{\frac{1}{2}}(1+\eta)^{\frac{1}{2}}$ (right). In these plots, red indicates that the complex argument of the function is 0, green indicates the argument to be $\pi/2$, cyan indicates $\pm\pi$ and so on.

In the chosen branch, the kernel factor $(1+\eta)^{\frac{1}{2}}$ (resp. $(1-\eta)^{\frac{1}{2}}$) is analytic in the subset of the η-plane including $\mathcal{R}_+$ (resp. $\mathcal{R}_-$). Recalling the positive imaginary part of $\hat{k}$, we find that the exponentials $e^{\pm i\hat{k}(1-\eta^2)^{\frac{1}{2}}y}$ decay to zero as $y \to \pm\infty$

when $\eta \in \mathcal{R}_+ \cap \mathcal{R}_-$ (because $(1-\eta^2)^{\frac{1}{2}}$ is real and positive on this segment). To keep (2.24) bounded as $|y| \to \infty$, we want $F_1(\eta) = 0$ when $y < 0$ and $F_2(\eta) = 0$ when $y > 0$. This means that the general solution,

$$U(\eta, y) = \begin{cases} F_1(\eta) e^{i\hat{k}\left(1-\eta^2\right)^{\frac{1}{2}} y} & y > 0, \\ F_2(\eta) e^{-i\hat{k}\left(1-\eta^2\right)^{\frac{1}{2}} y} & y < 0, \end{cases} \tag{2.25}$$

is used in the W-H technique with the unknowns $F_1(\eta)$ and $F_2(\eta)$.

2.2.1 Dirichlet case

For the Dirichlet case, we have the following unique conditions:

- (Boundary conditions) $\Phi_{\mathrm{S}}(x < 0, y = 0^{\pm}) = -e^{-i\hat{k}x\cos(\theta_{\mathrm{I}})}$.
- (Symmetry) Φ_{S} is symmetric[2] about $y = 0$ for all x and satisfies (2.5).
- (Edge conditions) $\Phi_{\mathrm{S}} = -1 + O\left(r^{\frac{1}{2}}\cos(\theta/2)\right)$ as $r \to 0$.

The symmetry condition implies that $U(\eta, y)$ is also symmetric about $y = 0$ for all η. This means that $F_1(\eta) = F_2(\eta)$. For simplicity, we drop the subscripts, then (2.25) becomes

$$U(\eta, y) = F(\eta) e^{i\hat{k}\left(1-\eta^2\right)^{\frac{1}{2}}|y|}. \tag{2.26}$$

Recall the definitions (2.17) which are analytic when η lies in the half-planes $\mathcal{R}_+$ and $\mathcal{R}_-$ respectively. These are used to create the following two functions:

$$\begin{aligned} V_+(\eta, y) &= \frac{1}{2}\left[\frac{\partial U_+}{\partial y}(\eta, y) - \frac{\partial U_+}{\partial y}(\eta, -y)\right], \\ V_-(\eta, y) &= \frac{1}{2}\left[\frac{\partial U_-}{\partial y}(\eta, y) - \frac{\partial U_-}{\partial y}(\eta, -y)\right]. \end{aligned} \tag{2.27}$$

[2]To see the symmetry we decompose Φ_{S} into its odd and even parts, and show that the odd part satisfies homogeneous Helmholtz equation, homogeneous Dirichlet boundary conditions and the radiation condition. Hence by uniqueness, the odd part has to be zero.

Note that $V_+(\eta, y)$ (resp. $V_-(\eta, y)$) is analytic when η is in the half-planes $\mathcal{R}_+$ (resp. $\mathcal{R}_-$). We use the identity $U(\eta, y) = U_+(\eta, y) + U_-(\eta, y)$, (2.26) and (2.27) to determine that at $y = 0^+$

$$U_+(\eta, 0^+) + U_-(\eta, 0^+) = F(\eta), \tag{2.28}$$

$$V_+(\eta, 0^+) + V_-(\eta, 0^+) = i\hat{k}\left(1 - \eta^2\right)^{\frac{1}{2}} F(\eta), \tag{2.29}$$

then we cancel out the unknown $F(\eta)$ to produce the W-H equation,

$$V_+(\eta, 0^+) + V_-(\eta, 0^+) = i\hat{k}\left(1 - \eta^2\right)^{\frac{1}{2}} \left[U_+(\eta, 0^+) + U_-(\eta, 0^+)\right]. \tag{2.30}$$

We can apply (2.5) to determine that $V_+(\eta, 0^+) = 0$. We can also evaluate $U_-(\eta, 0^+)$ using the boundary conditions (2.3),

$$U_-(\eta, 0^+) = -\int_{-\infty}^{0} e^{i\hat{k}x(\eta - \cos(\theta_\mathrm{I}))} \mathrm{d}x,$$

where the lower limit goes to zero when $\eta \in \mathcal{R}_-$ and hence

$$U_-(\eta, 0^+) = \frac{i}{\hat{k}(\eta - \cos(\theta_\mathrm{I}))}. \tag{2.31}$$

This means that the W-H equation (2.30) is simplified to

$$V_-(\eta, 0^+) = i\hat{k}\left(1 - \eta^2\right)^{\frac{1}{2}} U_+(\eta, 0^+) - \frac{(1 - \eta^2)^{\frac{1}{2}}}{(\eta - \cos(\theta_\mathrm{I}))}. \tag{2.32}$$

To continue with the W-H technique, we need to rewrite (2.32) such that one set of terms are analytic on $\mathcal{R}_+$ and the rest are analytic on $\mathcal{R}_-$. We divide (2.32) by $(1 - \eta)^{\frac{1}{2}}$ to factorise the kernel $(1 - \eta^2)^{\frac{1}{2}}$,

$$\frac{V_-(\eta, 0^+)}{(1 - \eta)^{\frac{1}{2}}} = i\hat{k}(1 + \eta)^{\frac{1}{2}} U_+(\eta, 0^+) - \frac{(1 + \eta)^{\frac{1}{2}}}{\eta - \cos(\theta_\mathrm{I})}. \tag{2.33}$$

The left hand side is analytic on the domain $\mathcal{R}_-$ and the first term on the right hand side is analytic on $\mathcal{R}_+$. The second term on the right hand side is only

analytic on the intersection $\mathcal{R}_+ \cap \mathcal{R}_-$ because it has a branch point at $\eta = -1$ and a pole at $\eta = \cos(\theta_\mathrm{I})$.

To make the right hand side of (2.33) analytic on $\mathcal{R}_+$, the pole must be cancelled out without affecting the analyticity of the left hand side. We achieve this by adding the following on both sides of (2.33),

$$\frac{(1+\cos(\theta_\mathrm{I}))^{\frac{1}{2}}}{\eta - \cos(\theta_\mathrm{I})}.$$

Then the W-H equation becomes

$$\frac{V_-(\eta, 0^+)}{(1-\eta)^{\frac{1}{2}}} + \frac{(1+\cos(\theta_\mathrm{I}))^{\frac{1}{2}}}{\eta - \cos(\theta_\mathrm{I})} = i\hat{k}(1+\eta)^{\frac{1}{2}} U_+(\eta, 0^+) - \frac{(1+\eta)^{\frac{1}{2}} - (1+\cos(\theta_\mathrm{I}))^{\frac{1}{2}}}{\eta - \cos(\theta_\mathrm{I})}. \tag{2.34}$$

The pole on the right hand side of (2.34) is now a removable singularity because

$$\lim_{\eta \to \cos(\theta_\mathrm{I})} \frac{(1+\eta)^{\frac{1}{2}} - (1+\cos(\theta_\mathrm{I}))^{\frac{1}{2}}}{\eta - \cos(\theta_\mathrm{I})} = \frac{1}{2}\left(1+\cos(\theta_\mathrm{I})\right)^{-\frac{1}{2}}.$$

This means that the left hand side of (2.34) is analytic in $\mathcal{R}_-$ and the right hand side is analytic in $\mathcal{R}_+$.

The final part of the W-H technique requires us to apply Liouville's theorem on the piecewise function

$$\Psi(\eta) = \begin{cases} \text{RHS}(2.34) & \eta \in \mathcal{R}_+, \\ \text{LHS}(2.34) & \eta \in \mathcal{R}_-, \\ (2.34) & \eta \in \mathcal{R}_+ \cap \mathcal{R}_-, \end{cases} \tag{2.35}$$

which, by analytic continuation, is an entire function. To use Liouville's theorem, we need to show that $\Psi(\eta)$ is bounded as $|\eta| \to \infty$. This behaviour is determined by the edge conditions and the following lemma (see Noble (1958)).

Lemma 1 *If $\mu > -1$ and $g(x)$ has the following behaviour as $x \to 0$,*

$$g(x) = O(|x|^\mu),$$

then for the Fourier Transforms,

$$G_+(\eta) = \int_0^\infty g(x)e^{i\hat{k}\eta x}dx, \quad G_-(\eta) = \int_{-\infty}^0 g(x)e^{i\hat{k}\eta x}dx,$$

we have the following behaviour as $|\eta| \to \infty$ *in* $\mathcal{R}_+$ *and* $\mathcal{R}_-$ *respectively,*

$$G_+(\eta) = O(|\eta|^{-\mu-1}), \quad G_-(\eta) = O(|\eta|^{-\mu-1}).$$

Using the definitions (2.17) and (2.27), we apply Lemma 1 to the Dirichlet edge condition (2.14) to show that as $|\eta| \to \infty$ in $\mathcal{R}_+$ and $\mathcal{R}_-$ respectively,

$$U_+(\eta, 0^+) = O\left(|\eta|^{-1}\right), \quad V_-(\eta, 0^+) = O\left(|\eta|^{-\frac{1}{2}}\right). \tag{2.36}$$

This means that $\Psi(\eta)$ has the following behaviour as $|\eta| \to \infty$

$$\Psi(\eta) = \begin{cases} O\left(|\eta|^{-\frac{1}{2}}\right) & \eta \in \mathcal{R}_+, \\ O\left(|\eta|^{-1}\right) & \eta \in \mathcal{R}_-, \end{cases} \tag{2.37}$$

hence $\Psi(\eta)$ is also bounded. Liouville's theorem is stated below.

Theorem 2 (Liouville's theorem) *Let* $f : \mathbb{C} \to \mathbb{C}$ *be an entire function. If there exists some real number* $M \geq 0$ *such that* $|f(z)| \leq M$ *for all* $z \in \mathbb{C}$*, then* f *is a constant function.*

The application of Liouville's theorem concludes that $\Psi(\eta)$ is constant. The decaying behaviour (2.37) implies that this constant is zero. This solves the W-H equation and allows us to conclude that,

$$U(\eta, y) = \frac{i\sqrt{2}\cos(\theta_{\mathrm{I}}/2)e^{i\hat{k}\left(1-\eta^2\right)^{\frac{1}{2}}|y|}}{\hat{k}(1+\eta)^{\frac{1}{2}}(\eta - \cos(\theta_{\mathrm{I}}))}. \tag{2.38}$$

Finally, we use the inverse formula for the Fourier Transform (2.16) to obtain the integral formula for the scattered wave,

$$\Phi_{\mathrm{S}}(x, y) = \frac{i\cos(\theta_{\mathrm{I}}/2)}{\sqrt{2}\pi} \int_{-\infty+0i}^{\infty-0i} \frac{e^{-i\hat{k}\left(\eta x - \left(1-\eta^2\right)^{\frac{1}{2}}|y|\right)}}{(1+\eta)^{\frac{1}{2}}(\eta - \cos(\theta_{\mathrm{I}}))} \mathrm{d}\eta. \tag{2.39}$$

Hence we found the integral solution to Sommerfeld's half-plane problem with Dirichlet boundary conditions.

2.2.2 Neumann case

For the Neumann case, we have the following unique conditions:

- (Boundary condition) $\frac{\partial \Phi_S}{\partial y}(x<0, y=0^{\pm}) = i\hat{k}\sin(\theta_I)e^{-i\hat{k}x\cos(\theta_I)}$.
- (Symmetry) Φ_S is anti-symmetric[3] about $y=0$ for all x and satisfies (2.6).
- (Edge Condition) $\Phi_S = \mathcal{A} - 1 + O\left(r^{\frac{1}{2}}\sin(\theta/2)\right)$ as $r \to 0$

The symmetry condition implies that $U(\eta, y)$ is also anti-symmetric about $y=0$ for all η. This means that $F_1(\eta) = -F_2(\eta)$. As before, we drop the subscripts and (2.25) becomes,

$$U(\eta, y) = \text{sgn}(y)F(\eta)e^{i\hat{k}\left(1-\eta^2\right)^{\frac{1}{2}}|y|}. \tag{2.40}$$

where $\text{sgn}(y)$ is the sign function,

$$\text{sgn}(y) = \frac{y}{|y|} = \begin{cases} 1 & y > 0, \\ -1 & y < 0, \end{cases} \tag{2.41}$$

Recall the definitions (2.17) which are analytic when $\eta \in \mathcal{R}_+$ and $\mathcal{R}_-$ respectively. These are used to create the following two functions,

$$\begin{aligned} V_+(\eta, y) &= \frac{1}{2}\left[U_+(\eta, y) - U_+(\eta, -y)\right], \\ V_-(\eta, y) &= \frac{1}{2}\left[U_-(\eta, y) - U_-(\eta, -y)\right]. \end{aligned} \tag{2.42}$$

Note that $V_+(\eta, y)$ (resp. $V_-(\eta, y)$) is analytic when η lies in $\mathcal{R}_+$ (resp. $\mathcal{R}_-$). We use the identity $U(\eta, y) = U_+(\eta, y) + U_-(\eta, y)$, (2.40) and (2.42) to determine that when $y = 0^+$,

$$V_+(\eta, 0^+) + V_-(\eta, 0^+) = F(\eta), \tag{2.43}$$

$$\frac{\partial U_+}{\partial y}(\eta, 0^+) + \frac{\partial U_-}{\partial y}(\eta, 0^+) = i\hat{k}(1-\eta^2)^{\frac{1}{2}}F(\eta), \tag{2.44}$$

[3] As before, to see the symmetry we decompose Φ_S into its odd and even parts, and show that the even part satisfies homogeneous Helmholtz equation, homogeneous Neumann boundary conditions and the radiation condition. Hence by uniqueness, the even part has to be zero.

then we cancel out the unknown $F(\eta)$ to produce the W-H equation,

$$\frac{\partial U_+}{\partial y}(\eta, 0^+) + \frac{\partial U_-}{\partial y}(\eta, 0^+) = i\hat{k}\left(1-\eta^2\right)^{\frac{1}{2}}\left[V_+(\eta, 0^+) + V_-(\eta, 0^+)\right]. \tag{2.45}$$

We apply (2.6) to show that $V_+(\eta, 0^+) = 0$. We can also evaluate $\frac{\partial U_-}{\partial y}(\eta, 0^+)$ by transforming the boundary conditions (2.4),

$$\frac{\partial U_-}{\partial y}(\eta, 0^+) = i\hat{k}\sin(\theta_{\mathrm{I}})\int_{-\infty}^{0} e^{i\hat{k}x(\eta-\cos(\theta_{\mathrm{I}}))}\mathrm{d}x.$$

The integral converges when $\eta \in \mathcal{R}_-$,

$$\frac{\partial U_-}{\partial y}(\eta, 0^+) = \frac{\sin(\theta_{\mathrm{I}})}{\eta - \cos(\theta_{\mathrm{I}})}. \tag{2.46}$$

Hence the W-H equation (2.45) is simplified to,

$$\frac{\partial U_+}{\partial y}(\eta, 0^+) + \frac{\sin(\theta_{\mathrm{I}})}{\eta - \cos(\theta_{\mathrm{I}})} = i\hat{k}\left(1-\eta^2\right)^{\frac{1}{2}} V_-(\eta, 0^+). \tag{2.47}$$

As before with the Dirichlet case, we need to rewrite (2.47) such that one set of terms are analytic on $\mathcal{R}_+$ and the rest are analytic on $\mathcal{R}_-$. We factorise the kernel $(1-\eta^2)^{\frac{1}{2}}$ and divide (2.47) by $(1+\eta)^{\frac{1}{2}}$,

$$\frac{1}{(1+\eta)^{\frac{1}{2}}}\frac{\partial U_+}{\partial y}(\eta, 0^+) + \frac{\sin(\theta_{\mathrm{I}})}{(1+\eta)^{\frac{1}{2}}(\eta - \cos(\theta_{\mathrm{I}}))} = i\hat{k}(1-\eta)^{\frac{1}{2}} V_-(\eta, 0^+). \tag{2.48}$$

The right hand side is analytic on the domain $\mathcal{R}_-$ and the first term on the left hand side is analytic on $\mathcal{R}_+$. The second term on the left hand side is only analytic on the intersection $\mathcal{R}_+ \cap \mathcal{R}_-$ because it has a branch point at $\eta = -1$ and a pole at $\eta = \cos(\theta_{\mathrm{I}})$.

To make the whole left hand side of (2.48) analytic on $\mathcal{R}_+$, this pole at $\eta = \cos(\theta_{\mathrm{I}})$ is cancelled out by adding the following on both sides of (2.48),

$$-\frac{\sin(\theta_{\mathrm{I}})}{(1+\cos(\theta_{\mathrm{I}}))^{\frac{1}{2}}(\eta - \cos(\theta_{\mathrm{I}}))}.$$

Then the W-H equation becomes

$$\frac{1}{(1+\eta)^{\frac{1}{2}}}\frac{\partial U_+}{\partial y}(\eta,0^+)+\frac{\sin(\theta_{\mathrm{I}})}{(\eta-\cos(\theta_{\mathrm{I}}))}\left[\frac{1}{(1+\eta)^{\frac{1}{2}}}-\frac{1}{(1+\cos(\theta_{\mathrm{I}}))^{\frac{1}{2}}}\right]$$
$$=i\hat{k}(1-\eta)^{\frac{1}{2}}V_-(\eta,0^+)-\frac{\sin(\theta_{\mathrm{I}})}{(1+\cos(\theta_{\mathrm{I}}))^{\frac{1}{2}}(\eta-\cos(\theta_{\mathrm{I}}))}. \quad (2.49)$$

The pole on the left hand side of (2.49) is now a removable singularity with the assigned value,

$$\lim_{\eta\to\cos(\theta_{\mathrm{I}})}\frac{(1+\eta)^{-\frac{1}{2}}-(1+\cos(\theta_{\mathrm{I}}))^{-\frac{1}{2}}}{(\eta-\cos(\theta_{\mathrm{I}}))}=-\frac{1}{2}(1+\cos(\theta_{\mathrm{I}}))^{-\frac{3}{2}}.$$

This means that the left hand side of (2.49) is analytic in $\mathcal{R}_+$ and the right hand side is analytic in $\mathcal{R}_-$.

Finishing the W-H technique requires us to apply Liouville's theorem on the piecewise function

$$\Psi(\eta)=\begin{cases}\text{LHS}(2.49) & \eta\in\mathcal{R}_+,\\ \text{RHS}(2.49) & \eta\in\mathcal{R}_-,\\ (2.49) & \eta\in\mathcal{R}_+\cap\mathcal{R}_-,\end{cases} \quad (2.50)$$

which is an entire function by analytic continuation. Before Liouville's theorem is applied however, we need to show that $\Psi(\eta)$ is bounded as $|\eta|\to\infty$. Using the definitions (2.17) and (2.42), we apply Lemma 1 to the Neumann edge condition (2.15) to show that as $|\eta|\to\infty$ in $\mathcal{R}_+$ and $\mathcal{R}_-$ respectively,

$$\frac{\partial U_+}{\partial y}(\eta,0^+)=O\left(|\eta|^{-\frac{1}{2}}\right),\quad V_-(\eta,0^+)=O\left(|\eta|^{-1}\right). \quad (2.51)$$

This implies that $\Psi(\eta)$ has the following behaviour as $|\eta|\to\infty$,

$$\Psi(\eta)=\begin{cases}O\left(|\eta|^{-1}\right) & \eta\in\mathcal{R}_+,\\ O\left(|\eta|^{-\frac{1}{2}}\right) & \eta\in\mathcal{R}_-,\end{cases} \quad (2.52)$$

hence $\Psi(\eta)$ is also bounded. As before, we apply Liouville's theorem and consider the decaying behaviour (2.52) to conclude that $\Psi(\eta) \equiv 0$. We use this to find the transformed solution of the scattered wave,

$$U(\eta, y) = \frac{\operatorname{sgn}(y)\sqrt{2}\sin(\theta_{\mathrm{I}}/2)e^{i\hat{k}\left(1-\eta^2\right)^{\frac{1}{2}}|y|}}{i\hat{k}(1-\eta)^{\frac{1}{2}}(\eta-\cos(\theta_{\mathrm{I}}))}. \tag{2.53}$$

Finally, we use the inverse formula for the Fourier Transform (2.16) to obtain the integral formula for the scattered wave,

$$\Phi_{\mathrm{S}}(x, y) = \frac{\operatorname{sgn}(y)\sin(\theta_{\mathrm{I}}/2)}{\sqrt{2}\pi i}\int_{-\infty+0i}^{\infty-0i} \frac{e^{-i\hat{k}\left(\eta x-\left(1-\eta^2\right)^{\frac{1}{2}}|y|\right)}}{(1-\eta)^{\frac{1}{2}}(\eta-\cos(\theta_{\mathrm{I}}))}\mathrm{d}\eta. \tag{2.54}$$

Hence we found the integral solution to Sommerfeld's half-plane problem with Neumann boundary conditions.

2.3 Fresnel integral formulation

In this section, we write the two integral solutions (2.39) and (2.54) in terms of Fresnel integrals. We start by neglecting the imaginary part of $\hat{k}$ and defining the general form of the scattered wave,

$$\Phi_{\mathrm{S}}(x, y) = \int_{-\infty+0i}^{\infty-0i} \frac{f(\eta, y)}{\eta-\cos(\theta_{\mathrm{I}})}e^{-ik\left(\eta x-\left(1-\eta^2\right)^{\frac{1}{2}}|y|\right)}\mathrm{d}\eta, \tag{2.55}$$

where $f(\eta, y)$ will have two definitions depending on the type of boundary condition,

$$\begin{aligned} \text{Dirichlet boundary condition:} \quad & f(\eta, y) = \frac{i\cos(\theta_{\mathrm{I}}/2)}{\sqrt{2}\pi(1+\eta)^{\frac{1}{2}}}, \\ \text{Neumann boundary condition:} \quad & f(\eta, y) = \frac{\operatorname{sgn}(y)\sin(\theta_{\mathrm{I}}/2)}{\sqrt{2}\pi i(1-\eta)^{\frac{1}{2}}}. \end{aligned} \tag{2.56}$$

The integration contour (displayed in Figure 2.6) runs above the branch point at $\eta = -1$, below the simple pole at $\eta = \cos(\theta_{\mathrm{I}})$ and below the branch point at $\eta = 1$.

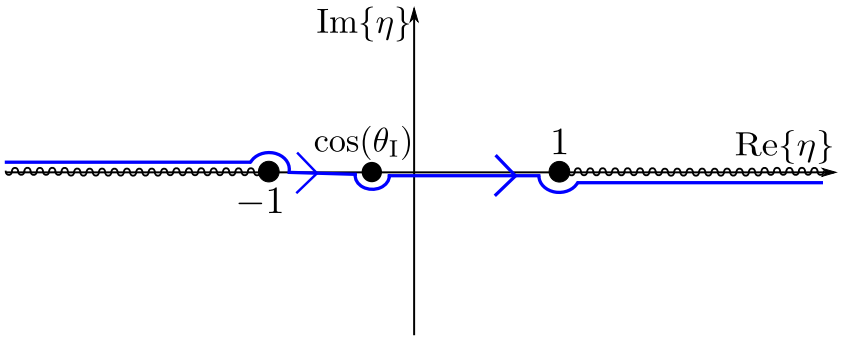

Figure 2.6: The integration path of the inverse Fourier transform where navigation around the three singularities of the integrand $\eta = \pm 1$ and $\cos(\theta_{\mathrm{I}})$ is shown.

Define $\mathcal{F}(z)$ as the Fresnel integral (see section 7.3 in Abramowitz and Stegun (1967) for other definitions),

$$\mathcal{F}(z) = \int_0^z e^{i\tau^2} \mathrm{d}\tau. \tag{2.57}$$

We follow a procedure detailed in Noble (1958), involving converting to polar coordinates, transforming (2.55) with $\eta = \cos(z)$ and using standard complex integration techniques. This allows us to rewrite the scattered wave (2.55) in terms of Fresnel integrals,

$$\begin{aligned}\Phi_{\mathrm{S}}(r,\theta) = & -\Phi_{\mathrm{I}}\left[\frac{1}{2} - \pi^{-\frac{1}{2}} e^{-\frac{i\pi}{4}} \mathcal{F}\left((2kr)^{\frac{1}{2}} \cos\left(\frac{1}{2}(\theta - \theta_{\mathrm{I}})\right)\right)\right] \\ & \mp \Phi_{\mathrm{R}}\left[\frac{1}{2} - \pi^{-\frac{1}{2}} e^{-\frac{i\pi}{4}} \mathcal{F}\left((2kr)^{\frac{1}{2}} \cos\left(\frac{1}{2}(\theta + \theta_{\mathrm{I}})\right)\right)\right].\end{aligned} \tag{2.58}$$

where the upper and lower signs are for the Dirichlet and Neumann cases respectively. Finally, the total wave field Φ is written as,

$$\begin{aligned}\Phi(r,\theta) = & \Phi_{\mathrm{I}}\left[\frac{1}{2} + \pi^{-\frac{1}{2}} e^{-\frac{i\pi}{4}} \mathcal{F}\left((2kr)^{\frac{1}{2}} \cos\left(\frac{1}{2}(\theta - \theta_{\mathrm{I}})\right)\right)\right] \\ & \mp \Phi_{\mathrm{R}}\left[\frac{1}{2} - \pi^{-\frac{1}{2}} e^{-\frac{i\pi}{4}} \mathcal{F}\left((2kr)^{\frac{1}{2}} \cos\left(\frac{1}{2}(\theta + \theta_{\mathrm{I}})\right)\right)\right],\end{aligned} \tag{2.59}$$

By using the asymptotic expansion for Fresnel integrals with large argument,

$$\mathcal{F}(z) = \frac{\mathrm{sgn}(z)}{2}\sqrt{\pi} e^{\frac{i\pi}{4}} + \frac{e^{iz^2 - \frac{i\pi}{2}}}{2z}\left[1 + O\left(\frac{1}{z^2}\right)\right], \quad \text{as} \quad z \to \pm\infty \tag{2.60}$$

we can obtain a high-frequency/far-field approximation ($kr \to \infty$) of the total wave field (2.59),

$$\Phi(r,\theta) \underset{kr\to\infty}{\sim} \mathcal{H}(\theta-\theta_{\mathrm{I}}+\pi)\Phi_{\mathrm{I}} \mp \mathcal{H}(\theta+\theta_{\mathrm{I}}-\pi)\Phi_{\mathrm{R}} + \frac{e^{ikr-\frac{3i\pi}{4}}}{2\sqrt{2\pi kr}}\left[\frac{1}{\cos\left(\frac{1}{2}(\theta-\theta_{\mathrm{I}})\right)} \pm \frac{1}{\cos\left(\frac{1}{2}(\theta+\theta_{\mathrm{I}})\right)}\right], \tag{2.61}$$

where $\mathcal{H}(z)$ is the Heaviside function. This formula is also known as the geometrical theory of diffraction (GTD) approximation. Key components of the GTD approximation include the GO component,

$$\Phi_{\mathrm{GO}} = \mathcal{H}(\theta-\theta_{\mathrm{I}}+\pi)\Phi_{\mathrm{I}} \mp \mathcal{H}(\theta+\theta_{\mathrm{I}}-\pi)\Phi_{\mathrm{R}}, \tag{2.62}$$

the high-frequency/far-field asymptotic behaviour, $e^{ikr}/\sqrt{kr}$, and the diffraction coefficient,

$$D(\theta,\theta_{\mathrm{I}}) = \frac{e^{-\frac{3i\pi}{4}}}{2\sqrt{2\pi}}\left[\frac{1}{\cos\left(\frac{1}{2}(\theta-\theta_{\mathrm{I}})\right)} \pm \frac{1}{\cos\left(\frac{1}{2}(\theta+\theta_{\mathrm{I}})\right)}\right]. \tag{2.63}$$

As explained earlier, the W-H technique has been a useful technique for many different problems (see Lawrie and Abrahams (2007) and references within), however it was thought to be ineffective for wedge diffraction problems due to the wedge faces not being parallel. We shall see in the next chapter that this is not the case.

To finish this chapter, we shall show plots of the solution to Sommerfeld's half-plane problem (2.59). Figures 2.7a and 2.7b display the solution with Dirichlet and Neumann boundary conditions respectively and $\theta_{\mathrm{I}} = \frac{\pi}{3}$.

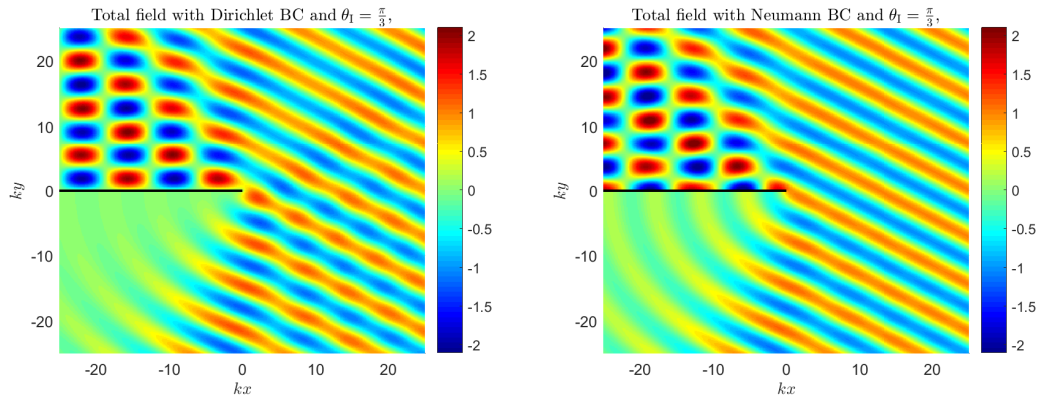

(a) Dirichlet case **(b)** Neumann case

Figure 2.7: Density plots of the solution to Sommerfeld's half-plane problem with Dirichlet (a) and Neumann (b) boundary conditions. Here we have $\theta_I = \frac{\pi}{3}$.

Chapter 3

Analytical methods for perfect wedge diffraction: a review

3.1 Article introduction

In this chapter, we will study the various techniques that have been applied to impenetrable wedge diffraction problems. We look at the problem from a mathematical perspective (i.e. without physical input or influence).

To do this we provide the latest version of the following paper (Nethercote et al., 2019b) which was co-written by Matthew Nethercote, Raphaël Assier and Ian David Abrahams. This manuscript is the revised version of a paper submitted to Wave Motion that incorporates some of the reviewers suggestions and comments. We are currently awaiting their second response.

This paper is a review of several analytical and asymptotic techniques adapted for perfect wedge diffraction with plane wave forcing. The main techniques include Sommerfeld-Malyuzhinets, Wiener-Hopf and the Kontorovich-Lebedev transform approaches. The less well-known but still interesting methods are the embedding formula, the random walk method and the Sobolev-Smirnoff method (also known

as the method of functionally invariant solutions). Furthermore, the wedge solution is used to rederive the half-plane solution (2.59) and we perform a numerical comparison between the exact solution and some asymptotic approximations such as Geometrical Theory of Diffraction. Lastly, there are two appendices on the classic Macdonald solution and detailed links to Green's integral operators.

In this paper, Nethercote wrote the reviews on the main techniques as well as the Sobolev-Smirnoff method, Macdonald's solution and the solution analysis section. Assier wrote the reviews on the embedding formula and the random walk method. Abrahams wrote the abstract as well as provided Nethercote with his invaluable expertise on his sections. All authors contributed to editing and revising the manuscript and responding to reviewers comments.

3.2 Journal article

Analytical methods for perfect wedge diffraction: a review

M. A. Nethercote[a], R. C. Assier[a,*], I. D. Abrahams[b]

[a] *School of Mathematics, University of Manchester, Oxford Road, Manchester, M13 9PL, UK*
[b] *Isaac Newton Institute, University of Cambridge, 20 Clarkson Road, Cambridge CB3 0EH, UK*

Abstract

The subject of diffraction of waves by sharp boundaries has been studied intensively for well over a century, initiated by groundbreaking mathematicians and physicists including Sommerfeld, Macdonald and Poincaré. The significance of such canonical diffraction models, and their analytical solutions, was recognised much more broadly thanks to Keller, who introduced a geometrical theory of diffraction (GTD) in the middle of the last century, and other important mathematicians such as Fock and Babich. This has led to a very wide variety of approaches to be developed in order to tackle such two and three dimensional diffraction problems, with the purpose of obtaining elegant and compact analytic solutions capable of easy numerical evaluation.

The purpose of this review article is to showcase the disparate mathematical techniques that have been proposed. For ease of exposition, mathematical brevity, and for the broadest interest to the reader, all approaches are aimed at one canonical model, namely diffraction of a monochromatic scalar plane wave by a two-dimensional wedge with perfect Dirichlet or Neumann boundaries. The first three approaches offered are those most commonly used today in diffraction theory, although not necessarily in the context of wedge diffraction. These are the Sommerfeld-Malyuzhinets method, the Wiener-Hopf technique, and the Kontorovich-Lebedev transform approach. Then follows three less well-known and somewhat novel methods, which would be of interest even to specialists in the field, namely the embedding method, a random walk approach, and the technique of functionally-invariant solutions.

Having offered the exact solution of this problem in a variety of forms, a numerical comparison between the exact solution and several powerful approximations such as GTD is performed and critically assessed.

Keywords: Canonical wave diffraction, wedge geometry, applied complex analysis

*Corresponding author

Email addresses: matthew.nethercote@postgrad.manchester.ac.uk (M. A. Nethercote), raphael.assier@manchester.ac.uk (R. C. Assier), i.d.abrahams@newton.ac.uk (I. D. Abrahams)

1. Introduction and formulation

At the close of the 19th century, wedge diffraction became a core problem in mathematical physics when renowned mathematicians Poincaré and Sommerfeld studied the diffraction of wave fields in angular domains (Poincaré, 1892, 1897; Sommerfeld, 1896, 1901). Sommerfeld made the first breakthrough when he solved his famous half-plane problem (Sommerfeld, 1896), during which he introduced the contour integral representation that we now know as the Sommerfeld integral. This work has now been translated to English in Sommerfeld (2003), with additional insightful comments. Sommerfeld would later be the first to solve problems of wedge diffraction (Sommerfeld, 1901) where the wedge has an interior angle equal to $m\pi/n$ ($m < n \in \mathbb{N}$).

For wedges with arbitrary interior angles, the solution was first obtained by Macdonald (1902). He did this by considering a line source incident wave and used separation of variables to get a series solution. The solution was rewritten in Sommerfeld integral form and he then provided the solution for an incident plane wave. We discuss this line source approach and provide an alternative way to obtain the plane wave solution in Appendix A.

In the 1950s, Malyuzhinets released a series of papers that culminated in the solution to the problem with impedance boundary conditions, (Malyuzhinets, 1955a,b, 1958b,c,a). This result created the first method that we discuss here in Section 2, the Sommerfeld-Malyuzhinets technique (S-M). Other authors who solved the impedance wedge problem independently were Senior (1959) and Williams (1959) but for more details on Malyuzhinets' method, see the review paper (Osipov and Norris, 1999) or the books (Budaev, 1995; Babich et al., 2007; Lyalinov and Zhu, 2013).

One of the most popular methods in diffraction theory is the Wiener-Hopf (W-H) technique, invented by Wiener and Hopf (1931) as a means to solve a special type of integral equation. It was soon discovered to be a useful method for diffraction problems and has appeared in a number of classic articles such as (Copson, 1946) and (Jones, 1952). Since then, applications of the technique have appeared in a wide array of research areas including diffraction, waveguides and flow problems.

The well-known textbook (Noble, 1958) provides an excellent tutorial for various aspects and extensions of the W-H technique. In 2007, the Journal of Engineering Mathematics published a W-H special issue led by a historical overview (Lawrie and Abrahams, 2007) along with a collection of articles applying the W-H technique to various problems. For wedge problems, the technique was thought to be ineffective due to the two boundaries not being parallel, however (see e.g. (Shanin, 1996; Daniele, 2003b)) this can be overcome as discussed later in Section 3.

Another key method is based on the Kontorovich-Lebedev (K-L) transform. First introduced by Kontorovich and Lebedev (1939), this transform is an effective tool when dealing with a radial coordinate. This makes it useful for wedge diffraction problems as evidenced by Abrahams (1986, 1987), since obtaining the general solution in that way is a very natural process. We shall discuss this further in Section 4, but

for more details on the transform and its applications, see (Lebedev, 1965), (Jones, 1964, 1980, 1986) and (Felsen and Marcuvitz, 1994).

In Section 5, we will focus on the asymptotic technique created by the classic paper (Keller, 1962), called the Geometrical Theory of Diffraction (GTD), see also the book by Borovikov and Kinber (1994). We will also follow the uniform GTD extension detailed in literature such as (Kouyoumjian and Pathak, 1974; James, 1986; Mcnamara et al., 1990) and (Babich et al., 2007).

Even though we will not use it in this review, for completeness, it is important to mention an alternative asymptotic technique applied to diffraction problems that is the Physical Theory of Diffraction (PTD) (Ufimtsev, 1971). This development was made possible in part thanks to Macdonald's work on Kirchhoff's approximation (see e.g. Ufimtsev (2014)). A useful paper that compares the GTD and PTD asymptotic techniques as well as the exact solution in series and integral form is (Hacivelioglu et al., 2011). Similar methods, describing creeping waves in diffraction by smooth obstacle, have also been developed in Fock (1965) for example.

Section 6 contains a number of alternative methods that are effective but less well-known for wedge diffraction. The first of these alternative methods is based on the very powerful concept of embedding formula. This reasonably recent approach consists in expressing the diffraction coefficient (which depends on both the incident and observer angles) of the diffracted field resulting from an incident plane wave in terms of the directivities (depending on one angle only) of simpler problems. These simpler problems are directly related to edge Green's functions. These are Green's functions for which the source is sent towards the geometric singularities of the obstacle. This method was primarily used for planar cracks and slits, and parallel combinations of these (see e.g. (Williams, 1982; Gautesen, 1983; Martin and Wickham, 1983; Biggs, 2001, 2002)). In (Craster and Shanin, 2005) it was shown that the method can be successfully adapted to wedges, as we will discuss later.

The second of these alternative methods is the so-called random walk approach. It is based on the known link between deterministic PDEs and stochastic differential equations (SDEs) given by the Feynman-Kac theorem. It allows to express the solution of a diffraction problem as the mean of a set of solutions to given SDEs with carefully chosen initial and final conditions. The method was developed through a series of papers by Budaev and Bogy (2001, 2002a,b, 2003), the latter being dedicated to wedge diffraction.

The last of these is the method of functionally-invariant solutions also known as the Sobolev-Smirnov method which has been used for a number of plane wave diffraction problems from half-planes (Sobolev, 1935; Smirnov, 1964) to wedges (Filippov, 1964; Komech et al., 2015; Babich, 2015). A very similar method that develops Busemann's "conical flow method" (Busemann, 1947) was also considered in Keller and Blank (1951) and Miles (1952) for example.

In this review (apart from Macdonald's approach discussed in Appendix A), we will focus primarily on plane wave incidence rather than line sources. It has to be

noted, however, that a broad range of work (Bromwich, 1915; Oberhettinger, 1954; Rawlins, 1987, 1989) has also been carried out for both acoustic and electromagnetic sources. For other reviews of some of the methods used for various types of incident waves (plane, cylindrical, spherical, dipole and pulse), see Oberhettinger (1958) and Bowman et al. (1987).

The elastic wedge problem has equally received a lot of attention. Knopoff (1969) wrote an interesting review of possible approaches to tackle this (still unsolved) problem, it includes attempts using the method of images, the W-H technique, the K-L transform and the conical flow method. More recent approaches by Croisille and Lebeau (1999) or Budaev and Bogy (1995, 1996, 1998) are also worth mentioning.

In Section 3.1, in the spirit of Wegert (2012), we will visualise complex functions using phase portraits in order to show domains of analyticity, locations of singularities and orientations of branch cuts. These portraits assign the argument of a complex function to a HSV colour model. For example, Figure 1 (left) shows the phase portrait of $f(z) = z$ which we use as a colour reference.

Wedge diffraction has a number of physical applications such as the scattering of acoustic pressure fields or electromagnetic fields by sharp structures, scattering of the Sun's radiation by cloud ice crystals and seismology. We shall study this from a more mathematical perspective. From here onward, we will assume that the problem is time-harmonic with time factor $e^{-i\omega t}$, which is henceforth suppressed, and we will consider solutions to the homogeneous Helmholtz equation,

$$\nabla^2\Phi + k^2\Phi = 0. \tag{1.1}$$

inside a wedge-shaped region described in polar coordinates by $\{0 < r < \infty,\ -\theta_{\mathrm{w}} < \theta < \theta_{\mathrm{w}}\}$ (see Figure 1 (right)). The complementary region, $\{0 < r < \infty,\ |\theta| > \theta_{\mathrm{w}}\}$ is considered to be the wedge scatterer. Defining $\bar{\theta}_{\mathrm{w}} = \pi - \theta_{\mathrm{w}}$, the interior angle of the wedge scatterer is $2\bar{\theta}_{\mathrm{w}}$. Throughout this paper, we will consider two cases of homogeneous boundary conditions (BCs), Dirichlet and Neumann, on both faces of the wedge,

$$\text{Dirichlet BCs:}\quad \Phi(\theta = \pm\theta_{\mathrm{w}}) = 0, \tag{1.2}$$

$$\text{Neumann BCs:}\quad \frac{1}{r}\frac{\partial\Phi}{\partial\theta}(\theta = \pm\theta_{\mathrm{w}}) = 0. \tag{1.3}$$

For acoustics, (1.2) and (1.3) are called sound-soft and sound-hard BCs respectively. For electromagnetic scattering by an electric (resp. magnetic) polarized plane wave, the solution to the perfect electric conducting (PEC) problem can be expressed in terms of a potential satisfying (1.2) (resp. (1.3)).

We define the incident plane wave as, $\Phi_{\mathrm{I}} = e^{-ikr\cos(\theta-\theta_{\mathrm{I}})}$ with wavenumber $k > 0$ and incident angle θ_{I}. Due to the symmetry of the problem, we restrict the incident angle to $\theta_{\mathrm{I}} \in [0, \theta_{\mathrm{w}}]$. Figure 1 (right) illustrates the geometry of the problem.

An initial approximation is found using classical Geometrical Optics (GO). The GO part of the solution consists of the incident wave and any reflected waves produced. The latter are all outgoing in the sense that they cannot bring energy into the

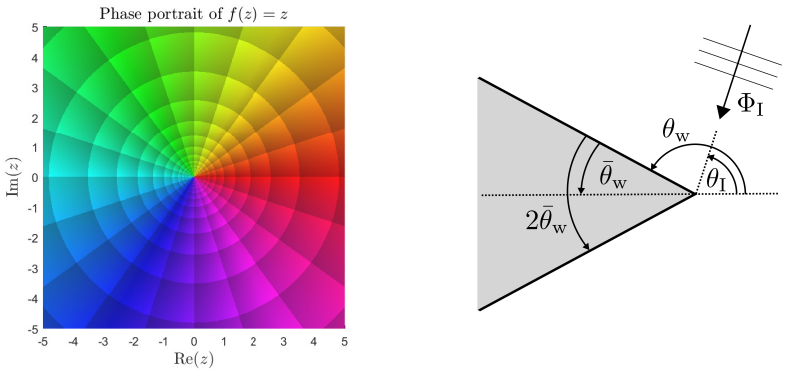

Figure 1: The left figure is a phase portrait of $f(z) = z$ which assigns colours to the complex argument of f (left). For example $\arg(f) = 0$ is indicated as red and $\arg(f) = \pi$ is indicated as cyan. The right figure is the geometry of the problem.

wedge domain from infinity. The remaining part of the solution is the diffracted field, Φ_{Diff}, which must be included to make the total field continuous and which satisfies a two-dimensional radiation condition (see (Schot, 1992) for a good review on this), written in integral form:

$$\lim_{r\to\infty} \int_{-\theta_{\mathrm{w}}}^{\theta_{\mathrm{w}}} \left| \frac{\partial \Phi_{\mathrm{Diff}}}{\partial r} - ik\Phi_{\mathrm{Diff}} \right|^2 r \, \mathrm{d}\theta = 0. \tag{1.4}$$

Lastly, there will be an edge (or Meixner) condition as r becomes small.

$$\Phi \sim \mathcal{A} + O\left(r^{\min(\delta,2)}\right), \quad \text{where} \quad \delta = \frac{\pi}{2\theta_{\mathrm{w}}}, \tag{1.5}$$

and $\mathcal{A} = 0$ for the case of Dirichlet BCs. Typically, the edge conditions can be derived using the Frobenius method (Bender and Orszag, 1999) while ensuring that the energy remains finite in any neighbourhood of the wedge edge. With the outgoing property of the diffracted and reflected waves, a finite-energy constraint, and specification of the incident wave, the Neumann or Dirichlet wedge diffraction problem has a unique solution.

2. The Sommerfeld-Malyuzhinets technique

The first method to be reviewed is the Sommerfeld-Malyuzhinets (S-M) technique. Here we will show briefly how to obtain the solution to the perfect wedge problem (1.1)-(1.5). For a more thorough explanation, consult Sections 1-4 of (Babich et al., 2007). This technique is based on the general solution of diffraction problems in angular domains being represented as the Sommerfeld integral

$$\Phi(r,\theta) = \frac{1}{2\pi i} \int_{\gamma_+} e^{-ikr\cos(z)} \left[s(\theta+z) - s(\theta-z) \right] \mathrm{d}z = \frac{1}{2\pi i} \int_{\gamma_+ + \gamma_-} e^{-ikr\cos(z)} s(\theta+z) \mathrm{d}z, \tag{2.1}$$

where $\gamma_\pm$ are contours defined in Figure 2 (left) and $s(z)$ is an unknown function to be determined. This representation ensures that the Helmholtz equation is automatically satisfied[1]. The form of the spectral part, $s(\theta+z)-s(\theta-z)$, is necessary for the radiation conditions to be satisfied. This can be proven by using the method of steepest descent to approximate the integral as $kr\to\infty$ (see section 3.7 of Babich et al. (2007)). The function $s(z)$, referred to as the spectral function, is assumed to be meromorphic in the domain

$$\begin{aligned}&\{-\pi-\theta_{\mathrm{w}}-\epsilon_1<\mathrm{Re}\,\{z\}<\theta_{\mathrm{w}}+\epsilon_1,\quad \mathrm{Im}\,\{z\}>-\epsilon_2\}\cup\\&\{-\theta_{\mathrm{w}}-\epsilon_1<\mathrm{Re}\,\{z\}<\pi+\theta_{\mathrm{w}}+\epsilon_1,\quad \mathrm{Im}\,\{z\}<\epsilon_2\},\end{aligned}\tag{2.2}$$

for some $\epsilon_{1,2}>0$ and analytic in the same domain with $\epsilon_{1,2}=0^+$, see Figure 2 (right). The poles of $s(z)$ will be seen to correspond to the geometrical optics part of the wave field. The structure of (2.1) means that $s(z)$ is defined up to an additive constant. Using the edge conditions, we can assume that $s(z)$ has the following behaviour as $|\mathrm{Im}\,\{z\}|\to\infty$,

$$s(z)=\pm A+O(e^{-\delta|\mathrm{Im}\{z\}|}),\tag{2.3}$$

where $A=0$ for the Dirichlet case.[2] It is also important to note that $e^{-ikr\cos(z)}$ is an entire 2π-periodic function of z, which decays rapidly as $|\mathrm{Im}\,\{z\}|\to\infty$ only in the set of half-strips,

$$\begin{aligned}&\{z:\ (2m-1)\pi<\mathrm{Re}\,\{z\}<2m\pi,\quad \mathrm{Im}\,\{z\}<0,\quad m\in\mathbb{Z}\}\cup\\&\{z:\ 2m\pi<\mathrm{Re}\,\{z\}<(2m+1)\pi,\quad \mathrm{Im}\,\{z\}>0,\quad m\in\mathbb{Z}\},\end{aligned}\tag{2.4}$$

displayed in Figure 2 (left), and grows rapidly in the complementary set. The Sommerfeld contours $\gamma_\pm$ are defined so that the integrand is analytic and decays as $|\mathrm{Im}\,\{z\}|\to\infty$ along these contours.[3]

A crucial part to the S-M technique is Malyuzhinets' Theorem or the Sommerfeld Nullification Theorem. This is an important theorem because it allows us to obtain a functional equation satisfied by the spectral function. The theorem and its proof are presented by Malyuzhinets in (Malyuzhinets, 1958b) and more recently in Section 3.4 of (Babich et al., 2007).

Theorem 1 (Malyuzhinets' Theorem or Sommerfeld Nullification Theorem) *Let the function $\Upsilon(z)$ be analytic and single-valued inside the half-strip,*

$$\{z:-\pi-\epsilon_1\le\mathrm{Re}\{z\}\le\epsilon_1,\quad \mathrm{Im}\{z\}\ge\epsilon_2>0\},\quad \epsilon_1,\epsilon_2>0.\tag{2.5}$$

[1]This is proven using integration by parts and noting that $e^{-ikr\cos(z)}$ satisfies the Helmholtz equation with polar coordinates (r,z).

[2]We assume (2.3) for convenience later. Say we assumed $s(z)\to A_\pm$ as $\mathrm{Im}\,\{z\}\to\pm\infty$ where $A_++A_-\neq 0$ instead. Then a later step will require us to redefine $s(z)$ using the additive constant property such that $A_++A_-=0$ implying (2.3).

[3]Note that the Sommerfeld contours are contained in the domain (2.2) with $\epsilon_1=\epsilon_2=0^+$.

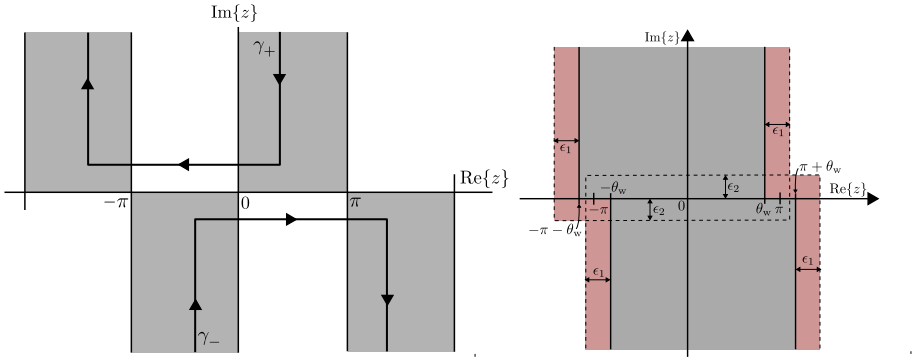

Figure 2: The Sommerfeld contours $\gamma_\pm$ and the grey half-strips of exponential decay (left), and regions where $s(z)$ is analytic or meromorphic (right)

If for some constant D, the function has the following behaviour as $\mathrm{Im}\{z\} \to \infty$ *in this half-strip,*

$$|\Upsilon(z)| \leq \text{constant } e^{D\mathrm{Im}\{z\}}, \tag{2.6}$$

and for any $R > 0$,

$$\frac{1}{2\pi i}\int_{\gamma_+} e^{-iR\cos(z)}\Upsilon(z)dz = 0, \tag{2.7}$$

then,

$$\Upsilon(z) \equiv 0 \quad \textit{if} \quad D < 1, \tag{2.8}$$

$$\Upsilon(z) = \sin(z)\left[\sum_{j=0}^{d-1} c_j(\cos(z))^j\right] \quad \textit{if} \quad D \geq 1, \tag{2.9}$$

where d is the integer part of D and the coefficients c_j are constants.

With Malyuzhinets' theorem, we have all the tools required to determine the spectral function $s(z)$. Recall that it was assumed to be meromorphic in the domain (2.2), moreover it has only one simple pole with unit residue at $z = \theta_\mathrm{I}$ within the strip $|\mathrm{Re}\{z\}| < \theta_\mathrm{w}$ corresponding to the incident wave Φ_I.

2.1. Dirichlet boundary condition

Applying the Dirichlet BCs (1.2) to the general solution (2.1) implies that

$$\frac{1}{2\pi i}\int_{\gamma_+} e^{-ikr\cos(z)}\left[s(\pm\theta_\mathrm{w}+z) - s(\pm\theta_\mathrm{w}-z)\right]\mathrm{d}z = 0. \tag{2.10}$$

Due to (2.3), we can apply Malyuzhinets' theorem to (2.10) to produce a pair of functional equations for $s(z)$,

$$s(\pm\theta_\mathrm{w}+z) - s(\pm\theta_\mathrm{w}-z) = 0. \tag{2.11}$$

These equations imply that $s(z)$ is symmetric about $z = \pm\theta_w$ and as a consequence is $4\theta_w$ periodic. Because the pole at $z = \theta_I$ produces the incident wave, its residue should be 1, i.e.

$$\lim_{z\to\theta_I}\left[(z-\theta_I)s(z)\right] = 1.$$

Because this pole is the only singularity in the strip $|\mathrm{Re}\{z\}| \leq \theta_w$, then by the determined symmetry, we also have poles at $z = 2\theta_w - \theta_I$ and $-2\theta_w - \theta_I$ with residue -1. These two poles correspond to the top and bottom reflected waves respectively. The periodicity implies that each of the poles are repeated every $4\theta_w$ with the same residue. We can therefore express $s(z)$ as a sum of poles,

$$s(z) = \sum_{n=-\infty}^{\infty} \frac{1}{z-\theta_I-4\theta_w n} - \sum_{n=-\infty}^{\infty} \frac{1}{z+\theta_I-2\theta_w-4\theta_w n}. \tag{2.12}$$

Using the definition $\delta = \frac{\pi}{2\theta_w}$ and pole expansion of $\cot(z)$,

$$\cot(z) = \sum_{n=-\infty}^{\infty} \frac{1}{z-n\pi},$$

we rewrite $s(z)$ as follows,

$$s(z) = \frac{\delta}{2}\left[\cot\left(\frac{(z-\theta_I)\delta}{2}\right) - \cot\left(\frac{(z-2\theta_w+\theta_I)\delta}{2}\right)\right] = \frac{\delta\cos(\delta\theta_I)}{\sin(\delta z)-\sin(\delta\theta_I)}. \tag{2.13}$$

It is easy to check that (2.13) satisfies the functional equations (2.11), satisfies the estimate $O(e^{-\delta|\mathrm{Im}\{z\}|})$ as $|\mathrm{Im}\{z\}| \to \infty$, and has a single pole with unit residue in the strip $|\mathrm{Re}\{z\}| \leq \theta_w$. This means that the solution to the exterior wedge problem with Dirichlet BCs is,

$$\Phi(r,\theta) = \frac{1}{2\pi i}\int_{\gamma_+-\gamma_-} e^{-ikr\cos(z)} \frac{\delta\cos(\delta\theta_I)}{\sin(\delta(\theta+z))-\sin(\delta\theta_I)}\,\mathrm{d}z. \tag{2.14}$$

2.2. Neumann boundary condition

Solving for the Neumann case is done in a very similar way. Applying the Neumann BCs (1.3) to the general solution (2.1) implies that

$$\frac{1}{2\pi i}\int_{\gamma_+} e^{-ikr\cos(z)}\left[s'(\pm\theta_w+z) - s'(\pm\theta_w-z)\right]\mathrm{d}z = 0. \tag{2.15}$$

We integrate by parts and apply the Malyuzhinets' theorem to (2.15) to obtain the following pair of functional equations for $s(z)$,

$$s(\pm\theta_w+z) + s(\pm\theta_w-z) = c_\pm. \tag{2.16}$$

Applying (2.3) determines that $c_\pm = 0$. Then the functional equations become,

$$s(\pm\theta_\mathrm{w} + z) + s(\pm\theta_\mathrm{w} - z) = 0. \tag{2.17}$$

These equations imply that $s(z)$ is antisymmetric about $z = \pm\theta_\mathrm{w}$. This symmetry also shows that $s(z)$ is a $4\theta_\mathrm{w}$ periodic function. Because θ_I is the only pole of $s(z)$ in the strip $|\mathrm{Re}\{z\}| \leq \theta_\mathrm{w}$ and has unit residue, then due to the antisymmetry and periodicity of $s(z)$, there are more poles located at $z = \theta_\mathrm{I} + 4\theta_\mathrm{w}n$ and $z = 2\theta_\mathrm{w} - \theta_\mathrm{I} + 4\theta_\mathrm{w}n$ for $n \in \mathbb{Z}$, all with unit residue. We can therefore express $s(z)$ as a sum of poles,

$$\begin{aligned} s(z) &= \sum_{n=-\infty}^{\infty} \frac{1}{z - \theta_\mathrm{I} - 4\theta_\mathrm{w}n} + \sum_{n=-\infty}^{\infty} \frac{1}{z + \theta_\mathrm{I} - 2\theta_\mathrm{w} - 4\theta_\mathrm{w}n} \\ &= \frac{\delta}{2}\left[\cot\left(\frac{(z-\theta_\mathrm{I})\delta}{2}\right) + \cot\left(\frac{(z-2\theta_\mathrm{w}+\theta_\mathrm{I})\delta}{2}\right)\right] = \frac{\delta\cos(\delta z)}{\sin(\delta z) - \sin(\delta\theta_\mathrm{I})}. \end{aligned} \tag{2.18}$$

It is easy to check that (2.18) satisfies the functional equations (2.17), satisfies the estimate (2.3) as $|\mathrm{Im}\{z\}| \to \infty$, and has one simple pole with unit residue in the strip $|\mathrm{Re}\{z\}| \leq \theta_\mathrm{w}$. Finally, the solution to the exterior wedge problem with Neumann BCs is,

$$\Phi(r,\theta) = \frac{1}{2\pi i}\int_{\gamma_+ + \gamma_-} e^{-ikr\cos(z)} \frac{\delta\cos(\delta(\theta+z))}{\sin(\delta(\theta+z)) - \sin(\delta\theta_\mathrm{I})}\,\mathrm{d}z. \tag{2.19}$$

Critical analysis. The main advantage of the S-M technique is its ease of implementation. Once in the right form, a natural deformation to the steepest descent contour can transform it into a very simple and fast converging integral (see Section 5). This aspect clearly makes it the gold standard representation of the general solution to the perfect wedge problem. Moreover, because of the form of the integrand, one can somehow think of the solution as a weighted superposition of plane waves.

Another advantage of such method is its flexibility. It is indeed possible to use it for more complicated problems such as the impedance wedge (Malyuzhinets, 1958a) or with various types of incident waves (Bowman et al., 1987). It has also been employed on the quarter-plane problem to infer some results about the far-field structure (Lyalinov, 2013).

A disadvantage of the method is that it is not particularly constructive. In fact, it often starts with a form of the solution being posed and shown *a posteriori* to satisfy all the required conditions in a non-straightforward manner. The Appendix B addresses this issue by showing that the two-contour representation of the solution comes naturally from Green's identity.

3. The Wiener-Hopf technique

The second method to be reviewed is the Wiener-Hopf (W-H) technique. Before authors such as Shanin and Daniele used the W-H technique for wedge problems, it was mostly used for waveguide problems or more complicated half-plane problems. In the two papers (Shanin, 1996, 1998), Shanin looks at solving wedge problems with inhomogeneous impedance BCs via the W-H technique. In a series of papers and internal reports (Daniele, 2000, 2001, 2003a,b), Daniele develops several aspects of his method for wedge diffraction problems in an electromagnetic setting including the definition of the so-called generalised W-H equations.

In this section, we will combine elements from both (Shanin, 1996) and (Daniele, 2003b) to rederive (2.14) and (2.19) using the W-H technique. The idea is to Laplace transform Φ and its θ derivative on the two wedge faces, $\theta = \pm\theta_{\mathrm{w}}$, and the line of symmetry $\theta = 0$. These transforms are used to produce the W-H equations. After the BCs are considered, a mapping to a new complex plane is introduced so that the W-H technique can be applied to produce a solution that will match (2.14) and (2.19). We will start by studying this mapping.

3.1. A useful mapping

As we will see later, when the W-H equations are derived, they cannot be easily factorised using standard methods. To counter this issue, we will need to map these equations onto a new complex plane so that they can be reduced to classical W-H equations like those in (Noble, 1958). In order to do that, Shanin and Daniele use slightly different mappings,

$$\text{Shanin's mapping:} \quad \eta(\alpha) = \cos\left(\frac{2\theta_{\mathrm{w}}}{\pi}\cos^{-1}(\sqrt{\alpha})\right) = \cos\left(\frac{\theta_{\mathrm{w}}}{\pi}\cos^{-1}(2\alpha-1)\right),$$

$$\text{Daniele's mapping:}^{4} \quad \eta(\alpha) = k\cos\left(\frac{\theta_{\mathrm{w}}}{\pi}\cos^{-1}\left(\frac{\alpha}{k}\right)\right),$$

where η and α are the old and new complex variables. Though the two mappings are conceptually equivalent, we will study Daniele's mapping in what follows. Note though that in his work, Daniele has assumed that k has a small imaginary part in order to have a strip of analyticity for the W-H equations. However this is not strictly necessary, and here we will consider $k \in \mathbb{R}^{+}$, essentially reducing the W-H problem to a Riemann-Hilbert problem (see e.g. (Kisil, 2015)). This means that k does not need to appear explicitly in the mapping, and we can simply use

$$\eta(\alpha) = \cos\left(\frac{\theta_{\mathrm{w}}}{\pi}\cos^{-1}(\alpha)\right), \tag{3.1}$$

[4] In Daniele's papers, the mapping has $-k$ in place of k because he uses $e^{i\omega t}$ as time factor.

with the corresponding inverse,

$$\alpha(\eta) = \cos\left(\frac{\pi}{\theta_{\rm w}}\cos^{-1}(\eta)\right). \tag{3.2}$$

We also consider the intermediate mapping and corresponding inverse,

$$z(\alpha) = \frac{\theta_{\rm w}}{\pi}\cos^{-1}(\alpha), \quad \alpha(z) = \cos\left(\frac{\pi}{\theta_{\rm w}}z\right). \tag{3.3}$$

The mapping (3.1) has a single branch cut along the real line segment $\alpha \in (-\infty, -1]$ where the local argument of the chosen branch is $(-\pi, \pi]$. This is done by choosing the branch of the inverse cosine such that $\pi - \cos^{-1}(x) = \cos^{-1}(-x)$, which is standard for programs such as Mathematica and MATLAB. Note that the intermediate mapping limits z to belong to the strip $\mathrm{Re}\{z\} \in [0, \theta_{\rm w}]$.

One of the most important features of the mapping (3.1) is that the upper half plane (UHP) $\mathrm{Im}\{\alpha\} \geq 0$ is mapped to a subset of the UHP $\mathrm{Im}\{\eta\} \geq 0$ as shown in Figures 3a and 3b. This implies in particular that if a function $f(\eta)$ is analytic in the η UHP, then the function $f(\eta(\alpha))$ is analytic in the α UHP. Another noteworthy property is that if a function $g(\alpha)$ has no branch point at $\alpha = 1$ (or -1), then the function $g(\alpha(z))$ will be symmetric with respect to $z = 0$ (or $z = \theta_{\rm w}$) in the z-plane.

The mapping (3.1) is designed specifically for manipulation of the following functions,

$$\begin{aligned} f_1(\eta) = \sqrt{1-\eta^2}, \quad f_2(\eta) = \eta\cos(\theta_{\rm w}) + \sqrt{1-\eta^2}\sin(\theta_{\rm w}), \\ f_3(\eta) = \eta\sin(\theta_{\rm w}) - \sqrt{1-\eta^2}\cos(\theta_{\rm w}), \end{aligned} \tag{3.4}$$

where the branch for the square root is chosen such that $f_1(0) = 1$. For context, f_2 is used to identify domains of analyticity whereas, f_1 and f_3 are kernel functions that need to be factorised. Noting that η and z have the relation $\eta = \cos(z)$, we map f_1 to the z and α planes.

$$f_1(\cos(z)) = \sin(z), \quad f_1(\eta(\alpha)) = \sin\left(\frac{\theta_{\rm w}}{\pi}\cos^{-1}(\alpha)\right). \tag{3.5}$$

In the α plane, $f_1(\eta(\alpha))$ has branch cuts on the segments $\alpha \in (-\infty, -1]$ and $\alpha \in [1, \infty)$ (see Figure 4b which is a phase plot of f_1 on the α-plane).

Similarly we can map f_2 in the z and α planes.

$$f_2(\cos(z)) = \cos(\theta_{\rm w} - z), \quad f_2(\eta(\alpha)) = \cos\left(\frac{\theta_{\rm w}}{\pi}\cos^{-1}(-\alpha)\right) = \eta(-\alpha). \tag{3.6}$$

In the α plane, $f_2(\eta(\alpha))$ has a single branch cut on the segment $\alpha \in [1, \infty)$ and is related to $\eta(\alpha)$ by the identity $f_2(\eta(\alpha)) = \eta(-\alpha)$, as shown by comparing the phase portraits in Figures 4a and 4c. The consequence is that the lower half plane (LHP)

$\mathrm{Im}\{\alpha\} \leq 0$ is mapped to a subset of the region $\mathrm{Im}\{f_2(\eta)\} \geq 0$ as can be seen from comparing Figures 3c and 3d. This also implies, in particular, that if a function $f(f_2)$ is analytic in the f_2 UHP, then the function $f(f_2(\eta(\alpha)))$ is analytic in the α LHP.

Lastly, we study the effect of the mapping on f_3,

$$f_3(\cos(z)) = \sin(\theta_w - z), \quad f_3(\eta(\alpha)) = \sin\left(\frac{\theta_w}{\pi}\cos^{-1}(-\alpha)\right) = f_1(\eta(-\alpha)), \tag{3.7}$$

showing that f_1 and f_3 are closely related in the α-plane, in the sense that $f_3(\eta(\alpha))$ and $f_1(\eta(\alpha))$ have the same branch cuts but their phase plots are the symmetric images of each other about $z = 0$, as illustrated in Figures 4b and 4d. This relationship means that factorising f_3 in the α plane is analogous to factorising f_1.

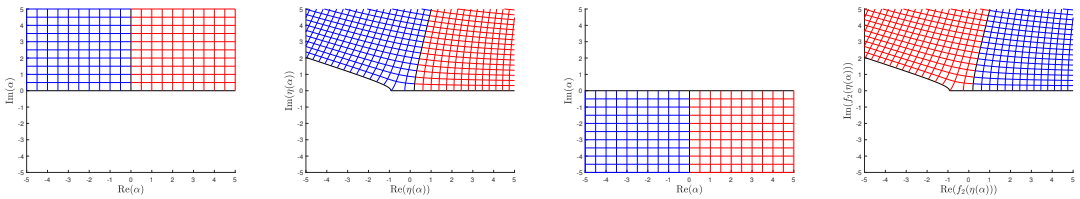

(a) **(b)** **(c)** **(d)**

Figure 3: With $\theta_w = 7\pi/8$, these are pictures of characteristic domains showing that an upper half α-plane (a) is mapped onto an upper half η-plane (b) and a lower half α-plane (c) is mapped onto an upper half f_2-plane (d).

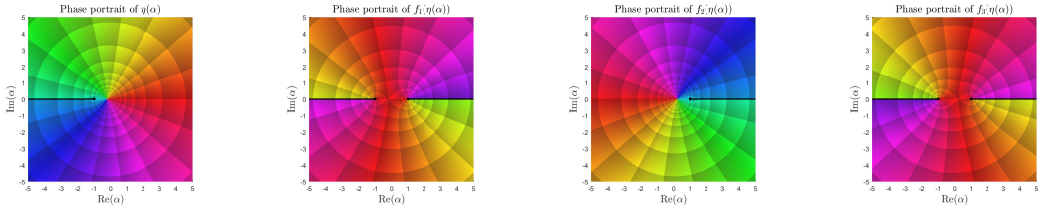

(a) $\eta(\alpha)$ **(b)** $f_1(\eta(\alpha))$ **(c)** $f_2(\eta(\alpha))$ **(d)** $f_3(\eta(\alpha))$

Figure 4: Phase plots of η, f_1, f_2 and f_3 after being mapped onto the α-plane. These illustrate any branch cuts and show the relationships between the four functions with $\theta_w = 7\pi/8$

Before performing such factorisation, let us define the domains $\mathcal{R}_\pm$ on which this factorisation will be done:

$$\mathcal{R}_+ = \{\alpha : \mathrm{Im}\{\alpha\} > 0\} \cup \{\alpha : \mathrm{Re}\{\alpha\} > -1, \mathrm{Im}\{\alpha\} = 0\} \tag{3.8}$$
$$\mathcal{R}_- = \{\alpha : \mathrm{Im}\{\alpha\} < 0\} \cup \{\alpha : \mathrm{Re}\{\alpha\} < 1, \mathrm{Im}\{\alpha\} = 0\} \tag{3.9}$$

Note that $\mathcal{R}_+ \cup \mathcal{R}_- = \mathbb{C}$ and $\mathcal{R}_+ \cap \mathcal{R}_- = (-1, 1)$. Factorising f_1, requires to write

$$f_1(\eta(\alpha)) = f_{1+}(\alpha) f_{1-}(\alpha), \tag{3.10}$$

where f_{1+} is analytic in $\mathcal{R}_+$ and f_{1-} is analytic in $\mathcal{R}_-$. We expect that f_{1+} will have a branch cut starting at $\alpha = -1$ and f_{1-} a branch cut starting at $\alpha = 1$. Hence $f_{1+}(\alpha(z))$ and $f_{1-}(\alpha(z))$ will be symmetric about the points $z = 0$ and θ_w respectively. We can realise this factorisation by using the fact that both the leading order behaviour of f_1 as $\alpha \to 1$ and the jump across the cut are consistent with the function $\sqrt{1-\alpha}$. This means that we can define f_{1-} and f_{1+} by,

$$f_{1-}(\alpha) = \sqrt{\frac{1-\alpha}{2}}, \quad f_{1+}(\alpha) = \frac{\sin\left(\frac{\theta_\text{w}}{\pi}\cos^{-1}(\alpha)\right)}{\sqrt{\frac{1-\alpha}{2}}}. \tag{3.11}$$

Clearly f_{1-} has a branch cut on the segment $\alpha \in [1, \infty)$ and is analytic at $\alpha = -1$. While f_{1+} retains the branch cut on the segment $\alpha \in (-\infty, -1]$, and dividing by $\sqrt{1-\alpha}$ has made $\alpha = 1$ become a removable singularity and cancelled out the cut discontinuity. Hence we can assign the limiting value to $\alpha = 1$ and make f_{1+} analytic at that point. Recalling the definition $\delta = \frac{\pi}{2\theta_\text{w}}$, we also map f_{1-} and f_{1+} to the z-plane as follows:

$$f_{1-}(\alpha(z)) = \sin(\delta z), \quad f_{1+}(\alpha(z)) = \frac{\sin(z)}{\sin(\delta z)}. \tag{3.12}$$

As anticipated, due to the absence of the branch point at $\alpha = -1$, $f_{1-}(\alpha(z))$ is symmetric about $z = \theta_\text{w}$. Similarly, due to the absence of the branch point at $\alpha = 1$, $f_{1+}(\alpha(z))$ is symmetric about $z = 0$. Figure 5 illustrates this factorisation by the relationship (3.10).

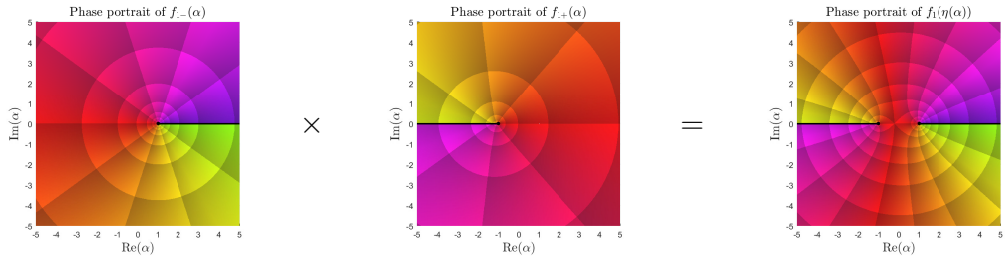

(a) $f_{1-}(\alpha)$ **(b)** $f_{1+}(\alpha)$ **(c)** $f_1(\eta(\alpha))$

Figure 5: Various phase plots helping to illustrate the factorisation (3.10) by displaying each of the parts of f_1 in the α plane for $\theta_\text{w} = 7\pi/8$.

Now we factorise f_3 using the established relation $f_3(\eta(\alpha)) = f_1(\eta(-\alpha))$ (see (3.7)) to find that $f_{3+}(\alpha) = f_{1-}(-\alpha)$ and $f_{3-}(\alpha) = f_{1+}(-\alpha)$. It can be shown that f_{3+} has a branch cut on the segment $\alpha \in (-\infty, -1]$, is analytic at $\alpha = 1$ and $f_{3+}(\alpha(z))$ is symmetric about $z = 0$, while f_{3-} has a branch cut on the segment $\alpha \in [1, \infty)$, can be made analytic at $\alpha = -1$ and $f_{3-}(\alpha(z))$ is symmetric about $z = \theta_\text{w}$.

3.2. Derivation of the Wiener-Hopf equations

Daniele derives the W-H equations by rewriting the Helmholtz equation in terms of an oblique Cartesian coordinate system and uses a Laplace transformation in each of the new coordinates (Daniele, 2003b). However this procedure is a general method for arbitrary angular regions, therefore for the aim of this paper we prefer to use a different method.

(Shanin, 1996) tackles an interior wedge problem with inhomogeneous impedance BCs. In this geometry, only one W-H equation is derived, which is obtained via Green's second identity. However we will need to split the exterior wedge region into two halves to obtain two W-H equations. Take Green's second identity for functions u, v, twice continuously differentiable on domain $\Omega \in \mathbb{R}^2$ with boundary $\partial\Omega$,

$$\int_\Omega \left(v\nabla^2 u - u\nabla^2 v\right) \mathrm{d}\Omega = \int_{\partial\Omega} \left(v\frac{\partial u}{\partial \boldsymbol{n}} - u\frac{\partial v}{\partial \boldsymbol{n}}\right) \mathrm{d}S, \tag{3.13}$$

where $\frac{\partial}{\partial \boldsymbol{n}}$ is the normal derivative. Here u is the unknown solution Φ and we choose a suitable test function for v that satisfies the Helmholtz equation (1.1). Then the left hand side of (3.13) is automatically zero. We do this for two wedge regions $\theta \in [0, \theta_\mathrm{w}]$ and $\theta \in [-\theta_\mathrm{w}, 0]$ which require different test functions. The right hand side of (3.13) has two parts, the wedge boundary at $\theta = \pm\theta_\mathrm{w}$ and an imaginary boundary at $\theta = 0$. For the upper region, we choose the test function $v = e^{ikr\cos(\theta - z)}$, leading (3.13) to become

$$\begin{aligned}\int_0^\infty \left[\frac{1}{ikr}\frac{\partial\Phi}{\partial\theta}\bigg|_{\theta=0} - \sin(z)\ \Phi|_{\theta=0}\right] e^{ikr\cos(z)}\mathrm{d}r \\ = \int_0^\infty \left[\frac{1}{ikr}\frac{\partial\Phi}{\partial\theta}\bigg|_{\theta=\theta_\mathrm{w}} + \sin(\theta_\mathrm{w} - z)\ \Phi|_{\theta=\theta_\mathrm{w}}\right] e^{ikr\cos(\theta_\mathrm{w} - z)}\mathrm{d}r.\end{aligned} \tag{3.14}$$

For the lower region, $\theta \in [-\theta_\mathrm{w}, 0]$, we choose the slightly modified test function $v = e^{ikr\cos(\theta + z)}$, leading (3.13) to become

$$\begin{aligned}\int_0^\infty \left[\frac{1}{ikr}\frac{\partial\Phi}{\partial\theta}\bigg|_{\theta=0} + \sin(z)\ \Phi|_{\theta=0}\right] e^{ikr\cos(z)}\mathrm{d}r \\ = \int_0^\infty \left[\frac{1}{ikr}\frac{\partial\Phi}{\partial\theta}\bigg|_{\theta=-\theta_\mathrm{w}} - \sin(\theta_\mathrm{w} - z)\ \Phi|_{\theta=-\theta_\mathrm{w}}\right] e^{ikr\cos(\theta_\mathrm{w} - z)}\mathrm{d}r.\end{aligned} \tag{3.15}$$

Define the Laplace transform with the following inverse,

$$F(\eta) = \int_0^\infty f(r)e^{ikr\eta}\mathrm{d}r, \quad f(r) = \frac{k}{2\pi}\int_{-\infty}^\infty F(\eta)e^{-ikr\eta}\mathrm{d}\eta, \tag{3.16}$$

where $F(\eta)$ is analytic in the half-plane $\mathrm{Im}\{\eta\} > 0$, then we define the transforms of Φ and $\frac{1}{ikr}\frac{\partial\Phi}{\partial\theta}$,

$$U(\eta, \theta) = \int_0^\infty \Phi(r, \theta)e^{ikr\eta}\mathrm{d}r, \quad V(\eta, \theta) = \int_0^\infty \frac{1}{ikr}\frac{\partial\Phi}{\partial\theta}(r, \theta)e^{ikr\eta}\mathrm{d}r. \tag{3.17}$$

These transforms are applied to both (3.14) and (3.15) which produces the W-H equations,

$$\begin{aligned} &V(\cos(z),0) - \sin(z)U(\cos(z),0) \\ &\qquad = V(\cos(\theta_{\rm w}-z),\theta_{\rm w}) + \sin(\theta_{\rm w}-z)U(\cos(\theta_{\rm w}-z),\theta_{\rm w}), \\ &V(\cos(z),0) + \sin(z)U(\cos(z),0) \\ &\qquad = V(\cos(\theta_{\rm w}-z),-\theta_{\rm w}) - \sin(\theta_{\rm w}-z)U(\cos(\theta_{\rm w}-z),-\theta_{\rm w}). \end{aligned} \tag{3.18}$$

Adding and subtracting these two equations leads to,

$$\begin{aligned} 2V(\cos(z),0) &= V(\cos(\theta_{\rm w}-z),-\theta_{\rm w}) + V(\cos(\theta_{\rm w}-z),\theta_{\rm w}) \\ &\quad + \sin(\theta_{\rm w}-z)\left[U(\cos(\theta_{\rm w}-z),\theta_{\rm w}) - U(\cos(\theta_{\rm w}-z),-\theta_{\rm w})\right], \\ 2\sin(z)U(\cos(z),0) &= V(\cos(\theta_{\rm w}-z),-\theta_{\rm w}) - V(\cos(\theta_{\rm w}-z),\theta_{\rm w}) \\ &\quad - \sin(\theta_{\rm w}-z)\left[U(\cos(\theta_{\rm w}-z),\theta_{\rm w}) + U(\cos(\theta_{\rm w}-z),-\theta_{\rm w})\right]. \end{aligned} \tag{3.19}$$

These are the so-called generalised W-H equations. In this system, the functions $U(\cdot,\theta)$ and $V(\cdot,\theta)$ are analytic in a region containing the upper half plane regardless of the value of θ. We solve the system (3.19) for $U(\cos(z),0)$ and $V(\cos(z),0)$ using the boundary data on the right hand side. Noting that $\cos(\mathbb{R})$ is equal to γ_+ with the opposite orientation, the inverse transform of $U(\cos(z),\theta)$ is,

$$\Phi(r,\theta) = \frac{1}{2\pi i}\int_{\gamma_+} e^{-ikr\cos(z)}U(\cos(z),\theta)\,(ik\sin(z))\,\mathrm{d}z, \tag{3.20}$$

which is clearly very similar to the Sommerfeld integral. Applying Malyuzhinets' theorem, we find that,

$$ik\sin(z)U(\cos(z),\theta) = s(\theta+z) - s(\theta-z). \tag{3.21}$$

We can derive a second formula by comparing the inverse transform of $V(\cos(z),\theta)$ with the following,

$$\frac{1}{ikr}\frac{\partial\Phi}{\partial\theta}(r,\theta) = -\frac{1}{2\pi i}\int_{\gamma_+} e^{-ikr\cos(z)}\sin(z)\left[s(\theta+z)+s(\theta-z)\right]\mathrm{d}z, \tag{3.22}$$

which is obtained by differentiating (2.1) with respect to θ and integration by parts. Applying Malyuzhinets' theorem, we find that,

$$-ikV(\cos(z),\theta) = s(\theta+z) + s(\theta-z). \tag{3.23}$$

Adding (3.21) to (3.23) and setting $\theta = 0$ implies that for all z,

$$s(z) = \frac{ik}{2}\left[\sin(z)U(\cos(z),0) - V(\cos(z),0)\right], \tag{3.24}$$

establishing a link between the spectral function and the W-H unknowns. We will now apply the BCs to solve the W-H system (3.19). Note that a very similar expression is derived by Bernard (2005, 2006), though not in a Wiener-Hopf technique context. Instead, he makes use of Green's theorem. This very interesting approach will be re-visited in more details in Appendix B.

3.3. Dirichlet boundary condition

The transformed Dirichlet BCs are $U(\cos(\theta_\mathrm{w}-z),\pm\theta_\mathrm{w})=0$ which simplify (3.19) to,

$$\begin{aligned} 2V(\cos(z),0) &= V(\cos(\theta_\mathrm{w}-z),-\theta_\mathrm{w})+V(\cos(\theta_\mathrm{w}-z),\theta_\mathrm{w}),\\ 2\sin(z)U(\cos(z),0) &= V(\cos(\theta_\mathrm{w}-z),-\theta_\mathrm{w})-V(\cos(\theta_\mathrm{w}-z),\theta_\mathrm{w}). \end{aligned} \tag{3.25}$$

In this form the W-H technique cannot be applied, so (3.3) and (3.6) (discussed in Section 3.1) are used here,

$$2V(\cos(z(\alpha)),0) = V(\cos(z(-\alpha)),-\theta_\mathrm{w})+V(\cos(z(-\alpha)),\theta_\mathrm{w}), \tag{3.26}$$

$$2\sin(z(\alpha))U(\cos(z(\alpha)),0) = V(\cos(z(-\alpha)),-\theta_\mathrm{w})-V(\cos(z(-\alpha)),\theta_\mathrm{w}). \tag{3.27}$$

In the α-plane, $U(\cos(z(\alpha)),0)$ and $V(\cos(z(\alpha)),0)$ are analytic in $\mathcal{R}_+$, except for some potential poles on the real line segment $\mathcal{R}_+\cap\mathcal{R}_-$. Similarly, $V(\cos(z(-\alpha)),\pm\theta_\mathrm{w})$ are analytic in $\mathcal{R}_-$, except for some potential poles on $\mathcal{R}_+\cap\mathcal{R}_-$. We have already factorised $\sin(z(\alpha))=f_1(\eta(\alpha))$ in (3.11), leading (3.27) to become,

$$2f_{1+}(\alpha)U(\cos(z(\alpha)),0) = \frac{1}{f_{1-}(\alpha)}\left[V(\cos(z(-\alpha)),-\theta_\mathrm{w})-V(\cos(z(-\alpha)),\theta_\mathrm{w})\right]. \tag{3.28}$$

For both equations, (3.26) and (3.28), the left sides are meromorphic in $\mathcal{R}_+$ and the right sides are meromorphic in $\mathcal{R}_-$, however due to the potential poles, these equations cannot be used to create an entire function. To counteract this we remove the poles on the right side using the knowledge of the GO component of the solution. Assuming that $\theta_\mathrm{w}>\pi/2$, the GO components of $V(\cos(z(-\alpha)),\pm\theta_\mathrm{w})$ are,

$$\begin{aligned} V^{(\mathrm{GO})}(\cos(z(-\alpha)),\theta_\mathrm{w}) &= \frac{2i\sin(\theta_\mathrm{w}-\theta_\mathrm{I})}{k\cos(z(-\alpha))-k\cos(\theta_\mathrm{w}-\theta_\mathrm{I})},\\ V^{(\mathrm{GO})}(\cos(z(-\alpha)),-\theta_\mathrm{w}) &= -\frac{2i\sin(\theta_\mathrm{w}+\theta_\mathrm{I})\mathcal{H}(\pi-\theta_\mathrm{w}-\theta_\mathrm{I})}{k\cos(z(-\alpha))-k\cos(\theta_\mathrm{w}+\theta_\mathrm{I})}, \end{aligned}$$

where $\mathcal{H}$ is the Heaviside function. The two poles correspond to $z(-\alpha)=\pm(\theta_\mathrm{w}-\theta_\mathrm{I})$, i.e. to $z(\alpha)=\pm\theta_\mathrm{I}$. However there is no α in the chosen branch of inverse cosine that satisfies $z(\alpha)=-\theta_\mathrm{I}$. This means that the only pole that needs to be removed is that of $V^{(\mathrm{GO})}(\cos(z(-\alpha)),\theta_\mathrm{w})$ at $z(\alpha)=\theta_\mathrm{I}$, corresponding to $\alpha=\alpha_0=\cos(2\delta\theta_\mathrm{I})$. The residue at this pole is,

$$\lim_{\alpha\to\alpha_0}\left[(\alpha-\alpha_0)\,V^{(\mathrm{GO})}(\cos(z(-\alpha)),\theta_\mathrm{w})\right] = \frac{4\delta\sin(2\delta\theta_\mathrm{I})}{ik}. \tag{3.29}$$

With this residue, we remove the pole from equations (3.26) and (3.28),

$$V(\cos(z(\alpha)),0) - \frac{2\delta\sin(2\delta\theta_{\mathrm{I}})}{ik\left(\alpha-\cos(2\delta\theta_{\mathrm{I}})\right)}$$
$$= \frac{1}{2}\left[V(\cos(z(-\alpha)),-\theta_{\mathrm{w}}) + V(\cos(z(-\alpha)),\theta_{\mathrm{w}})\right] - \frac{2\delta\sin(2\delta\theta_{\mathrm{I}})}{ik\left(\alpha-\cos(2\delta\theta_{\mathrm{I}})\right)}, \tag{3.30}$$

$$f_{1+}(\alpha)U(\cos(z(\alpha)),0) + \frac{2\delta\sin(2\delta\theta_{\mathrm{I}})}{ikf_{1-}(\alpha_0)\left(\alpha-\cos(2\delta\theta_{\mathrm{I}})\right)}$$
$$= \frac{1}{2f_{1-}(\alpha)}\left[V(\cos(z(-\alpha)),-\theta_{\mathrm{w}}) - V(\cos(z(-\alpha)),\theta_{\mathrm{w}})\right] + \frac{2\delta\sin(2\delta\theta_{\mathrm{I}})}{ikf_{1-}(\alpha_0)\left(\alpha-\cos(2\delta\theta_{\mathrm{I}})\right)}. \tag{3.31}$$

In both equations (3.30) and (3.31), the left sides are now analytic in $\mathcal{R}_+$ and the right sides are analytic in $\mathcal{R}_-$. In order to apply Liouville's theorem, we must determine the behaviour of each part in equations (3.30) and (3.31) as $|\alpha|\to\infty$. The edge condition (1.5) for the Dirichlet case implies that $\Phi = O(r^{\delta})$ and $\frac{1}{r}\frac{\partial\Phi}{\partial\theta} = O(r^{\delta-1})$. Using the well-known fact that for any function $f(r)$ behaving like r^{δ} as $r\to 0$, its Laplace transform $F(\eta)$, as defined by (3.16), behaves like $|\eta|^{-\delta-1}$ as $|\eta|\to\infty$, and noting that $\eta(\alpha) = O(|\alpha|^{\frac{\theta_{\mathrm{w}}}{\pi}})$ as $|\alpha|\to\infty$, we can show that as $|\alpha|\to\infty$, $U(\cos(z(\alpha)),0) = O(|\alpha|^{-\frac{1}{2}-\frac{\theta_{\mathrm{w}}}{\pi}})$, and $V(\cos(z(\alpha)),0) = O(|\alpha|^{-\frac{1}{2}})$ within $\mathcal{R}_+$, while $V(\cos(z(-\alpha)),\pm\theta_{\mathrm{w}}) = O(|\alpha|^{-\frac{1}{2}})$ within $\mathcal{R}_-$. We can also determine that $f_{1-}(\alpha) = O(|\alpha|^{\frac{1}{2}})$ and $f_{1+}(\alpha) = O(|\alpha|^{\frac{\theta_{\mathrm{w}}}{\pi}-\frac{1}{2}})$ as $|\alpha|\to\infty$. This means that all parts of equations (3.30) and (3.31) are decaying as $|\alpha|\to\infty$ in the appropriate half plane. Construct the two functions,

$$\Psi_1(\alpha) = \begin{cases} \text{LHS}(3.30) & \text{in } \mathcal{R}_+, \\ \text{RHS}(3.30) & \text{in } \mathcal{R}_-, \\ (3.30) & \text{in } \mathcal{R}_+\cap\mathcal{R}_-, \end{cases} \qquad \Psi_2(\alpha) = \begin{cases} \text{LHS}(3.31) & \text{in } \mathcal{R}_+, \\ \text{RHS}(3.31) & \text{in } \mathcal{R}_-, \\ (3.31) & \text{in } \mathcal{R}_+\cap\mathcal{R}_-. \end{cases} \tag{3.32}$$

Both Ψ_1 and Ψ_2 are entire and decaying at infinity, therefore Liouville's theorem can be applied to show that $\Psi_1, \Psi_2 \equiv 0$. It is hence possible to determine $V(\cos(z),0)$ and $U(\cos(z),0)$,

$$V(\cos(z),0) = \frac{2\delta\sin(2\delta\theta_{\mathrm{I}})}{ik(\cos(2\delta z)-\cos(2\delta\theta_{\mathrm{I}}))}, \tag{3.33}$$

$$\sin(z)U(\cos(z),0) = -\frac{4\delta\cos(\delta\theta_{\mathrm{I}})\sin(\delta z)}{ik(\cos(2\delta z)-\cos(2\delta\theta_{\mathrm{I}}))}. \tag{3.34}$$

Equations (3.33) and (3.34) can be substituted into (3.24) to obtain,

$$s(z) = \frac{ik}{2}\left[\sin(z)U(\cos(z),0) - V(\cos(z),0)\right] = \frac{\delta\cos(\delta\theta_{\mathrm{I}})}{\sin(\delta z)-\sin(\delta\theta_{\mathrm{I}})}, \tag{3.35}$$

which is the exact spectral function (2.13) obtained using the S-M technique.

3.4. Neumann boundary condition

The Neumann problem is solved in a similar way to the Dirichlet problem. The transformed Neumann BCs are $V(\cos(\theta_{\rm w}-z),\pm\theta_{\rm w})=0$, leading to a simplification of (3.19). Again, in the resulting form, the W-H technique cannot be applied directly and we need the useful mapping of Section 3.1 together with the factorisation of $f_1(\eta(\alpha))=\sin(z(\alpha))$ and $f_3(\eta(\alpha))=\sin(z(-\alpha))$ given in the same section. This leads to

$$\begin{aligned}\frac{1}{f_{3+}(\alpha)}V(\cos(z(\alpha)),0)&=\frac{f_{3-}(\alpha)}{2}\left[U(\cos(z(-\alpha)),\theta_{\rm w})-U(\cos(z(-\alpha)),-\theta_{\rm w})\right],\\ \frac{f_{1+}(\alpha)}{f_{3+}(\alpha)}U(\cos(z(\alpha)),0)&=-\frac{f_{3-}(\alpha)}{2f_{1-}(\alpha)}\left[U(\cos(z(-\alpha)),\theta_{\rm w})+U(\cos(z(-\alpha)),-\theta_{\rm w})\right].\end{aligned}\tag{3.36}$$

The left (resp. right) sides of (3.36) are meromorphic in $\mathcal{R}_+$ (resp. $\mathcal{R}_-$) but as for the Dirichlet case, there are potential poles on $\mathcal{R}_+\cap\mathcal{R}_-$. To counteract this we remove the poles on the right side using the knowledge of the GO component of the solution. Assuming that $\theta_{\rm w}>\pi/2$, the GO components of $U(\cos(z(-\alpha)),\pm\theta_{\rm w})$ are,

$$\begin{aligned}U^{(\rm GO)}(\cos(z(-\alpha)),\theta_{\rm w})&=\frac{2i}{k(\cos(z(-\alpha))-\cos(\theta_{\rm w}-\theta_{\rm I}))},\\ U^{(\rm GO)}(\cos(z(-\alpha)),-\theta_{\rm w})&=\frac{2i\mathcal{H}(\pi-\theta_{\rm w}-\theta_{\rm I})}{k(\cos(z(-\alpha))-\cos(\theta_{\rm w}+\theta_{\rm I}))}.\end{aligned}$$

As in the Dirichlet case, we only need to remove the pole of $U^{(\rm GO)}(\cos(z(-\alpha)),\theta_{\rm w})$ at $\alpha=\alpha_0=\cos(2\delta\theta_{\rm I})$ with residue,

$$\lim_{\alpha\to\alpha_0}\left[(\alpha-\alpha_0)\,U^{(\rm GO)}(\cos(z(-\alpha)),\theta_{\rm w})\right]=\frac{4\delta\sin(2\delta\theta_{\rm I})}{ik\sin(\theta_{\rm w}-\theta_{\rm I})}.\tag{3.37}$$

Using this residue, and the fact that $f_{1-}(\alpha_0)=\sin(\delta\theta_{\rm I})$ and $f_{3-}(\alpha_0)=\frac{\sin(\theta_{\rm w}-\theta_{\rm I})}{\cos(\delta\theta_{\rm I})}$, we can remove this pole from the W-H system (3.36) to get

$$\begin{aligned}&\frac{1}{f_{3+}(\alpha)}V(\cos(z(\alpha)),0)-\frac{4\delta\sin(\delta\theta_{\rm I})}{ik(\alpha-\cos(2\delta\theta_{\rm I}))}\\ &\qquad=\frac{f_{3-}(\alpha)}{2}\left[U(\cos(z(-\alpha)),\theta_{\rm w})-U(\cos(z(-\alpha)),-\theta_{\rm w})\right]-\frac{4\delta\sin(\delta\theta_{\rm I})}{ik(\alpha-\cos(2\delta\theta_{\rm I}))},\end{aligned}\tag{3.38}$$

$$\begin{aligned}&\frac{f_{1+}(\alpha)}{f_{3+}(\alpha)}U(\cos(z(\alpha)),0)+\frac{4\delta}{ik(\alpha-\cos(2\delta\theta_{\rm I})}\\ &\qquad=-\frac{f_{3-}(\alpha)}{2f_{1-}(\alpha)}\left[U(\cos(z(-\alpha)),\theta_{\rm w})+U(\cos(z(-\alpha)),-\theta_{\rm w})\right]+\frac{4\delta}{ik(\alpha-\cos(2\delta\theta_{\rm I}))}.\end{aligned}\tag{3.39}$$

In both equations (3.38) and (3.39), the left (resp. right) sides are now analytic in $\mathcal{R}_+$ (resp. $\mathcal{R}_-$). As before, in order to apply Liouville's theorem, we must determine the behaviour of each part in equations (3.38) and (3.39) as $|\alpha| \to \infty$. Using the edge conditions (1.5) for the Neumann case, and the reasoning developed in the Dirichlet case, we can show that, as $|\alpha| \to \infty$, $U(\cos(z(\alpha)), 0) = O(|\alpha|^{-\frac{\theta_w}{\pi}})$ and $V(\cos(z(\alpha)), 0) = O(|\alpha|^{-\frac{1}{2}})$ within $\mathcal{R}_+$, while $U(\cos(z(-\alpha)), \pm\theta_w) = O(|\alpha|^{-\frac{\theta_w}{\pi}})$ within $\mathcal{R}_-$. We can also determine that $f_{1-}(\alpha), f_{3+}(\alpha) = O(|\alpha|^{\frac{1}{2}})$ and $f_{1+}(\alpha), f_{3-}(\alpha) = O(|\alpha|^{\frac{\theta_w}{\pi}-\frac{1}{2}})$ as $|\alpha| \to \infty$. As before we can hence construct two decaying entire functions and apply Liouville's theorem to obtain

$$V(\cos(z), 0) = \frac{4\delta \sin(\delta\theta_I)\cos(\delta z)}{ik(\cos(2\delta z) - \cos(2\delta\theta_I))}, \tag{3.40}$$

$$\sin(z)U(\cos(z), 0) = -\frac{2\delta \sin(2\delta z)}{ik(\cos(2\delta z) - \cos(2\delta\theta_I)}. \tag{3.41}$$

Equations (3.40) and (3.41) can be substituted into (3.24) to get,

$$s(z) = \frac{ik}{2}\left[\sin(z)U(\cos(z), 0) - V(\cos(z), 0)\right] = \frac{\delta\cos(\delta z)}{\sin(\delta z) - \sin(\delta\theta_I)}, \tag{3.42}$$

which is the exact spectral function (2.18) obtained using the S-M technique.

Critical analysis. The main disadvantage of this method is that, as our derivation shows, it is not naturally designed to tackle the wedge problem. As a result, we do not directly obtain a usual W-H equation, and have to rely on a sophisticated mapping in order to get back to the usual framework.

The advantage of this section, however, is to show the flexibility of the W-H method, and that it can work, even in non-flat/parallel geometries. As for the S-M technique it is possible to adapt such method to more complicated cases such as inhomogeneous impedance (Shanin, 1998), anisotropic impedance (Daniele and Lombardi, 2006) at skew incidence or even the penetrable wedge (Daniele and Lombardi, 2011).

Moreover, in usual flat geometries, it is known that the W-H technique can be adapted to handle finite structures. It generally results in matrix W-H problems. This is encouraging in our case since there is a chance of tackling geometries such as the truncated wedge (tip removed) with such method. It is perhaps surprising that this problem can be recast in an analytical continuation problem of the W-H problem type. This may give insight to the solution of a broader class of diffraction problems (Daniele and Zich, 2014).

4. The Kontorovich-Lebedev transform method

The third method to be reviewed relies on the Kontorovich-Lebedev (K-L) transform. Introduced in (Kontorovich and Lebedev, 1939), this transform is useful because

the resulting transformed Helmholtz equation is easy to solve. However, the inverse transform is known to have convergence issues, but there are alternative versions involving a convergence factor that can help with this (see e.g. (Jones, 1980)). For any function $f(r)$, define the K-L transform and its inverse (which can have many variations from numerous sources such as (Lebedev, 1965), (Abrahams, 1986) and (Jones, 1986)) as

$$F(\nu) = \int_0^\infty \frac{f(r)}{r} H_\nu^{(1)}(kr)\mathrm{d}r, \quad f(r) = \frac{1}{2}\int_{-i\infty}^{i\infty} \nu J_\nu(kr)F(\nu)\mathrm{d}\nu, \tag{4.1}$$

where J_ν and $H_\nu^{(1)}$ are the Bessel and Hankel functions of the first kind. The transform is valid if,

$$\left|\int_c^\infty \frac{f(r)e^{-ikr}}{r^{\frac{3}{2}}}\mathrm{d}r\right| < \infty, \quad \text{and} \quad \int_0^\epsilon \left|\frac{f(r)\ln(kr)}{r}\right|\mathrm{d}r < \infty, \tag{4.2}$$

for all $c > 0$ and $0 < \epsilon \ll 1$. Alternatively, if the second integral condition is not satisfied because $f(r)$ tends to a constant as $r \to 0$, then $F(\nu)$ contains a pole at $\nu = 0$ on the integration contour of the inverse transform. This pole is interpreted as,

$$\frac{1}{\nu} = \frac{1}{2}\lim_{\epsilon\to 0}\left[\frac{1}{\nu-\epsilon} + \frac{1}{\nu+\epsilon}\right]. \tag{4.3}$$

If the integrand of the inverse transform fails to converge as $\nu \to \pm i\infty$, an alternative version with a convergence factor (proposed by Jones (1980)), should be used:

$$f(r) = \frac{1}{2}\lim_{\epsilon\to 0}\left[\int_{-i\infty}^{i\infty} e^{\epsilon\nu^2}\nu J_\nu(kr)F(\nu)\mathrm{d}\nu\right]. \tag{4.4}$$

To adapt this to our problem, we first split the total wave field Φ into its incident and scattered parts $\Phi(r,\theta) = e^{-ikr\cos(\theta-\theta_\mathrm{I})} + \Phi_\mathrm{S}(r,\theta)$, where the scattered part Φ_S satisfies Helmholtz's equation (1.1) and two types of BCs,

$$\text{Dirichlet BCs:} \quad \Phi_\mathrm{S}(r,\pm\theta_\mathrm{w}) = -e^{-ikr\cos(\theta_\mathrm{w}\mp\theta_\mathrm{I})}, \tag{4.5}$$

$$\text{Neumann BCs:} \quad \frac{1}{r}\frac{\partial\Phi_\mathrm{S}}{\partial\theta}(r,\pm\theta_\mathrm{w}) = \mp ik\sin(\theta_\mathrm{w}\mp\theta_\mathrm{I})e^{-ikr\cos(\theta_\mathrm{w}\mp\theta_\mathrm{I})}. \tag{4.6}$$

For our problem, the K-L transform and the associated inverse are given below,

$$\Psi(\nu,\theta) = \int_0^\infty \frac{\Phi_\mathrm{S}(r,\theta)}{r} H_\nu^{(1)}(kr)\mathrm{d}r, \quad \Phi_\mathrm{S}(r,\theta) = \frac{1}{2}\int_{-i\infty}^{i\infty} \nu J_\nu(kr)\Psi(\nu,\theta)\mathrm{d}\nu, \tag{4.7}$$

where the first integral condition (4.2) is satisfied due to the radiation condition (1.4). The edge condition (1.5) implies that $\Psi(\nu,\theta)$ will have a pole at $\nu = 0$. Using (4.7),

we find the transformed boundary data,

$$\text{Dirichlet:} \quad \Psi^{\pm}(\nu) = \Psi(\nu, \pm\theta_{\mathrm{w}}) = -\int_0^{\infty} \frac{1}{r} e^{-ikr\cos(\theta_{\mathrm{w}} \mp \theta_{\mathrm{I}})} H_{\nu}^{(1)}(kr)\mathrm{d}r, \tag{4.8}$$

$$\text{Neumann:} \quad \Psi_{\theta}^{\pm}(\nu) = \frac{\partial \Psi}{\partial \theta}(\nu, \pm\theta_{\mathrm{w}}) = \mp ik\sin(\theta_{\mathrm{w}} \mp \theta_{\mathrm{I}}) \int_0^{\infty} e^{-ikr\cos(\theta_{\mathrm{w}} \mp \theta_{\mathrm{I}})} H_{\nu}^{(1)}(kr)\mathrm{d}r. \tag{4.9}$$

From equation 6.611.5 of (Gradshteyn and Ryzhik, 2014), for $\mathrm{Re}\{\nu\} \in (-1, 1)$, we know that

$$\int_0^{\infty} e^{-aR} H_{\nu}^{(1)}(R)\mathrm{d}R = \frac{i\left(\sqrt{a^2+1}+a\right)^{-\nu}}{\sin(\pi\nu)\sqrt{a^2+1}} \left[e^{-i\pi\nu} - \left(\sqrt{a^2+1}+a\right)^{2\nu}\right], \tag{4.10}$$

and integrating (4.10) with respect to a, we obtain

$$-\int_0^{\infty} \frac{e^{-aR}}{R} H_{\nu}^{(1)}(R)\mathrm{d}R = -\frac{i\left(\sqrt{a^2+1}+a\right)^{-\nu}}{\nu\sin(\pi\nu)} \left[e^{-i\pi\nu} + \left(\sqrt{a^2+1}+a\right)^{2\nu}\right]. \tag{4.11}$$

Now, let $R = kr$ and $a = i\cos(\theta_{\mathrm{w}} \mp \theta_{\mathrm{I}})$, then use (4.11) (resp. (4.10)) to evaluate (4.8) (resp. (4.9)) explicitly to get

$$\text{Dirichlet:} \quad \Psi^{\pm}(\nu) = \frac{2(-i)^{1+\nu}}{\nu\sin(\pi\nu)} \cos((\theta_{\mathrm{w}} \mp \theta_{\mathrm{I}} - \pi)\nu), \tag{4.12}$$

$$\text{Neumann:} \quad \Psi_{\theta}^{\pm}(\nu) = \mp\frac{2(-i)^{1+\nu}}{\sin(\pi\nu)} \sin((\theta_{\mathrm{w}} \mp \theta_{\mathrm{I}} - \pi)\nu). \tag{4.13}$$

The advantage of the K-L transform is that if Ψ satisfies the following governing equation,

$$\frac{\partial^2 \Psi}{\partial \theta^2} + \nu^2 \Psi = 0, \tag{4.14}$$

then Φ_{S} satisfies Helmholtz's equation. For the Dirichlet case, the solution of (4.14) is,

$$\Psi(\nu, \theta) = \frac{1}{\sin(2\theta_{\mathrm{w}}\nu)} \left[\Psi^{-}(\nu)\sin((\theta_{\mathrm{w}} - \theta)\nu) + \Psi^{+}(\nu)\sin((\theta_{\mathrm{w}} + \theta)\nu)\right]. \tag{4.15}$$

This means that the exact solution with Dirichlet BCs is

$$\begin{aligned}\Phi(r, \theta) = \int_{-i\infty}^{i\infty} \frac{J_{\nu}(kr)}{i^{1+\nu}\sin(\pi\nu)\sin(2\theta_{\mathrm{w}}\nu)} \big[&\cos((\theta_{\mathrm{w}} + \theta_{\mathrm{I}} - \pi)\nu)\sin((\theta_{\mathrm{w}} - \theta)\nu) \\ &+ \cos((\theta_{\mathrm{w}} - \theta_{\mathrm{I}} - \pi)\nu)\sin((\theta_{\mathrm{w}} + \theta)\nu)\big]\mathrm{d}\nu + e^{-ikr\cos(\theta - \theta_{\mathrm{I}})}.\end{aligned} \tag{4.16}$$

For the Neumann case, the solution of (4.14) is,

$$\Psi(\nu,\theta)=\frac{1}{\nu\sin(2\theta_{\mathrm{w}}\nu)}\left[\Psi_{\theta}^{-}(\nu)\cos((\theta_{\mathrm{w}}-\theta)\nu)-\Psi_{\theta}^{+}(\nu)\cos((\theta_{\mathrm{w}}+\theta)\nu)\right]. \tag{4.17}$$

This means that the exact solution with Neumann BCs is

$$\begin{aligned}\Phi(r,\theta)=\int_{-i\infty}^{i\infty}\frac{J_{\nu}(kr)}{i^{1+\nu}\sin(\pi\nu)\sin(2\theta_{\mathrm{w}}\nu)}\big[&\sin((\theta_{\mathrm{w}}+\theta_{\mathrm{I}}-\pi)\nu)\cos((\theta_{\mathrm{w}}-\theta)\nu)\\&+\sin((\theta_{\mathrm{w}}-\theta_{\mathrm{I}}-\pi)\nu)\cos((\theta_{\mathrm{w}}+\theta)\nu)\big]\mathrm{d}\nu+e^{-ikr\cos(\theta-\theta_{\mathrm{I}})}.\end{aligned} \tag{4.18}$$

While it is difficult to see it by inspection, these integral solutions (4.16) and (4.18) are equivalent to the Sommerfeld integral solutions (2.14) and (2.19). As we discuss in Appendix B, the connection between the Sommerfeld inverse formula (2.1) and the K-L inverse transform (4.1) was made in (Malyuzhinets, 1958c) by using the Sommerfeld integral form of Bessel functions. Here, we shall show equivalence by first rewriting the integrals (4.16) and (4.18) as series, then convert the result into Sommerfeld integrals.

The solutions (4.16) and (4.18) are evaluated by deforming the contour to the right and summing the residues of the poles crossed in the process. The double pole at $\nu=0$ is interpreted using (4.3). We can simplify the result using the Jacobi-Anger expansion of the incident wave to obtain the following series solutions for Dirichlet and Neumann BCs respectively,

$$\Phi(r,\theta)=2\delta\sum_{n=1}^{\infty}(-i)^{\delta n}J_{\delta n}(kr)\left[\cos((\theta-\theta_{\mathrm{I}})\delta n)-\cos((\theta-2\theta_{\mathrm{w}}+\theta_{\mathrm{I}})\delta n)\right], \tag{4.19}$$

$$\Phi(r,\theta)=2\delta J_0(kr)+2\delta\sum_{n=1}^{\infty}(-i)^{\delta n}J_{\delta n}(kr)\left[\cos((\theta-\theta_{\mathrm{I}})\delta n)+\cos((\theta-2\theta_{\mathrm{w}}+\theta_{\mathrm{I}})\delta n)\right], \tag{4.20}$$

where, as before, $\delta=\frac{\pi}{2\theta_{\mathrm{w}}}$. These series solutions can be matched with classical series solutions obtained by Macdonald (1902) (see Appendix A for more details).

Finally, we need to transform (4.19) and (4.20) into Sommerfeld integrals. We do this by using the Sommerfeld integral formula for the Bessel function of the first kind,

$$J_v(R)=-\frac{1}{2\pi}\int_{\gamma_+}e^{-iR\cos(z)+ivz+iv\frac{\pi}{2}}\mathrm{d}z, \tag{4.21}$$

and equation 1.461.2 from (Gradshteyn and Ryzhik, 2014)

$$1+2\sum_{n=1}^{\infty}e^{ina}\cos(nb)=\frac{i\sin(a)}{\cos(b)-\cos(a)}, \tag{4.22}$$

which converges if $\mathrm{Im}\{a\} > 0$. This means that (4.19) and (4.20) can be written in Sommerfeld integral form as

$$\Phi(r,\theta) = \frac{1}{2\pi i}\int_{\gamma_+} e^{-ikr\cos(z)}\left[\frac{\delta\sin(\delta z)}{\cos(\delta(\theta-\theta_\mathrm{I}))-\cos(\delta z)} \pm \frac{\delta\sin(\delta z)}{\cos(\delta(\theta+\theta_\mathrm{I}))+\cos(\delta z)}\right]\mathrm{d}z, \tag{4.23}$$

where the plus and minus signs denote the Dirichlet and Neumann solutions respectively. Using standard trigonometric identities, it is trivial to show that the square brackets in (4.23) are an alternate form of $s(\theta+z)-s(\theta-z)$. Hence the Kontorovich-Lebedev solutions (4.16) and (4.18) match with the Sommerfeld integrals (2.14) and (2.19) respectively.

Critical analysis. The main advantage of such transform is that it is a very natural way to tackle the wedge problem. It hence leads to a constructive proof of the form of the solution in the K-L space, see e.g. (4.15). In addition, it leads easily to a near-field expansion of the solution.

The clear disadvantage of such method lies in the convergence issues of the inverse K-L transform. It does require some regularisation in order to be evaluated numerically, and even in this case, the computation of inverse K-L transform remains cumbersome. To evaluate the far-field it is usually necessary to convert it into a Sommerfeld type integral.

5. Solution analysis and evaluation

We shall now compare the exact integral and series solutions with some GTD approximations and evaluate them for some representative values of θ_w. Note that the K-L integrals do not need to be plotted since we have already shown that they are equivalent to the Sommerfeld integrals (2.14) and (2.19). Numerical computation of the Sommerfeld integrals can be slow if $kr \gg 1$ because $e^{-ikr\cos(z)}$ will oscillate rapidly along the Sommerfeld contours.

Another way to evaluate these integrals is to deform the Sommerfeld contours to the steepest descent contours shown on the left side of Figure 6. During this deformation, all poles on the real line segment $|\mathrm{Re}\{z\}| \leq \pi$ are crossed. Their contribution, which can be calculated exactly using residues, correspond to the GO component of the field, Φ_GO, leaving behind the diffracted part Φ_Diff. The steepest descent contour SDC_0 is repeated twice in opposite directions so is cancelled out and the other two contours are translations of each other. The exponential term $e^{-ikr\cos(z)}$ does not oscillate along these contours so computation time is significantly reduced, even for large kr. This means that the S-M integrals (2.14)-(2.19) are equivalent to,

$$\Phi = \Phi_\mathrm{GO} + \Phi_\mathrm{Diff} = \Phi_\mathrm{GO} + \frac{1}{2\pi i}\int_{SDC_{-\pi}+SDC_\pi} e^{-ikr\cos(z)}s(\theta+z)\mathrm{d}z. \tag{5.1}$$

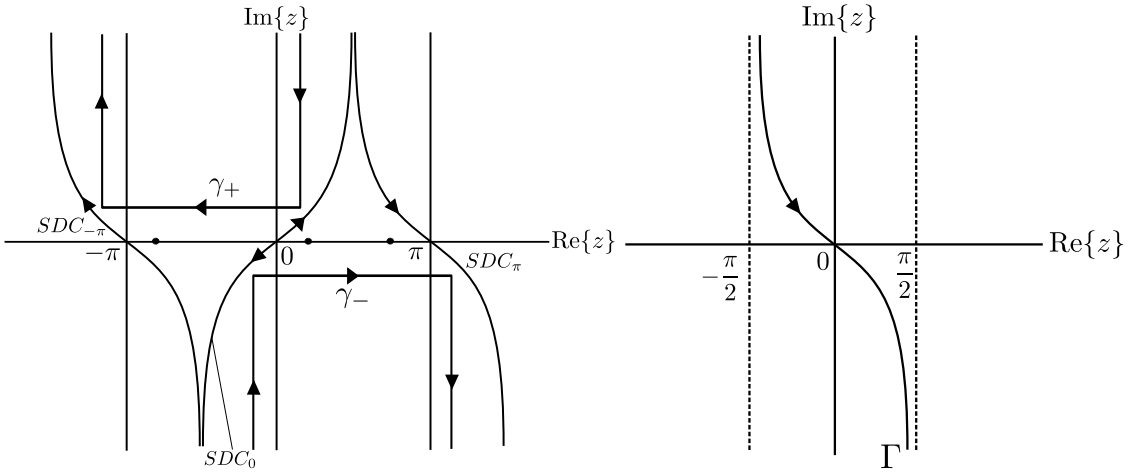

Figure 6: The Sommerfeld contours $\gamma_\pm$, the steepest descent contours $SDC_{-\pi}$, SDC_0, SDC_π and, shown as dots, possible poles on the real line (left) and the Γ contour (right)

Since they are translations of each other, we can transform $SDC_{-\pi}$ and SDC_π onto the Γ contour which is illustrated on the right side of Figure 6,

$$\Phi_{\text{Diff}} = \frac{1}{2\pi i}\int_\Gamma e^{ikr\cos(z)}\left[s(\theta+z+\pi)-s(\theta+z-\pi)\right]\mathrm{d}z. \tag{5.2}$$

By the method of steepest descent, Γ satisfies,

$$\Gamma(\tau) = \cosh^{-1}\left(\frac{1}{\cos(\tau)}\right), \quad \text{and} \quad \sin(\tau)\sinh(\Gamma(\tau)) \le 0, \tag{5.3}$$

where $\mathrm{Re}\{z\} = \tau \in (-\frac{\pi}{2}, \frac{\pi}{2})$. This is rewritten in terms of the Gudermannian function $\mathrm{gd}(x)$,

$$\Gamma(\tau) = i\,\mathrm{gd}(i\tau) = \ln\left|\sec(\tau)-\tan(\tau)\right|. \tag{5.4}$$

Using the following parametrisation, $z = \tau + i\Gamma(\tau)$, and noting these identities,

$$\sinh(\Gamma(\tau)) = -\tan(\tau), \quad \frac{\mathrm{d}\Gamma}{\mathrm{d}\tau} = -\sec(\tau),$$

the diffracted part is written as a simple integral:

$$\Phi_{\text{Diff}} = \frac{e^{ikr}}{2\pi i}\int_{-\frac{\pi}{2}}^{\frac{\pi}{2}} e^{-kr\sin(\tau)\tan(\tau)}\left[s(\theta+\pi+\tau+i\Gamma(\tau))-s(\theta-\pi+\tau+i\Gamma(\tau))\right](1-i\sec(\tau))\,\mathrm{d}\tau. \tag{5.5}$$

As stated earlier, this integral will be much faster to evaluate numerically than the S-M integrals (2.14)-(2.19). However, difficulties can arise when θ is in a small neighbourhood of the GO discontinuities because one of the poles will be very close to the contour of integration, which will cause numerical issues.

5.1. Comparison with simpler problems

In this subsection we will show that the solution is consistent with the simple case when the wedge opens up to form a half-space or closes to make a half-plane. First, we look at the case where $\theta_{\mathrm{w}} = \pi/2$ to form a half-space problem. The solution is easily obtainable via the method of images,

$$\Phi(r,\theta) = \Phi_{\mathrm{I}} \mp \Phi_{\mathrm{R}}. \tag{5.6}$$

Here the upper and lower signs denote the Dirichlet and Neumann solutions respectively. Obviously (5.6) is equal to the GO component so we need to show that the diffracted part (5.2) is identically zero. Expressing $s(z)$ in terms of the cotangent, we find that,

$$\begin{aligned} s(z+\pi) - s(z-\pi) = \frac{1}{2}\left[\cot\left(\frac{1}{2}(z-\theta_{\mathrm{I}}+\pi)\right) \mp \cot\left(\frac{1}{2}(z+\theta_{\mathrm{I}})\right)\right] \\ - \frac{1}{2}\left[\cot\left(\frac{1}{2}(z-\theta_{\mathrm{I}}-\pi)\right) \mp \cot\left(\frac{1}{2}(z+\theta_{\mathrm{I}}-2\pi)\right)\right], \end{aligned} \tag{5.7}$$

which is identically zero due to the periodicity of cotangent. This implies that $\Phi_{\mathrm{Diff}} \equiv 0$, as required.

For another comparison, we look at the case where the wedge closes to form a half-plane. Hence we let $\theta_{\mathrm{w}} = \pi$ and match the S-M integrals (2.14)-(2.19) with the known solution to the half-plane problem in terms of Fresnel integrals,

$$\begin{aligned} \Phi(r,\theta) = \Phi_{\mathrm{I}}\left[\frac{1}{2} + \pi^{-\frac{1}{2}} e^{-\frac{i\pi}{4}} \mathcal{F}\left((2kr)^{\frac{1}{2}} \cos\left(\frac{1}{2}(\theta-\theta_{\mathrm{I}})\right)\right)\right] \\ \mp \Phi_{\mathrm{R}}\left[\frac{1}{2} - \pi^{-\frac{1}{2}} e^{-\frac{i\pi}{4}} \mathcal{F}\left((2kr)^{\frac{1}{2}} \cos\left(\frac{1}{2}(\theta+\theta_{\mathrm{I}})\right)\right)\right], \end{aligned} \tag{5.8}$$

where the upper and lower signs correspond to the Dirichlet and Neumann solution respectively, $\Phi_{\mathrm{R}} = e^{-ikr\cos(\theta+\theta_{\mathrm{I}})}$ is the reflected wave and $\mathcal{F}(v)$ is the Fresnel integral defined[5] by

$$\mathcal{F}(v) = \int_0^v e^{iu^2} \mathrm{d}u. \tag{5.9}$$

Having $\theta_{\mathrm{w}} = \pi$ implies that $\delta = 1/2$ and,

$$s(z) = \frac{1}{4}\left[\cot\left(\frac{1}{4}(z-\theta_{\mathrm{I}})\right) \mp \cot\left(\frac{1}{4}(z+\theta_{\mathrm{I}}-2\pi)\right)\right]. \tag{5.10}$$

[5]Fresnel integrals can be written in many different ways, see for example (Abramowitz and Stegun, 1967; Noble, 1958; Assier and Peake, 2012b) and references therein.

Hence, we can rewrite the S-M integrals (2.14)-(2.19) in the following form,

$$\Phi(r,\theta) = \Phi_{\mathcal{F}}(r,\theta-\theta_{\mathrm{I}}) \mp \Phi_{\mathcal{F}}(r,\theta+\theta_{\mathrm{I}}-2\pi), \tag{5.11}$$

where

$$\Phi_{\mathcal{F}}(r,\lambda) = \frac{1}{8\pi i}\int_{\gamma_+-\gamma_-} e^{-ikr\cos(z)}\cot\left(\frac{1}{4}(z+\lambda)\right)\mathrm{d}z. \tag{5.12}$$

It is possible to express (5.12) in terms of a Fresnel integral (a procedure to do this can be found in section 5.3 in (Babich et al., 2007)), leading to

$$\Phi_{\mathcal{F}}(r,\lambda) = e^{-ikr\cos(\lambda)}\left[\frac{1}{2}+\pi^{-\frac{1}{2}}e^{-\frac{i\pi}{4}}\mathcal{F}\left((2kr)^{\frac{1}{2}}\cos\left(\frac{\lambda}{2}\right)\right)\right]. \tag{5.13}$$

Using this, we recover exactly (5.8) from (5.11), as expected. Now that the solution matches with that of the half-space and half-plane problems, we shall focus on deriving the GTD approximation for non-degenerate wedges.

5.2. Geometrical Theory of Diffraction (GTD)

Keller (1962) defined the Geometrical Theory of Diffraction to be an extension of classic Geometrical Optics including diffraction terms. The GTD approximation is simply an asymptotic approximation of the total wave field as $kr \to \infty$, creating a high-frequency or far-field approximation. To derive the GTD approximation of the case presented here, we continue with the method of steepest descent applied to (5.2) as $kr \to \infty$. Equation (5.2) is of the form $\Phi_{\mathrm{Diff}} = \int_\Gamma g(z)e^{-kr\psi(z)}\,\mathrm{d}z$, where kr is a large parameter, $g(z) = \frac{(s(\theta+z+\pi)-s(\theta+z-\pi))}{2\pi i}$ and $\psi(z) = -i\cos(z)$. The latter has a saddle point at $z=0$ and is such that $\psi''(0) = i \neq 0$. Since $g(0)$ is also not zero, we can apply the method of steepest descent in its simplest form (see e.g. (Bleistein and Handelsman, 2010)) to get

$$\Phi_{\mathrm{Diff}} \underset{kr\to\infty}{\sim} \sqrt{\frac{2\pi}{kr\psi''(0)}}g(0)e^{-kr\psi(0)} = \frac{e^{ikr+i\pi/4}}{\sqrt{2\pi kr}}(s(\theta-\pi)-s(\theta+\pi)) \tag{5.14}$$

Hence we can write

$$\Phi(r,\theta) \underset{kr\to\infty}{\sim} \Phi_{\mathrm{GO}} + \frac{e^{ikr+\frac{i\pi}{4}}}{\sqrt{2\pi kr}}\left[s(\theta-\pi)-s(\theta+\pi)\right]. \tag{5.15}$$

In this GTD approximation, the term,

$$D(\theta,\theta_{\mathrm{I}}) = \frac{e^{\frac{i\pi}{4}}}{\sqrt{2\pi}}\left[s(\theta-\pi)-s(\theta+\pi)\right], \tag{5.16}$$

is known as the diffraction coefficient. Unfortunately, this GTD approximation is singular for certain values of θ, for example in the case where $\theta_{\mathrm{w}} > \pi/2$, the GTD is invalid at $\theta_{\mathrm{I}} - \pi$, $2\theta_{\mathrm{w}} - \theta_{\mathrm{I}} - \pi$ and $\pi - 2\theta_{\mathrm{w}} - \theta_{\mathrm{I}}$, which correspond to the GO discontinuities. This is the main issue with GTD: while it is a much more accurate approximation than the Geometrical Optics, it becomes invalid at the GO discontinuities. The pursuit of an approximation that is uniformly valid for all θ has led to the improved Uniform Geometrical Theory of Diffraction (Kouyoumjian and Pathak, 1974). We follow section 5.5 in (Babich et al., 2007) to find the uniform GTD approximation (UTD).

Restricting ourselves to the specific case where $\theta_{\mathrm{w}} > \pi/2$ and $|\theta_{\mathrm{I}}| < \bar{\theta}_{\mathrm{w}} = \pi - \theta_{\mathrm{w}}$, there are only two values where the standard GTD is invalid, $\theta = \pi - 2\theta_{\mathrm{w}} - \theta_{\mathrm{I}}$ and $2\theta_{\mathrm{w}} - \pi - \theta_{\mathrm{I}}$. To produce the uniform approximation, we first construct a function that is a linear combination of Φ and $\Phi_{\mathcal{F}}$ defined by (5.12). The idea is to remove the poles causing the singularities in (5.15) and then use the method of steepest descent. Consider the following,

$$\Xi(r,\theta) = \Phi(r,\theta) \pm \Phi_{\mathcal{F}}(r,\theta + \theta_{\mathrm{I}} - 2\theta_{\mathrm{w}}) \pm \Phi_{\mathcal{F}}(r,\theta + \theta_{\mathrm{I}} + 2\theta_{\mathrm{w}}), \tag{5.17}$$

where $\Phi_{\mathcal{F}}$ is defined in (5.12). The upper and lower signs denote the Dirichlet and Neumann solutions respectively. The combination of Φ and $\Phi_{\mathcal{F}}$ has effectively removed the poles at $2\theta_{\mathrm{w}} - \theta_{\mathrm{I}} - \theta$ and $-2\theta_{\mathrm{w}} - \theta_{\mathrm{I}} - \theta$, but the pole at $\theta_{\mathrm{I}} - \theta$ remains for all values of θ. We use the method of steepest descent to approximate Ξ,

$$\begin{aligned}\Xi(r,\theta) \sim \Phi_{\mathrm{I}} + \frac{e^{ikr+\frac{i\pi}{4}}}{\sqrt{2\pi kr}}\Bigg[& s(\theta-\pi) - s(\theta+\pi) \mp \frac{1}{2}\sec\left(\frac{1}{2}(\theta+\theta_{\mathrm{I}}-2\theta_{\mathrm{w}})\right) \\ & \mp \frac{1}{2}\sec\left(\frac{1}{2}(\theta+\theta_{\mathrm{I}}+2\theta_{\mathrm{w}})\right)\Bigg].\end{aligned} \tag{5.18}$$

We rearrange (5.17) and use (5.13) and (5.18) to find the UTD approximation.

$$\begin{aligned}\Phi(r,\theta) \sim \Phi_{\mathrm{I}} & \mp \Phi_{\mathrm{R}_1}\left[\frac{1}{2} + \pi^{-\frac{1}{2}}e^{-\frac{i\pi}{4}}\mathcal{F}\left((2kr)^{\frac{1}{2}}\cos\left(\frac{\theta+\theta_{\mathrm{I}}-2\theta_{\mathrm{w}}}{2}\right)\right)\right] \\ & \mp \Phi_{\mathrm{R}_2}\left[\frac{1}{2} + \pi^{-\frac{1}{2}}e^{-\frac{i\pi}{4}}\mathcal{F}\left((2kr)^{\frac{1}{2}}\cos\left(\frac{\theta+\theta_{\mathrm{I}}+2\theta_{\mathrm{w}}}{2}\right)\right)\right] \\ & + \frac{e^{ikr+\frac{i\pi}{4}}}{\sqrt{2\pi kr}}\left[s(\theta-\pi) - s(\theta+\pi) \mp \frac{1}{2}\sec\left(\frac{1}{2}(\theta+\theta_{\mathrm{I}}-2\theta_{\mathrm{w}})\right) \mp \frac{1}{2}\sec\left(\frac{1}{2}(\theta+\theta_{\mathrm{I}}+2\theta_{\mathrm{w}})\right)\right]\end{aligned} \tag{5.19}$$

where $\Phi_{\mathrm{R}_1} = e^{-ikr\cos(\theta-2\theta_{\mathrm{w}}+\theta_{\mathrm{I}})}$ and $\Phi_{\mathrm{R}_2} = e^{-ikr\cos(\theta+2\theta_{\mathrm{w}}+\theta_{\mathrm{I}})}$ are the reflections of the incident wave from the top and bottom face respectively. If we restricted the incident angle to $\theta_{\mathrm{I}} > \pi - \theta_{\mathrm{w}}$ instead, we would need to use the following function,

$$\Xi(r,\theta) = \Phi(r,\theta) - \Phi_{\mathcal{F}}(r,\theta - \theta_{\mathrm{I}}) \pm \Phi_{\mathcal{F}}(r,\theta + \theta_{\mathrm{I}} - 2\theta_{\mathrm{w}}), \tag{5.20}$$

where the same method as the first case will produce another UTD approximation for Φ

$$\begin{aligned}\Phi(r,\theta) \sim\ & \Phi_{\mathrm{I}}\left[\frac{1}{2}+\pi^{-\frac{1}{2}}e^{-\frac{i\pi}{4}}\mathcal{F}\left((2kr)^{\frac{1}{2}}\cos\left(\frac{\theta-\theta_{\mathrm{I}}}{2}\right)\right)\right] \\ & \mp \Phi_{\mathrm{R}_1}\left[\frac{1}{2}+\pi^{-\frac{1}{2}}e^{-\frac{i\pi}{4}}\mathcal{F}\left((2kr)^{\frac{1}{2}}\cos\left(\frac{\theta+\theta_{\mathrm{I}}-2\theta_{\mathrm{w}}}{2}\right)\right)\right] \\ & + \frac{e^{ikr+\frac{i\pi}{4}}}{\sqrt{2\pi kr}}\left[s(\theta-\pi)-s(\theta+\pi)+\frac{1}{2}\sec\left(\frac{1}{2}(\theta-\theta_{\mathrm{I}})\right)\mp\frac{1}{2}\sec\left(\frac{1}{2}(\theta+\theta_{\mathrm{I}}-2\theta_{\mathrm{w}})\right)\right].\end{aligned} \tag{5.21}$$

These two approximations are uniformly valid for $-\theta_{\mathrm{w}} < \theta < \theta_{\mathrm{w}}$, however the BCs are only satisfied in the limit $kr \to \infty$. Another potential accuracy issue occurs when θ_{I} approaches $\bar{\theta}_{\mathrm{w}}$. This situation corresponds to a transition in the GO field, from a case when only one reflected wave is present to a case when two reflected waves occur. Finally, note that using the asymptotic expansions for large argument for the Fresnel integrals will simplify the above formulas to produce the GTD approximation (5.15) again.

5.3. Graphical comparison of evaluation methods

The exact solution to the perfect wedge problem has been written as a Sommerfeld integral on the usual Sommerfeld contour as in (2.14)-(2.19) or on its steepest descent contour as in (5.5). Both formulations are exact and equivalent, but the latter is much easier to evaluate numerically. We have also presented three different approximations, a truncated infinite series (4.19), a GTD approximation (5.15) and a UTD approximation (5.19) or (5.21). In this subsection, we will plot the exact solution and each of the approximations and compare their accuracy and computational speed. For the series solutions we shall truncate at 100 terms, which is enough for the wavenumbers considered here.

In Figure 7, we will consider the wedge defined by $2\bar{\theta}_{\mathrm{w}} = \pi/4$ for zero incidence angle, $\theta_{\mathrm{I}} = 0$. This corresponds to a case where the GO part of the field exhibits two reflected waves. In Figure 8, we consider the same wedge, but with an incident angle $\theta_{\mathrm{I}} = \pi/2$, corresponding to a GO field with a single reflected wave. In both cases, we will plot the real part of the total field Φ against θ for different values of kr and different BCs. In both figures, the thick plain line represents the exact Sommerfeld solution (SI/SDC), the thick dashed line is the truncated series approximation, the dotted line and the thin line represent the UTD and GTD approximations respectively.

In both Figures 7 and 8, we confirm that,

- The series solution is very accurate despite the truncation. However if we want to consider larger values of kr, more terms will be required to remain accurate, which will slow down its computation.

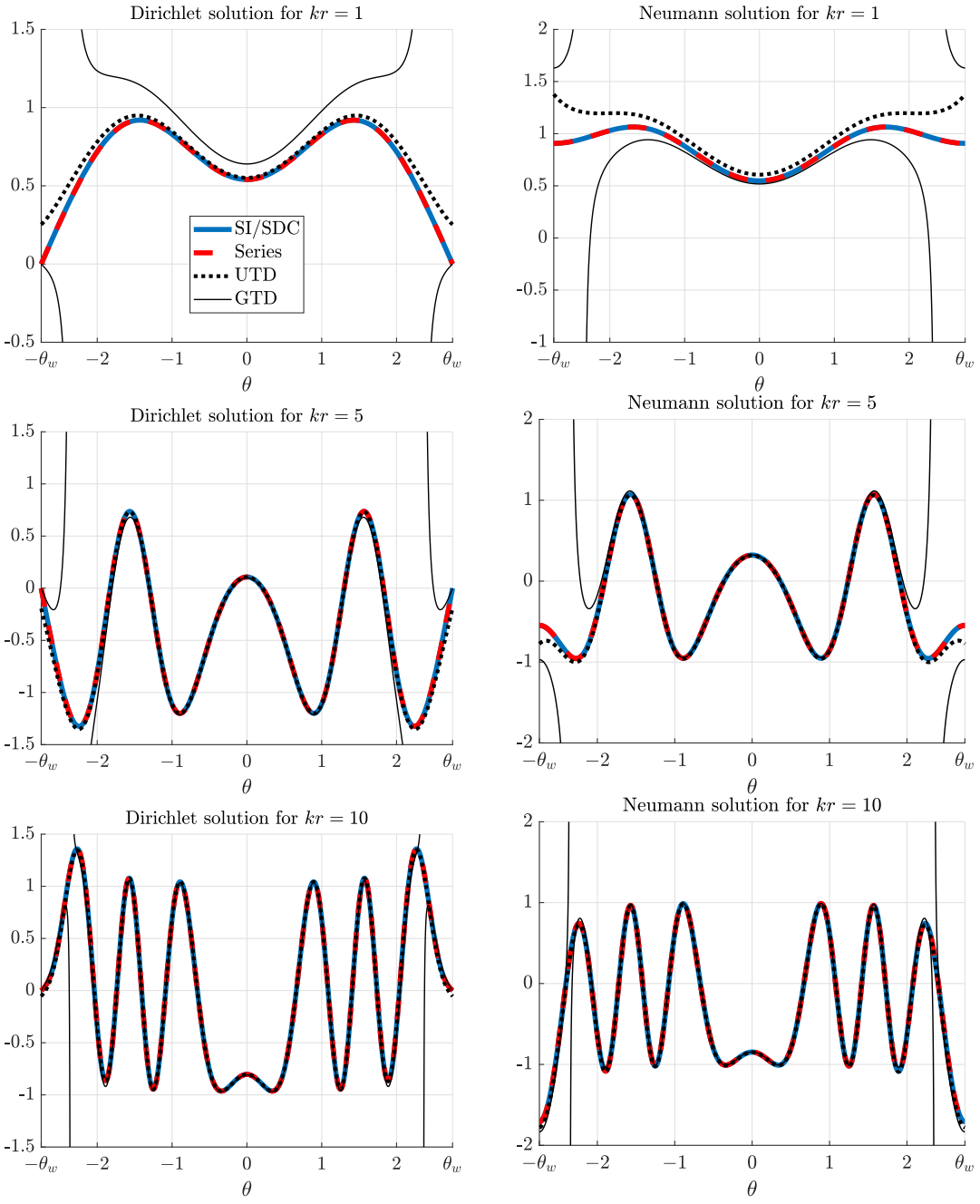

Figure 7: Comparison between the real part of the exact solution (SI/SDC) and various approximations for Dirichlet and Neumann BCs, for $kr = 1, 5, 10$ and for a wedge characterised by $\theta_{\mathrm{w}} = 7\pi/8$ and an incident angle $\theta_{\mathrm{I}} = 0$.

- The GTD approximation has the least overall accuracy and becomes invalid when θ is close to any GO discontinuities $\theta_{\mathrm{I}} - \pi$, $2\theta_{\mathrm{w}} - \theta_{\mathrm{I}} - \pi$ and $-2\theta_{\mathrm{w}} - \theta_{\mathrm{I}} + \pi$.

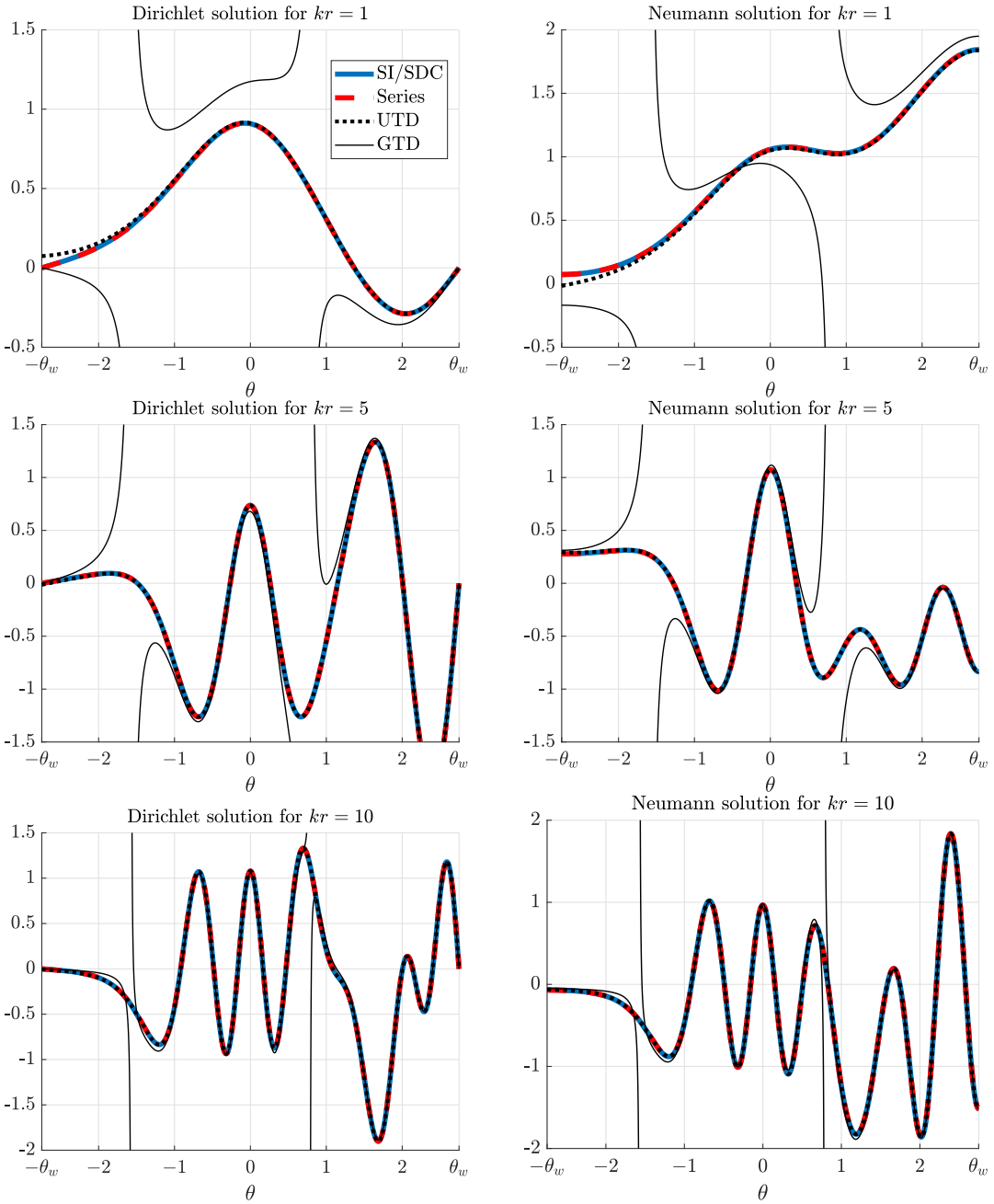

Figure 8: Comparison between the real part of the exact solution (SI/SDC) and various approximations for Dirichlet and Neumann BCs, for $kr = 1, 5, 10$ and for a wedge characterised by $\theta_{\mathrm{w}} = 7\pi/8$ and an incident angle $\theta_{\mathrm{I}} = \pi/2$.

It does however satisfy the correct BCs.

- The UTD approximation is a clear improvement to the standard GTD approx-

imation away from the boundaries, in particular it does not have any singularities, but fails to satisfy the BCs.

Both the GTD and UTD approximations appear to improve their accuracy as kr gets larger. To show this, we take the Dirichlet case with $\theta_{\mathrm{I}} = 0$ and look at the quantities GTD Error $= |(2.14) - (5.15)|$ and UTD Error $= |(2.14) - (5.19)|$ against θ for $kr = 1, 5, 10, 25$. Figure 9 (left) illustrates the GTD error and shows that it is a good approximation, provided that kr is large enough and θ is not too close to one of the singular angles $\theta = 2\theta_{\mathrm{w}} - \theta_{\mathrm{I}} - \pi$ and $-2\theta_{\mathrm{w}} - \theta_{\mathrm{I}} + \pi$ (which are indicated by a thin vertical dashed line). In Figure 9 (right), it is clear that the UTD error at the boundary decreases significantly as kr increases, rendering it a very good approximation everywhere if kr is large enough. We also reconfirm that the UTD approximation is a large improvement in comparison to the GTD approximation.

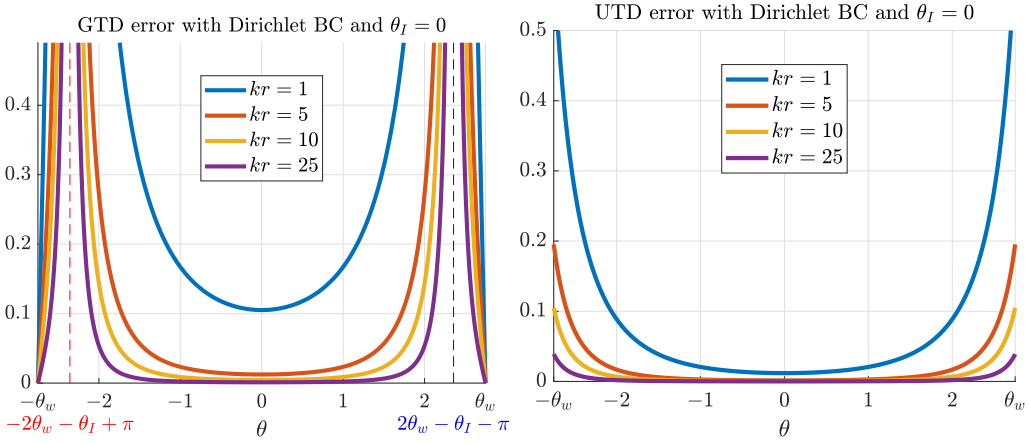

Figure 9: Comparison of the GTD (left) and UTD (right) error for Dirichlet BCs, incident angle $\theta_{\mathrm{I}} = 0$ and increasing values of kr, in the case of a wedge characterised by $\theta_{\mathrm{w}} = 7\pi/8$.

Finally, for completeness, we replicate some plots from existing literature using the UTD approximation. Specifically, we replicate the first and last plots of figure 5 in (Haciveliogl u et al., 2011) which is a comparison of an alternate definition for (5.5), the series solution with 100 terms and a similar UTD approximation. In order to replicate these plots, we need to adapt to their geometric configuration by making the substitutions $\theta = \theta_{\mathrm{w}} - \hat{\theta}$ and $\theta_{\mathrm{I}} = \theta_{\mathrm{w}} - \hat{\theta}_{\mathrm{I}}$. We use (5.21) with $\bar{\theta}_{\mathrm{w}} = \pi/36$ and $kr = 10\pi$. Figure 10 (left) is the Dirichlet case with $\hat{\theta}_{\mathrm{I}} = \pi/2$. Figure 10 (right) is the Neumann case with $\hat{\theta}_{\mathrm{I}} = 2\pi/3$.

6. Alternative methods

Sections 2, 3 and 4 cover methods that are most commonly used in diffraction theory. In this section, we will briefly present three alternative methods that have been tailored to tackle the perfect wedge problem.

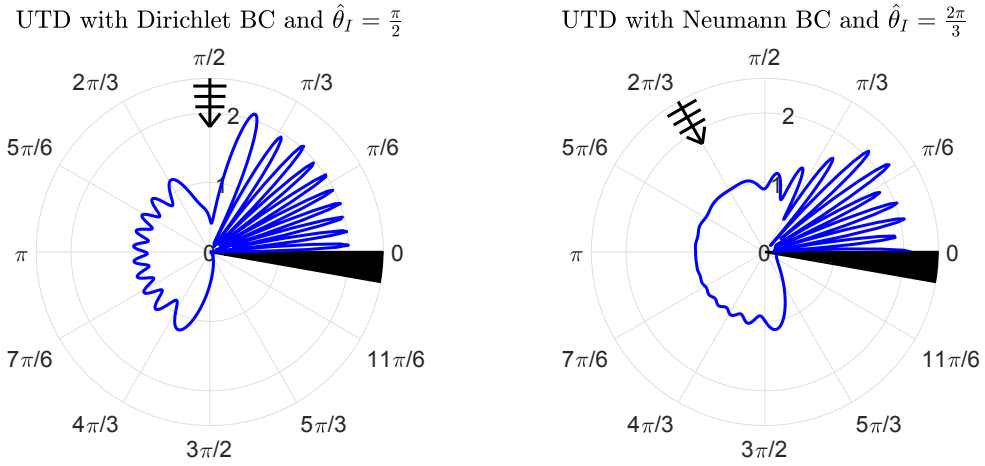

Figure 10: Replication of the top left and bottom right plots of figure 5 in (Haciveliogl u et al., 2011) using (5.21).

6.1. Embedding Formula technique

The first method to be reviewed is based on the idea of embedding. This idea is relatively new in diffraction theory (Williams, 1982), and has mainly been used for planar cracks and slits, as well as parallel combinations of these (Gautesen, 1983; Martin and Wickham, 1983; Biggs, 2001, 2002). Though, recently, in (Craster and Shanin, 2005) it was adapted to wedges with a rational angle. We will here attempt to summarise this method and consider again our wedge region characterised by θ_{w}. We seek the total field Φ satisfying the Helmholtz equation (1.1), subjected to Dirichlet (1.2) or Neumann (1.3) BCs, as well as radiation and edge conditions (1.4) and (1.5) for a plane wave incidence $\Phi_{\mathrm{I}} = e^{-ikr\cos(\theta-\theta_{\mathrm{I}})}$, with incident angle θ_{I}. The aim of the method is to recover the diffraction coefficient of the diffracted field Φ_{Diff}.

The diffraction coefficient. Using classical separation of variables in the polar coordinates (r, θ) and the edge conditions, it can be shown that the total field Φ has an eigenfunction expansion of the form

$$\Phi(r,\theta) = \sum_{m=0}^{\infty} (2/k)^{\nu_m}\Gamma(1+\nu_m)K_m(\theta_{\mathrm{I}})u_m(r,\theta), \tag{6.1}$$

where $\nu_m = m\delta = m\pi/(2\theta_{\mathrm{w}})$ and u_m is a product of Bessel functions $J_{\nu_m}(kr)$ and some trigonometric functions of θ satisfying the BCs[6]. In the Dirichlet case, the $m = 0$ term in the sum is equal to zero. Note that using the series results (4.19) and (4.20) of Macdonald type, we can recover K_m exactly, but we will not use this here.

[6]The multiplicative factor $(2/k)^{\nu_m}\Gamma(1+\nu_m)$ is just here to compensate the near-field behaviour of the Bessel functions, and, doing so, somehow normalise the expansion.

The aim is to determine the diffraction coefficient $D(\theta, \theta_{\rm I})$, already defined in (5.16), that is such that

$$\Phi_{\rm Diff}(r,\theta) \underset{r\to\infty}{\sim} D(\theta,\theta_{\rm I})\frac{e^{ikr}}{\sqrt{kr}} \tag{6.2}$$

The edge Green's functions. In order to do this, as is customary with embedding, we need to introduce an auxiliary problem[7]. In fact here, we will introduce infinitely many of them. Let $m \in \mathbb{N}\backslash\{0\}$, and consider the function $\widehat{u}_{m,\varepsilon}$ that is the tailored Green's function (i.e. that satisfies the BCs) for the Helmholtz equation resulting from m point sources given by $z_j = \varepsilon e^{i(\varphi_j - \theta_{\rm w})}$, $j = 1, \dots, m$, where $\varphi_j = (2j-1)\theta_{\rm w}/m$ for Dirichlet BC and $\varphi_j = 2j\theta_{\rm w}/m$ for Neumann BC. The strength A_j of each source is given by $A_j = (-1)^j \pi \varepsilon^{-\nu_m}$, as illustrated in Figure 11.

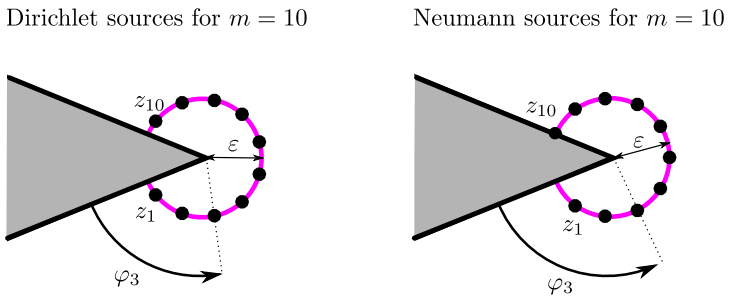

Figure 11: Position of the sources in Dirichlet and Neumann cases for $m = 10$

The mth edge Green's function is then defined by

$$\widehat{u}_m = \lim_{\varepsilon\to 0} \widehat{u}_{m,\varepsilon} \tag{6.3}$$

The near field behaviour of the edge Green's function can be studied by considering $\widehat{u}_{m,\varepsilon}$ for fixed ε, close to the wedge edge. In that vicinity, we can scale the space variables to show that $\widehat{u}_{m,\varepsilon}$ behaves locally like $\widehat{u}^{\rm inner}_{m,\varepsilon}$, which is the exact same Green's function, but for Laplace's equation instead of Helmholtz. Using the method of images in a half-space, and the mapping $z = w^{1/\delta}$, it is possible to find $\widehat{u}^{\rm inner}_{m,\varepsilon}$ explicitly[8] as

$$\widehat{u}^{\rm inner}_{m,\varepsilon} = -\frac{\varepsilon^{-\nu_m}}{2}{\rm Re}\left\{\ln\left(\frac{Z^{\nu_m} - a\varepsilon^{\nu_m}}{Z^{\nu_m} + a\varepsilon^{\nu_m}}\right)\right\} \text{ with } \begin{cases} a = i \text{ for Dirichlet BC} \\ a = 1 \text{ for Neumann BC} \end{cases}$$

[7]Here the auxiliary problems will be constructed from point sources. However, another type of embedding formulae can be obtained with plane wave auxiliary problems, see (Biggs, 2006) for example.

[8]Note that in (Craster and Shanin, 2005), only the Dirichlet formula is given, and is slightly different from this one (the factors i are missing), which we think is a typographical error.

where $Z = re^{i\varphi}$, φ being the angle measured from the bottom face of the wedge, so that we have $\varphi = \theta + \theta_{\mathrm{w}}$. Looking at the leading order of $\widehat{u}^{\mathrm{inner}}_{m,\varepsilon}$ as $\varepsilon \to 0$, using the fact that $\ln(z) \underset{z\to 1}{\sim} 1 - 1/z$, we get

$$\widehat{u}^{\mathrm{inner}}_{m,\varepsilon} \underset{\varepsilon\to 0}{\sim} r^{-\nu_m} \begin{cases} \sin(\nu_m\varphi) & \text{for Dirichlet BC} \\ \cos(\nu_m\varphi) & \text{for Neumann BC} \end{cases}, \tag{6.4}$$

which by construction, is also the local behaviour of $\widehat{u}_m$ near the wedge edge. Note that the edge Green's function is singular on the wedge edge and does not satisfy the edge condition, we say that it is *oversingular*. It does however satisfy the Helmholtz equation everywhere outside the wedge. This leads to the exact representation of $\widehat{u}_m$ as:

$$\widehat{u}_m(r,\theta) = \frac{\pi i}{\Gamma(\nu_m)}(k/2)^{\nu_m} H^{(1)}_{\nu_m}(k_0 r) \begin{cases} \sin\left(\nu_m\left(\theta+\theta_{\mathrm{w}}\right)\right) & \text{for Dirichlet BC} \\ \cos\left(\nu_m\left(\theta+\theta_{\mathrm{w}}\right)\right) & \text{for Neumann BC} \end{cases}, \tag{6.5}$$

since it is clear that the above expression has the right type of singularity, and satisfies the boundary and radiation conditions, as well as the Helmholtz equation.

It is also natural to define the directivity $\widehat{D}_m(\theta)$ for each edge Green's function by

$$\widehat{u}_m(r,\theta) \underset{r\to\infty}{\sim} \widehat{D}_m(\theta)\frac{e^{ikr}}{\sqrt{kr}}, \tag{6.6}$$

and using the asymptotic behaviour of the Hankel function for large argument, (6.5) and (6.6) imply that

$$\widehat{D}_m(\theta) = \frac{\sqrt{2\pi}(k/2)^{\nu_m} e^{-\frac{i\nu_m\pi}{2}}}{\Gamma(\nu_m)} \begin{cases} \sin\left(\nu_m\left(\theta+\theta_{\mathrm{w}}\right)\right) & \text{for Dirichlet BC} \\ \cos\left(\nu_m\left(\theta+\theta_{\mathrm{w}}\right)\right) & \text{for Neumann BC} \end{cases}. \tag{6.7}$$

It is important to note the main difference between the directivities $\widehat{D}_m(\theta)$ and the diffraction coefficient $D(\theta,\theta_{\mathrm{I}})$: the former only depends on one angular variable, while the latter depends on two. Remarkably, using the reciprocity principle, it is possible to relate the far-field of the edge Green's functions to the near-field of each components of the eigenfunction expansion (6.1) as follows:

$$\widehat{D}_m(\theta_{\mathrm{I}}) = \frac{m\pi}{2} K_m(\theta_{\mathrm{I}}) \tag{6.8}$$

The operator $\boldsymbol{H}_p$. As mentioned above, this method can only be applied to rational angles[9], so let us set $2\theta_{\mathrm{w}} = \frac{q\pi}{p}$ for some positive integers p and q. Now define, the

[9] Shanin and Craster (2010) have extended this work by considering a pseudo-differential operator $\mathbf{K}_\mu$ instead of the differential operator $\mathbf{H}_p$. Note that for an integer n, $\mathbf{K}_n$ reduces to $C_n T_n\left(\frac{i}{k}\frac{\partial}{\partial x}\right)$ for some constant C_n, which establishes the link with the theory developed here. This new operator can however be used when $\mu \notin \mathbb{N}$ to produce an embedding formula valid for wedges with non-rational angles, though it cannot be used for polygons.

operator $\mathbf{H}_p$ as follows:

$$\mathbf{H}_p = (-ik)^p \left[T_p\left(\frac{i}{k}\frac{\partial}{\partial x}\right) - T_p(\cos(\theta_{\mathrm{I}})) \right],$$

where T_p is the pth Chebyshev polynomial, and it is understood that for some integer n, $\left(a\frac{\partial}{\partial x}\right)^n = a^n \frac{\partial^n}{\partial x^n}$. From now on, for brevity, we will focus solely on the Dirichlet case. It is relatively easy to show that for every $m \in \mathbb{N}\backslash\{0\}$, $\mathbf{H}_p[u_m]$ satisfies the Helmholtz equation, the correct boundary conditions and the radiation condition, and that $\mathbf{H}_p[\Phi_{\mathrm{I}}] = 0$. It is also possible to prove (though it is more difficult) that

$$\begin{aligned}\mathbf{H}_p[\Phi] \underset{r\to 0}{\sim} 2^{p-1}(-1)^{q-p+1} \sum_{m=1}^{q-1} K_m(\theta_{\mathrm{I}})\nu_m(\nu_m-1)\dots(\nu_m-p+1) r^{-\nu_{q-m}} \sin(\nu_{q-m}\varphi) \\ + \text{terms that satisfy the edge conditions} \end{aligned} \tag{6.9}$$

We refer to (Craster and Shanin, 2005) for the details of the proof, but it relies on a careful analysis of the near-field and far-field behaviour of $\mathbf{H}_p[u_m]$. It also uses the identity $\nu_m \pm p = \nu_{m\pm q}$, which explains how q enters the scene.

Embedding formula. Note now that the behaviour of each term in (6.9) reminds of that of the $(q-m)$th edge Green's function (see (6.4)). This motivates the introduction of the auxiliary function

$$W = \mathbf{H}_p[\Phi] - 2^{p-1}(-1)^{q-p+1} \sum_{m=1}^{q-1} K_m(\theta_{\mathrm{I}})\nu_m(\nu_m-1)\dots(\nu_m-p+1)\widehat{u}_{q-m}.$$

By construction, W satisfies the edge condition, and it is also clear from what has been done above, that it satisfies the Helmholtz equation, the boundary and the radiation conditions. Hence, by uniqueness, we conclude that $W \equiv 0$, and we obtain the *weak* form of the embedding formula

$$\mathbf{H}_p[\Phi] = 2^{p-1}(-1)^{q-p+1} \sum_{m=1}^{q-1} K_m(\theta_{\mathrm{I}})\nu_m(\nu_m-1)\dots(\nu_m-p+1)\widehat{u}_{q-m}, \tag{6.10}$$

valid everywhere, that relates the total field Φ to the edge Green's functions. Focusing now on the far-field, (6.10) makes it possible to express the diffraction coefficient $D(\theta,\theta_{\mathrm{I}})$ in terms of the directivities of some of the edge Green's functions, as summarised in the equation below:

$$D(\theta,\theta_{\mathrm{I}}) = \sum_{m=1}^{q-1} \frac{(-1)^{q-p+1}\nu_m(\nu_m-1)\dots(\nu_m-p+1)}{m\pi(ik/2)^p(\cos(p\theta)-(-1)^p\cos(p\theta_{\mathrm{I}}))} \widehat{D}_m(\theta_{\mathrm{I}})\widehat{D}_{q-m}(\theta) \tag{6.11}$$

The formula (6.11) is the main result of (Craster and Shanin, 2005) and is referred to as the *Embedding formula*. It is remarkable in the sense that it allows to express

the diffraction coefficient, depending on two angular variables, in terms of a sum of products of simpler directivities depending on one angular variable only. Moreover, in that case, thanks to (6.7), we know the directivities exactly and we can then recover a new analytical expression for the diffraction coefficient. For a given rational angle, it is possible to show that it is indeed equal to that given in (5.16).

Critical analysis. The concept of embedding is very general in diffraction theory, which makes this method very adaptable to all kinds of geometries such as slits, wedges, plane sectors, cubes (Skelton et al., 2010) and curved geometries (Moran et al., 2016). In that respect, instead of being seen as a method, one can consider the embedding structure as an inherent property of diffraction problems.

Its main advantage is that once derived explicitly, the embedding formula of a given diffraction problem allows one to obtain a very efficient way of computing the diffraction coefficient resulting from a incident plane wave for all observation and incident angles.

Even though the weak embedding formulae of the type (6.10) are valid everywhere, the power of embedding formulae only becomes apparent in the far-field, where it can be written in its strong form (see (6.11) for the present case). In that sense, such formula is not particularly helpful to shed some light on the near field behaviour of diffraction problems. Though because of this emphasis on the far-field, one can consider structures with multiple diffracting parts such as polygons for example.

6.2. Random Walk method

This method, developed in a series of papers (Budaev and Bogy, 2001, 2002a,b), and applied to the wedge problem in (Budaev and Bogy, 2003), is based on the Feynman-Kac formula (see e.g. (Feynman, 1948), (Kac, 1949) and (Freidlin, 1985)). This formula implies, in particular, that the solution u of a deterministic PDE on a domain Ω with Dirichlet condition $u|_{\partial\Omega} = f(r,\theta)$ on the boundary $\partial\Omega$

$$\frac{\sigma_1^2(r,\theta)}{2}\frac{\partial^2 u}{\partial r^2} + \frac{\sigma_2^2(r,\theta)}{2}\frac{\partial^2 u}{\partial \theta^2} + A_1(r,\theta)\frac{\partial u}{\partial r} + A_2(r,\theta)\frac{\partial u}{\partial \theta} + B(r,\theta)u = 0 \tag{6.12}$$

with real-valued coefficients $\sigma_{1,2}$, $A_{1,2}$ and B, can be written as

$$u(r,\theta) = \mathbf{E}\left\{ f(\xi_\tau^1, \xi_\tau^2) e^{\int_0^\tau B(\xi_s^1,\xi_s^2)\mathrm{d}s} \right\}, \tag{6.13}$$

where $\mathbf{E}$ represents the mean operator, and $\xi_t^{1,2}$ are random motions governed by the two coupled stochastic differential equations (SDE) with drift coefficient $A_{1,2}$ and diffusion coefficient $\sigma_{1,2}$

$$\mathrm{d}\xi_t^1 = A_1(\xi_t^1,\xi_t^2)\mathrm{d}t + \sigma_1(\xi_t^1,\xi_t^2)\mathrm{d}W_t^1 \text{ and } \mathrm{d}\xi_t^2 = A_2(\xi_t^1,\xi_t^2)\mathrm{d}t + \sigma_2(\xi_t^1,\xi_t^2)\mathrm{d}W_t^2, \tag{6.14}$$

with initial conditions (ICs) $\xi_0^1 = r$ and $\xi_0^2 = \theta$, where $W_t^{1,2}$ are Brownian motions (also known as Wiener processes)[10]. The exit time τ is the time when each computation should be stopped and it corresponds to the first time t such that $(\xi_t^1, \xi_t^2) \in \partial\Omega$.

If the coefficients in (6.12) and (6.14) are complex-valued (which as we will see will be the case for the problem at hand), then the Feynman-Kac representation is still valid, but it becomes difficult to determine and define the exit time τ. In fact if the coefficients are complex, then so will be the random motions $\xi_t^{1,2}$, and since the points of $\partial\Omega$ belong to $\mathbb{R}^2$, we cannot easily characterise the fact that (ξ_t^1, ξ_t^2) hits this boundary. This can be addressed by considering the "continuation" of the boundary $\partial\Omega$ into a manifold of real dimension 2 within the space $\mathbb{C}^2$ and by multiplying (6.12) by $q^2(r,\theta)$, where q is a complex-valued function. For a suitable function q, it becomes possible to define an exit time τ, and the solution to the PDE is given by

$$u(r,\theta) = \mathbf{E}\left\{ f(\xi_\tau^1, \xi_\tau^2) e^{\int_0^\tau q^2(\xi_s^1,\xi_s^2) B(\xi_s^1,\xi_s^2) \mathrm{d}s} \right\}, \tag{6.15}$$

where $\xi_t^{1,2}$ are random motions governed by the two coupled stochastic differential equations (SDE)

$$\mathrm{d}\xi_t^{1,2} = q^2(\xi_t^1,\xi_t^2) A_{1,2}(\xi_t^1,\xi_t^2)\mathrm{d}t + q(\xi_t^1,\xi_t^2)\sigma_{1,2}(\xi_t^1,\xi_t^2)\mathrm{d}W_t^{1,2}$$

with ICs $\xi_0^1 = r$ and $\xi_0^2 = \theta$.

In order to fit within this framework, for the wedge problem in (Budaev and Bogy, 2003), the authors aim to solve the Helmholtz equation (1.1), subject to the radiation condition and to Dirichlet BCs of the type $\Phi(r, \pm\theta_\mathrm{w}) = F(r, \pm\theta_\mathrm{w})$. They seek a solution of the form $\Phi = ue^{iS}$ for some unknown functions u and S. The Helmholtz equation becomes

$$\Delta u + 2i\nabla u \cdot \nabla S + iu\Delta S + u(k^2 - \nabla S \cdot \nabla S) = 0 \tag{6.16}$$

If the solution is in the Liouville form, we choose $S(r,\theta) = kr$. In this case, S automatically satisfies the eikonal equation $\nabla S \cdot \nabla S = k^2$ and, after multiplication by $\frac{i}{2k}$, (6.16) becomes

$$\frac{i}{2k}\left(\frac{\partial^2 u}{\partial r^2} + \frac{1}{r^2}\frac{\partial^2 u}{\partial \theta^2}\right) + \left(\frac{i}{2kr} - 1\right)\frac{\partial u}{\partial r} - \frac{1}{2r}u = 0$$

and we can write the BCs $u(r, \pm\theta_\mathrm{w}) = e^{-ikr}F(r, \pm\theta_\mathrm{w}) = f(r, \pm\theta_\mathrm{w})$. This fits exactly within the realm of (6.12), but with complex coefficients. It is shown in (Budaev and

[10] We do not intend to insist on the rigorous mathematical definitions of these objects here, however we refer the interested reader to general textbooks on the topic, such as (Voss, 2013, Chapter 6) for example, where Brownian motions, SDEs (and their resolution via the Euler-Maruyama scheme) and Itô calculus are introduced.

Bogy, 2003) that a suitable choice of the function q is $q^2(r,\theta) = -ikr^2$. The manifold extending the boundary is chosen as $\partial\mathfrak{G}$, where

$$\mathfrak{G} = \left\{(r,\theta) \in \mathbb{C}^2, r \in \mathbb{C}, -\theta_{\mathrm{w}} < \mathrm{Re}\{\theta\} < \theta_{\mathrm{w}}\right\}.$$

In this particular case, the two SDEs to consider become

$$\mathrm{d}\xi_t^1 = \xi_t^1\left(ik\xi_t^1 + \frac{1}{2}\right)\mathrm{d}t + \xi_t^1 \mathrm{d}W_t^1 \quad \text{and} \quad \mathrm{d}\xi_t^2 = \mathrm{d}W_t^2 \tag{6.17}$$

with ICs $\xi_0^1 = r$ and $\xi_0^2 = \theta$ and exit time τ defined such that $\xi_\tau^2 = \pm\theta_{\mathrm{w}}$, which now makes sense since the random process ξ_t^2 is now real for all times. Using (6.15), we can hence write the solution[11] as

$$u(r,\theta) = \mathbf{E}\left\{f(\xi_\tau^1,\xi_\tau^2)e^{\frac{ik}{2}\int_0^\tau \xi_s^1 \mathrm{d}s}\right\} \quad \text{or} \quad u(r,\theta) = \frac{1}{\sqrt{r}}\mathbf{E}\left\{f(\xi_\tau^1,\xi_\tau^2)\sqrt{\xi_\tau^1}e^{-\frac{1}{2}W_\tau^1}\right\}, \tag{6.18}$$

where the second part of (6.18) is derived from the first using Itô calculus. Note that for this to be valid, f should be chosen such that it can be analytically continued for $r \in \mathbb{C}$. The second arguments in (6.18) do not pose any problem since by definition $\xi_\tau^2 = \pm\theta_{\mathrm{w}}$. The two SDEs (6.17) are reasonably straightforward to solve numerically (see Figure 12, left) using Euler-Maruyama with time step $\Delta t = 0.01$. If the solution we are trying to find is continuous everywhere, the solution (6.18) can be implemented and works well. To illustrate this point we use the same example as in (Budaev and Bogy, 2003) and apply this method to reproduce the function $H_0^{(1)}(kr)$, which is well known to satisfy the Helmholtz equation and the radiation condition. In order to do so we tailored the BCs to be $f(r,\pm\theta_{\mathrm{w}}) = e^{-ikr}H_0^{(1)}(kr)$ and plotted an illustration of the result in Figure 12.

If the solution we are seeking has some discontinuities, then the method should be adapted slightly. We are interested in this since what we want to compute is the diffracted field $\Phi_{\mathrm{Diff}}(r,\theta)$ resulting from an incident plane wave with incident angle θ_{I}, which satisfies homogeneous Dirichlet BCs and the radiation condition. In what follows, we choose θ_{I} such that both wedge faces are illuminated. As shown in Section 5, the field Φ_{Diff} has GO discontinuities[12] at $\theta = \theta_1 = 2\theta_{\mathrm{w}} - \theta_{\mathrm{I}} - \pi$ and $\theta = \theta_2 = -2\theta_{\mathrm{w}} - \theta_{\mathrm{I}} + \pi$, and the knowledge of the GO field allows us to derive the following jump conditions across $\theta_{1,2}$:

$$[u]_{\theta_1} = 1, \quad [u]_{\theta_2} = -1, \quad [\partial u/\partial\theta]_{\theta_{1,2}} = 0,$$

[11] Note that in (Budaev and Bogy, 2003), in their equivalent of the second part of (6.18) (their equation (26)), the argument of the exponential is $-\frac{1}{2}\mathrm{d}W_\tau^1$. We believe it to be a typographical error.

[12] Note that in (Budaev and Bogy, 2003), the convention to choose the index of θ_1 or θ_2 is different, but we have made that choice in order to be consistent with the rest of the review.

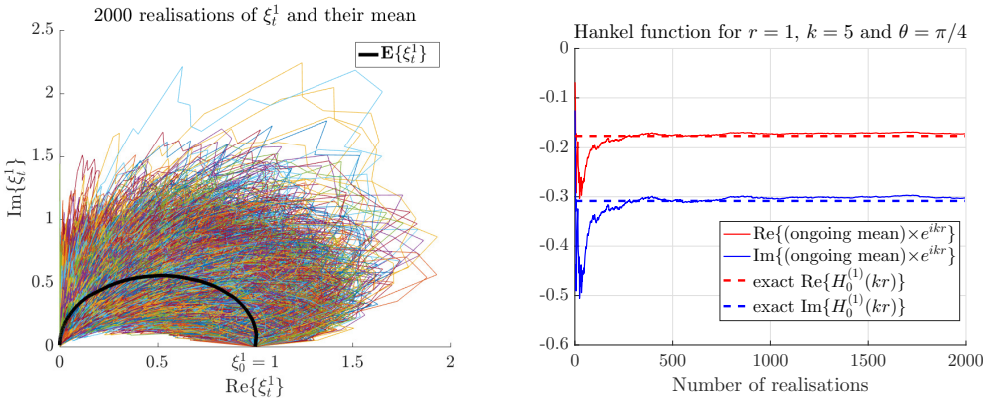

Figure 12: (Left) 2000 realisations of the SDE governing ξ_t^1 and their mean, plotted in the complex plane with initial condition $\xi_0^1 = r = 1$. (right) The ongoing mean computed by (6.18) for the Hankel function up to 2000 realisations for $\theta = \pi/4$, $r = 1$ and $k = 5$.

where u is defined such that $\Phi_{\text{Diff}}(r,\theta) = u(r,\theta)e^{ikr}$, and the bracket $[u]_{\theta_{1,2}} = u(r,\theta_{1,2}+0) - u(r,\theta_{1,2}-0)$. Using these jump conditions, it can be shown that (6.18) can be rewritten as

$$u(r,\theta) = \mathbf{E}\left\{\sum_{\tau_\nu<\tau}(-1)^{m_\nu}\delta_\nu e^{\frac{ik}{2}\int_0^{\tau_\nu}\xi_s^1 \mathrm{d}s}\right\} \text{ or } u(r,\theta) = \frac{1}{\sqrt{r}}\mathbf{E}\left\{\sum_{\tau_\nu<\tau}(-1)^{m_\nu}\delta_\nu\sqrt{\xi_{\tau_\nu}^1}e^{-\frac{1}{2}W_{\tau_\nu}^1}\right\}, \tag{6.19}$$

where for each simulation, the τ_ν represent the times of crossings between ξ_t^2 and the discontinuous lines $\theta_{1,2}$. If θ_1 (resp. θ_2) is crossed, then $m_\nu = 2$ (resp. 1). If the crossing is from above (resp. below), then $\delta_\nu = 1$ (resp. -1). As illustrated in Figure 13 (left), many such crossings can occur before the exit time τ is reached. The method has been implemented for a wedge characterised by $\theta_{\text{w}} = 7\pi/8$, and the results, obtained for 2000 realisations (simulated by Euler-Maruyama with time step $\Delta t = 0.01$), are shown at an observation point $r = 1$, $\theta = \pi/4$ for $k = 5$. Note that if the method was described in (Budaev and Bogy, 2003), it was only implemented for a half-plane, and not for a wedge. Though, as predicted in (Budaev and Bogy, 2003) the error is of the order of 0.01 and the method works well[13].

Critical analysis. This method has the advantage of being very adaptable to all sorts of geometries since it is based on the Feynman-Kac theorem that is a very general result (both in terms of geometry and in terms of equation). This adaptability is confirmed by the fact that it has been used in the context of cones (Budaev and Bogy, 2003), quarter-plane (Budaev and Bogy, 2005) and other geometries.

[13]Note that in (Budaev and Bogy, 2003), there is a factor $\frac{1}{2}$ in front of $\mathbf{E}$ in the formulae (6.19). This was a typographical error.

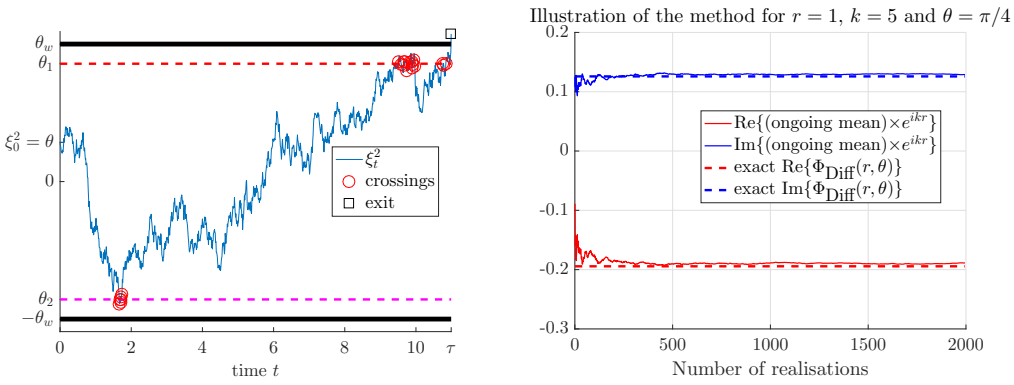

Figure 13: (Left) Illustration of one realisation of ξ_t^2, its crossings with $\theta_{1,2}$ and its exit time τ. (Right) The ongoing mean up to 2000 realisations computed by (6.19) for a plane wave incident at an angle $\theta_{\text{I}} = 0$ on a wedge characterised by $\theta_{\text{w}} = 7\pi/8$ for $\theta = \pi/4$, $r = 1$ and $k = 5$.

It has to be said however, that for the Helmholtz equation, the PDE and SDE coefficients become complex. This renders the determination of the end time rather more complicated than the real coefficient case. It necessitates to find a convenient complex coefficient to multiply our equations by, and also to find a way of somehow extending the real geometries in a higher dimension complex space.

This method can also become very computational very quickly. Indeed, if one would like for example to recreate a heat map similar to those presented in Figure 15, one would need about 2000 simulations of the SDE system per point, which for a good resolution may lead to a very long computational time.

Another comment that can be made about this method, is that it stands out from all the other methods presented here in terms of the type of mathematics used. This can be considered as an advantage for researchers open to exploring many areas of mathematics, though, this also means that for the usual specialists in diffraction theory, this may result in a steep learning curve.

6.3. The method of functionally-invariant solutions

The third and final alternative method to be reviewed is also known as the Sobolev-Smirnov method. Some recent publications using this method include (Komech et al., 2015; Babich, 2015). The former studies wedge diffraction with a number of different combinations of Dirichlet and Neumann BCs, while the latter studies the impedance wedge problem.

The idea behind this method is to identify the time-harmonic problem with an elementary time-dependent problem where the incident plane wave is replaced with a Heaviside step function such that no diffraction occurs before the time $t = 0$. This means that the solution to this elementary problem (call it $u(r, \theta, t)$) satisfies the following conditions,

- The governing equation is the linear wave equation $\nabla^2 u - \frac{1}{c^2}\frac{\partial^2 u}{\partial t^2} = 0$.

- Dirichlet or Neumann BCs at $\theta = \pm\theta_{\mathrm{w}}$.
- u can be linearly decomposed into incident and scattered parts, $u = u_{\mathrm{I}} + u_{\mathrm{S}}$, where $u_{\mathrm{I}}(r,\theta,t) = \mathcal{H}\left(t + \frac{r}{c}\cos(\theta - \theta_{\mathrm{I}})\right)$.

For simplicity, we shall restrict values of the incident angle and the wedge angle such that, $\pi - \theta_{\mathrm{w}} < \theta_{\mathrm{I}} < \theta_{\mathrm{w}} - \frac{\pi}{2}$. This restriction means that for $t < 0$, the incident wave does not reach the wedge until $t = 0$ when it first touches the wedge at its corner. For $t > 0$, the incident wave has passed the wedge corner and reflected and diffracted waves have appeared. Figure 14 describes this configuration and gives known values of u outside the diffraction circle which are found by Geometrical Optics.

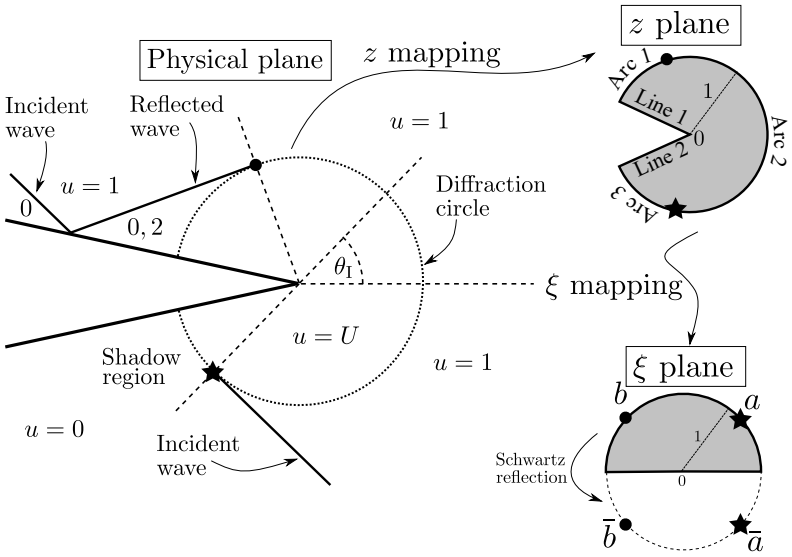

Figure 14: Physical diagram and images of the diffraction disc in the z and ξ planes.

The radius of the diffraction circle is ct and we call the unknown solution inside, i.e. within the diffraction disc, $U(r,\theta,t)$. We need to look at a particular class of solutions to the wave equation and express U in terms of a complex variable. Noting that a real solution is required, we write

$$U(r,\theta,t) = \mathrm{Re}\left\{V(z)\right\}, \quad \text{where,} \quad z = \frac{ct}{r}\left(1 - \sqrt{1 - \left(\frac{r}{ct}\right)^2}\right)e^{i\theta}, \tag{6.20}$$

ensuring that the wave equation is automatically satisfied. Sections 52-53 in (Smirnov, 1964) gives a detailed explanation as to why this is the case. Note also that within the diffraction disc (i.e. $0 \le r \le ct$), the pre-exponential factor in (6.20) is real and positive, varying from 0 to 1. As a result, $z(r,\theta,t)$ maps the diffraction disc onto the unit disc $|z| \le 1$. Therefore, we need to find a function $V(z)$ that is analytic inside

the unit disc and has the following boundary values,

$$\begin{aligned}
\text{Both: } &\operatorname{Re}\{V(z)\} = 0 \text{ on Arc 3}, \quad \operatorname{Re}\{V(z)\} = 1 \text{ on Arc 2},\\
\text{Dirichlet: } &\operatorname{Re}\{V(z)\} = 0 \text{ on Arc 1}, \quad \operatorname{Re}\{V(z)\} = 0 \text{ on Lines 1 \& 2},\\
\text{Neumann: } &\operatorname{Re}\{V(z)\} = 2 \text{ on Arc 1}, \quad \operatorname{Re}\{izV'(z)\} = 0 \text{ on Lines 1 \& 2},
\end{aligned}$$

where the arc and line numbers are given in Figure 14.

We will now use a conformal mapping to transform this problem into a Riemann-Hilbert problem. In order to do so, we define $\xi = e^{\frac{i\pi}{2}} z^{\delta}$, where as before $\delta = \frac{\pi}{2\theta_{\mathrm{w}}}$, which transforms the indented unit disc of the z plane onto the unit upper-half semi-disc of the ξ plane, as illustrated in Figure 14. The branch of the root is defined such that the cut is on the negative real axis and $\xi(z=1) = e^{\frac{i\pi}{2}}$. Let $\widetilde{V}(\xi) = V(z(\xi))$, then we analytically continue $\widetilde{V}$ into the unit lower-half semi-disc by Schwarz reflection principle (see Figure 14) using anti-symmetry (Dirichlet case) or symmetry (Neumann case). Let $a = e^{i(\frac{\pi}{2} - \delta(\pi - \theta_{\mathrm{I}}))}$ and $b = e^{i(\frac{3\pi}{2} - \delta(\pi + \theta_{\mathrm{I}}))}$ then $\widetilde{V}(\xi)$ has the following boundary values for the Dirichlet and Neumann cases,

$$\text{Dir: } \begin{cases} \operatorname{Re}\{\widetilde{V}(\xi)\} = -1 \text{ on arc } (\bar{b}, \bar{a}), & \operatorname{Re}\{\widetilde{V}(\xi)\} = 1 \text{ on arc } (a, b),\\ \operatorname{Re}\{\widetilde{V}(\xi)\} = 0 \text{ on real line } (-1, 1), & \operatorname{Re}\{\widetilde{V}(\xi)\} = 0 \text{ on arcs } (\bar{a}, a) \text{ and } (b, \bar{b}), \end{cases} \tag{6.21}$$

$$\text{Neu: } \begin{cases} \operatorname{Re}\{\widetilde{V}(\xi)\} = 0 \text{ on arc } (\bar{a}, a), & \operatorname{Re}\{\widetilde{V}(\xi)\} = 2 \text{ on arc } (b, \bar{b}),\\ \operatorname{Re}\{i\xi\widetilde{V}'(\xi)\} = 0 \text{ on real line } (-1, 1), & \operatorname{Re}\{\widetilde{V}(\xi)\} = 1 \text{ on arcs } (a, b) \text{ and } (\bar{b}, \bar{a}). \end{cases} \tag{6.22}$$

The method to solve these two Riemann-Hilbert problems is detailed in section 54 in (Smirnov, 1964). The respective solutions to (6.21) and (6.22) are,

$$\widetilde{V}(\xi) = \frac{1}{\pi i} \ln\left(\frac{\bar{b} - \xi}{a - \xi}\right) - \frac{1}{\pi i} \ln\left(\frac{\bar{a} - \xi}{b - \xi}\right), \tag{6.23}$$

$$\widetilde{V}(\xi) = \frac{1}{\pi i} \ln\left(\frac{\bar{b} - \xi}{a - \xi}\right) + \frac{1}{\pi i} \ln\left(\frac{\bar{a} - \xi}{b - \xi}\right) - 2\delta, \tag{6.24}$$

where the used logarithm $\ln(Z)$ has a branch point at $Z = 0$ with a branch cut along the positive real axis. Using this solution, it is easy to recover the physical solution $U(r, \theta, t)$ inside the diffraction disc, and hence the whole solution $u(r, \theta, t)$. We will now see that using a simple Fourier transform, we can recover the sought-after time-harmonic problem from this solution $u(r, \theta, t)$. Consider the evaluation to the following integral, assuming that ω has a small positive imaginary increment so that $e^{i\omega t} \to 0$ as $t \to \infty$,

$$-\int_{-\infty}^{\infty} u_{\mathrm{I}}(r, \theta, t) \frac{\mathrm{d}}{\mathrm{d}t}\left(e^{i\omega t}\right) \mathrm{d}t = \left[e^{i\omega t}\right]_{\infty}^{-\frac{r}{c}\cos(\theta - \theta_{\mathrm{I}})} = \Phi_{\mathrm{I}}. \tag{6.25}$$

With this in mind, we can determine the total field Φ from u by using a similar integral,

$$\Phi(r,\theta) = -\int_{-\infty}^{\infty} u(r,\theta,t)\frac{\mathrm{d}}{\mathrm{d}t}\left(e^{i\omega t}\right)\mathrm{d}t, \tag{6.26}$$

and thus, we have found the solution to the time-harmonic problem.

Critical analysis. This particular method is tailored to the time-dependent problem, which differs from all methods previously presented in this article that were tailored to the time-harmonic problem. This is excellent if one is interested in the tracking of wave fronts in time for example, but it means that if one is interested in the time-harmonic problem, one would have to take the Fourier transform in time of the solution, as per (6.26), which can prove quite expensive numerically. This method, though in essence designed for the wedge geometry, has been shown to be adaptable to various BCs. One can refer to (Babich, 2015) for example for the case of impedance BCs.

7. Final plots and conclusions

In this review article, we have discussed six different methods that have been applied to the problem of diffraction by wedges with perfect Dirichlet or Neumann boundary conditions. The three main methods discussed were the Sommerfeld-Malyuzhinets technique, the Wiener-Hopf technique and the Kontorovich-Lebedev transform technique. The three alternative methods reviewed were the embedding formula, the random walk method and the method of functionally-invariant solutions (Sobolev-Smirnov). We also looked at two approximation methods, the Geometrical Theory of Diffraction and the Uniform Geometrical Theory of Diffraction.

This list is by no means exhaustive and we should also mention Budaev's method for elastic wedge scattering (Budaev and Bogy, 1998), the Physical Theory of Diffraction (Ufimtsev, 2014) and an interesting method called the Wiener–Hopf–Hankel formulation (Teixeira, 1991; Castro and Kapanadze, 2010). We note that (Israilov, 2013) could also be applied to the wedge geometry.

We evaluated numerically the exact solution and the associated approximations (series, GTD, UTD) for several configurations and studied their relative performances. We found that the best way to evaluate the exact solution was to consider the integral defined on the steepest descent contour. As regard to the approximations, the truncated series solutions performs very well with low wavenumbers, and we found that while the UTD approximation takes longer to compute, it is a better approximation compared with the GTD because it is uniformly valid and more accurate at lower values of kr. It has however two main disadvantages, the inaccuracy at the wedge boundary, and also the fact that (5.19) and (5.21) are not continuous across the Geometrical Optics limit $\theta_{\mathrm{I}} = \pi - \theta_{\mathrm{w}}$.

As emphasised in the critical analysis of each section, the use of the six techniques in this review is not limited to the perfect wedge problem. Examples of extensions include for example impedance wedges (Malyuzhinets, 1958a; Babich, 2015), penetrable wedges (Rawlins, 1999; Lyalinov, 1999; Daniele and Lombardi, 2011) and quarter-plane diffraction (Shanin, 2005; Assier and Peake, 2012a; Budaev and Bogy, 2005; Lyalinov, 2013).

To conclude this review, using the UTD approximation, we produce some density plots of the real part of the diffracted field Φ_{Diff} and the total field Φ in Figure 15 for a wedge defined by $2\bar{\theta}_{\text{w}} = \pi/4$ and two incident waves, $\theta_{\text{I}} = 0$ and $\theta_{\text{I}} = \pi/2$ and a wavenumber $k = 2$. As expected, we see clear discontinuities in the diffracted wave, which are due to GO discontinuities. For the total field, as expected, we see the GO behaviour in the relevant regions, the boundary conditions, and a decaying diffracted field.

Acknowledgements

Nethercote acknowledges the financial support from EPSRC (DTA studentship). Assier acknowledges that part of this work was supported by EPSRC (EP/N013719/1). Abrahams acknowledges the support by UKRI under grant no EP/K032208/1. The authors thank the anonymous reviewers for their help in improving this work. Assier would also like to thank A.V. Shanin for fruitful discussions, especially on the topic of Appendix B, and B. Budaev for being so responsive when queried about detailed aspects of the random walk method.

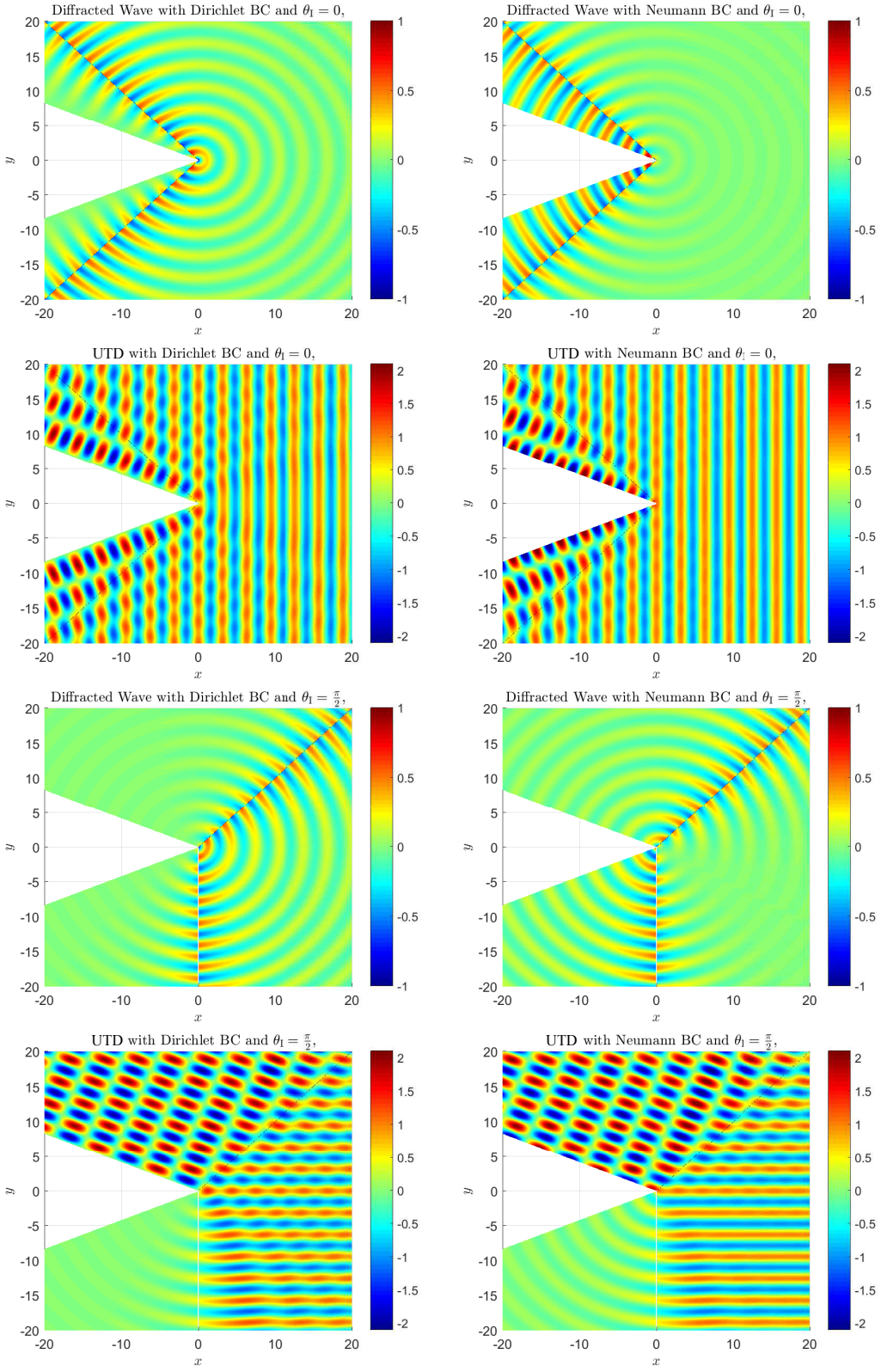

Figure 15: Density plots of the UTD approximation of $\mathrm{Re}\{\Phi_{\mathrm{Diff}}\}$ and $\mathrm{Re}\{\Phi\}$ for Dirichlet and Neumann BCs, for $k = 2$ and for a wedge characterised by $\theta_w = 7\pi/8$ and two incident angles $\theta_I = 0$ and $\theta_I = \pi/2$.

Abrahams, I. D., 1986. Diffraction by a semi-infinite membrane in the presence of a vertical barrier. J. Sound Vib. 111 (2), 191–207.

Abrahams, I. D., 1987. On the Sound Field Generated by Membrane Surface Waves on a Wedge-Shaped Boundary. Proc. R. Soc. A Math. Phys. Eng. Sci. 411, 239–250.

Abramowitz, M., Stegun, I. A., 1967. Handbook of Mathematical Functions: With Formulas, Graphs and Mathematical Tables, 6th Edition. National Bureau of Standards, Washington D.C.

Assier, R. C., Peake, N., 2012a. On the diffraction of acoustic waves by a quarter-plane. Wave Motion 49 (1), 64–82.

Assier, R. C., Peake, N., 2012b. Precise description of the different far fields encountered in the problem of diffraction of acoustic waves by a quarter-plane. IMA J. Appl. Math. 77 (5), 605–625.

Babich, V. M., 2015. Solution of the Diffraction Problem of a Plane Wave by an Impedance Wedge (Non-Stationary Case, Smirnov-Sobolev Method). Russ. J. Math. Phys. 22 (2), 145–152.

Babich, V. M., Lyalinov, M. A., Grikurov, V. E., 2007. Diffraction Theory: The Sommerfeld-Malyuzhinets Technique (Alpha Science Series on Wave Phenomena). Alpha Science.

Bender, C. M., Orszag, S. A., 1999. Advanced Mathematical Methods for Scientists and Engineers I: Asymptotic Methods and Perturbation Theory. Springer-Verlag, New York.

Bernard, J. M. L., 2005. Scattering by a three-part impedance plane: A new spectral approach. Q. J. Mech. Appl. Math. 58 (3), 383–418.

Bernard, J. M. L., 2006. A spectral approach for scattering by impedance polygons. Q. J. Mech. Appl. Math. 59 (4), 517–550.

Biggs, N. R. T., 2001. Wave Diffraction Through a Perforated Barrier of Non-Zero Thickness. Q. J. Mech. Appl. Math. 54 (4), 523–547.

Biggs, N. R. T., 2002. Wave Scattering by a Perforated Duct. Q. J. Mech. Appl. Math. 55 (2), 249–272.

Biggs, N. R. T., 2006. A new family of embedding formulae for diffraction by wedges and polygons. Wave Motion 43 (7), 517–528.

Bleistein, N., Handelsman, R. A., 2010. Asymptotic Expansions of Integrals (Dover Books on Mathematics). Dover Publications.

Borovikov, V. A., Kinber, B. Y., 1994. Geometrical Theory of Diffraction. Institution of Electrical Engineers, London.

Bowman, J. J., Senior, T. B. A., Uslenghi, P. L. E., 1987. Electromagnetic and Acoustic Scattering by Simple Shapes. Hemisphere Publishing Corporation.

Bromwich, T. J., 1915. Diffraction of Waves by a Wedge. Proc. London Math. Soc. 14 (1), 450–463.

Budaev, B. V., 1995. Diffraction by Wedges, 1st Edition. CRC Press.

Budaev, B. V., Bogy, D. B., 1995. Rayleigh wave scattering by a wedge. Wave Motion 22 (1), 239–257.

Budaev, B. V., Bogy, D. B., 1996. Rayleigh wave scattering by a wedge II. Wave Motion 24 (3), 307–314.

Budaev, B. V., Bogy, D. B., 1998. Rayleigh wave scattering by two adhering elastic wedges. Proc. R. Soc. A Math. Phys. Eng. Sci. 454 (1979), 2949–2996.

Budaev, B. V., Bogy, D. B., 2001. Probabilistic solutions of the Helmholtz equation. J. Acoust. Soc. Am. 109 (5), 2260–2262.

Budaev, B. V., Bogy, D. B., 2002a. Application of random walk methods to wave propagation. Q. J. Mech. Appl. Math. 55 (2), 209–226.

Budaev, B. V., Bogy, D. B., 2002b. Random walk methods and wave diffraction. Int. J. Solids Struct. 39 (21-22), 5547–5570.

Budaev, B. V., Bogy, D. B., 2003. Random walk approach to wave propagation in wedges and cones. J. Acoust. Soc. Am. 114 (4), 1733–1741.

Budaev, B. V., Bogy, D. B., 2005. Diffraction of a plane wave by a sector with Dirichlet or Neumann boundary conditions. IEEE Trans. Antennas Propag. 53 (2), 711–718.

Busemann, A., 1947. Infinitesimal conical supersonic flow. Tech. rep., National Advisory Committee for Aeronautics, Washington D.C.

Castro, L. P., Kapanadze, D., 2010. Exterior Wedge Diffraction Problems with Dirichlet, Neumann and Impedance Boundary Conditions. Acta Appl. Math. 110, 289–311.

Copson, E. T., 1946. On an integral equation arising in the theory of diffraction. Q. J. Math. 17 (1), 19–34.

Craster, R., Shanin, A. V., 2005. Embedding formulae for diffraction by rational wedge and angular geometries. Proc. R. Soc. A Math. Phys. Eng. Sci. 461 (2059), 2227–2242.

Croisille, J.-P., Lebeau, G., 1999. Diffraction by an Immersed Elastic Wedge. Springer-Verlag.

Daniele, V. G., 2000. Generalized Wiener-Hopf Technique for Wedge Shaped Regions of Arbitrary Angles. In: VIII-th Int. Conf. Math. Methods Electromagn. Theory. Kharkov Ukraine, pp. 432–434.

Daniele, V. G., 2001. New analytical Methods for wedge problems. In: Proc. 2001 Int. Conf. Electromagn. Adv. Appl. pp. 385–393.

Daniele, V. G., 2003a. Rotating waves in the Laplace domain for angular regions. Electromagnetics 23 (3), 223–236.

Daniele, V. G., 2003b. The Wiener-Hopf Technique for Impenetrable Wedges having Arbitrary Aperture Angle. SIAM J. Appl. Math. 63 (4), 1442–1460.

Daniele, V. G., Lombardi, G., 2006. Wiener-Hopf solution for impenetrable wedges at skew incidence. IEEE Trans. Antennas Propag. 54 (9), 2472–2485.

Daniele, V. G., Lombardi, G., 2011. The Wiener-Hopf solution of the isotropic penetrable wedge problem: Diffraction and total field. IEEE Trans. Antennas Propag. 59 (10), 3797–3818.

Daniele, V. G., Zich, R. S., 2014. The Wiener-Hopf Method in Electromagnetics. Scitech, Edison, New Jersey.

Felsen, L. B., Marcuvitz, N., 1994. Radiation and scattering of waves, 2nd Edition. John Wiley & Sons, Hoboken, N.J.

Feynman, R. P., 1948. Space-time approach to non-relativistic quantum mechanics. Rev. Mod. Phys. 20, 367–387.

Filippov, A. F., 1964. Diffraction of an arbitrary acoustic wave by a wedge. J. Appl. Math. Mech. 28 (2), 372–388.

Fock, V. A., 1965. Electromagnetic Diffraction and Propagation Problems. Pergamon Press.

Freidlin, M., 1985. Functional Integration and Partial Differential Equations. (AM-109), Volume 109 (Annals of Mathematics Studies). Princeton University Press.

Gautesen, A. K., 1983. On the Green's function for acoustical diffraction by a strip. The Journal of the Acoustical Society of America 74 (2), 600.

Gradshteyn, I. S., Ryzhik, I. M., 2014. Table of Integrals, Series, and Products, 8th Edition. Academic Press.

Hacivelioglu, F., Sevgi, L., Ufimtsev, P. Y., 2011. Electromagnetic Wave Scattering from a Wedge with Perfectly Reflecting Boundaries : Analysis of Asymptotic Techniques. IEEE Antennas Propag. Mag. 53 (3), 232–253.

Israilov, M. S., 2013. Diffraction of acoustic and elastic waves on a half-plane for boundary conditions of various types. Mechanics of Solids 48 (3), 337–347.

James, G. L., 1986. Geometrical Theory of Diffraction for Electromagnetic Waves, 3rd Edition. Institution of Engineering and Technology, London.

Jones, D. S., 1952. A simplifying technique in the solution of a class of diffraction problems. Q. J. Math. 3 (1), 189–196.

Jones, D. S., 1964. The Theory of Electromagnetism. Pergamon Press, London.

Jones, D. S., 1980. The Kontorovich-Lebedev Transform. IMA J. Appl. Math. 26 (2), 133–141.

Jones, D. S., 1986. Acoustic and Electromagnetic Waves. Oxford University Press, Oxford.

Kac, M., 1949. On the distribution of certain Wiener functionals. Trans. Am. Math. Soc. 65 (1), 1–13.

Keller, J. B., 1962. Geometrical Theory of Diffraction. J. Opt. Soc. Am. 52 (2), 116–130.

Keller, J. B., Blank, A., 1951. Diffraction and reflection of pulses by wedges and corners. Commun. Pure Appl. Math. 4 (1), 75–94.

Kisil, A. V., 2015. The relationship between a strip Wiener-Hopf problem and a line Riemann-Hilbert problem. IMA J. Appl. Math. 80, 1569–1581.

Knopoff, L., 1969. Elastic Wave Propagation in a Wedge. In: Miklowitz, J. (Ed.), Wave Propag. Solids. ASME, Los Angeles, pp. 3–43.

Komech, A. I., Merzon, A. E., Mendez, J. E. D. l. P., 2015. Time-dependent scattering of generalized plane waves by a wedge. Math. Methods Appl. Sci. 38 (18), 4774–4785.

Kontorovich, M. J., Lebedev, N. N., 1939. On a method of solution of some problems of the diffraction theory. J. Phys. (Academy Sci. U.S.S.R.) 1 (3), 229–241.

Kouyoumjian, R. G., Pathak, P. H., 1974. A uniform GTD for an edge in a perfectly conducting surface. Proc. IEEE 62 (11), 1448–1461.

Kythe, P. K., 2011. Green's Functions and Linear Differential Equations. Chapman and Hall/CRC.

Lawrie, J. B., Abrahams, I. D., 2007. A brief historical perspective of the Wiener-Hopf technique. J. Eng. Math. 59 (4), 351–358.

Lebedev, N. N., 1965. Special Functions and Their Application. Eaglewood Cliffs.

Lyalinov, M. A., 1999. Diffraction by a highly contrast transparent wedge. J. Phys. A. Math. Gen. 32 (11), 2183–2206.

Lyalinov, M. A., 2013. Scattering of acoustic waves by a sector. Wave Motion 50 (4), 739–762.

Lyalinov, M. A., Zhu, N. Y., 2013. Scattering of Waves by Wedges and Cones with Impedance Boundary Conditions. Scitech, Edison, New Jersey.

Macdonald, H. M., 1902. Electric Waves. University Press.

Malyuzhinets, G. D., 1955a. Sound radiation by vibrating faces of arbitrary wedge. Part I. Akust. Zhurnal (in Russ.) 1 (2), 144–164.

Malyuzhinets, G. D., 1955b. Sound radiation by vibrating faces of arbitrary wedge. Part II. Akust. Zhurnal (in Russ.) 1 (3), 226–234.

Malyuzhinets, G. D., 1958a. Excitation, reflection and emission of surface waves from a wedge with given face impedances. Sov. Phys. Dokl. 3, 752–755.

Malyuzhinets, G. D., 1958b. Inversion formula for Sommerfeld integral. Sov. Phys. Dokl. 3, 52–56.

Malyuzhinets, G. D., 1958c. Relation between the inversion formulas for the Sommerfeld Integral and the formulas of Kontorovich-Lebedev. Sov. Phys. Dokl. 3, 266–268.

Martin, P. A., Wickham, G. R., 1983. Diffraction of Elastic Waves by a Penny-Shaped Crack: Analytical and Numerical Results. Proc. R. Soc. A Math. Phys. Eng. Sci. 390 (1798), 91–129.

Mcnamara, D. A., Pistorius, C. W. I., Malherbe, J. A. G., 1990. Introduction to the Uniform Geometrical Theory of Diffraction. Artech House.

Miles, J. W., 1952. On the diffraction of an acoustic pulse by a wedge. Proc. R. Soc. A Math. Phys. Eng. Sci. 212 (1111), 543–547.

Moran, C. A. J., Biggs, N. R. T., Chamberlain, P. G., 2016. Embedding formulae for wave diffraction by a circular arc. Wave Motion 67, 32–46.

Noble, B., 1958. Methods based on the Wiener-Hopf Technique for the solution of partial differential equations (1988 reprint). Chelsea Publishing Company, New York.

Oberhettinger, F., 1954. Diffraction of Waves by a Wedge. Commun. Pure Appl. Math. 7 (3), 551–563.

Oberhettinger, F., 1958. On the diffraction and reflection of waves and pulses by wedges and corners. J. Res. Natl. Bur. Stand. 61 (5), 343–365.

Osipov, A. V., Norris, A. N., 1999. The Malyuzhinets theory for scattering from wedge boundaries: a review. Wave Motion 29, 313–340.

Poincaré, H., 1892. Sur la Polarisation par Diffraction. Acta Math. (in French) 16, 297–339.

Poincaré, H., 1897. Sur la Polarisation par Diffraction: Seconde partie. Acta Math. (in French) 20, 313–355.

Rawlins, A. D., 1987. Plane-wave diffraction by a rational wedge. Proc. R. Soc. A Math. Phys. Eng. Sci. 411 (1841), 265–283.

Rawlins, A. D., 1989. A Green's function for diffraction by a rational wedge. Math. Proc. Cambridge Philos. Soc. 105 (1), 185–192.

Rawlins, A. D., 1999. Diffraction by, or diffusion into, a penetrable wedge. Proc. R. Soc. A Math. Phys. Eng. Sci. 455 (1987), 2655–2686.

Schot, S., 1992. Eighty years of Sommerfeld's radiation condition. Historia Mathematica 19 (4), 385–401.

Senior, T. B. A., 1959. Diffraction by an Imperfectly Conducting Wedge. Commun. Pure Appl. Math. 12 (2), 337–372.

Shanin, A. V., 1996. On Wave Excitation in a Wedge-Shaped Region. Acoust. Phys. 42 (5), 612–617.

Shanin, A. V., 1998. Excitation of Waves in a Wedge-Shaped Region. Acoust. Phys. 44 (5), 592–597.

Shanin, A. V., 2005. Modified Smyshlyaev's formulae for the problem of diffraction of a plane wave by an ideal quarter-plane. Wave Motion 41 (1), 79–93.

Shanin, A. V., Craster, R. V., 2010. Pseudo-differential operators for embedding formulae. J. Comput. Appl. Math. 234, 1637–1646.

Skelton, E. A., Craster, R. V., Shanin, A. V., Valyaev, V. Y., 2010. Embedding formulae for scattering by three-dimensional structures. Wave Motion 47 (5), 299–317.

Smirnov, V. I., 1964. A Course of Higher Mathematics. Volume 3, Part 2. Pergamon Press.

Sobolev, S. L., 1935. General Theory of Diffraction of Waves on Riemann Surfaces. In: Sel. Work. S. L. Sobolev Vol I. New York, pp. 201–262.

Sommerfeld, A., 1896. Mathematische Theorie der Diffraction. Math. Ann. (in Ger.) 47, 317–374.

Sommerfeld, A., 1901. Theoretical about the diffraction of X-rays. Zeitschrift für Math. und Phys. (in Ger.) 46, 11–97.

Sommerfeld, A., 2003. Mathematical Theory of Diffraction. Birkhauser, Boston.

Teixeira, F., 1991. Diffraction by a rectangular wedge: Wiener-Hopf-Hankel formulation. Integr. Equations Oper. Theory 14 (3), 436–454.

Ufimtsev, P. Y., 1971. Method of edge waves in the physical theory of diffraction. (from the Russian "Metod krayevykh voln v fizicheskoy teorii difraktsii" Izd-Vo Sov. Radio, pp-243, 1962), translation prepared by the U.S. Air Force Foreign Technology Division.

Ufimtsev, P. Y., 2014. Fundamentals of the Physical Theory of Diffraction, 2nd Edition. John Wiley & Sons.

Voss, J., 2013. An Introduction to Statistical Computing: A Simulation-based Approach. Wiley.

Wegert, E., 2012. Visual Complex Functions. Birkhauser Basel.

Wiener, N., Hopf, E., 1931. Über eine klasse singulärer integralgleichungen. Sitzungsberichte der Preuss. Akad. der Wissenschaften, Phys. Klasse (in Ger.) 31, 696–706.

Williams, M. H., 1982. Diffraction by a finite strip. Q. J. Mech. Appl. Math. 35, 103–124.

Williams, W. E., 1959. Diffraction of an E-polarized plane wave by an imperfectly conducting wedge. Proc. R. Soc. A Math. Phys. Eng. Sci. 252 (1270), 376–393.

Appendix A. Macdonald's series solution

In this section we shall briefly discuss the separation of variables method applied by Macdonald (1902) to the wedge problem with line source incidence. After this, departing slightly from Macdonald's approach, we shall use a limiting procedure in order to recover the series solutions (4.19) and (4.20) to the plane wave incidence problem.

The wedge problem forced by a line source of strength $\mathcal{A}$ with polar coordinates $(r_\mathrm{I}, \theta_\mathrm{I})$, has the following governing equation,

$$\nabla^2\Phi + k^2\Phi = \frac{\mathcal{A}}{r}\hat{\delta}(r - r_\mathrm{I})\hat{\delta}(\theta - \theta_\mathrm{I}), \tag{A.1}$$

where $\hat{\delta}$ is the Dirac delta function. The total field, Φ, is decomposed into incident and scattered parts $\Phi = \Phi_\mathrm{I} + \Phi_\mathrm{S}$ where the incident wave is given by

$$\Phi_\mathrm{I} = \frac{\mathcal{A}}{4i}H_0^{(1)}\left(k\sqrt{r^2 + r_\mathrm{I}^2 - 2rr_\mathrm{I}\cos(\theta - \theta_\mathrm{I})}\right), \tag{A.2}$$

and is subjected to BCs, (1.2) or (1.3). Considering the ansatz $\Phi = R(r)\Theta(\theta)$, using separation of variables and applying the BCs, we obtain the following series solutions:

$$\text{Dirichlet case:} \quad \Phi(r,\theta) = \sum_{n=1}^{\infty} A_n R_n(r)\sin((\theta - \theta_\mathrm{w})\delta n), \tag{A.3}$$

$$\text{Neumann case:} \quad \Phi(r,\theta) = \sum_{n=0}^{\infty} B_n R_n(r)\cos((\theta - \theta_\mathrm{w})\delta n). \tag{A.4}$$

Because of the source location at $r = r_\mathrm{I}$, and the need to satisfy both the edge and the radiation conditions (satisfied by the Bessel and Hankel functions respectively), we pose

$$R_n(r) = \begin{cases} C_n J_{\delta n}(kr) & r < r_\mathrm{I}, \\ D_n H_{\delta n}^{(1)}(kr) & r > r_\mathrm{I}. \end{cases} \tag{A.5}$$

To ensure continuity across $r = r_\mathrm{I}$, we require $C_n = H_{\delta n}^{(1)}(kr_\mathrm{I})$ and $D_n = J_{\delta n}(kr_\mathrm{I})$. We can determine the coefficients A_n and B_n by deriving and applying a jump condition across $r = r_\mathrm{I}$.

In the Dirichlet case, substitute (A.3) into (A.1), and multiply the resulting equation by $r\sin((\theta - \theta_\mathrm{w})\delta m)$. Integrating w.r.t. θ from $-\theta_\mathrm{w}$ to θ_w, and using the orthogonality of sine, we obtain

$$A_m\frac{\partial}{\partial r}(rR_m'(r)) + A_m\left(k^2 - \frac{\delta^2 m^2}{r^2}\right)rR_m(r) = \frac{\mathcal{A}}{\theta_\mathrm{w}}\hat{\delta}(r - r_\mathrm{I})\sin((\theta_\mathrm{I} - \theta_\mathrm{w})\delta m). \tag{A.6}$$

Now integrating (A.6) from $r = r_\mathrm{I} - \epsilon$ to $r_\mathrm{I} + \epsilon$ and taking the limit $\epsilon \to 0$ leads to the jump condition

$$A_m r_\mathrm{I}\left[R_m'(r)\right]_{r_\mathrm{I}^-}^{r_\mathrm{I}^+} = \frac{\mathcal{A}}{\theta_\mathrm{w}}\sin((\theta_\mathrm{I} - \theta_\mathrm{w})\delta m). \tag{A.7}$$

Lastly, we use (A.5) and the Wronskian result $J_\nu(z)H_\nu^{(1)'}(z) - J_\nu'(z)H_\nu^{(1)}(z) = \frac{2i}{\pi z}$ to determine that $A_n = -i\delta\mathcal{A}\sin((\theta_\mathrm{I} - \theta_\mathrm{w})\delta n)$. Hence, the series solution with line source incidence and Dirichlet BCs is

$$\Phi = \sum_{n=1}^{\infty} i\delta\mathcal{A}\sin((\theta_\mathrm{w} - \theta_\mathrm{I})\delta n)\sin((\theta - \theta_\mathrm{w})\delta n)J_{\delta n}(kr_<)H_{\delta n}^{(1)}(kr_>), \tag{A.8}$$

where $r_< = \min(r, r_\mathrm{I})$ and $r_> = \max(r, r_\mathrm{I})$. This agrees with Macdonald's solution[14].

For the Neumann case, the coefficients B_n are found by the same method using the orthogonality relation for cosine, leading to

$$\Phi = -\sum_{n=0}^{\infty} i\varepsilon_n\delta\mathcal{A}\cos((\theta_\mathrm{w} - \theta_\mathrm{I})\delta n)\cos((\theta - \theta_\mathrm{w})\delta n)J_{\delta n}(kr_<)H_{\delta n}^{(1)}(kr_>), \tag{A.9}$$

where $\varepsilon_0 = 1/2$ and $\varepsilon_n = 1$ for $n \geq 1$.

To recover the plane wave solution, we send the source and its strength to infinity in a way that ensures that Φ_I (as defined in (A.2)) behaves like $e^{-ikr\cos(\theta-\theta_\mathrm{I})}$ as $r_\mathrm{I} \to \infty$. This can be done by choosing $\mathcal{A} = \sqrt{8\pi kr_\mathrm{I}}e^{-ikr_\mathrm{I}+\frac{3\pi i}{4}}$ and leads to

$$\lim_{r_\mathrm{I}\to\infty} A_n H_{\delta n}^{(1)}(kr_\mathrm{I}) = 4\delta(-i)^{\delta n}\sin((\theta_\mathrm{I} - \theta_\mathrm{w})\delta n), \tag{A.10}$$

$$\lim_{r_\mathrm{I}\to\infty} B_n H_{\delta n}^{(1)}(kr_\mathrm{I}) = 4\varepsilon_n\delta(-i)^{\delta n}\cos((\theta_\mathrm{w} - \theta_\mathrm{I})\delta n). \tag{A.11}$$

Hence, for plane wave forcing with Dirichlet or Neumann BCs respectively, the series solutions are

$$\Phi(r,\theta) = 4\delta\sum_{n=1}^{\infty}(-i)^{\delta n}J_{\delta n}(kr)\sin((\theta - \theta_\mathrm{w})\delta n)\sin((\theta_\mathrm{I} - \theta_\mathrm{w})\delta n),$$

$$\Phi(r,\theta) = 2\delta J_0(kr) + 4\delta\sum_{n=1}^{\infty}(-i)^{\delta n}J_{\delta n}(kr)\cos((\theta - \theta_\mathrm{w})\delta n)\cos((\theta_\mathrm{w} - \theta_\mathrm{I})\delta n),$$

which matches perfectly with (4.19) and (4.20) as required. Note that these exact series solutions have a natural embedding structure (see Section 6.1) in the sense that they are simply sums of products of functions of one variable only.

Appendix B. A link between the spectral function $s(z)$ and Green's integral operator

In this appendix, we propose to establish a link between the spectral function s and a Green's integral operator occurring naturally while applying Green's third identity to wedge-shaped domains. This approach has been successfully implemented and generalised by Bernard (2005, 2006) in order to obtain functional equations for complicated angular scatterers such as impedance polygons.

[14]Note that Macdonald (1902) uses the alternate time factor $e^{i\omega t}$.

Appendix B.1. Preliminary definitions and Green's function representation

Let us introduce the generic plane wave function w_z by

$$w_z(r,\theta) = \exp(ikr\cos(z-\theta)) \tag{B.1}$$

It is important to note that for any $\Theta \in [-\pi,\pi]$, $w_z(r,\Theta)$ is exponentially decaying as $r \to \infty$ as long as $z \in \Omega_\Theta = \Omega_0 + \Theta$, where both Ω_0 and Ω_Θ are understood as open sets (do not contain their boundaries) and are illustrated in Figure B.16.

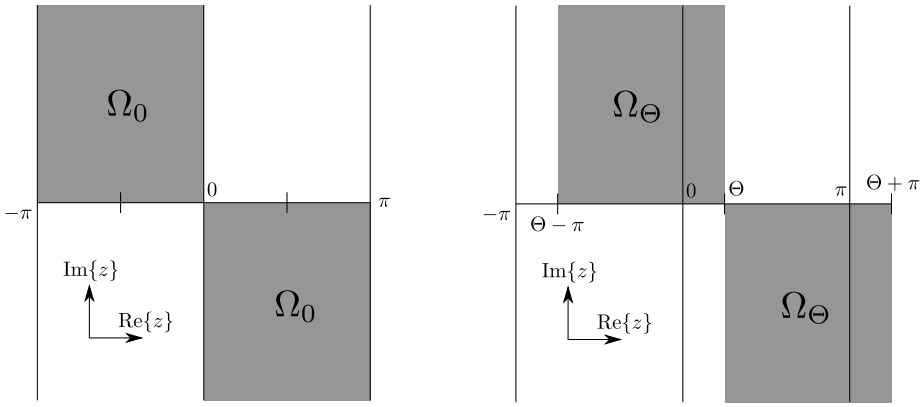

Figure B.16: The domains Ω_0 and Ω_Θ

Using the notations of Section 5, the total, diffracted and geometrical optics fields are denoted Φ, Φ_{Diff} and Φ_{GO}. For the exterior wedge, Φ_{GO} consists of an incident wave and one or two reflected waves and can hence be written in the form $\Phi_{\text{GO}}(r,\theta) = \sum_i a_i(\theta) w_{z_i}(r,\theta)$, where $a_i(\theta)$ is either zero or a given constant. Typically in our problem the incident wave corresponds to $z_i = \theta_{\text{I}} + \pi$, and the reflected waves to either $z_i = 2\theta_{\text{w}} - \theta_{\text{I}} + \pi$ or $z_i = -2\theta_{\text{w}} - \theta_{\text{I}} + \pi$ or both depending on how many reflections we have.

For a given function Ψ, let us now introduce the Green integral operator $\mathcal{S}_\Theta(z)[\Psi]$ defined by

$$\mathcal{S}_\Theta(z)[\Psi] = \int_0^\infty \left[\Psi \frac{\partial w_z}{\partial\theta} - \frac{\partial\Psi}{\partial\theta} w_z\right]_{\theta=\Theta} \frac{\mathrm{d}r}{r}. \tag{B.2}$$

In the contest of this review, $\Theta \in [-\theta_{\text{w}}, \theta_{\text{w}}]$. Moreover, using standard integration, one can show that $\mathcal{S}_\Theta(z)[w_{z_i}] = \tan\left(\frac{z_i - z}{2}\right)$, and hence we can write

$$\mathcal{S}_\Theta(z)[\Phi] = \mathcal{S}_\Theta(z)[\Phi_{\text{Diff}}] + \sum_i a_i(\Theta)\tan\left(\frac{z_i - z}{2}\right), \tag{B.3}$$

which implies in particular that each of the $z_i + \pi$ are simple poles of $\mathcal{S}_\Theta(z)[\Phi]$ with residue -2. The objective of this appendix is to find a connection between the spectral

function $s(z)$ and $\mathcal{S}_\Theta(z)[\Phi]$. In order to do that, we shall make use of the theory of Green's functions as follows.

Let us pick a point $(r^\star, \theta^\star)$, and pick two angles φ_a and φ_b (the subscripts a and b stand for *above* and *below*) chosen such that $-\pi/2 < \varphi_b < \theta^\star < \varphi_a < \pi/2$, and a radius $R_\mathcal{A} > r^\star$. Now consider the domain $\Omega^\star(\varphi_b, \varphi_a, R_\mathcal{A})$ to be the corresponding sector described in Figure B.17. Let us further assume that $\partial\Omega^\star$ is oriented anti-clockwise, and that the normals $\boldsymbol{n}$ to $\partial\Omega^\star$ are chosen to be outgoing.

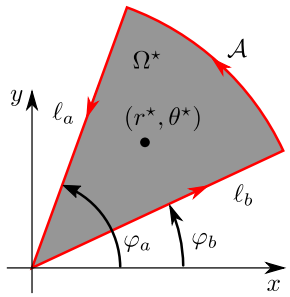

Figure B.17: The angular domain $\Omega^\star$

Let $G_\star(r, \theta)$ be a short notation for $G(r, \theta; r^\star, \theta^\star)$, the free-space Green's function for the Helmholtz equation resulting from a point source at $(r^\star, \theta^\star)$. Using the respective governing equations of Φ and $G_\star$, and the divergence theorem, we have

$$\iint_{\Omega^\star} (\Phi \Delta G_\star - G_\star \Delta \Phi) \mathrm{d}A = \Phi(r^\star, \theta^\star) = \oint_{\partial\Omega^\star} (\Phi \nabla G_\star - G_\star \nabla \Phi) \cdot \boldsymbol{n} \mathrm{d}s$$

Hence, using that on ℓ_b, $\boldsymbol{n} = -\boldsymbol{e}_\theta$, on $\mathcal{A}$, $\boldsymbol{n} = \boldsymbol{e}_r$ and on ℓ_a, $\boldsymbol{n} = \boldsymbol{e}_\theta$, we get

$$\Phi(r^\star, \theta^\star) = \underbrace{-\int_0^{R_\mathcal{A}} \left(\Phi \frac{\partial G_\star}{\partial \theta} - G_\star \frac{\partial \Phi}{\partial \theta} \right)_{\theta=\varphi_b} \frac{\mathrm{d}r}{r}}_{\ell_b \text{ component: } I_{\ell_b}[\Phi]} + \underbrace{\int_{\varphi_b}^{\varphi_a} \left(\Phi \frac{\partial G_\star}{\partial r} - G_\star \frac{\partial \Phi}{\partial r} \right)_{r=R_\mathcal{A}} R_\mathcal{A} \mathrm{d}\theta}_{\text{Arc } \mathcal{A} \text{ component: } I_\mathcal{A}[\Phi]}$$
$$\underbrace{+\int_0^{R_\mathcal{A}} \left(\Phi \frac{\partial G_\star}{\partial \theta} - G_\star \frac{\partial \Phi}{\partial \theta} \right)_{\theta=\varphi_a} \frac{\mathrm{d}r}{r}}_{\ell_a \text{ component: } I_{\ell_a}[\Phi]}. \tag{B.4}$$

Using the Hankel representation of $G_\star$, its far-field asymptotics, and the method of steepest descent, we can show that the only part of the far-field leading to any contribution of the arc integral as $R_\mathcal{A} \to \infty$ is an incident plane wave coming from within the sector. More precisely, if $\theta_\mathrm{I} \in (\varphi_b, \varphi_a)$,

$$\lim_{R_A \to \infty} I_\mathcal{A} \left[e^{-ikr\cos(\theta - \theta_\mathrm{I})} \right] = e^{-ikr^\star \cos(\theta^\star - \theta_\mathrm{I})} = \Phi_\mathrm{I}(r^\star, \theta^\star).$$

All other components (reflected waves, diffracted field, incident waves from outside the sector) can be shown to have zero contribution. Hence, taking the limit as $R_\mathcal{A} \to \infty$

in (B.4), we get

$$\Phi(r^\star,\theta^\star) = -\int_0^\infty \left(\Phi\frac{\partial G_\star}{\partial\theta} - G_\star\frac{\partial\Phi}{\partial\theta}\right)_{\theta=\varphi_b}\frac{\mathrm{d}r}{r} + \int_0^\infty \left(\Phi\frac{\partial G_\star}{\partial\theta} - G_\star\frac{\partial\Phi}{\partial\theta}\right)_{\theta=\varphi_a}\frac{\mathrm{d}r}{r} + \Phi_{\mathrm{I}}^{ab}(r^\star,\theta^\star), \tag{B.5}$$

where $\Phi_{\mathrm{I}}^{ab} = \Phi_{\mathrm{I}}$ if $\theta_{\mathrm{I}} \in (\varphi_a, \varphi_b)$ and zero otherwise. Hence the knowledge of $G_\star$ and $\frac{\partial G^\star}{\partial\theta}$ on oblique lines of constant θ is important. At this stage, it is important to realise, at least informally, that if we could write them in terms of w_z somehow, then we have a chance to link Φ and the Green integral operator.

Appendix B.2. Green's functions on oblique lines

Before finding formulae for $G_\star$, we will focus on the Green's function G_0 corresponding to a point source at the origin. First of all, it is well known (see e.g. Kythe (2011)) that $G_0(r,\theta) = \frac{-i}{4}H_0^{(1)}(kr)$. Moreover, the Hankel function has the following integral representation[15]

$$H_0^{(1)}(r) = \frac{1}{\pi}\int_\Gamma e^{ir\cos(z)}\mathrm{d}z \quad \text{leading to} \quad G_0(r,\theta) = \frac{+1}{4\pi i}\int_\Gamma e^{ikr\cos(z)}\mathrm{d}z, \tag{B.6}$$

where Γ is described in Figure 6. We will now endeavour to find formulae for G_0 valid on an oblique half-space and hence on any line that crosses the x axis with an angle $\varphi \in (-\pi/2, \pi/2)$ say, and lies above (see Figure B.18 (left)) or below (see Figure B.18 (right)) the origin.

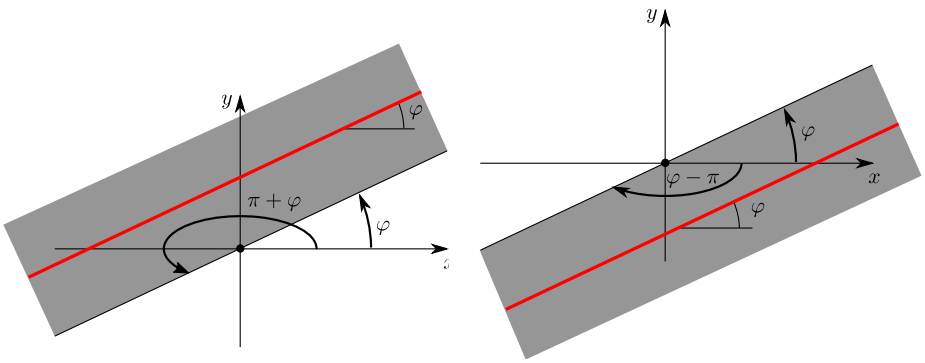

Figure B.18: The two half-spaces under consideration for a given φ: above (left) and below (right)

[15] See, e.g. Sommerfeld (2003) eq (6) p19, together with translators' note 4 on p78, here we use $\beta = \frac{\pi}{2}$.

Oblique line above the origin. Let us consider the half-space $\varphi < \theta < \pi + \varphi$, the grey area of Figure B.18 (left) . Let us start from (B.6) and shift the contour Γ to the contour $\Gamma + \frac{\pi}{2} - (\theta - \varphi)$, where the new contour height is adjusted so that it goes through the origin. Because of the restriction on θ, we can do that without leaving Ω_0, where our integrand is analytic and exponentially decaying, and so the value of the integral and its convergence property remain unchanged. We can now perform the substitution $z' \leftrightarrow z + \theta$ to get

$$G_0(r,\theta) = \frac{1}{4\pi i}\int_{\gamma_a(\varphi;\theta)} w_{z'}(r,\theta)\mathrm{d}z', \tag{B.7}$$

where the contour $\gamma_a(\varphi;\theta) = \Gamma + \frac{\pi}{2} + \varphi$ goes through the point $z = \theta$ of the real axis, as shown in Figure B.19 (left). This formula is valid (and the integral converges exponentially) on any oblique line with angle φ that lies above the origin.

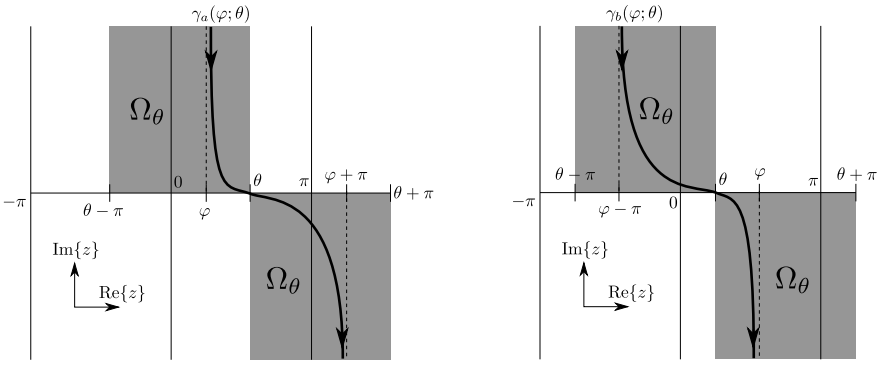

Figure B.19: The contours $\gamma_a(\varphi;\theta)$ and $\gamma_b(\varphi;\theta)$

Note that here r is finite, and the integrand is analytic, so we can in principle deform all the contours $\gamma_a(\varphi;\theta)$ to $\gamma_a(\varphi;\varphi)$, it is important to note that the latter crosses the real axis at $z = \varphi$ and is included (only just!) in Ω_φ. This contour will just be referred to as $\gamma_a(\varphi)$ thereafter, and we get

$$G_0(r,\theta) = \frac{1}{4\pi i}\int_{\gamma_a(\varphi)} w_z(r,\theta)\mathrm{d}z \tag{B.8}$$

Oblique lines below the origin. In a very similar way, we can consider the half-space $\varphi - \pi < \theta < \varphi$ and shift the contour Γ to a height adjusted $\Gamma - \frac{\pi}{2} + (\varphi - \theta)$ passing through the origin. Upon performing the substitution $z \leftrightarrow z+\theta$, we obtain an integral over a contour $\gamma_b(\varphi;\theta)$ illustrated on Figure B.19 (right). Again by analyticity of the integrand, such integral can safely be deformed to the contour $\varphi_b(\varphi) \equiv \varphi_b(\varphi;\varphi)$ that crosses the real axis at $z = \varphi$ and lies within Ω_φ, to get

$$G_0(r,\theta) = \frac{1}{4\pi i}\int_{\gamma_b(\varphi)} w_z(r,\theta)\mathrm{d}z, \tag{B.9}$$

Back to $G_\star$. In order to get back to $G_\star$, we just need to replace r by r' and θ by θ' in (B.8) and (B.9), where r' and θ' are the polar coordinates centred at $(r^\star, \theta^\star)$. Upon noting that $r'e^{i\theta'} = re^{i\theta} - r^\star e^{i\theta^\star}$, we find that

$$w_z(r', \theta') = w_z(r, \theta)e^{-ikr^\star \cos(z-\theta^\star)} \quad \text{and} \quad G_\star(r, \theta) = \frac{1}{4\pi i}\int_{\gamma_s(\varphi_s)} w_z(r, \theta)e^{-ikr^\star \cos(z-\theta^\star)}\mathrm{d}z,$$

where from now on, the subscript s is either a or b. Since $\gamma_s(\varphi_s)$ is independent of θ, we get a similar formula for $\frac{\partial G_\star}{\partial \theta}$. In particular, in the configuration of Figure B.17, since the oblique line ℓ_a (resp. ℓ_b) lies above (resp. below) the source $(r^\star, \theta^\star)$ and make an angle φ_a (resp. φ_b) with the real axis, we have

$$G_\star|_{\ell_s} = G_\star(r, \varphi_s) \quad \text{and} \quad \left.\frac{\partial G_\star}{\partial \theta}\right|_{\ell_s} = \frac{1}{4\pi i}\int_{\gamma_s(\varphi_s)} \frac{\partial w_z}{\partial \theta}(r, \varphi_s)e^{-ikr^\star \cos(z-\theta^\star)}\mathrm{d}z. \tag{B.10}$$

Appendix B.3. Connection formula between $s(z)$ and $S_0(z)$

Before making use of our results (B.5) and (B.10), we need to make use of some properties of the Green integral operator:

Proposition 2

1. *Apart from eventual poles on the real line, as a function of z, $\mathcal{S}_\Theta(z)[\Phi]$ is analytic for $z \in \Omega_\Theta = \Omega_0 + \Theta$.*
2. *If $z \in \Omega_{\Theta_1} \cap \Omega_{\Theta_2}$, then $\mathcal{S}_{\Theta_1}(z)[\Phi] = \mathcal{S}_{\Theta_2}(z)[\Phi]$. Note that by analytic continuation, this allows to extend the natural domain of analyticity of $\mathcal{S}_{\Theta_{1,2}}(z)$ to $\Omega_{\Theta_1} \cup \Omega_{\Theta_2}$.*

Now, we can input (B.10) into (B.5), and, since we made sure that $\gamma_s(\varphi_s) \subset \Omega_{\varphi_s}$, we can exchange the order of integration. Let us furthermore assume that $\varphi_b < 0 < \varphi_a$, then the formula can be evaluated at $\theta^\star = 0$ to get

$$\Phi(r^\star, 0) = \frac{-1}{4\pi i}\int_{\gamma_b(\varphi_b)} e^{-ikr^\star \cos(z)}\mathcal{S}_{\varphi_b}(z)[\Phi]\mathrm{d}z + \frac{1}{4\pi i}\int_{\gamma_a(\varphi_a)} e^{-ikr^\star \cos(z)}\mathcal{S}_{\varphi_a}(z)[\Phi]\mathrm{d}z + \Phi_{\mathrm{I}}^{ab}(r^\star, 0), \tag{B.11}$$

where an illustration of the contour configuration is displayed in Figure B.20 (left). Making use of point 2 of Proposition 2, the integrands of both integrals in (B.11) are actually analytical continuations of each other, and hence we can write

$$\Phi(r^\star, 0) = \frac{1}{4\pi i}\int_{(\gamma_b(\varphi_b))^c + \gamma_a(\varphi_a)} e^{-ikr^\star \cos(z)}\mathcal{S}_{\varphi_b}(z)[\Phi]\mathrm{d}z + \Phi_{\mathrm{I}}^{ab}(r^\star, 0),$$

where $(\gamma_b(\varphi_b))^c$ is a notation for $\gamma_b(\varphi_b)$ going in the other direction. Let us consider the contours as angular (we can do that by analytic deformation), as depicted in

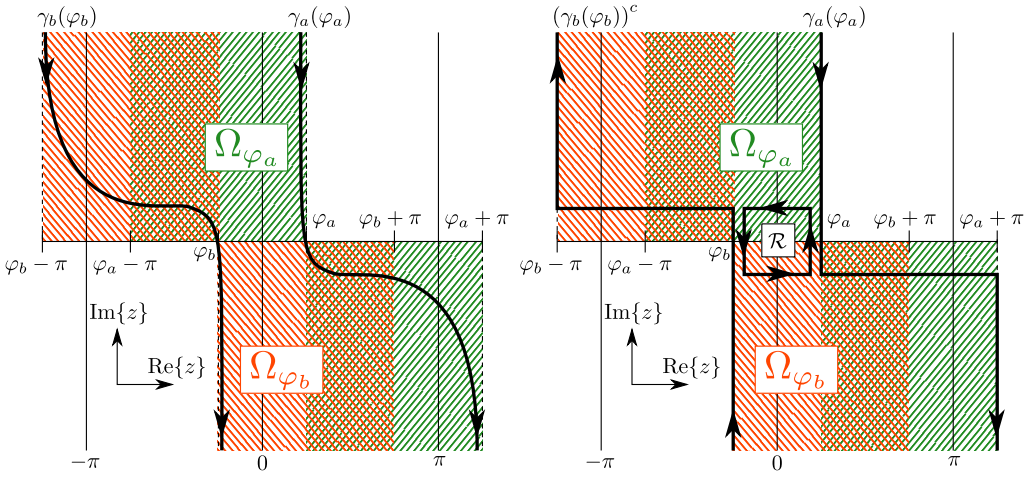

Figure B.20: The two contours $\gamma_b(\varphi_b)$ and $\gamma_a(\varphi_a)$ for $-\pi < \varphi_b < 0 < \varphi_a < \pi$ (left), their angular counterparts and the contour $\mathcal{R}$ (right)

Figure B.20 (right). Let us also introduce a new contour $\mathcal{R}$, that is rectangular, with its centre at the origin and oriented anticlockwise, such that its left (resp. right) lateral side coincides with a part of $(\gamma_b(\varphi_b))^c$ (resp. $\gamma_a(\varphi_a)$), but in the opposite direction.

We can always choose φ_a and φ_b close enough to zero, such that no poles related to reflected waves exist within $\mathcal{R}$. In this case, one can show that the only possible singularity is a pole corresponding to the incident wave, and we have

$$\frac{1}{4\pi i}\oint_{\mathcal{R}} e^{-ikr^\star\cos(z)}\mathcal{S}_{\varphi_b}(z)[\Phi]\mathrm{d}z = \Phi_{\mathrm{I}}^{ab}(r^\star, 0). \tag{B.12}$$

This ensures that we can write

$$\Phi(r^\star, 0) = \frac{1}{4\pi i}\int_{(\gamma_b(\varphi_b))^c+\gamma_a(\varphi_a)+\mathcal{R}} e^{-ikr^\star\cos(z)}\mathcal{S}_{\varphi_b}(z)[\Phi]\mathrm{d}z. \tag{B.13}$$

Now, the coinciding lateral parts cancel each other, and the remaining contour is simply $\gamma_+ + \gamma_-$ (see Figure 2 (left)). Now taking the limit as $\varphi_b \to 0$, or using the fact that $\mathcal{S}_{\varphi_b}(z)$ is an analytic continuation of $\mathcal{S}_0(z)$ by Proposition 2, we get

$$\begin{aligned}\Phi(r^\star, 0) &= \frac{1}{4\pi i}\int_{\gamma_+-\gamma_-} e^{-ikr^\star\cos(z)}\mathcal{S}_0(z)[\Phi]\mathrm{d}z \\ &= \frac{1}{2\pi i}\int_{\gamma_+} e^{-ikr^\star\cos(z)}\left(\frac{\mathcal{S}_0(z)[\Phi] - \mathcal{S}_0(-z)[\Phi]}{2}\right)\mathrm{d}z\end{aligned} \tag{B.14}$$

Everything that has been done in this subsection can be used to get a similar formula for $\frac{\partial\Phi}{\partial\theta}$ to get

$$-\frac{1}{ikr^\star}\frac{\partial\Phi}{\partial\theta}(r^\star, 0) = \frac{1}{2\pi i}\int_{\gamma_+} e^{-ikr^\star\cos(z)}\sin(z)\left(\frac{\mathcal{S}_0(z)[\Phi] + \mathcal{S}_0(-z)[\Phi]}{2}\right)\mathrm{d}z \tag{B.15}$$

Now, comparing (B.14) and (B.15) to equations (2.1) and (3.22), it is clear that we can apply Theorem 1 to find that

$$\frac{1}{2}(\mathcal{S}_0(z)[\Phi] \mp \mathcal{S}_0(-z)[\Phi]) = s(z) \mp s(-z) \tag{B.16}$$

leading to the sought-after formula

$$s(z) = \frac{1}{2}\mathcal{S}_0(z)[\Phi], \tag{B.17}$$

linking the spectral function $s(z)$ to the Green's operator $\mathcal{S}_0(z)[\Phi]$. Note that this formula could have been recovered from what was done at the end of the Wiener-Hopf section (Section 3) in particular it is a consequence of (3.24), but this appendix is showing this link from Green's identity only. This can also be seen as a constructive way of getting to the form of the Sommerfeld integral. We can also follow the paper (Malyuzhinets, 1958c) to directly link the spectral function $s(z)$ with the Kontorovich-Lebedev transform of the scattered wave Ψ,

$$\begin{aligned}\Psi(\nu,\theta) = \frac{1}{\pi i \nu}\int_{-i\infty}^{i\infty} e^{-i\nu(z+\pi/2)}\left[s(\theta+z) - s(\theta-z)\right]\mathrm{d}z \\ + \frac{2(-i)^{1+\nu}}{\nu\sin(\pi\nu)}\cos\left(\left(|\theta-\theta_\mathrm{I}|-\pi\right)\nu\right)\end{aligned} \tag{B.18}$$

Note that the work done in this appendix is very general and can possibly be applied to geometries other than the wedge.

Chapter 4

Literature review: penetrable wedge diffraction

From now on, we will start looking at problems of diffraction by penetrable wedges. This chapter reviews some of the different formulations of the penetrable wedge problem and various attempts to find asymptotic and numerical solutions. We shall concentrate on four different papers, Rawlins (1999); Lyalinov (1999); Shanin (1998) and Daniele and Lombardi (2011), that each define a unique problem and method. It is important to note that this list is by no means exhaustive.

Radlow (1964) tackles the electromagnetic problem with a right-angled wedge and theoretically finds a solution as a two-dimensional inverse Laplace transform, but this solution is impractical and was also claimed incorrect by Kraut and Lehman (1969).

Budaev and Bogy looked at finding the pressure field of a special case of acoustic wave diffraction by penetrable wedges (Budaev and Bogy, 1999). They designed the problem symmetrically with an antisymmetric incident field, so that they could formulate it on a half-space domain and the symmetry condition became a boundary condition.

After the Sommerfeld-Malyuzhinets (S-M) technique is applied, all poles are separated from the spectral functions. This sum of poles represented the geometrical optic field. The separation lead to a system of difference equations that were solved via singular integral operators and a Neumann series expansion with the assumptions that the host wedge region is very thin and the ratio of densities is close to unity.

More recently, the approaches using simple layer potentials discussed in Croisille and Lebeau (1999) for elastic wedge diffraction, highly influenced studies by Mokeeva in the well-posedness of the penetrable wedge problem (Mokeeva, 2006, 2007). Alongside Babich, she would show that the problem has a unique solution (Babich and Mokeeva, 2008) and they would later develop a numerical solution of these simple layer potentials (Babich et al., 2012).

It is worth mentioning here the highly active research area of hybrid numerical-asymptotic (HNA) boundary element methods. These methods have arisen from numerical computation issues in high-frequency scattering problems. The main issue is the determination of wave fields in problems with finite-sized scatterers as the wavenumber becomes large, because it has proven to be very computationally expensive. With inspiration from exact solutions to canonical diffraction problems, these methods seek to enhance the basis functions used in the boundary element method in an educated way. For a good review on these HNA methods applied to various problems with impenetrable scatterers, see Chandler-Wilde et al. (2012).

HNA approaches have been considered for more difficult situations with convex polygons or other complex-shaped scatterers. Articles such as Groth et al. (2015, 2018) have attempted to use HNA methods for penetrable convex polygons. However, for penetrable convex polygons, the basis functions in these methods are not optimal and it has been stated in these articles that better knowledge of the penetrable wedge problem is required to improve their results. This is because at

high frequencies, the corner regions of a penetrable convex polygon can be approximated by penetrable wedges, hence, the solution to the penetrable wedge problem can be used as a component in penetrable convex polygon diffraction.

4.1 Diffraction by, or diffusion into, a penetrable wedge, (Rawlins, 1999)

Rawlins has worked on many different diffraction problems including rational wedges (Rawlins, 1987, 1989) and penetrable wedges (Rawlins, 1977, 1999) for both acoustic and electromagnetic settings.

In (Rawlins, 1977), he uses Green's second identity and the Green's function for the two-dimensional Helmholtz equation, to create Fredholm integral equations (FIE's) of the second kind, and defined a Neumann series solution assuming that the host and scatterer wavenumbers are of similar size ($k_2/k_1 \approx 1$). The result is used to obtain a far-field approximation for when an E-polarised plane wave is incident on a perfect dielectric right-angle wedge. Over twenty years later, another method is given for a similar problem with arbitrary angled wedges (Rawlins, 1999) with this same low-contrast between the wavenumbers.

Formulation and method Consider two dielectric wedge regions defined by different cylindrical coordinate systems,

$$\begin{aligned} S_1 &= \{(r,\theta):\ 0 \le r < \infty,\ -\theta_{\mathrm{w}} < \theta < \theta_{\mathrm{w}}\}, \\ S_2 &= \{(r,\bar{\theta}):\ 0 \le r < \infty,\ -\bar{\theta}_{\mathrm{w}} < \bar{\theta} < \bar{\theta}_{\mathrm{w}}\}, \end{aligned} \tag{4.1}$$

where $\bar{\theta}_{\mathrm{w}} = \pi - \theta_{\mathrm{w}}$. These two coordinate systems are connected by the formula $\bar{\theta} = \theta - \mathrm{sgn}(\theta)\pi$.[1] The regions S_1 and S_2 have wavenumbers k and kn respectively where $0 \le n - 1 \ll 1$. Figure 4.1 describes the wedge regions (4.1).

[1] Recall sgn(x) as the sign function (2.41).

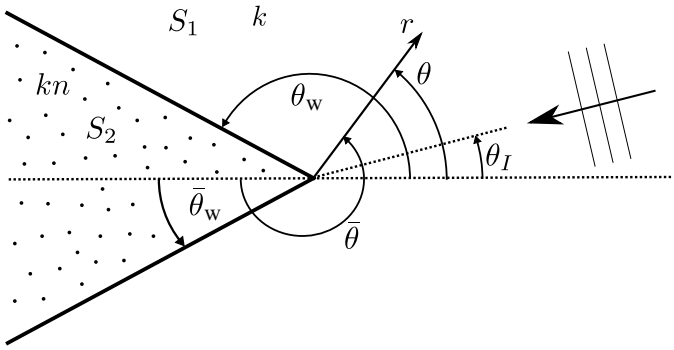

Figure 4.1: This diagram has been recreated from figure 1 in Rawlins (1999) to describe the wedge regions (4.1) and their associated coordinate systems.

There are two simultaneous problems, electric or magnetic polarised, where we solve for E_z and H_z respectively (see Section 1.1.2). The chosen polarisation reduces the three-dimensional vector problem to a two-dimensional scalar problem. Rawlins sought time-harmonic solutions with time factor $e^{-i\omega t}$ and defined the incident wave in S_1 as $\Phi_{\mathrm{I}} = e^{-ikr\cos(\theta-\theta_{\mathrm{I}})}$ where $0 \leq \theta_{\mathrm{I}} \leq \theta_{\mathrm{w}}$. He defined the total field Φ in the host region S_1 to satisfy the following conditions,

$$\begin{cases} \dfrac{1}{r}\dfrac{\partial}{\partial r}\left(r\dfrac{\partial \Phi}{\partial r}\right) + \dfrac{1}{r^2}\dfrac{\partial^2 \Phi}{\partial \theta^2} + k^2\Phi = 0 & \text{(Governing equation)}, \quad (4.2a) \\ \Phi_{\mathrm{Diff}} = \Phi - \Phi_{\mathrm{GO}} \underset{kr\to\infty}{=} O\left(\dfrac{e^{ikr}}{\sqrt{kr}}\right) & \text{(Radiation condition)}, \quad (4.2b) \\ \Phi \underset{r\to 0}{=} \text{constant} + O\left(r^{\hat{\delta}}\right) & \text{(Edge condition)}, \quad (4.2c) \end{cases}$$

where $\hat{\delta} \in (0,1)$. In the scatterer region S_2, the total field Ψ satisfies a similar set of conditions, with θ and k replaced with $\bar{\theta}$ and kn respectively. Note that Rawlins had an additional radiation condition: if $\mathrm{Im}\{k\} > 0$ then the diffracted fields must decay exponentially as $r \to \infty$. At the wedge faces, the total fields satisfy the following boundary conditions:

$$\Phi|_{\theta=\pm\theta_{\mathrm{w}}} = \Psi|_{\bar{\theta}=\mp\bar{\theta}_{\mathrm{w}}}, \quad \left.\frac{\partial \Phi}{\partial \theta}\right|_{\theta=\pm\theta_{\mathrm{w}}} = \lambda \left.\frac{\partial \Psi}{\partial \bar{\theta}}\right|_{\bar{\theta}=\mp\bar{\theta}_{\mathrm{w}}}, \quad (4.3)$$

where $\lambda = \frac{\mu_1}{\mu_2}, \ \frac{\epsilon_1}{\epsilon_2}$ for the electric-polarised and magnetic-polarised cases respectively. Our formulation is very similar to this one (which we discussed in detail in

Section 1.2) and only differs by the extra coordinate system that we keep for consistency with (Rawlins, 1999). Later in the paper, Rawlins specified the E-polarised case with a perfect dielectric wedge (i.e. $\lambda = 1$).

His method used the Kontorovich-Lebedev transform and a conversion to the associated diffusion problem by replacing k with $i\kappa$. Application of the boundary conditions and several integral results created a system of singular FIE's of the second kind to determine four unknown functions. It is assumed that these four functions can be written as an infinite Neumann series of the form,

$$G(\sigma) = \sum_{m=0}^{\infty} G^{(m)}(\sigma) \left(1 - \frac{1}{n^2}\right)^m, \tag{4.4}$$

valid for $\left|1 - \frac{1}{n^2}\right| < 1$. The FIE's were solved by iteration using this Neumann series expansion and the first two terms were determined to create a first-order approximation. While it is theoretically possible to obtain higher order coefficients, the process is quite algebraically intensive and even Rawlins acknowledged that this can be tedious to obtain. The results were substituted into the general solution and replacing κ with $-ik$ converted back into the diffraction problem.

Final solution and graphical results The result was then used to calculate near-field, far-field and total field approximations, the latter of which is the following:[2]

$$\begin{aligned}\Phi(r,\theta) = \Phi_{\mathrm{I}}(r,\theta) + \frac{1}{8}\left(1 - \frac{1}{n^2}\right) \Bigg[&\left[\cot(\bar{\theta}_{\mathrm{w}} + \theta_{\mathrm{I}}) + \cot(\bar{\theta}_{\mathrm{w}} - \theta_{\mathrm{I}})\right] K(\theta - \theta_{\mathrm{I}}) \\ &+ \frac{J(\theta - \theta_{\mathrm{I}}) - J(\theta + \theta_{\mathrm{I}} + 2\bar{\theta}_{\mathrm{w}})}{2\sin^2(\bar{\theta}_{\mathrm{w}} + \theta_{\mathrm{I}})} - \frac{J(\theta - \theta_{\mathrm{I}}) + J(2\bar{\theta}_{\mathrm{w}} - \theta_{\mathrm{I}} - \theta)}{2\sin^2(\bar{\theta}_{\mathrm{w}} - \theta_{\mathrm{I}})} \Bigg] \\ &+ O\left(\left(1 - \frac{1}{n^2}\right)^2\right),\end{aligned} \tag{4.5}$$

[2]Note that the equation for Ψ has suspected typographical errors that are corrected here.

$$\Psi(r,\bar{\theta}) = \Phi_{\mathrm{I}}(r,\theta\left(\bar{\theta}\right)) + \frac{1}{8}\left(1-\frac{1}{n^2}\right)\Bigg[\cot(\bar{\theta}_{\mathrm{w}}+\theta_{\mathrm{I}})K(\pi+\theta_{\mathrm{I}}-\bar{\theta}) + \cot(\bar{\theta}_{\mathrm{w}}-\theta_{\mathrm{I}})K(\pi-\theta_{\mathrm{I}}+\bar{\theta}) - 4ikr\cos(\theta\left(\bar{\theta}\right)-\theta_{\mathrm{I}})e^{-ikr\cos(\theta\left(\bar{\theta}\right)-\theta_{\mathrm{I}})} - \frac{J(\pi+\theta_{\mathrm{I}}-\bar{\theta})+J(2\bar{\theta}_{\mathrm{w}}-\pi+\theta_{\mathrm{I}}+\bar{\theta})}{2\sin^2(\bar{\theta}_{\mathrm{w}}+\theta_{\mathrm{I}})} - \frac{J(\pi-\theta_{\mathrm{I}}+\bar{\theta})+J(2\bar{\theta}_{\mathrm{w}}-\pi-\theta_{\mathrm{I}}-\bar{\theta})}{2\sin^2(\bar{\theta}_{\mathrm{w}}-\theta_{\mathrm{I}})}\Bigg] + O\left(\left(1-\frac{1}{n^2}\right)^2\right), \tag{4.6}$$

where $\theta\left(\bar{\theta}\right) = \bar{\theta} - \mathrm{sgn}\left(\bar{\theta}\right)\pi$ and the two functions $K(\psi)$ and $J(\psi)$ take the form,

$$K(\psi) = \frac{\partial J(\psi)}{\partial\psi}, \quad J(\psi) = \int_{-i\infty}^{i\infty}\frac{\sin(\psi v)}{\sin(\pi v)}e^{\frac{i\pi v}{2}}H_v^{(1)}(kr)\mathrm{d}v, \quad |\psi| \le \frac{3\pi}{2}. \tag{4.7}$$

To use the full ranges of the angular variables θ, θ_{w} and θ_{I}, the integrals (4.7) will need to be valid for the extended range $-3\pi < \psi < 3\pi$. To do this, Rawlins asymptotically approximated the integrals as $kr \to \infty$ using the method of stationary phase. This produced the following approximation for $J(\psi)$ in terms of the complementary error function,

$$J(\psi) \sim 4[\mathcal{H}(\psi-\pi)-\mathcal{H}(-\psi-\pi)]e^{-ikr\cos(\psi)} + 2e^{-ikr\cos(\psi)}\mathrm{sgn}\left(\cos\left(\psi/2\right)\right)\sin\left(\psi/2\right)\mathrm{erfc}\left(e^{-\frac{i\pi}{4}}\sqrt{kr(1+\cos(\psi))}\right), \tag{4.8}$$

where $\mathcal{H}(z)$ is the Heaviside function and $\mathrm{erfc}(z)$ is the complementary error function given by,

$$\mathrm{erfc}(z) = \frac{2}{\sqrt{\pi}}\int_z^\infty e^{-v^2}\mathrm{d}v. \tag{4.9}$$

A similar expression for $K(\psi)$ can be obtained by differentiating $J(\psi)$.

Near the end of (Rawlins, 1999) were several graphical results using a wide range of incident and wedge angles. As an example, we shall replicate figures 2 and 5 in Figure 4.2 using equations (4.5) and (4.6) with the far-field approximation (4.8).

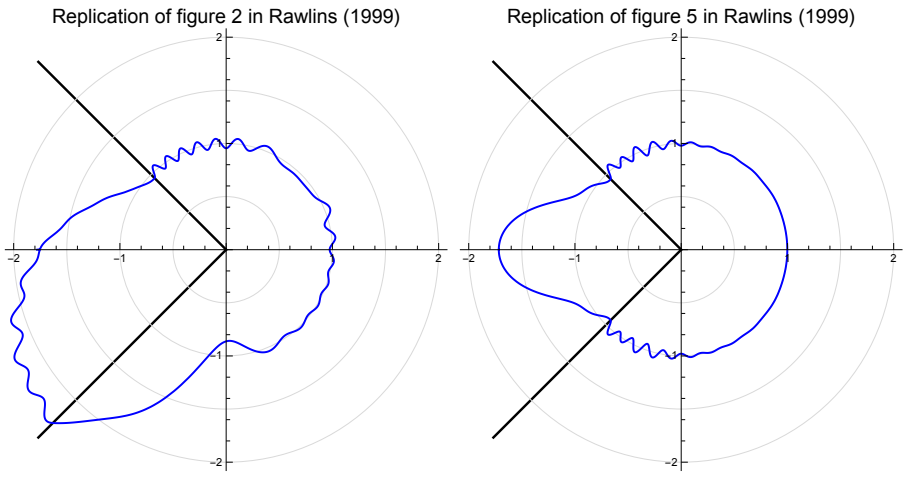

Figure 4.2: Replication of figures in Rawlins (1999) using formulae (4.5) and (4.6) with the approximation (4.8) and the parameter values $kr = 10\pi$, $n = 1.05$ and $\bar{\theta}_{\mathrm{w}} = \frac{\pi}{4}$. The left (resp. right) figure recreates figure 2 (resp. 5) with incident angle $\theta_{\mathrm{I}} = \frac{\pi}{2}$ (resp. 0).

Critical analysis In summary, Rawlins (1999) detailed an effective method for low contrast penetrable wedge problems, although it is very algebraically intensive for even the perfect dielectric case. While in principal it is possible to obtain higher order coefficients, the process will be tedious for larger orders. The final equations to create Figure 4.2 are easy to use and fast computationally. If we compare these formulae with the figures in Rawlins (1977), we find that the result for the exterior solution (4.5) is in agreement but (4.6) is not.

This discrepancy can be explained by (4.6) algebraically growing in kr. Rawlins stated that the choice of kr in his figures was a compromise. It had to be large enough for asymptotic values to be valid (see (4.8)) but it could not be too large because the term,

$$-\frac{1}{2}\left(1-\frac{1}{n^2}\right) ikr\cos(\theta-\theta_{\mathrm{I}})e^{-ikr\cos(\theta-\theta_{\mathrm{I}})},$$

in (4.6) grows algebraically. This term came from expanding $e^{-iknr\cos(\theta-\theta_{\mathrm{I}})}$ in powers of $\left(1-\frac{1}{n^2}\right)$ which was necessary for the boundary conditions at the wedge faces to be satisfied to first order.

Overall, the expansion obtained is a regular perturbation expansion which is clearly only valid with $kr\left(1-\frac{1}{n^2}\right)$ small. It is finally stated that a singular perturbation approach with multiple scales may be more appropriate. This work was extended in Salem et al. (2006) for line source incidence and compared with finite difference frequency domain simulations.

4.2 Diffraction by a highly contrast transparent wedge, (Lyalinov, 1999)

In his research portfolio, Lyalinov has studied various diffraction problems including impedance wedges (Lyalinov and Zhu, 2006; Babich et al., 2007), cones (Lyalinov, 2011; Lyalinov and Zhu, 2013) and plane angle sectors (Lyalinov, 2013a,b, 2015), however we shall follow his research on high-contrast wedge diffraction.

In Lyalinov (1999), he defined the problem from a mathematical perspective while acknowledging the same physical settings as we do in Section 1.1. He also used the same wedge region definitions as previously defined (1.33).[3] A key component of the paper is the contrast parameter λ which is defined in the same way as (1.48),

$$\lambda = \underbrace{\frac{\rho_1}{\rho_2}}_{\text{acoustic}}, \quad \underbrace{\frac{\mu_1}{\mu_2}}_{\text{E-pol}}, \quad \text{or} \quad \underbrace{\frac{\epsilon_1}{\epsilon_2}}_{\text{H-pol}}. \tag{4.10}$$

The aim of the paper was to develop an asymptotic scheme for when this contrast parameter is small ($\lambda \ll 1$). Another important parameter is the wavenumber ratio (otherwise written as the ratio of refractive indexes) $\lambda_k = k_1/k_2 \in (0,1)$ which is treated independently from λ.

[3] We should note that Lyalinov restricts the wedge angle to $\frac{\pi}{2} < \theta_{\text{w}} < \pi$.

Formulation and method Lyalinov assumed and suppressed the time dependence, $e^{-i\omega t}$ and considered plane wave excitation, $\Phi_{\mathrm{I}} = e^{-ik_1 r\cos(\theta-\theta_{\mathrm{I}})}$ where $0 \leq \theta_{\mathrm{I}} \leq \theta_{\mathrm{w}}$. The total wave fields, Φ and Ψ satisfy the following problem in the host (Ω_1 with $k = k_1$) and scatterer (Ω_2 with $k = k_2$) regions respectively,

$$\begin{cases} \nabla^2\Upsilon + k^2\Upsilon = 0 & \text{(Governing equation)}, \quad (4.11a) \\ \Upsilon_{\mathrm{Diff}} \underset{kr\to\infty}{=} \dfrac{e^{ikr}}{\sqrt{kr}}\left(C(\theta) + O\left(\dfrac{1}{kr}\right)\right) & \text{(Radiation condition)}, \quad (4.11b) \\ \Upsilon \underset{r\to 0}{=} \text{constant} + O\left(r^{\hat{\delta}}\right), \quad \hat{\delta} > 0 & \text{(Edge condition)}, \quad (4.11c) \end{cases}$$

where $\Upsilon_{\mathrm{Diff}} = \Upsilon - \Upsilon_{\mathrm{GO}}$. The total fields are connected by the interface conditions on the wedge faces,

$$\Phi|_{\theta=\pm\theta_{\mathrm{w}}} = \Psi|_{\theta=\pi\mp\bar{\theta}_{\mathrm{w}}}, \quad \left.\frac{\partial\Phi}{\partial\theta}\right|_{\theta=\pm\theta_{\mathrm{w}}} = \lambda \left.\frac{\partial\Psi}{\partial\theta}\right|_{\theta=\pi\mp\bar{\theta}_{\mathrm{w}}}, \tag{4.12}$$

Note that in the special limiting case where $\lambda \to 0$, the problem reduces to the perfect wedge problem with Neumann boundary conditions. Lyalinov stated that $\hat{\delta}$ in (4.11c) is the smallest positive root of

$$\cot(\hat{\delta}\theta_{\mathrm{w}}) - \lambda\cot(\hat{\delta}\bar{\theta}_{\mathrm{w}}) = 0, \tag{4.13}$$

where for small λ, the solution for $\hat{\delta}$ is approximately,

$$\hat{\delta} = \frac{\pi}{2\theta_{\mathrm{w}}} - \frac{1}{2}\lambda\sin\left(\frac{\pi}{\theta_{\mathrm{w}}}\right) + O(\lambda^2). \tag{4.14}$$

This means that $\hat{\delta} < \delta = \frac{\pi}{2\theta_{\mathrm{w}}}$ when $\theta_{\mathrm{w}} \in \left(\frac{\pi}{2}, \pi\right)$ and λ is sufficiently small, implying that the edge singularity is stronger than the impenetrable case. However, we believe that these last two equations are somewhat erroneous because they do not match with ours (see (1.57) from the introduction and equations (2.12) and (2.13) in Nethercote et al. (2019a) given in the next chapter). Evidence of our validity over Lyalinov can be shown by considering table 5.1 of Van Bladel (2006), which is a table of values for the singularity exponent $\hat{\delta}$ in the dielectric wedge case.

Numerical solutions of (4.13) are inconsistent with these values whereas numerical solutions of (1.57) are.[4]

Lyalinov sought a general solution for the total fields in the form of a Sommerfeld integral (see Nethercote et al. (2019b), Section 2 for definition). These two Sommerfeld integrals were connected by a mapping equating the exponential argument[5],

$$\beta(\alpha) = \cos^{-1}\left(\lambda_k \cos(\alpha)\right), \quad \alpha(\beta) = \cos^{-1}\left(\frac{1}{\lambda_k}\cos(\beta)\right). \tag{4.15}$$

Both $\beta(\alpha)$ and $\alpha(\beta)$ have branch cuts defined such that;

- $f(-z) = -f(z)$
- $f(z^*) = (f(z))^*$
- $f(z + n\pi) = f(z) + n\pi$ for all $n \in \mathbb{Z}$
- $f(z) \sim z$ as $\mathrm{Im}\{z\} \to \pm\infty$
- $f\left(\frac{\pi}{2} + iy\right) = \frac{\pi}{2} + i\hat{f}(y)$ where $y, \hat{f} \in \mathbb{R}$.

Figure 4.3 illustrates the complex functions $\beta(\alpha)$ and $\alpha(\beta)$, including their branch cuts. These mappings are very important to define correctly and will be discussed in more detail in a later chapter.

The mappings (4.15) allowed the use of Malyuzhinets theorem which reduced the problem to a pair of coupled Malyuzhinets equations. Lyalinov sought to solve for the spectral functions asymptotically as $\lambda \to 0$ by an asymptotic scheme of the form,

$$f = f^{(0)} + \lambda f^{(1)} + \lambda^2 f^{(2)} + ... \tag{4.16}$$

[4]We also believe (4.14) is incorrect because upon substitution into (4.13), it does not satisfy it to order $O(\lambda)$ as intended and there is further evidence in the half-space case (where $\theta_\mathrm{w} = \frac{\pi}{2}$) because we should have $\hat{\delta} = 1$ but (4.14) implies $\hat{\delta} = 1 - \frac{1}{2}\lambda\sin(2) + O(\lambda^2)$ instead.

[5]This particular mapping has appeared in several wedge-themed publications including (Larsen, 1981; Budaev, 1995; Budaev and Bogy, 1999).

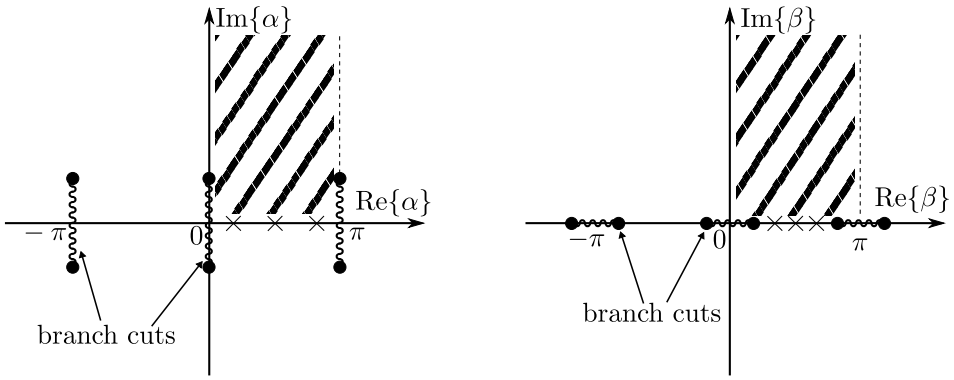

Figure 4.3: This is a simplified recreation of figure 3 in (Lyalinov, 1999) featuring the complex functions $\beta(\alpha)$ (left) and $\alpha(\beta)$ (right). The function $\beta(\alpha)$ maps the crosses and the shaded region on the left in the α complex plane onto the same on the right in the β complex plane ($\alpha(\beta)$ has the opposite effect).

Each of the terms in the asymptotic series were written in terms of integral operators which were obtained in appendix A in Lyalinov (1999).[6] These integral operators are defined to invert the difference operators in the coupled Malyuzhinets equations.

Final formulae and graphical results After the definition of the integral operators, Lyalinov assessed the singularities of the spectral functions and their roles in the total wave fields. This included geometrical optic components, the diffraction coefficient and lateral waves. The paper concluded with a uniform (with respect to θ) far-field approximation of the exterior solution Φ to leading order with only one side of the wedge illuminated by the incident wave, ($\pi - \theta_{\mathrm{w}} < \theta_{\mathrm{I}} < \theta_{\mathrm{w}}$),

[6]The derivation of these integral operators is highly influenced by Tuzhilin's theory of S-integrals (Tuzhilin, 1973).

and $\lambda \ll 1$,

$$\begin{aligned}\Phi(r,\theta) = {} & e^{-ik_1 r\cos(\theta-\theta_{\mathrm{I}})} F\left(\sqrt{2k_1 r}\cos\left(\frac{1}{2}(\theta-\theta_{\mathrm{I}})\right)\right) \\ & + R(\theta_{\mathrm{w}}-\theta_{\mathrm{I}}) e^{-ik_1 r\cos(\theta+\theta_{\mathrm{I}}-2\theta_{\mathrm{w}})} F\left(\sqrt{2k_1 r}\cos\left(\frac{1}{2}(\theta+\theta_{\mathrm{I}}-2\theta_{\mathrm{w}})\right)\right) \\ & + \left[\frac{1}{2\cos\left(\frac{1}{2}(\theta-\theta_{\mathrm{I}})\right)} + \frac{R(\theta_{\mathrm{w}}-\theta_{\mathrm{I}})}{2\cos\left(\frac{1}{2}(\theta+\theta_{\mathrm{I}}-2\theta_{\mathrm{w}})\right)} + s^{(\mathcal{N})}(\theta-\pi)\right. \\ & \left. - R(\pi-\theta_{\mathrm{w}}+\theta)s^{(\mathcal{N})}(\theta+\pi)\right] \frac{e^{ik_1 r+\frac{i\pi}{4}}}{(2\pi k_1 r)^{\frac{1}{2}}} + O(\lambda) + O\left(\frac{1}{(k_1 r)^{\frac{3}{2}}}\right). \quad (4.17)\end{aligned}$$

Here $R(z)$ is the reflection coefficient given by,

$$R(z) = \frac{\beta'(z)-\lambda}{\beta'(z)+\lambda} = 1 - \frac{2\lambda}{\beta'(z)+\lambda}, \quad (4.18)$$

and $F(z)$ is Lyalinov's definition of the Fresnel integral,

$$F(z) = \frac{e^{-\frac{i\pi}{4}}}{\sqrt{\pi}} \int_{-\infty}^{z} e^{iv^2}\mathrm{d}v = \frac{1}{2} + \frac{e^{-\frac{i\pi}{4}}}{\sqrt{2}} \int_{0}^{\sqrt{\frac{2}{\pi}}z} e^{\frac{i\pi}{2}\ v^2}\mathrm{d}v. \quad (4.19)$$

Although this approximation can be easily plotted, it is not uniform with respect to θ as claimed. This is because at the shadow boundary ($\theta = \theta_{\mathrm{I}} - \pi$) the two terms,

$$\frac{1}{2\cos\left(\frac{1}{2}(\theta-\theta_{\mathrm{I}})\right)} \quad \text{and} \quad R(\pi-\theta_{\mathrm{w}}+\theta)s^{(\mathcal{N})}(\theta+\pi)$$

have simple poles with residues that do not cancel out. To show this, Figure 4.4 displays two polar plots of the absolute value of (4.17) for different values of θ_{I}. We can clearly see in both plots, the formula (4.17) has a singularity at $\theta = \theta_{\mathrm{I}} - \pi$ hence is not uniform with respect to θ as claimed.

Critical analysis In conclusion, Lyalinov developed a powerful technique for diffraction of high-contrast wedges that theoretically could be used for a wide range of parameters, however, there are a few difficulties.

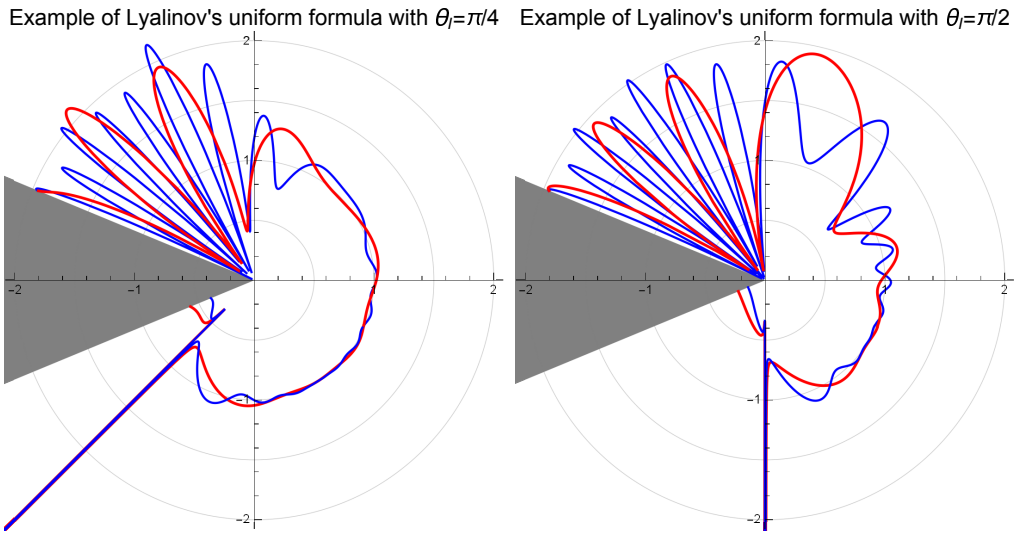

Figure 4.4: Absolute value of (4.17) at $k_1 r = 10$ (red) and 25 (blue) with $\theta_{\mathrm{I}} = \frac{\pi}{4}$ (left) and $\frac{\pi}{2}$ (right). Here we have $\theta_{\mathrm{w}} = \frac{7\pi}{8}$, $\lambda = \frac{1}{100}$ and $\lambda_k = \frac{1}{2}$.

The mapping (4.15) is a crucial step in obtaining the Malyuzhinets equations. When I first studied this mapping, I believed that it could be tricky to correctly define it for use in mathematical software (MATLAB etc.). In hindsight, it is certainly possible to do so efficiently and we discuss how in an appendix of Nethercote et al. (2019a)

It could also be difficult to use the integral operators in practice if we want to know the interior field or obtain higher order approximations due to their complexity, the mapping (4.15) and the large number of impactful singularities in each integrand.

It is important to have a better understanding of the spectral functions because this can lead to an improved uniform asymptotic formula compared to (4.17). Apart from the pole issue, this formula appears to work well and we shall use it again later as a means of comparison.

Defining the edge conditions correctly will also be important for determining the asymptotic behaviour of each term in the recurrence relation. This could aid

us in the creation of an accurate near-field approximations.

We believe it will be simpler to define the high-contrast iteration scheme before applying the S-M technique. This will split the penetrable wedge problem into an infinite set of impenetrable wedge problems.

It should be noted that Davis (1996) considered acoustic line-source diffraction by a high-contrast penetrable wedge. Here Davis split the problem into symmetric and antisymmetric parts, utilised Green's function integrals and created a high-contrast asymptotic scheme assuming that the density of the host is much bigger than that of the wedge scatterer ($\lambda \to \infty$) instead.

4.3 On Waves Excitation in a Wedge-Shaped Region (Shanin, 1996)

Much of Shanin's research is in the application of the embedding formulae to various geometries to find diffraction coefficients e.g. rational wedges (Craster and Shanin, 2005). In this section, we will follow his earlier work where he used the Wiener-Hopf (W-H) technique for diffraction in angular regions (Shanin, 1996, 1998) which influenced Section 3 of Nethercote et al. (2019b). These papers are different to the others in this chapter because the formulation is not a conventional penetrable wedge problem.

Formulation and method Shanin (1996) considered a single angular region $\Gamma_1 = \{(r,\theta) : \ 0 \leq r < \infty, \ 0 \leq \theta \leq \theta_{\rm w}\}$ with an interior angle $0 < \theta_{\rm w} < \pi$ where the excitation source is in the form of inhomogeneous impedance forcing on the wedge boundaries. With the assumption that the time dependence is $e^{i\omega t}$, he defined Φ as the total field satisfying the homogeneous Helmholtz equation in Γ_1 with wavenumber k. This wavenumber is assumed to have a small negative

imaginary increment. Note that Shanin (1996) did not define an edge or a radiation condition for Φ to satisfy. The source of the problem is impedance boundary conditions on $\theta = 0$ and θ_w with the forcing terms $f_1(r)$ and $f_2(r)$, respectively,

$$\frac{1}{ik}\frac{\partial \Phi}{\partial \boldsymbol{n}} - \sin(\varphi)\Phi = f_{1,2}(r), \tag{4.20}$$

where $\mathrm{Re}\{\varphi\} \in (0, \pi/2]$ is constant and $\boldsymbol{n}$ is the inward pointing normal to the boundary.

Shanin decomposed the problem into symmetric (subscript "s") and antisymmetric (subscript "a") components. The symmetric part $\Phi_\mathrm{s}(r,\theta) = \frac{1}{2}(\Phi(r,\theta) + \Phi(r,\theta_\mathrm{w}-\theta))$ has $f_\mathrm{s}(r) = \frac{1}{2}(f_1(r)+f_2(r))$ as both forcing terms in (4.20), whereas the antisymmetric part $\Phi_\mathrm{a}(r,\theta) = \frac{1}{2}(\Phi(r,\theta)-\Phi(r,\theta_\mathrm{w}-\theta))$ has $\pm f_\mathrm{a}(r) = \frac{1}{2}(f_1(r)-f_2(r))$ as forcing terms for $\theta = 0$ and θ_w, respectively.

For each component, Green's second identity in Γ_1 alongside the following variation of the Laplace transform,

$$G(\eta) = \int_0^\infty g(r)e^{-ikr\eta}\mathrm{d}r, \quad g(r) = \frac{k}{2\pi}\int_{-\infty-0i}^{\infty+0i} G(\eta)e^{ikr\eta}\mathrm{d}\eta, \tag{4.21}$$

produced a single W-H equation. Solving this equation was achieved in a similar way to Section 3 of Nethercote et al. (2019b) with the aid of Cauchy's integral formula and an alternate mapping of the form,

$$\eta(\alpha) = \cos\left(\frac{2\theta_\mathrm{w}}{\pi}\cos^{-1}\left(\sqrt{\alpha}\right)\right) = \cos\left(\frac{\theta_\mathrm{w}}{\pi}\cos^{-1}\left(2\alpha-1\right)\right). \tag{4.22}$$

The Malyuzhinets problem and relation to Sommerfeld integrals Shanin tested this method by choosing $f_{1,2}(r)$ such that (4.20) symbolically represented the homogeneous impedance boundary conditions otherwise known as the Malyuzhinets problem. This meant that

$$\begin{aligned} f_1(r) &= \left(-\frac{1}{ikr}\frac{\partial \Phi_I}{\partial \theta} + \sin(\varphi)\Phi_I\right)\Big|_{\theta=0}, \\ f_2(r) &= \left(\frac{1}{ikr}\frac{\partial \Phi_I}{\partial \theta} + \sin(\varphi)\Phi_I\right)\Big|_{\theta=\theta_\mathrm{w}}, \end{aligned} \tag{4.23}$$

where $\Phi_I = e^{ikr\cos(\theta-\theta_I)}$ and $\theta_I \in (0, \theta_\mathrm{w}/2]$. Following this method, he obtained a formula for the Laplace transform of the scattered field and finished by constructing a relation between this solution and the spectral function of Sommerfeld integrals. The Sommerfeld representation he used is equivalent to,

$$\Phi(r,\theta) = \frac{1}{2\pi i}\int_C e^{ikr\cos(z)}\left[s(\theta+z) - s(\theta-z)\right]\mathrm{d}z, \tag{4.24}$$

where C is defined as the U-shaped contour running from $\frac{3\pi}{2} + i\infty$ to $-\frac{\pi}{2} + i\infty$,[7] and the relation between the Laplace transform of the total field $U(\cos(z), 0)$ and the spectral function $s(z)$ is[8]

$$s(z) = \frac{k}{2i}(\sin(z) + \sin(\varphi))U(\cos(z), 0). \tag{4.25}$$

This formula can be found using the same strategy to obtain equation (3.21) in Nethercote et al. (2019b). If we set $\varphi = 0$ as well, then the solution should be the problem with homogeneous Neumann boundary conditions. This solution is given as

$$s(z) = \frac{\pi}{2\theta_\mathrm{w}}\left[\frac{\sin(\pi z/\theta_\mathrm{w})}{\cos(\pi z/\theta_\mathrm{w}) - \cos(\pi\theta_\mathrm{I}/\theta_\mathrm{w})}\right]. \tag{4.26}$$

However, when we compare the above with our previous solution (3.42) of Nethercote et al. (2019b) (accounting for the change in geometry and parameter definitions), we find that (3.42) $= -2 \times$ (4.26).[9]

The extension paper (Shanin, 1998) reused this method but there were a few changes. The more significant of these were: the problem was not split into symmetric and antisymmetric parts; the factorisations were defined differently and the mapping (4.22) was changed to $\eta(\alpha) = \cos\left(\frac{\theta_\mathrm{w}}{\pi}\cos^{-1}(\alpha)\right)$. He also briefly discussed

[7] This contour is equivalent to the conjugate of γ_- (see Nethercote et al. (2019b) Section 2).

[8] In Shanin's version of (4.25) the wavenumber is in the denominator instead. We believe that this is a typographical error.

[9] We are not certain if this discrepancy is due to an error in the paper or in our interpretation of it.

the case where $\theta_w > \pi$ and quickly pointed out that this requires the whole angular domain to be split into two via some intermediate angle which created two coupled W-H equations to solve. The rest of this paper discussed the special case where $\theta_w = \pi/m$, $m \in \mathbb{Z}$ using a reflection procedure.

Critical analysis Overall, Shanin developed a simple method to obtain functional equations of the W-H type for angular regions and found a highly theoretical but effective way to allow the application of the W-H technique. There are potential improvements to be made though.

Splitting the problem into symmetric and antisymmetric parts is not very advantageous because it creates two problems that are not much simpler than the original. The mapping $\alpha = \cos(\pi z/\theta_w)$, although underemphasised in Shanin (1998), is likely to be a better fit for its purpose. Some of the factorisations and integral formulae given are generally difficult to use practically. However, it is possible that certain special cases can be evaluated analytically such as the case (4.23) described earlier.

4.4 The Wiener-Hopf Solution of the Isotropic Penetrable Wedge Problem: Diffraction and Total Field (Daniele and Lombardi, 2011)

Many recent publications using the Wiener-Hopf (W-H) technique for wedge diffraction have been authored (or co-authored) by Daniele. As previously mentioned in Nethercote et al. (2019b), papers such as (Daniele, 2003a,b) (where the W-H technique was applied to impenetrable wedge problems) helped to prove that this technique was more versatile than previously thought. Since then, Daniele and Lombardi have worked to extend the technique to include skew incidence (Daniele

and Lombardi, 2006) or more complicated geometries (Daniele et al., 2018).

For their research with penetrable wedges, almost all components can be traced back to earlier publications, leading to the subject of this section (Daniele and Lombardi, 2011) which presented the diffraction problem with an electromagnetic plane wave at skew incidence. This paper was an extension of (Daniele, 2010) and the companion paper (Daniele, 2011) in which the incident wave was electric-polarised and had no skew incidence. To keep this review brief, we will formulate this simpler problem and recreate some of the final plots of Daniele and Lombardi (2011). In all their papers, they assumed that the problem is time-harmonic with the time factor $e^{i\omega t}$ and frequency ω.

Formulation and method In their formulation, the penetrable wedge is immersed in free-space with the relative permittivity ϵ_r and the free space parameters $\epsilon_1 = \epsilon$, $\mu_1 = \mu$ and $k_1 = k = \omega\sqrt{\mu\epsilon}$. The wavenumber k was assumed to have a small negative imaginary part. For the specified electric-polarised case, the definition of the incident wave was given as $E_{z\mathrm{I}} = E_0 e^{ikr\cos(\theta-\theta_\mathrm{I})}$, where we will set $E_0 = 1$ for the test cases in Daniele and Lombardi (2011). There were four angular regions in this problem, separated by the half lines $\theta = 0,\ \pm\theta_\mathrm{w}$ and π. Figure 4.5 illustrates these angular regions and their associated parameters.

Daniele created a system of W-H equations comprising of two Laplace transforms of the electromagnetic components E_z and $H_r = \frac{1}{i\omega\mu}\frac{\partial E_z}{\partial\theta}$,

$$V(\eta,\theta) = \int_0^\infty E_z(r,\theta)e^{i\eta r}\mathrm{d}r, \quad I(\eta,\theta) = \int_0^\infty H_r(r,\theta)e^{i\eta r}\mathrm{d}r. \tag{4.27}$$

The W-H equations were derived from the same type of procedure as appendix A in Daniele (2003a) using an oblique coordinate system. This W-H system is simplified using mappings of the form

$$\eta(\alpha_j) = -k_j\cos\left(\frac{\Theta_j}{\pi}\cos^{-1}\left(-\frac{\alpha_j}{k_j}\right)\right), \quad j = 1,2, \tag{4.28}$$

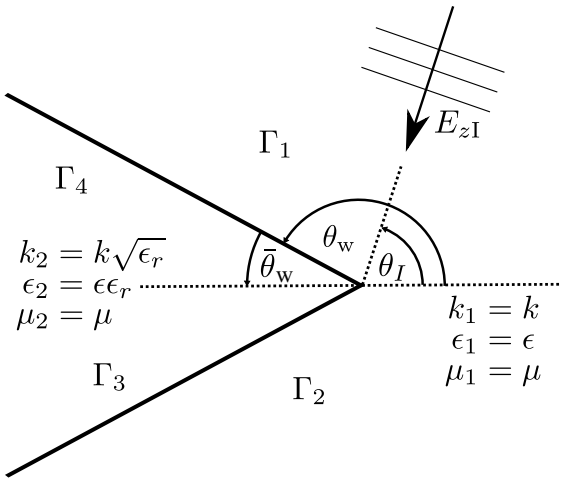

Figure 4.5: In this diagram, $\Gamma_1 - \Gamma_4$ are the angular regions $\theta \in [0, \theta_{\mathrm{w}})$, $\theta \in [-\theta_{\mathrm{w}}, 0)$, $\theta \in [-\pi, -\theta_{\mathrm{w}})$ and $\theta \in [\theta_{\mathrm{w}}, \pi)$ respectively. The two regions Γ_1 and Γ_2 have the parameters of free space: $k_1 = k$, $\epsilon_1 = \epsilon$ and $\mu_1 = \mu$. The other two regions, Γ_3 and Γ_4, have the parameters: $k_2 = k\sqrt{\epsilon_r}$, $\epsilon_2 = \epsilon\epsilon_r$ and $\mu_2 = \mu$.

where $\Theta_1 = \theta_{\mathrm{w}}$, $\Theta_2 = \bar{\theta}_{\mathrm{w}}$ and the inverse cosine branch is defined such that $\cos^{-1}(-z) = -\pi - \cos^{-1}(z)$. Further simplification is achieved by factorising several components in the α_j-planes. This leads to a simplified system of W-H equations,

$$\begin{aligned} Y_j(\alpha_j) &= X_j(\alpha_j) + (-1)^j \frac{k_j + \alpha_j}{(k_j^2 - \alpha_j^2)^{\frac{1}{2}}} \hat{X}_j(\alpha_j), \\ Y_{j+2}(\alpha_j) &= X_{j+2}(\alpha_j) + (-1)^j \frac{k_j + \alpha_j}{(k_j^2 - \alpha_j^2)^{\frac{1}{2}}} \hat{X}_{j+2}(\alpha_j), \end{aligned} \tag{4.29}$$

where $j = 1$ or 2. Here each Y_j represents one of the Laplace transforms to be found and the functions X_j and $\hat{X}_j$ are combinations of various transforms of the unknown boundary data.

A Fredholm factorisation method (which was discussed in great detail in section 3 of Daniele and Lombardi (2007)) applied to the W-H system (4.29) completes

the W-H technique,

$$Y_j(\alpha_j) = \frac{i(-1)^j}{2\pi}\text{P.V.}\int_{-\infty}^{\infty}\left(\frac{k_j+\beta}{(k_j^2-\beta^2)^{\frac{1}{2}}}-\frac{k_j+\alpha_j}{(k_j^2-\alpha_j^2)^{\frac{1}{2}}}\right)\frac{\hat{X}_j(\beta)}{\beta-\alpha_j}\mathrm{d}\beta+\frac{R_j}{\alpha_j-\alpha_0},$$
$$Y_{j+2}(\alpha_j) = \frac{i(-1)^j}{2\pi}\text{P.V.}\int_{-\infty}^{\infty}\left(\frac{k_j+\beta}{(k_j^2-\beta^2)^{\frac{1}{2}}}-\frac{k_j+\alpha_j}{(k_j^2-\alpha_j^2)^{\frac{1}{2}}}\right)\frac{\hat{X}_{j+2}(\beta)}{\beta-\alpha_j}\mathrm{d}\beta+\frac{R_{j+2}}{\alpha_j-\alpha_0}, \tag{4.30}$$

where P.V. indicates the Cauchy principal value, $\alpha_0 = -k\cos\left(\frac{\pi}{\theta_\text{w}}\theta_\text{I}\right)$ and $R_2 = R_4 = 0$. Pieced together with (4.29), this constructs a system of four FIE's of the second kind.

The integration contours of the FIE system are deformed to straight lines connecting the two points $\alpha_j = \pm ik_j$ which has the parametrisation,

$$\alpha_j(u_j) = -k_j\cos\left(-\frac{\pi}{2}+iu_j\right). \tag{4.31}$$

This deformation is aimed to enhance the convergence of the FIE's. The next step is define a mapping $u_2 = u_2(u_1)$ by equating $k_2\cos\left(\frac{\bar{\theta}_\text{w}}{2}+\frac{i\bar{\theta}_\text{w}}{\pi}u_2\right) = k_1\cos\left(\frac{\theta_\text{w}}{2}+\frac{i\theta_\text{w}}{\pi}u_1\right)$.[10] This mapping created connection formulae between the unknown boundary data transforms, hence reducing the system to four equations with four unknowns; X_1, $\hat{X}_1$, X_3 and $\hat{X}_3$. The system is solved numerically using a combination of uniform sampling on the contour and a quadrature scheme.

Apparently because the kernels of the FIE's have well-suited behaviour, this method yields stable and accurate numerical solutions. However this only allows us to assemble solutions for $\{V,I\}(-k_1\cos(z_1),0)$ (resp. $\{V,I\}(-k_2\cos(z_2),\pi)$) in a local strip $-\theta_\text{w} \leq \text{Re}\{z_1\} \leq 0$ (resp. $-\bar{\theta}_\text{w} \leq \text{Re}\{z_2\} \leq 0$).[11] Analytic continuation to wider regions is possible through recursive relations derived from symmetry in the W-H equations.

[10] This mapping is similar to (4.15) but the branch choice is defined differently (see appendix II in Daniele and Lombardi (2011)).

[11] Here $\{V,I\}$ is shorthand notation for V or I.

A uniform geometrical theory of diffraction (UTD) approximation of the total wave field is then obtained in terms of these Laplace transforms. This method was validated using four test cases varying the wedge angle, incident angle and relative permittivity. We shall use plot data of the UTD approximation kindly provided by the authors to illustrate some of their results. Figure 4.6 displays two of the test cases by recreating figures 13 and 16a from (Daniele and Lombardi, 2011).

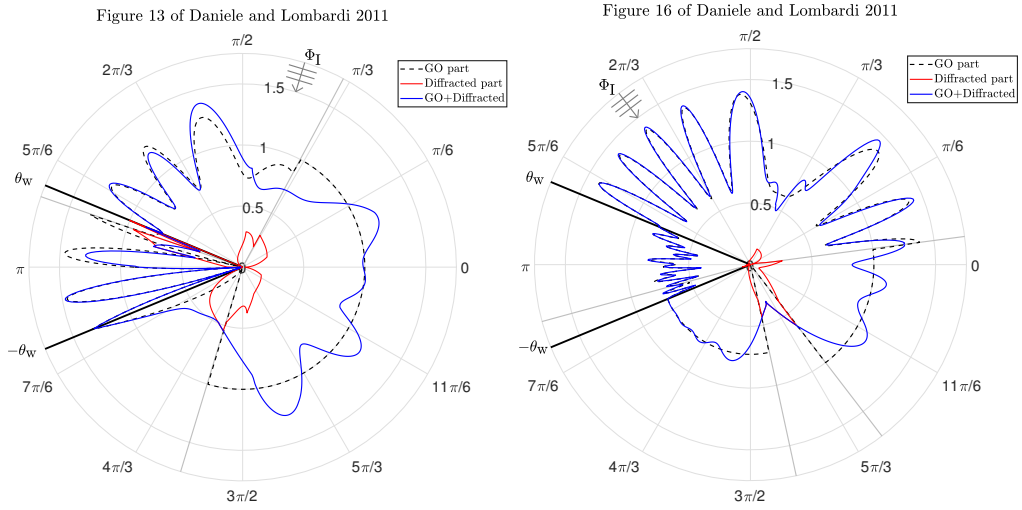

Figure 4.6: Replication of the figure from (Daniele and Lombardi, 2011) using plot data provided by the authors. This plot data includes the GO component, the diffracted component and the UTD approximation. The left plot is a replication of figure 13 with the parameters, $\theta_w = 7\pi/8$, $\theta_I = 13\pi/32$, $\epsilon_r = 3$ and $kr = 10$ and the right is a plot figure 16a with parameters, $\theta_w = 7\pi/8$, $\theta_I = 17\pi/24$, $\epsilon_r = 2$ and $kr = 10\pi$. The grey lines indicate GO discontinuities.

Although there are a couple of places in these plots where the total field does not appear to be continuous or smooth (for example, in Figure 4.6 (left), see $\theta \approx \frac{11\pi}{24}$ or $\frac{11\pi}{12}$), the numerical results appear to be accurate.

Critical analysis To conclude this review, Daniele and Lombardi tackled a very general penetrable wedge diffraction problem and utilised the W-H technique to form a system of FIE's, which was solved numerically by using simple quadrature

schemes. Doing so has greatly shown the versatility of the W-H technique.

Their chosen method of obtaining each of the W-H equations via oblique co-ordinate systems (Daniele, 2003a) is based on the characteristic Green's function procedure (Felsen and Marcuvitz, 1994). Our preference is for a quicker procedure based on Green's second identity instead (see Shanin (1996); Nethercote et al. (2019b)).

There are a numerous mappings used for both the W-H technique and the reduction of the FIE's. These mappings are important and they can be difficult to define correctly. It may be better to define Laplace transforms of the form (4.21) with the wavenumber and exclude it from (4.28).

The quadrature scheme seems to be remarkably accurate despite its simplicity. At the points in Figure 4.6 where the plots are not smooth, the loss of precision is attributed to the non-smooth behaviour of the mapping between u_1 and u_2. One does also question the extent of the schemes stability and what parameter cases, if any, does it fail? The performance of the scheme also seems to be remarkable as the full implementation is reported to take less than five minutes on a low performance CPU. Because of the wide range of aspects required, we have not reproduced the code to implement this scheme in our studies. As we do not have access to the original code, then we have not been able to make our own plots for comparison.

Of all the methods reviewed in this chapter, this one has the least parameter restriction and has been shown to be applicable to a large number of different diffraction problems. Many of these problems including waveguide and wedge scatterers were discussed in Daniele and Zich (2014). There have been recent efforts to extend this procedure even further to more complex geometries by viewing the complicated domains as a network of angular and layered domains (Daniele et al., 2017c). This means that similar procedures could be applied to more complex

geometries such as a wedge on a dielectric slab (Daniele et al., 2017a,b) or multiple wedges (Daniele et al., 2018).

4.5 Summary and comparison

To summarise the chapter, we have reviewed the literature surrounding the penetrable wedge diffraction problem. We have concentrated on four variations of the problem and the different techniques to solve them. We have also given a critical analysis of each method and pointed out some strengths and weaknesses.

All these methods are quite theoretical and because some have strict conditions, it is difficult to make a direct comparison between them. For example, Rawlins' approximation requires a highly transparent wedge, whereas Lyalinov's requires a highly opaque wedge instead. While Shanin does not have answers for the penetrable wedge problem, the ideas in his methodology can be extended to such problems. Daniele's technique seems to be the most extendable and has the least parameter restriction. However, the difficulty in creating the required code scripts restricts the ability to thoroughly compare.

Another means of comparison is graphical. It is important to note that Daniele and Lombardi provided us with figure data from (Daniele and Lombardi, 2011), so we are restricted to their test cases. In all of these test cases the contrast parameter (4.10) is unity, hence Lyalinov's formulae will not converge. We also are not able to compare (Shanin, 1996) with the others because technically it is not a penetrable wedge problem. We can however, recreate figure 3 of Daniele and Lombardi (2011) and compare with the final formulae of Rawlins (1999). Figure 4.7 illustrates this comparison with the parameters $\theta_{\mathrm{w}} = 3\pi/4$, $\theta_{\mathrm{I}} = \pi/8$, $\epsilon_r = 3$ and $kr = 10$.

One can easily see that Rawlins' approximation is not very good inside the

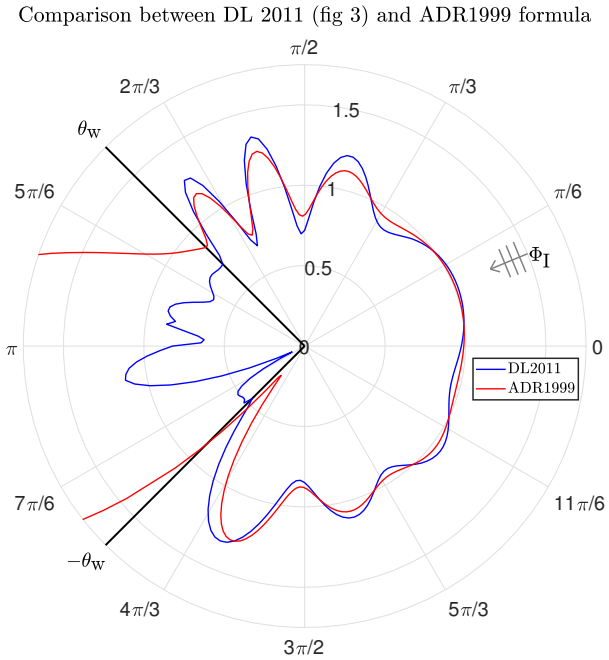

Figure 4.7: Comparison of the UTD approximation plot data of figure 3 from (Daniele and Lombardi, 2011) with the formulae (4.5) and (4.6) of (Rawlins, 1999). Here we have the parameters, $\theta_{\mathrm{w}} = 3\pi/4$, $\theta_{\mathrm{I}} = \pi/8$, $\epsilon_r = 3$ and $kr = 10$.

wedge but the two are very similar on the exterior. With these parameters, we are pushing the limits of Rawlins' approximation since the parameter $\left(1 - \frac{1}{n^2}\right) kr$ is supposed to be small for it to be valid. While we do not illustrate it here, we have performed a similar comparison with figures 13 and 16a in Daniele and Lombardi (2011) and came to the same conclusion with an additional inconsistency in shadow regions.

It is the author's opinion that Lyalinov (1999) has a simple and effective formulation but solving the coupled Malyuzhinets equations is simpler if one were to perform the high-contrast approximation earlier and combine the methodology of Shanin (1996) and Daniele (2003a) to work out the individual components. Some of the techniques shown in Shanin (1998) and Daniele and Lombardi (2011) could also be useful in the evaluation of the resulting spectral solutions.

Chapter 5

High-contrast approximation for penetrable wedge diffraction

5.1 Article introduction

In this chapter, we will present a new approach to the penetrable wedge diffraction problem. In the process of undertaking this research, we submitted a manuscript to the 2019 IMA Lighthill Thwaites prize. This manuscript reached the final stage and was invited to be presented at the British Applied Mathematics Colloquium 2019 in the University of Bath. Here, we provide a preprint article that has been submitted to the IMA Journal of Applied Mathematics for a special issue that is exclusive to Lighthill Thwaites prize finalists. This article was co-authored by Matthew Nethercote, Raphaël Assier and Ian David Abrahams and relies heavily on the review paper Nethercote et al. (2019b).

We formulate the problem as explained in Section 1.2 and assume that the contrast parameter λ (defined by (1.48)) is small. From here, we design an iterative scheme where the 'difficult' penetrable wedge problem is decomposed into an infinite sequence of 'easier' impenetrable ones. Each of these problems are solved

by combining the Sommerfeld-Malyuzhinets and Wiener-Hopf techniques to obtain solutions in integral form. We finish by discussing some numerical evaluation strategies for these integral solutions.

When the Sommerfeld-Malyuzhinets technique was discussed in section 2 of Nethercote et al. (2019b), we assumed that the spectral function was analytic in a half-strip region and meromorphic in a slightly wider region to define the Sommerfeld integral. In this new problem, the existence of branch cuts in the spectral functions will need to be considered and therefore, we must assume that there exists similar analytic and meromorphic half-strips where the branch cuts are restricted outside. After this adjusted assumption, the Sommerfeld-Malyuzhinets technique does not change. For brevity, we do not discuss this in the article.

We are planning to make two amendments to the article when the reviews come back. One of the amendments is an additional validation check made by plotting our results alongside simulated results by the finite element solver COMSOL. The other amendment involves writing a readily accessible version of our MATLAB code (which was used to produce the graphical results) then upload them to an online repository (github, for example) and provide the link on the article.

Following the article, there will be some extra notes that provides clarity to certain aspects and an alternate strategy to evaluate Sommerfeld integrals.

The ideas presented in the article originated in discussions between all authors from the conclusions of Chapter 4. All the detailed mathematics, numerical strategies and figures were defined, undertaken and produced by Nethercote with guidance from the co-authors. Nethercote wrote the original manuscript before Assier and Abrahams made their edits and suggestions.

5.2 Journal article

IMA Journal of Applied Mathematics (2019) Page 1 of 43
doi:10.1093/imamat/iarxxx

High-contrast approximation for penetrable wedge diffraction

M. A. NETHERCOTE* AND R. C. ASSIER
School of Mathematics, University of Manchester, Oxford Road, Manchester, M13 9PL, UK
*matthew.nethercote@manchester.ac.uk

AND

I. D. ABRAHAMS
Isaac Newton Institute, 20 Clarkson Road, Cambridge, CB3 0EH, UK

[Received on 13 August 2019; revised on XX XX XXXX; accepted on XX XX XXXX]

The important open canonical problem of wave diffraction by a penetrable wedge is considered in the high-contrast limit. Mathematically, this means that the contrast parameter, the ratio of a specific material property of the host and the wedge scatterer, is assumed small. The relevant material property depends on the physical context and is different for acoustic and electromagnetic waves for example. Based on this assumption, a new asymptotic iterative scheme is constructed. The solution to the penetrable wedge is written in terms of infinitely many solutions to (possibly inhomogeneous) impenetrable wedge problems. Each impenetrable problem is solved using a combination of the Sommerfeld-Malyuzhinets and Wiener-Hopf techniques. The resulting approximated solution to the penetrable wedge involves a large number of nested complex integrals and is hence difficult to evaluate numerically. In order to address this issue, a subtle method (combining asymptotics, interpolation and complex analysis) is developed and implemented, leading to a fast and efficient numerical evaluation. This asymptotic scheme is shown to have excellent convergent properties and leads to a clear improvement on extant approaches.

Keywords: Wave diffraction, Penetrable wedge

1. Introduction

Waves diffraction by edges, wedges and ledges has been studied in numerous physical contexts (acoustics, elasticity, electromagnetism) by many distinguished scientists. Its rigorous mathematical treatment was established in the late 19$^{\text{th}}$ century thanks to Sommerfeld who solved the famous half-plane problem (Sommerfeld, 1896) (for the English translation see (Sommerfeld, 2003)), and later conceived the first solution that models impenetrable wedge diffraction (with the wedge being a rational multiple of π) using the method of images (Sommerfeld, 1901). This topic has remained an active and productive area of research ever since.

Macdonald was the first to solve impenetrable wedge problems with arbitrary wedge angles (Macdonald, 1902). In this paper, he considered an incident line source and obtained a series solution before converting it into an integral form similar to that conceived by Sommerfeld (commonly known as Sommerfeld integrals) and provided the solution for an incident plane wave.

Since then, several ingenious mathematical procedures have been developed to tackle diffraction problems. These include the Wiener-Hopf technique (Wiener & Hopf, 1931; Noble, 1958; Lawrie & Abrahams, 2007), the Sommerfeld-Malyuzhinets technique (Babich et al., 2007) and the Kontorovich-Lebedev transform (Kontorovich & Lebedev, 1939). Several asymptotic techniques have also been developed, including Keller's geometrical theory of diffraction (Keller, 1962), the uniform geometri-

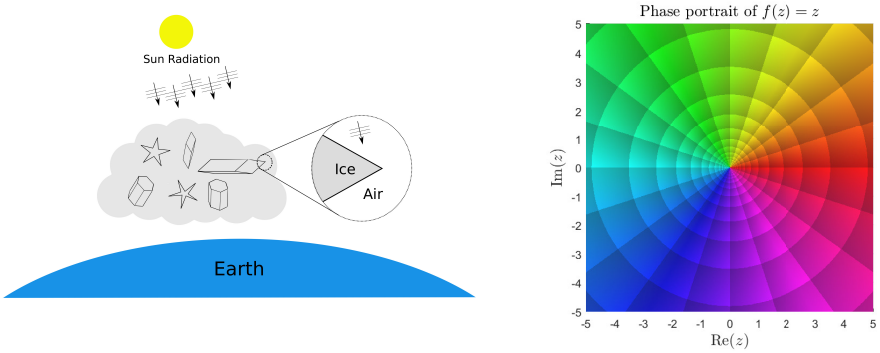

FIG. 1: Diagram outlining the application to ice crystal diffraction (left). The phase portrait of an identity map ($f(z) = z$) which assigns colours to the complex argument of f (right). For example, red will imply that $\arg(f) = 0$, green indicates $\arg(f) = \pi/2$, cyan indicates $\arg(f) = \pm\pi$ and so on.

cal theory of diffraction (Kouyoumjian & Pathak, 1974) and Kirchhoff's physical theory of diffraction (Ufimtsev, 2014). Many of these techniques have been successfully applied to impenetrable wedge diffraction (see Nethercote et al. (2019) for a review of these methods). It is also worth mentioning the important research undertaken for wedges subjected to impedance boundary condition (Malyuzhinets, 1958; Senior, 1959; Williams, 1959) or elastic wedges (Knopoff, 1969; Budaev & Bogy, 1998; Croisille & Lebeau, 1999).

Despite such progress, a clear analytical solution remains to be found for some wedge diffraction problems. This is the case for the penetrable wedge.

As one of the building blocks of the geometrical theory of diffraction, a full analytical solution to this problem would have a major impact on diffraction theory. For example, this would permit to approximate accurately and rapidly the fields diffracted by complicated structures such as penetrable truncated wedges or polygons subject to high frequency incident waves. Physical applications include noise transmission in non-viscous fluids, antenna theory and seismology.

Our initial interest in this problem was however triggered by another application related to climate modelling, that of light diffraction by ice crystals within clouds (transparent scatterers with sharp features, see Figure 1, left). Such effect is one of the big uncertainties when calculating the Earth radiation budget, which feeds directly into climate change models (Smith et al., 2015).

This application also motivated Groth et al. (2015, 2018) to extend the work by Chandler-Wilde et al. (2012) (dedicated to penetrable scatterers) to combine the strengths of numerical and asymptotic schemes to produce an accurate approximation to the problem of diffraction by penetrable convex polygons (which could represent ice crystals for example). This technique, known as hybrid numerical-asymptotic, is based on enriching the basis functions used in the boundary element method in an educated way, inspired by exact solutions to canonical diffraction problems. The aim is to create numerical methods that do not become overly expensive at high-frequency. It is acknowledged by these authors that the choice of basis functions in the penetrable case is not yet optimal and could be improved tremendously with a better understanding of the penetrable wedge problem.

Over the past few decades, there have been numerous attempts to find computational and/or asymptotic solutions to penetrable wedge problems.

Rawlins looked at the electromagnetic penetrable wedge case where the refractive index is close to

unity. In Rawlins (1977, 1999), he considered an electromagnetic incident plane wave and reduced the problem to Fredholm integral equations of the second kind using either Green's second identity or the Kontorovich-Lebedev transform and a Neumann-type perturbation series. The result of Rawlins (1999) is a formula that is simple and fast to implement. However, this particular limit of unit refractive index is not particularly suited to the applications we have in mind, and, as acknowledged by the author, the method developed can be difficult to extend to higher orders.

Budaev & Bogy (1999) looked at finding the acoustic pressure field for a special case of penetrable wedge diffraction. Relying on previous papers on Rayleigh wave scattering by elastic wedges (Budaev & Bogy, 1995, 1996, 1998), they designed the problem symmetrically with an antisymmetric incident field so that they could formulate it on a half-space domain. They derived a system of difference equations that were solved via singular integral operators and a Neumann series using the assumptions that the host wedge region is very thin and the ratio of densities is close to unity.

We should also note some recent approaches using simple layer potentials discussed in (Croisille & Lebeau, 1999) for elastic wedge diffraction. These ideas highly influenced the research by Mokeeva on the well-posedness of the penetrable wedge problem (Mokeeva, 2006, 2007). Alongside Babich, she would show the uniqueness of the problem (Babich & Mokeeva, 2008) and would later develop a numerical solution of these simple layer potentials (Babich et al., 2012).

More related to the physical assumptions of the present paper, there is an earlier attempt to create a high-contrast asymptotic approximation. Lyalinov (1999) uses the Sommerfeld-Malyuzhinets technique and asymptotically approximates the spectral functions assuming high-contrast between the material of the wedge and that of the host. The result is a leading order uniform asymptotic formula that is very fast to evaluate. The advantages and inconveniences of this approach will be discussed when comparing it to our results.

Shanin (1996, 1998) looks at solving wedge problems with inhomogeneous impedance boundary conditions via the Wiener-Hopf technique. He first considers the case where the angular domain containing the total wave field has an interior angle less than π. He later extends the method to angles exceeding π and applies a reflection method to a special case where the angle is rational of the form π/m. This method was key to showing the Wiener-Hopf technique capability to be applied to wedge problems and, as we will see, it can be extended to the penetrable wedge.

Building on their previous work (Daniele, 2003b,a, 2010, 2011) and (Daniele & Lombardi, 2006, 2007), Daniele & Lombardi (2011) have adapted the Wiener-Hopf technique to electromagnetic wave diffraction by penetrable wedges. This is achieved through a combination of multiple complex mappings, Fredholm factorisation and analytical continuation via functional difference equations. Quadrature schemes are used to solve the resulting Fredholm integral equations and numerical results are given for four representative test cases. The authors have more recently begun to extend this method to more complex geometries such as a composition of wedges and slabs (Daniele et al., 2017a,b,c, 2018).

Finally, it should be noted that Radlow (1964) adapted his ideas of two-complex variables Wiener-Hopf technique to the right-angled penetrable wedge and claimed to have found an analytic closed-form solution, though his solution was shown to be erroneous by Kraut & Lehman (1969). Functions of several complex variables are nevertheless a promising avenue in diffraction theory and have recently been exploited in (Assier & Shanin, 2019) and (Assier & Abrahams, 2019) for example.

In the present work, we propose an asymptotic scheme to solve the penetrable wedge problem, based on a high-contrast assumption. Throughout this article, we will rely on the knowledge of the locations of singularities and branch cuts of complex functions. In order for it to be simpler, we shall use MATLAB to visualise such functions in the style of Wegert (2012), using complex phase portraits. These plots of a complex function's argument allow for an easy and instantaneous visualisation of the location and

nature of the function's singularities. The right side of Figure 1 is a phase portrait of $f(z) = z$ which we will refer to as a colour reference.

We start by formulating the penetrable wedge diffraction problem in Section 2 and define two separate regions, the host and the scatterer, and their respective wave fields connected at the wedge faces. The high-contrast assumption is made and its physical meaning is discussed. This allows us to design a high-contrast iterative scheme in Section 3 that splits the penetrable wedge problem into an infinite number of impenetrable wedge problems that can be dealt with separately.

In Section 4, following the methods developed by Shanin (1996), Daniele (2003b) and Nethercote et al. (2019), each impenetrable wedge problem is solved, leading to a closed-form solution in terms of nested integrals. As a proof of concept for our asymptotic expansion method, we apply it to the simple case where the wedge has opened up to create a half-space, for which an exact solution is known.

In Section 5 we discuss the numerical strategies used to evaluate the nested integrals. This is done by a subtle combination of interpolation, asymptotic analysis and analytic continuation via functional difference equations which leads to an efficient approximation of the host and scatterer wave fields for sufficiently high-contrast. We study the convergence and the speed of our method and compare our results to the existing literature, showing clear improvements.

The appendices discuss the derivation of an important complex mapping that is used to link the wave fields in spectral space as well as some asymptotic analysis of the integral solutions.

2. Problem formulation

The problem we are considering is the diffraction of a plane wave normally incident on an infinite penetrable wedge. We assume that the problem is time-harmonic with time factor $e^{-i\omega t}$, where ω is the frequency, allowing us to reduce the linear wave equation to the Helmholtz equation and work in the frequency domain. We define Ω_1 (resp. Ω_2) to be the region outside (resp. inside) the wedge scatterer. These two angular domains have two different sets of material parameters i.e. density ($\rho_{1,2}$), magnetic permeability ($\mu_{1,2}$) or electric permittivity ($\varepsilon_{1,2}$). There will also be different wave speeds ($c_{1,2}$) and different wavenumbers ($k_{1,2}$) which satisfy $\omega = c_1 k_1 = c_2 k_2$. For simplicity, we shall assume that the wave parameters are independent of the material parameters. The angular domains will have the following definitions,

$$\Omega_1 = \{(r,\theta) : r > 0,\ -\theta_{\rm w} < \theta < \theta_{\rm w}\}, \quad \Omega_2 = \{(r,\theta) : r > 0,\ \theta_{\rm w} < \theta < 2\pi - \theta_{\rm w}\}, \tag{2.1}$$

where $0 < \theta_{\rm w} < \pi$. Defining $\bar{\theta}_{\rm w} = \pi - \theta_{\rm w}$, the interior angle of the wedge scatterer is $2\bar{\theta}_{\rm w}$, as illustrated in Figure 2.

Let the total wave solutions in Ω_1 and Ω_2 be called Φ and Ψ respectively. In an acoustic setting, Φ and Ψ represent pressure fields whereas in an electromagnetic setting, they represent either the electric or magnetic field components parallel to the wedge edge (depending on the polarisation of the incident wave). These two solutions satisfy the homogeneous Helmholtz equation with wavenumbers k_1 and k_2 respectively,

$$\nabla^2\Phi + k_1^2\Phi = 0, \ \text{ in } \ \Omega_1, \tag{2.2}$$

$$\nabla^2\Psi + k_2^2\Psi = 0, \ \text{ in } \ \Omega_2. \tag{2.3}$$

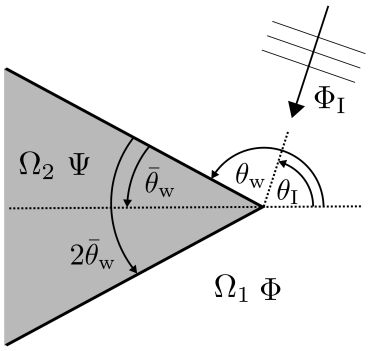

FIG. 2: The geometry of the problem where the white region is the host (Ω_1), the grey region is the wedge scatterer (Ω_2) and Φ_{I} is the incident plane wave.

At the two wedge faces $\theta = \pm\theta_{\mathrm{w}}$, Φ and Ψ must satisfy the following interface conditions,

$$\text{Top Face: } \Phi|_{\theta=\theta_{\mathrm{w}}} = \Psi|_{\theta=\pi-\bar{\theta}_{\mathrm{w}}}, \quad \left.\frac{\partial\Phi}{\partial\theta}\right|_{\theta=\theta_{\mathrm{w}}} = \lambda \left.\frac{\partial\Psi}{\partial\theta}\right|_{\theta=\pi-\bar{\theta}_{\mathrm{w}}}, \tag{2.4}$$

$$\text{Bottom Face: } \Phi|_{\theta=-\theta_{\mathrm{w}}} = \Psi|_{\theta=\pi+\bar{\theta}_{\mathrm{w}}}, \quad \left.\frac{\partial\Phi}{\partial\theta}\right|_{\theta=-\theta_{\mathrm{w}}} = \lambda \left.\frac{\partial\Psi}{\partial\theta}\right|_{\theta=\pi+\bar{\theta}_{\mathrm{w}}}. \tag{2.5}$$

where the contrast parameter λ is defined as,

$$\lambda = \frac{\rho_1}{\rho_2}, \ \frac{\mu_1}{\mu_2} \ \text{ or } \ \frac{\varepsilon_1}{\varepsilon_2} \tag{2.6}$$

in the acoustic, electric polarised and magnetic polarised cases respectively. For an acoustic setting, these interface conditions will ensure the continuity of the pressure and the normal velocity across the wedge faces. In an electromagnetic setting, the interface conditions will ensure the continuity of tangential electromagnetic field components across the wedge faces. In this paper we consider λ to be a small, positive parameter ($\lambda \ll 1$).

The incident wave (illustrated in Figure 2 as Φ_{I}) is a unit-amplitude plane wave with wavenumber k_1 and incident angle θ_{I}. This incident wave satisfies (2.2) but not (2.3) so it is a component of the host wave field Φ only,

$$\Phi_{\mathrm{I}} = e^{-ik_1 r\cos(\theta-\theta_{\mathrm{I}})}, \ \ (r,\theta) \in \Omega_1, \ \ \theta_{\mathrm{I}} \in [0,\theta_{\mathrm{w}}] \tag{2.7}$$

where we say $\theta_{\mathrm{I}} \geqslant 0$ for convenience due to the symmetry of the problem.

Both the total wave solutions can be decomposed into geometrical-optic (GO) and diffracted (Diff) wave components. The GO components, Φ_{GO} and Ψ_{GO}, contain the incident wave and all reflected and transmitted waves produced by the wedge scatterer. The remaining diffracted wave components, Φ_{Diff}

and Ψ_{Diff}, satisfy the two-dimensional Sommerfeld-radiation condition which we write in integral form:

$$\lim_{r\to\infty}\int_{-\theta_{\text{w}}}^{\theta_{\text{w}}}\left|\frac{\partial\Phi_{\text{Diff}}}{\partial r}-ik_1\Phi_{\text{Diff}}\right|^2 r\text{d}\theta=0,\quad\text{and}\quad\lim_{r\to\infty}\int_{\pi-\bar{\theta}_{\text{w}}}^{\pi+\bar{\theta}_{\text{w}}}\left|\frac{\partial\Psi_{\text{Diff}}}{\partial r}-ik_2\Psi_{\text{Diff}}\right|^2 r\text{d}\theta=0. \tag{2.8}$$

Lastly we will have edge conditions at the origin. These are obtained using the Frobenius method (see Bender & Orszag (1999) for a good treatise on the method) on the Helmholtz equation, resulting in the following asymptotic approximation as $r\to 0$,

$$\Phi(r,\theta)\underset{r\to 0}{\sim}\mathcal{A}+\left[\mathcal{B}_1\cos(\widehat{\delta}\theta)+\mathcal{B}_2\sin(\widehat{\delta}\theta)\right]r^{\widehat{\delta}}-\frac{\mathcal{A}}{4}(k_1r)^2+\ldots, \tag{2.9}$$

$$\Psi(r,\theta)\underset{r\to 0}{\sim}\mathcal{A}+\left[\mathcal{B}_3\cos(\widehat{\delta}\theta)+\mathcal{B}_4\sin(\widehat{\delta}\theta)\right]r^{\widehat{\delta}}-\frac{\mathcal{A}}{4}(k_2r)^2+\ldots, \tag{2.10}$$

where $\widehat{\delta}>0$. After applying the boundary conditions, (2.4) and (2.5), we find that $\widehat{\delta}$ must satisfy

$$(\cot(\widehat{\delta}\theta_{\text{w}})+\lambda\cot(\widehat{\delta}\bar{\theta}_{\text{w}}))(\cot(\widehat{\delta}\bar{\theta}_{\text{w}})+\lambda\cot(\widehat{\delta}\theta_{\text{w}}))=0. \tag{2.11}$$

To be consistent with the impenetrable wedge problem with Neumann boundary conditions ($\lambda=0$), we require that $\widehat{\delta}$ tends to $\delta=\frac{\pi}{2\theta_{\text{w}}}$ continuously as $\lambda\to 0$. This implies that the corresponding factor of (2.11) should remain zero,

$$\cot(\widehat{\delta}\theta_{\text{w}})+\lambda\cot(\widehat{\delta}\bar{\theta}_{\text{w}})=0. \tag{2.12}$$

We can hence Taylor expand $\widehat{\delta}$ about $\lambda=0$ to get,

$$\widehat{\delta}=\delta-\frac{\lambda}{\theta_{\text{w}}}\tan(\delta\pi)+O(\lambda^2), \tag{2.13}$$

which suggests that the singularity is *weaker* than the impenetrable wedge case when $\theta_{\text{w}}>\pi/2$ because

$$\tan(\delta\pi)<0,\ \text{ for all }\ \theta_{\text{w}}\in\left(\frac{\pi}{2},\pi\right). \tag{2.14}$$

This statement is supported by table 5.1 in Van Bladel (2006), which is a table of values for $\hat{\delta}$ with respect to λ and θ_{w}. This means that we define the edge conditions to be,

$$\Phi,\Psi\underset{r\to 0}{\sim}\mathcal{A}+O\left(r^{\min\left(\widehat{\delta},2\right)}\right), \tag{2.15}$$

where $\mathcal{A}$ is constant. We seek solutions to the Helmholtz equation in the form of a Sommerfeld integral,

$$\Phi(r,\theta)=\frac{1}{2\pi i}\int_{\gamma_+\gamma_-}e^{-ik_1r\cos(z)}s(\theta+z)\text{d}z, \tag{2.16}$$

$$\Psi(r,\theta)=\frac{1}{2\pi i}\int_{\gamma_+\gamma_-}e^{-ik_2r\cos(z)}q(\theta-\pi+z)\text{d}z, \tag{2.17}$$

where γ_+ and γ_- are known as the Sommerfeld contours (illustrated in Figure 3) and the spectral functions $s(z)$ and $q(z)$ are the unknowns to be determined. These Sommerfeld integrals automatically satisfy

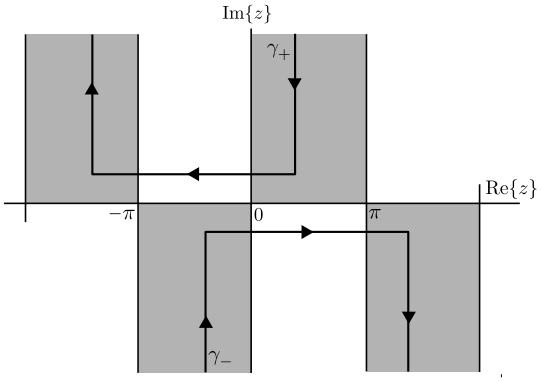

FIG. 3: The Sommerfeld contours are $\gamma_\pm$ and the grey half-strips are where the Sommerfeld integrand rapidly decays.

the relevant Helmholtz equation and radiation condition (see Babich et al. (2007), Bowman et al. (1987) and Sommerfeld (1954) for thorough explanation of their derivation and properties).

In order to connect the two Sommerfeld integrals (2.16) and (2.17), we will need to derive a mapping $g(z)$ and associated inverse $h(z)$ from the following identities,[1]

$$k_2\cos(g(z)) = k_1\cos(z), \;\; k_1\cos(h(z)) = k_2\cos(z). \tag{2.18}$$

Both of these mappings have an infinite number of branch cuts which need to be defined in a very specific way. They also satisfy the following set of properties,

- $f(-z) = -f(z)$,
- $f(z^*) = (f(z))^*$ where z^* is the complex conjugate of z,
- $f(z+n\pi) = f(z)+n\pi$, for all $n \in \mathbb{Z}$,
- $f(z) \sim z$ as $\mathrm{Im}\{z\} \to \pm\infty$,

where f can be either g or h. Following the constructive procedure detailed in Appendix A, we obtain the following form of $g(z)$ and $h(z)$ where $\lambda_k = k_1/k_2 \in [0,1]$,

$$\begin{aligned} g(z) &= z - i\ln(ie^{-iz}) \\ &\quad + i\ln\left(i\lambda_k\cos(z) - i\left(i\lambda_k\sin(z) - (1-\lambda_k^2)^{\frac{1}{2}}\right)^{\frac{1}{2}}\left(i\lambda_k\sin(z) + (1-\lambda_k^2)^{\frac{1}{2}}\right)^{\frac{1}{2}}\right), \end{aligned} \tag{2.19}$$

$$\begin{aligned} h(z) &= z - i\ln(ie^{-iz}) - i\ln(\lambda_k) \\ &\quad + i\ln\left(i\cos(z) + \left(\sin(z) - (1-\lambda_k^2)^{\frac{1}{2}}\right)^{\frac{1}{2}}\left(\sin(z) + (1-\lambda_k^2)^{\frac{1}{2}}\right)^{\frac{1}{2}}\right). \end{aligned} \tag{2.20}$$

[1]This mapping has been used by a number of authors in a wedge context (Larsen, 1981; Budaev, 1995; Lyalinov, 1999).

The individual square roots are defined by (A.5) and (A.7) for $g(z)$ and $h(z)$ respectively. Both these definitions satisfy all of the required conditions including them being the inverse of each other. It will be useful later to state the derivatives of $g(z)$ and $h(z)$ implicitly,

$$g'(z) = \frac{\lambda_k \sin(z)}{\sin(g(z))}, \quad h'(z) = \frac{\sin(z)}{\lambda_k \sin(h(z))}, \tag{2.21}$$

and note the asymptotic expansions of $g(z)$ and $h(z)$ as $\mathrm{Im}\{z\} \to \pm\infty$,

$$g(z) = z \pm i\ln(\lambda_k) \mp \frac{i(1-\lambda_k^2)}{\lambda_k^2} e^{\pm 2iz} + O\left(e^{\pm 4iz}\right), \tag{2.22}$$

$$h(z) = z \mp i\ln(\lambda_k) \pm i(1-\lambda_k^2) e^{\pm 2iz} + O\left(e^{\pm 4iz}\right). \tag{2.23}$$

As an example, Figure 4 illustrates a phase portrait of (2.19) and (2.20) evaluated by MATLAB, where $\lambda_k = 1/2$.

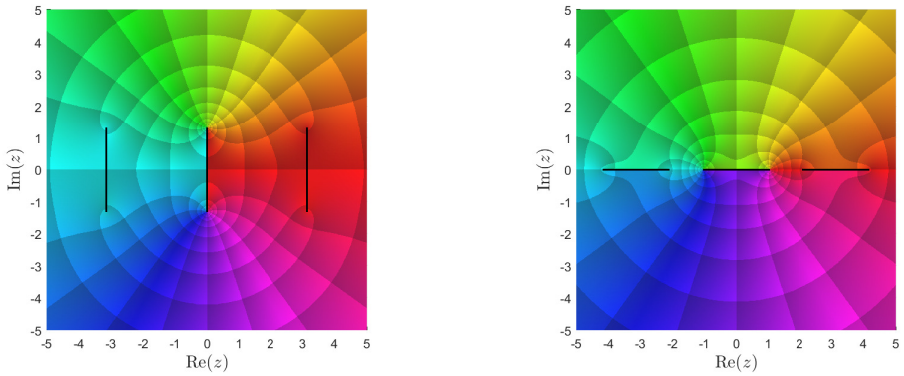

FIG. 4: Phase portraits of the mappings $g(z)$ (left) and $h(z)$ (right) by the formulae (2.19) and (2.20) respectively where $\lambda_k = 1/2$. In these figures the black lines represent branch cuts. See Figure 1 (right) for colour reference.

3. High-contrast approximation

We want to simplify the penetrable wedge problem by using a high-contrast ($\lambda \ll 1$) approximation. The idea being to decompose the 'difficult' penetrable problem into an infinite set of 'simpler' impenetrable ones. To this end, we pose the following asymptotic series,

$$\Phi = \Phi^{(0)} + \lambda\Phi^{(1)} + \lambda^2\Phi^{(2)} + O\left(\lambda^3\right), \tag{3.1}$$

$$\Psi = \Psi^{(0)} + \lambda\Psi^{(1)} + \lambda^2\Psi^{(2)} + O\left(\lambda^3\right). \tag{3.2}$$

Each of the components of (3.1) (respectively (3.2)) satisfy the Helmholtz equation and the radiation conditions with wavenumber k_1 (respectively k_2).

It is important to understand how this high-contrast approximation affects the interface conditions. By substituting (3.1) and (3.2) into (2.4) and (2.5), then organising with respect to λ, we obtain

$$\begin{gathered}\left(\Phi^{(0)}|_{\theta=\pm\theta_{\mathrm{w}}}-\Psi^{(0)}|_{\theta=\pi\mp\bar{\theta}_{\mathrm{w}}}\right)+\lambda\left(\Phi^{(1)}|_{\theta=\pm\theta_{\mathrm{w}}}-\Psi^{(1)}|_{\theta=\pi\mp\bar{\theta}_{\mathrm{w}}}\right)+\ldots=0,\\ \left(\left.\frac{\partial\Phi^{(0)}}{\partial\theta}\right|_{\theta=\pm\theta_{\mathrm{w}}}\right)+\lambda\left(\left.\frac{\partial\Phi^{(1)}}{\partial\theta}\right|_{\theta=\pm\theta_{\mathrm{w}}}-\left.\frac{\partial\Psi^{(0)}}{\partial\theta}\right|_{\theta=\pi\mp\bar{\theta}_{\mathrm{w}}}\right)+\ldots=0.\end{gathered}\tag{3.3}$$

Each of these brackets must be identically equal to zero for the interface conditions to be satisfied. The first component, $\Phi^{(0)}$, will hence satisfy homogeneous Neumann boundary conditions and all others will satisfy inhomogeneous Dirichlet or Neumann boundary conditions where the forcing depends explicitly on the previously obtained component.

Since the incident plane wave has no dependence on λ and is only present in Ω_1, then it has no direct influence on any components other than $\Phi^{(0)}$. This means that the source of excitation for all other components are the forcing in the inhomogeneous boundary conditions.

The edge conditions (2.9)-(2.10) can also be split up among each of the components by Taylor expanding $\widehat{\delta}$ and $\mathcal{A}$ about $\lambda=0$ (see (2.13) for example). We can show that all components have the edge condition of the form,

$$\Phi^{(j)},\Psi^{(j)}\underset{r\to0}{\sim}\mathcal{A}^{(j)}+O\left(r^{\delta}(\ln(r))^{j},r^{2}\right)+\ldots\ \text{ where }\ j=0,1,2,\ldots.\tag{3.4}$$

Note that $O\left(r^{\delta}(\ln(r))^{j},r^{2}\right)$ is equal to $O\left(r^{\delta}(\ln(r))^{j}\right)$ (resp. $O(r^{2})$) when $\delta\leqslant2$ (resp. $\delta>2$). For brevity, we shall just consider the case where $\delta\leqslant2$, however the methodology of this article will remain the same in the alternate case.

Each of the problems for the high-contrast approximation components, $\Phi^{(j)}$ and $\Psi^{(j)}$ are independent of λ and hence create an iterative scheme to approximate the solution to the penetrable wedge problem.

The initial problem, call it $\mathcal{P}_{\Phi}^{(0)}$, is for the leading order component of the exterior solution, $\Phi^{(0)}$, defined in Ω_1.

$$\mathcal{P}_{\Phi}^{(0)}:\begin{cases}\nabla^{2}\Phi^{(0)}+k_{1}^{2}\Phi^{(0)}=0 & \text{(Governing equation)} \quad (3.5a)\\ \left.\dfrac{\partial\Phi^{(0)}}{\partial\theta}\right|_{\theta=\pm\theta_{\mathrm{w}}}=0 & \text{(Boundary conditions)} \quad (3.5b)\\ \Phi_{\mathrm{I}}^{(0)}=e^{-ik_{1}r\cos(\theta-\theta_{\mathrm{I}})} & \text{(Plane wave forcing)} \quad (3.5c)\\ \lim\limits_{r\to\infty}\displaystyle\int_{-\theta_{\mathrm{w}}}^{\theta_{\mathrm{w}}}\left|\frac{\partial\Phi_{\mathrm{Diff}}^{(0)}}{\partial r}-ik_{1}\Phi_{\mathrm{Diff}}^{(0)}\right|^{2}r\mathrm{d}\theta=0 & \text{(Radiation condition)} \quad (3.5d)\\ \Phi^{(0)}\underset{r\to0}{=}\mathcal{A}^{(0)}+O\left(r^{\delta}\right) & \text{(Edge condition)} \quad (3.5e)\end{cases}$$

$\mathcal{P}_{\Phi}^{(0)}$ is exactly the same as the impenetrable wedge problem with Neumann boundary conditions. The solution to this problem is stated in the form of a Sommerfeld integral,

$$\Phi^{(0)}=\frac{1}{2\pi i}\int_{\gamma_{+}}e^{-ik_{1}r\cos(z)}\left[s^{(0)}(\theta+z)-s^{(0)}(\theta-z)\right]\mathrm{d}z,\tag{3.6}$$

where $s^{(0)}(z)$ is the unknown spectral function to find. The solution is well-known and is solvable with numerous different methods (see Nethercote et al. (2019)). The resulting solution is,

$$s^{(0)}(z) = \frac{\delta\cos(\delta z)}{\sin(\delta z)-\sin(\delta\theta_{\rm I})}, \text{ where, } \delta = \frac{\pi}{2\theta_{\rm w}}. \tag{3.7}$$

This spectral function has a few useful properties that will be reused later.

$$\text{Antisymmetry:} \quad s^{(0)}(\pm 2\theta_{\rm w} - z) = -s^{(0)}(z) \tag{3.8}$$

$$\text{Periodicity:} \quad s^{(0)}(4\theta_{\rm w} + z) = s^{(0)}(z) \tag{3.9}$$

$$\text{Conjugacy:} \quad s^{(0)}(z^*) = \left(s^{(0)}(z)\right)^* \tag{3.10}$$

Lastly we shall note the asymptotic series for $s^{(0)}(z)$ as $\mathrm{Im}\{z\} \to \pm\infty$,

$$s^{(0)}(z) = \mp i\delta - 2\delta\sin(\delta\theta_{\rm I})e^{\pm i\delta z} + O\left(e^{\pm 2i\delta z}\right). \tag{3.11}$$

All of the other components satisfy one of two types of problems. The first type, $\mathcal{P}_{\Psi}^{(j)}$ for $j = 0,1,2...$, is for the components of the interior solution $\Psi^{(j)}$ which are defined in Ω_2. This type has no incoming plane waves and satisfies inhomogeneous Dirichlet boundary conditions depending on the known $\Phi^{(j)}$ component.

$$\mathcal{P}_{\Psi}^{(j)}: \begin{cases} \nabla^2\Psi^{(j)} + k_2^2\Psi^{(j)} = 0 & \text{(Governing equation)} \quad (3.12a) \\ \Psi^{(j)}|_{\theta=\pi\mp\bar{\theta}_{\rm w}} = \Phi^{(j)}|_{\theta=\pm\theta_{\rm w}} & \text{(Boundary conditions)} \quad (3.12b) \\ \text{Not applicable here} & \text{(Plane wave forcing)} \quad (3.12c) \\ \lim\limits_{r\to\infty}\int_{\pi-\bar{\theta}_{\rm w}}^{\pi+\bar{\theta}_{\rm w}} \left|\dfrac{\partial\Psi_{\rm Diff}^{(j)}}{\partial r} - ik_2\Psi_{\rm Diff}^{(j)}\right|^2 r\mathrm{d}\theta = 0 & \text{(Radiation condition)} \quad (3.12d) \\ \Psi^{(j)} \underset{r\to 0}{=} \mathcal{A}^{(j)} + O\left(r^{\delta}(\ln(r))^j\right) & \text{(Edge condition)} \quad (3.12e) \end{cases}$$

We seek a solution satisfying (3.12a) and (3.12d) in the form of (2.17),

$$\Psi^{(j)} = \frac{1}{2\pi i}\int_{\gamma_+} e^{-ik_2 r\cos(z)}\left[q^{(j)}(\theta-\pi+z) - q^{(j)}(\theta-\pi-z)\right]\mathrm{d}z, \tag{3.13}$$

where, due to (3.12e), $q^{(j)}(z)$ has the following leading order behaviour as $\mathrm{Im}\{z\} \to \pm\infty$,[2]

$$q^{(j)}(z) = \pm A^{(j)} + O\left(z^j e^{\pm i\delta z}\right). \tag{3.14}$$

with $A^{(j)} = -i\mathcal{A}^{(j)}/2$. A consequence of no incoming plane waves is that $q^{(j)}(z)$ has no poles in the strip,

$$\left\{z : -\bar{\theta}_{\rm w} < \mathrm{Re}\{z\} < \bar{\theta}_{\rm w}\right\}. \tag{3.15}$$

[2]Note that in the alternative case where $\delta > 2$, $z^j e^{\pm i\delta z}$ would be replaced with $e^{\pm 2iz}$. This will also be true for (3.22)

We apply the boundary conditions, (3.12b), to obtain,

$$\int_{\gamma_+} e^{-ik_2 r\cos(z)}\left[q^{(j)}(\mp\bar{\theta}_\mathrm{w}+z)-q^{(j)}(\mp\bar{\theta}_\mathrm{w}-z)\right]\mathrm{d}z = \int_{\gamma_+} e^{-ik_1 r\cos(z)}\left[s^{(j)}(\pm\theta_\mathrm{w}+z)-s^{(j)}(\pm\theta_\mathrm{w}-z)\right]\mathrm{d}z. \tag{3.16}$$

From (2.20), we apply the mapping $h(z)$ to transform the right integral and match the two exponentials. The mapped Sommerfeld contour can be deformed back to the original so that the two integrals are combined to produce,

$$\int_{\gamma_+} e^{-ik_2 r\cos(z)}\Big[q^{(j)}(\mp\bar{\theta}_\mathrm{w}+z)-q^{(j)}(\mp\bar{\theta}_\mathrm{w}-z) - h'(z)\left[s^{(j)}(\pm\theta_\mathrm{w}+h(z))-s^{(j)}(\pm\theta_\mathrm{w}-h(z))\right]\Big]\mathrm{d}z = 0. \tag{3.17}$$

We can now apply Malyuzhinets' theorem (see section 3.4 of Babich et al. (2007) for details) to nullify the integral and produce the following set of functional equations,

$$q^{(j)}(\mp\bar{\theta}_\mathrm{w}+z)-q^{(j)}(\mp\bar{\theta}_\mathrm{w}-z) = h'(z)\left[s^{(j)}(\pm\theta_\mathrm{w}+h(z))-s^{(j)}(\pm\theta_\mathrm{w}-h(z))\right]. \tag{3.18}$$

Note that in the initial case, $j=0$, we can apply the antisymmetry property (3.8) to simplify (3.18),

$$q^{(0)}(\mp\bar{\theta}_\mathrm{w}+z)-q^{(0)}(\mp\bar{\theta}_\mathrm{w}-z) = 2h'(z)s^{(0)}(\pm\theta_\mathrm{w}+h(z)). \tag{3.19}$$

The second type of problem, $\mathcal{P}_\Phi^{(j)}$ where $j=1,2,3...$, is for the higher order components of the exterior solution $\Phi^{(j)}$, which are defined in Ω_1. These problems do not have any incoming plane waves either and satisfy inhomogeneous Neumann boundary conditions depending on the known $\Psi^{(j-1)}$ component.

$$\mathcal{P}_\Phi^{(j)}:\begin{cases} \nabla^2\Phi^{(j)}+k_1^2\Phi^{(j)}=0 & \text{(Governing equation)} \quad (3.20a)\\ \left.\dfrac{\partial\Phi^{(j)}}{\partial\theta}\right|_{\theta=\pm\theta_\mathrm{w}} = \left.\dfrac{\partial\Psi^{(j-1)}}{\partial\theta}\right|_{\theta=\pi\mp\bar{\theta}_\mathrm{w}} & \text{(Boundary conditions)} \quad (3.20b)\\ \text{Not applicable here} & \text{(Plane wave forcing)} \quad (3.20c)\\ \lim\limits_{r\to\infty}\int_{-\theta_\mathrm{w}}^{\theta_\mathrm{w}}\left|\dfrac{\partial\Phi_\mathrm{Diff}^{(j)}}{\partial r}-ik_1\Phi_\mathrm{Diff}^{(j)}\right|^2 r\mathrm{d}\theta=0 & \text{(Radiation condition)} \quad (3.20d)\\ \Phi^{(j)}=\mathcal{A}^{(j)}+O\left(r^\delta(\ln(r))^j\right) & \text{(Edge condition)} \quad (3.20e)\end{cases}$$

We seek a solution satisfying (3.20a) and (3.20d) in the form of (2.16),

$$\Phi^{(j)} = \frac{1}{2\pi i}\int_{\gamma_+} e^{-ik_1 r\cos(z)}\left[s^{(j)}(\theta+z)-s^{(j)}(\theta-z)\right]\mathrm{d}z, \tag{3.21}$$

where, due to (3.20e), $s^{(j)}(z)$ has the following leading order behaviour as $\mathrm{Im}\{z\}\to\pm\infty$,

$$s^{(j)}(z) = \pm A^{(j)}+O\left(z^j e^{\pm i\delta z}\right). \tag{3.22}$$

Note that for all j, $A^{(j)}$ in (3.22) is the same as $A^{(j)}$ in (3.14). No incoming plane waves means that $s^{(j)}(z)$ has no poles in the strip,

$$\{z : -\theta_{\mathrm{w}} < \mathrm{Re}\{z\} < \theta_{\mathrm{w}}\}. \tag{3.23}$$

Applying the boundary conditions, (3.20b), leads to the following,

$$\begin{aligned}\int_{\gamma_+} e^{-ik_1 r\cos(z)}(k_1\sin(z))\left[s^{(j)}(\pm\theta_{\mathrm{w}}+z)+s^{(j)}(\pm\theta_{\mathrm{w}}-z)\right]\mathrm{d}z \\ = \int_{\gamma_+} e^{-ik_2 r\cos(z)}(k_2\sin(z))\left[q^{(j-1)}(\mp\bar{\theta}_{\mathrm{w}}+z)+q^{(j-1)}(\mp\bar{\theta}_{\mathrm{w}}-z)\right]\mathrm{d}z.\end{aligned} \tag{3.24}$$

Here we apply the mapping $g(z)$, to transform the RHS of (3.24), deform the mapped Sommerfeld contour back to the original and apply Malyuzhinets' theorem to produce the following set of functional equations,

$$s^{(j)}(\pm\theta_{\mathrm{w}}+z)+s^{(j)}(\pm\theta_{\mathrm{w}}-z) = q^{(j-1)}(\mp\bar{\theta}_{\mathrm{w}}+g(z))+q^{(j-1)}(\mp\bar{\theta}_{\mathrm{w}}-g(z)). \tag{3.25}$$

The two types of unsolved problems stated above will be called inhomogeneous Dirichlet ($\mathcal{P}^{(j)}_{\Psi}$) and inhomogeneous Neumann ($\mathcal{P}^{(j)}_{\Phi}$). In the next section, we shall combine elements from the papers Shanin (1998); Daniele (2003b) and Nethercote et al. (2019) (that use the Wiener-Hopf technique for impenetrable wedge problems) to find the unknown spectral functions $q^{(j)}(z)$ and $s^{(j)}(z)$.

4. Formulation and solution of the Wiener-Hopf problems

The basis of this method is to Laplace transform the total field, Φ or Ψ, and their θ derivative on the two wedge faces, $\theta = \pm\theta_{\mathrm{w}}$, and the line of symmetry $\theta = 0$ or π. These transforms are used to produce the Wiener-Hopf equations. After the boundary conditions are considered, a mapping to a new complex plane is introduced so that the Wiener-Hopf technique can be applied to produce a solution. Much of this procedure is discussed in section 3 of Nethercote et al. (2019).

Following the same method as section 3.2 in Nethercote et al. (2019), we solve these wedge problems by deriving two Wiener-Hopf equations. Let u represent one of the total fields ($\Phi^{(j)}$ or $\Psi^{(j)}$) and use the following definition of the Laplace transform (and associated inverse),

$$F(\eta) = \int_0^\infty f(r)e^{ikr\eta}\mathrm{d}r, \quad f(r) = \frac{k}{2\pi}\int_{-\infty}^{\infty} F(\eta)e^{-ikr\eta}\mathrm{d}\eta, \tag{4.1}$$

where $F(\eta)$ is analytic in the upper half-plane $\mathrm{Im}\{\eta\} > 0$. Hence we can define the following transforms of u and its θ derivative,

$$U(\eta,\theta) = \int_0^\infty u(r,\theta)e^{ikr\eta}\mathrm{d}r, \quad V(\eta,\theta) = \int_0^\infty \frac{1}{ikr}\frac{\partial u}{\partial\theta}(r,\theta)e^{ikr\eta}\mathrm{d}r. \tag{4.2}$$

This is done for two wedge regions $\theta \in [0,\Theta]$ and $\theta \in [-\Theta,0]$, where $\Theta = \theta_{\mathrm{w}}$ or $\bar{\theta}_{\mathrm{w}}$ and results in the two Wiener-Hopf equations,

$$\begin{aligned}2V(\cos(z),0) &= V(\cos(\Theta-z),-\Theta)+V(\cos(\Theta-z),\Theta) \\ &\quad -\sin(\Theta-z)\left[U(\cos(\Theta-z),-\Theta)-U(\cos(\Theta-z),\Theta)\right], \\ 2\sin(z)U(\cos(z),0) &= V(\cos(\Theta-z),-\Theta)-V(\cos(\Theta-z),\Theta) \\ &\quad -\sin(\Theta-z)\left[U(\cos(\Theta-z),-\Theta)+U(\cos(\Theta-z),\Theta)\right].\end{aligned} \tag{4.3}$$

We solve the system (4.3) for $U(\cos(z),0)$ and $V(\cos(z),0)$ in terms of the known boundary data $V(\cos(\Theta-z),\pm\Theta)$ or $U(\cos(\Theta-z),\pm\Theta)$. From section 3.2 of Nethercote et al. (2019), it can be shown that if u is written as a Sommerfeld integral,

$$u(r,\theta)=\frac{1}{2\pi i}\int_{\gamma_+}e^{-ikr\cos(z)}\left[p(\theta+z)-p(\theta-z)\right]\mathrm{d}z, \tag{4.4}$$

then the Laplace transforms U and V can be written in terms of the spectral function $p(z)$,

$$U(\cos(z),\theta)=\frac{p(\theta+z)-p(\theta-z)}{ik\sin(z)}, \tag{4.5}$$

$$V(\cos(z),\theta)=\frac{i}{k}\left[p(\theta+z)+p(\theta-z)\right], \tag{4.6}$$

to show that,

$$p(z)=\frac{k}{2i}\left[V(\cos(z),0)-\sin(z)U(\cos(z),0)\right]. \tag{4.7}$$

For the initial homogeneous Neumann problem we will have $u=\Phi^{(0)},\ p=s^{(0)},\ k=k_1,\ \Theta=\theta_\mathrm{w}$ and the boundary conditions, $V(\cos(\Theta-z),\pm\theta_\mathrm{w})=0$. In this case we needed to factorise $\sin(z)$ and remove the poles on the right hand side of (4.3) to ensure that the two sides have a common domain of analyticity. With the boundedness of the terms, we used Liouville's theorem to determine both $U(\cos(z),0)$ and $V(\cos(z),0)$ and hence show (3.7) (see section 3 of Nethercote et al. (2019) for further details).

For the other problems, we will have inhomogeneous Neumann/Dirichlet boundary conditions and we will also need to alternate between wavenumbers $k=k_1,k_2$ and the wedge angle $\Theta=\theta_\mathrm{w},\bar{\theta}_\mathrm{w}$. Fortunately there are no plane wave sources that need removing this time.

4.1 *Inhomogeneous Dirichlet problem* $\left(\mathcal{P}_\Psi^{(j)}\right)$

In these problems, the total wave field $\Psi^{(j)}$ is in the interior of the wedge (Ω_2) hence we have $k=k_2$ and $\Theta=\bar{\theta}_\mathrm{w}$. To make this a little simpler, put Green's second identity in the $(r,\widehat{\theta})$ coordinate system where $\widehat{\theta}=\theta-\pi$. Hence we have $u(r,\widehat{\theta})=\Psi^{(j)}(r,\pi+\widehat{\theta})$ (with $j=0,1,2...$). Define the known boundary data as U_1 and U_2 using the following definitions,[3]

$$U_1(z)=U(\cos(\bar{\theta}_\mathrm{w}-z),\bar{\theta}_\mathrm{w})=\int_0^\infty\Psi^{(j)}(r,\pi+\bar{\theta}_\mathrm{w})e^{ik_2r\cos(\bar{\theta}_\mathrm{w}-z)}\mathrm{d}r, \tag{4.8}$$

$$U_2(z)=U(\cos(\bar{\theta}_\mathrm{w}-z),-\bar{\theta}_\mathrm{w})=\int_0^\infty\Psi^{(j)}(r,\pi-\bar{\theta}_\mathrm{w})e^{ik_2r\cos(\bar{\theta}_\mathrm{w}-z)}\mathrm{d}r. \tag{4.9}$$

Both of these definitions can be expressed explicitly in terms of $s^{(j)}$ using the identity (4.5) and the boundary functional conditions (3.18),

$$U_1(z)=\frac{h'(\bar{\theta}_\mathrm{w}-z)}{ik_2\sin(\bar{\theta}_\mathrm{w}-z)}\left[s^{(j)}(-\theta_\mathrm{w}+h(\bar{\theta}_\mathrm{w}-z))-s^{(j)}(-\theta_\mathrm{w}-h(\bar{\theta}_\mathrm{w}-z))\right], \tag{4.10}$$

$$U_2(z)=\frac{h'(\bar{\theta}_\mathrm{w}-z)}{ik_2\sin(\bar{\theta}_\mathrm{w}-z)}\left[s^{(j)}(\theta_\mathrm{w}+h(\bar{\theta}_\mathrm{w}-z))-s^{(j)}(\theta_\mathrm{w}-h(\bar{\theta}_\mathrm{w}-z))\right]. \tag{4.11}$$

[3] In this subsection and the next, we do not state the j dependency for the functions U, V, U_1, U_2, V_1 and V_2 for ease of notation.

The Wiener-Hopf system (4.3) becomes,

$$\begin{aligned} V(\cos(z),0) =& \frac{1}{2}\left[V(\cos(\bar{\theta}_\mathrm{w}-z),-\bar{\theta}_\mathrm{w})+V(\cos(\bar{\theta}_\mathrm{w}-z),\bar{\theta}_\mathrm{w})\right]+\frac{1}{2}\sin(\bar{\theta}_\mathrm{w}-z)\left[U_1(z)-U_2(z)\right], \\ \sin(z)U(\cos(z),0) =& \frac{1}{2}\left[V(\cos(\bar{\theta}_\mathrm{w}-z),-\bar{\theta}_\mathrm{w})-V(\cos(\bar{\theta}_\mathrm{w}-z),\bar{\theta}_\mathrm{w})\right]-\frac{1}{2}\sin(\bar{\theta}_\mathrm{w}-z)\left[U_1(z)+U_2(z)\right]. \end{aligned} \tag{4.12}$$

In this form, the Wiener-Hopf technique fails because this system cannot be factorised. To counter this issue, we will need to map these equations onto a new complex plane so that they can be reduced to classical Wiener-Hopf equations similar to those in Noble (1958). We will conformally map z so that $U(\cos(z),0)$ and $V(\cos(z),0)$ are analytic on an upper half plane and $V(\cos(\bar{\theta}_\mathrm{w}-z),\pm\bar{\theta}_\mathrm{w})$ are analytic on a lower half plane. This is achieved using the following mapping with $\Theta=\bar{\theta}_\mathrm{w}$,

$$z(\alpha)=\frac{\Theta}{\pi}\cos^{-1}(\alpha),\quad \alpha(z)=\cos\left(\frac{\pi}{\Theta}z\right). \tag{4.13}$$

(4.13) has a single branch cut along the real line segment $\alpha\in(-\infty,-1]$ where the local argument of the chosen branch is $(-\pi,\pi]$. This is done by choosing the branch of the inverse cosine such that $\Theta-z(\alpha)=z(-\alpha)$. Note that this mapping limits z to belong to the strip $\mathrm{Re}\{z\}\in[0,\Theta]$. For further details, see section 3.1 of Nethercote et al. (2019).

Now we apply (4.13) to the Wiener-Hopf system (4.12) to transform it onto the α-plane,

$$\begin{aligned} V(\cos(z(\alpha)),0) =& \frac{1}{2}\left[V(\cos(z(-\alpha)),-\bar{\theta}_\mathrm{w})+V(\cos(z(-\alpha)),\bar{\theta}_\mathrm{w})\right] \\ &+\frac{1}{2}\sin(z(-\alpha))\left[U_1(z(\alpha))-U_2(z(\alpha))\right], \end{aligned} \tag{4.14}$$

$$\begin{aligned} \sin(z(\alpha))U(\cos(z(\alpha)),0) =& \frac{1}{2}\left[V(\cos(z(-\alpha)),-\bar{\theta}_\mathrm{w})-V(\cos(z(-\alpha)),\bar{\theta}_\mathrm{w})\right] \\ &-\frac{1}{2}\sin(z(-\alpha))\left[U_1(z(\alpha))+U_2(z(\alpha))\right]. \end{aligned} \tag{4.15}$$

To proceed with the Wiener-Hopf method, we will require to factorise $\sin(z(\alpha))$ in equation (4.15). Before performing this factorisation, we shall define the domains $\mathcal{R}_\pm$ on which this factorisation will be done:

$$\mathcal{R}_+=\{\alpha:\mathrm{Im}\{\alpha\}>0\}\cup\{\alpha:\mathrm{Re}\{\alpha\}>-1,\mathrm{Im}\{\alpha\}=0\} \tag{4.16}$$

$$\mathcal{R}_-=\{\alpha:\mathrm{Im}\{\alpha\}<0\}\cup\{\alpha:\mathrm{Re}\{\alpha\}<1,\mathrm{Im}\{\alpha\}=0\} \tag{4.17}$$

Note that $\mathcal{R}_+\cup\mathcal{R}_-$ is the whole complex plane and $\mathcal{R}_+\cap\mathcal{R}_-$ is the real line segment $\alpha\in(-1,1)$. We expect $V(\cos(z(\alpha)),0)$ and $U(\cos(z(\alpha)),0)$ to be analytic on $\mathcal{R}_+$ and have a branch cut on the real line segment $\alpha\in(-\infty,-1]$. We also expect $V(\cos(z(-\alpha)),\pm\bar{\theta}_\mathrm{w})$ to be analytic on $\mathcal{R}_-$ and have a branch cut on the real line segment $\alpha\in[1,\infty)$. However $\sin(z(\alpha))$ has both branch cuts, which is why it must be factorised. To factorise $\sin(z(\alpha))$, we refer to section 3.1 of Nethercote et al. (2019)k, where it was found that,

$$\sin(z(\alpha))=f_-(\alpha)\times f_+(\alpha)=\frac{\sqrt{2-2\alpha}}{2}\times\left(\frac{\sin\left(\frac{\bar{\theta}_\mathrm{w}}{\pi}\cos^{-1}(\alpha)\right)}{\frac{\sqrt{2-2\alpha}}{2}}\right). \tag{4.18}$$

This means that (4.15) after factorisation becomes,

$$f_+(\alpha)U(\cos(z(\alpha)),0) = \frac{1}{2f_-(\alpha)}\left[V(\cos(z(-\alpha)),-\bar{\theta}_\mathrm{w}) - V(\cos(z(-\alpha)),\bar{\theta}_\mathrm{w})\right] - \frac{\sin(z(-\alpha))}{2f_-(\alpha)}\left[U_1(z(\alpha)) + U_2(z(\alpha))\right]. \tag{4.19}$$

The first terms in (4.14) and (4.19) are analytic at $\alpha = 1$, hence are analytic on the upper half α-plane $\mathcal{R}_+$. The second terms are analytic at $\alpha = -1$, hence are analytic on the lower half α-plane $\mathcal{R}_-$. The last terms in both equations are only analytic on the real line segment $\alpha \in \mathcal{R}_+ \cap \mathcal{R}_-$. We define $M_1(\alpha)$ and $M_2(\alpha)$ as,

$$\begin{aligned} M_1(\alpha) &= \frac{1}{2}\sin(z(-\alpha))\left[U_1(z(\alpha)) - U_2(z(\alpha))\right], \\ M_2(\alpha) &= \frac{\sin(z(-\alpha))}{2f_-(\alpha)}\left[U_1(z(\alpha)) + U_2(z(\alpha))\right]. \end{aligned} \tag{4.20}$$

We use Cauchy's integral formula to sum split (4.20) into two terms analytic in $\mathcal{R}_+$ and $\mathcal{R}_-$ respectively. For $n = 1, 2$, we use the following sum split, $M_n(\alpha) = M_{n+}(\alpha) + M_{n-}(\alpha)$,

$$\text{where, } M_{n+}(\alpha) = \frac{1}{2\pi i}\int_{C_-} \frac{M_n(\beta)}{\beta - \alpha}\mathrm{d}\beta, \quad M_{n-}(\alpha) = -\frac{1}{2\pi i}\int_{C_+} \frac{M_n(\beta)}{\beta - \alpha}\mathrm{d}\beta. \tag{4.21}$$

Using these formulae, $M_{n+}(\alpha)$ (resp. $M_{n-}(\alpha)$) can be analytically continued onto the half-plane $\mathcal{R}_+$ (resp. $\mathcal{R}_-$).

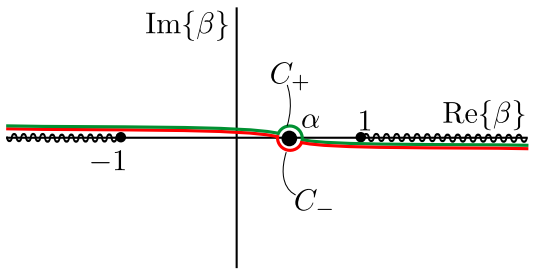

FIG. 5: Diagram of the contours C_- (in red) and C_+ (in green) in the β-plane. Here there is a pole at $\beta = \alpha$ and branch points at $\beta = \pm 1$.

The contour C_- runs from $-\infty + i0$ to $\infty - i0$ underneath the simple pole at $\beta = \alpha$. The contour C_+ runs between $-\infty + i0$ to $\infty - i0$ above C_- and above the simple pole at $\beta = \alpha$. Both these contours are illustrated on Figure 5 in red and green respectively. We create the following entire functions from the

Wiener-Hopf equations.

$$\mathcal{M}_1(\alpha)=\begin{cases} V(\cos(z(\alpha)),0)-M_{1+}(\alpha) & \alpha\in\mathcal{R}_+,\\ \frac{1}{2}\left[V(\cos(z(-\alpha)),-\bar{\theta}_{\mathrm{w}})+V(\cos(z(-\alpha)),\bar{\theta}_{\mathrm{w}})\right]+M_{1-}(\alpha) & \alpha\in\mathcal{R}_-,\\ (4.14) & \alpha\in\mathcal{R}_+\cap\mathcal{R}_-, \end{cases}$$

$$\mathcal{M}_2(\alpha)=\begin{cases} \frac{2\sin(z(\alpha))}{\sqrt{2-2\alpha}}U(\cos(z(\alpha)),0)+M_{2+}(\alpha) & \alpha\in\mathcal{R}_+,\\ \frac{1}{\sqrt{2-2\alpha}}\left[V(\cos(z(-\alpha)),-\bar{\theta}_{\mathrm{w}})-V(\cos(z(-\alpha)),\bar{\theta}_{\mathrm{w}})\right]-M_{2-}(\alpha) & \alpha\in\mathcal{R}_-,\\ (4.19) & \alpha\in\mathcal{R}_+\cap\mathcal{R}_-, \end{cases}$$

Noting that due to the edge conditions, we can show that each of these terms tends to zero as $|\alpha|\to\infty$. This means that we can apply Liouville's theorem to get,

$$V(\cos(z),0)=M_{1+}(\alpha(z)), \tag{4.22}$$

$$\sin(z)U(\cos(z),0)=-\sin\left(\bar{\delta}z\right)M_{2+}(\alpha(z)). \tag{4.23}$$

where we have used $f_-(\alpha(z))=\sin(\bar{\delta}z)$ with $\bar{\delta}=\pi/(2\bar{\theta}_{\mathrm{w}})$. We write $q^{(j)}(z)$ in terms of these Cauchy integrals,

$$\begin{aligned} q^{(j)}(z)&=\frac{k_2}{2i}\left[V(\cos(z),0)-\sin(z)U(\cos(z),0)\right],\\ &=\frac{k_2}{2i}\left[M_{1+}(\alpha(z))+\sin\left(\bar{\delta}z\right)M_{2+}(\alpha(z))\right],\\ &=\frac{1}{2\pi i}\int_{C_-}\frac{k_2(M_1(\beta)+\sin\left(\bar{\delta}z\right)M_2(\beta))}{2i(\beta-\alpha(z))}\mathrm{d}\beta. \end{aligned} \tag{4.24}$$

We substitute the definitions (4.20) for M_1 and M_2 and use (4.13) to obtain

$$\begin{aligned} q^{(j)}(z)=\frac{1}{2\pi i}\int_{C_-}\frac{k_2\sin\left(\bar{\theta}_{\mathrm{w}}-\zeta(\beta)\right)}{2i(\beta-\alpha(z))\sqrt{2-2\beta}}\Bigg[&\left(\sqrt{\frac{1-\beta}{2}}+\sin\left(\bar{\delta}z\right)\right)U_1(\zeta(\beta))\\ &-\left(\sqrt{\frac{1-\beta}{2}}-\sin\left(\bar{\delta}z\right)\right)U_2(\zeta(\beta))\Bigg]\mathrm{d}\beta, \end{aligned} \tag{4.25}$$

where $\zeta(\beta)=\frac{\bar{\theta}_{\mathrm{w}}}{\pi}\cos^{-1}(\beta)$. We want to transform (4.25) to the ζ-plane. Noting that,

$$\beta=\cos\left(2\bar{\delta}\zeta\right),\ \sqrt{\frac{1-\beta}{2}}=\sin\left(\bar{\delta}\zeta\right),\ \text{and}\ \frac{\mathrm{d}\beta}{\mathrm{d}\zeta}=-2\bar{\delta}\sin\left(2\bar{\delta}\zeta\right), \tag{4.26}$$

(4.25) becomes,

$$\begin{aligned} q^{(j)}(z)=\frac{1}{4\pi i}\int_C\Bigg(&\frac{\bar{\delta}\cos\left(\bar{\delta}\zeta\right)}{\sin\left(\bar{\delta}\zeta\right)+\sin\left(\bar{\delta}z\right)}\left(ik_2\sin\left(\bar{\theta}_{\mathrm{w}}-\zeta\right)U_2(\zeta)\right)\\ &-\frac{\bar{\delta}\cos\left(\bar{\delta}\zeta\right)}{\sin\left(\bar{\delta}\zeta\right)-\sin\left(\bar{\delta}z\right)}\left(ik_2\sin\left(\bar{\theta}_{\mathrm{w}}-\zeta\right)U_1(\zeta)\right)\Bigg)\mathrm{d}\zeta. \end{aligned} \tag{4.27}$$

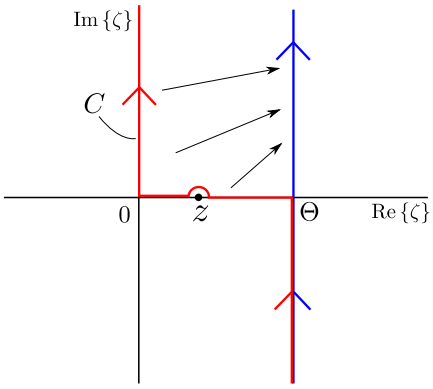

FIG. 6: Diagram of the contour C_- before and after deformation (in red and blue respectively) in the ζ-plane.

The original contour C_- is transformed to C (shown on Figure 6 in red where $\Theta = \bar{\theta}_\mathrm{w}$) which runs from $\zeta = \bar{\theta}_\mathrm{w} - i\infty$ to $i\infty$ via the points $\bar{\theta}_\mathrm{w}$, 0 and above the pole at $\zeta = z$. We deform the contour to the straight line running from $\zeta = \bar{\theta}_\mathrm{w} - i\infty$ to $\bar{\theta}_\mathrm{w} + i\infty$ (shown on Figure 6 in blue).

This deformation does not cross any singularities so,

$$q^{(j)}(z) = \frac{1}{4\pi i}\int_{\bar{\theta}_\mathrm{w}-i\infty}^{\bar{\theta}_\mathrm{w}+i\infty}\left(\frac{\bar{\delta}\cos\left(\bar{\delta}\zeta\right)}{\sin\left(\bar{\delta}\zeta\right)+\sin\left(\bar{\delta}z\right)}\left(ik_2\sin\left(\bar{\theta}_\mathrm{w}-\zeta\right)U_2(\zeta)\right)\right.$$
$$\left.-\frac{\bar{\delta}\cos\left(\bar{\delta}\zeta\right)}{\sin\left(\bar{\delta}\zeta\right)-\sin\left(\bar{\delta}z\right)}\left(ik_2\sin\left(\bar{\theta}_\mathrm{w}-\zeta\right)U_1(\zeta)\right)\right)\mathrm{d}\zeta. \tag{4.28}$$

We substitute the two definitions for $U_1(\zeta)$ and $U_2(\zeta)$, (4.10) and (4.11), to put the integrands in terms of $s^{(j)}$

$$q^{(j)}(z) = \frac{1}{4\pi i}\int_{\bar{\theta}_\mathrm{w}-i\infty}^{\bar{\theta}_\mathrm{w}+i\infty}\left(\frac{\bar{\delta}\cos\left(\bar{\delta}\zeta\right)h'(\bar{\theta}_\mathrm{w}-\zeta)}{\sin\left(\bar{\delta}\zeta\right)+\sin\left(\bar{\delta}z\right)}\left[s^{(j)}(\theta_\mathrm{w}+h(\bar{\theta}_\mathrm{w}-\zeta))-s^{(j)}(\theta_\mathrm{w}-h(\bar{\theta}_\mathrm{w}-\zeta))\right]\right.$$
$$\left.-\frac{\bar{\delta}\cos\left(\bar{\delta}\zeta\right)h'(\bar{\theta}_\mathrm{w}-\zeta)}{\sin\left(\bar{\delta}\zeta\right)-\sin\left(\bar{\delta}z\right)}\left[s^{(j)}(-\theta_\mathrm{w}+h(\bar{\theta}_\mathrm{w}-\zeta))-s^{(j)}(-\theta_\mathrm{w}-h(\bar{\theta}_\mathrm{w}-\zeta))\right]\right)\mathrm{d}\zeta. \tag{4.29}$$

This integrand can be simplified further with the substitution, $\zeta \mapsto \bar{\theta}_\mathrm{w} - \zeta$ to obtain the final formula,

$$q^{(j)}(z) = \frac{1}{4\pi i}\int_{-i\infty}^{i\infty}\left(\frac{\bar{\delta}\sin\left(\bar{\delta}\zeta\right)h'(\zeta)}{\cos\left(\bar{\delta}\zeta\right)+\sin\left(\bar{\delta}z\right)}\left[s^{(j)}(\theta_\mathrm{w}+h(\zeta))-s^{(j)}(\theta_\mathrm{w}-h(\zeta))\right]\right.$$
$$\left.-\frac{\bar{\delta}\sin\left(\bar{\delta}\zeta\right)h'(\zeta)}{\cos\left(\bar{\delta}\zeta\right)-\sin\left(\bar{\delta}z\right)}\left[s^{(j)}(-\theta_\mathrm{w}+h(\zeta))-s^{(j)}(-\theta_\mathrm{w}-h(\zeta))\right]\right)\mathrm{d}\zeta. \tag{4.30}$$

Evaluation of this integral formula is difficult due to the numerous singularities of the integrand. The functions $h(\zeta)$ and $h'(\zeta)$ indicate the presence of an infinite number of branch cuts, however their

combination causes the cut centred at the origin to be cancelled out. The spectral functions $s^{(j)}$ have an infinite number of simple poles, which we will call the spectral poles, located either on the real line or the branch cuts. The rest of the integrand contributes one last set of simple poles located at $\zeta = (2n-1)\bar{\theta}_w \pm z$ where $n \in \mathbb{Z}$ which we will call the z-poles.

This integral formula for $q^{(j)}(z)$ is valid for $|\mathrm{Re}\{z\}| < \bar{\theta}_w$, however, when z is outside this strip, the contour must deform so that it passes in between the pair of poles at $\zeta = \pm\bar{\theta}_w - z$ and also in between the pair of poles at $\zeta = \pm\bar{\theta}_w + z$. This is demonstrated in Figure 7 with $\Theta = \bar{\theta}_w$.

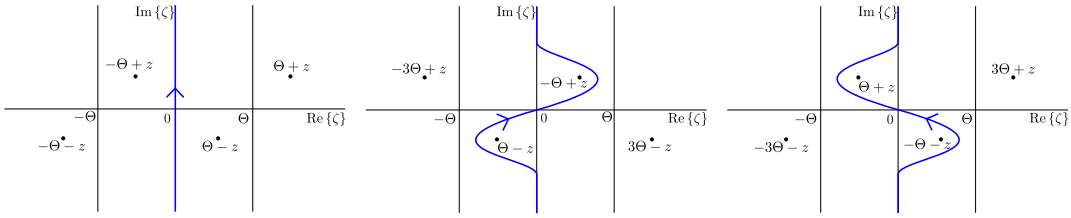

FIG. 7: The local pole locations and the normal integration contour for $|\mathrm{Re}\{z\}| < \Theta$ (left). The local pole locations and the adapted integration contour for $\mathrm{Re}\{z\} > \Theta$ (middle). The local pole locations and the adapted integration contour for $\mathrm{Re}\{z\} < -\Theta$ (right). Note that if $\mathrm{Im}\{z\} < 0$ then all these images are flipped vertically.

Using the ideas from Figure 7, it is not difficult to show that the formula (4.30) satisfies the boundary functional conditions (3.18). For the initial inhomogeneous Dirichlet problem (for $j = 0$), the formula (4.30) simplifies further using the antisymmetry property (3.8),

$$q^{(0)}(z) = \frac{1}{2\pi i}\int_{-i\infty}^{i\infty}\left(\frac{\bar{\delta}\sin\left(\bar{\delta}\zeta\right)h'(\zeta)s^{(0)}(\theta_w + h(\zeta))}{\cos\left(\bar{\delta}\zeta\right)+\sin\left(\bar{\delta}z\right)} - \frac{\bar{\delta}\sin\left(\bar{\delta}\zeta\right)h'(\zeta)s^{(0)}(-\theta_w + h(\zeta))}{\cos\left(\bar{\delta}\zeta\right)-\sin\left(\bar{\delta}z\right)}\right)\mathrm{d}\zeta. \tag{4.31}$$

We discuss the asymptotic behaviour of (4.31) as $\mathrm{Im}\{z\} \to \pm\infty$ in Appendix B. We should also note that if $s^{(j)}(z^*) = \left(s^{(j)}(z)\right)^*$, then $q^{(j)}(z^*) = \left(q^{(j)}(z)\right)^*$, which can be shown using (4.30) for all j.

4.2 *Inhomogeneous Neumann problem* $\left(\mathcal{P}_{\Phi}^{(j+1)}\right)$

For these problems, the total wave field $\Phi^{(j+1)}$ is exterior to the wedge scatterer hence we have $k = k_1$, $\Theta = \theta_w$, $u(r,\theta) = \Phi^{(j+1)}(r,\theta)$ (with $j = 0, 1, 2...$). We define the known boundary data as V_1 and V_2 with the following definitions,

$$V_1(z) = V(\cos(\theta_w - z), \theta_w) = \int_0^\infty \frac{1}{ik_1 r}\frac{\partial \Phi^{(j+1)}}{\partial \theta}\bigg|_{\theta=\theta_w} e^{ik_1 r\cos(\theta_w - z)}\mathrm{d}r, \tag{4.32}$$

$$V_2(z) = V(\cos(\theta_w - z), -\theta_w) = \int_0^\infty \frac{1}{ik_1 r}\frac{\partial \Phi^{(j+1)}}{\partial \theta}\bigg|_{\theta=-\theta_w} e^{ik_1 r\cos(\theta_w - z)}\mathrm{d}r. \tag{4.33}$$

Both of these definitions can be expressed explicitly in terms of $q^{(j)}$ using the identity (4.6) and the boundary functional conditions (3.25), leading to

$$V_1(z) = \frac{i}{k_1}\left[q^{(j)}(-\bar{\theta}_\mathrm{w} + g(\theta_\mathrm{w} - z)) + q^{(j)}(-\bar{\theta}_\mathrm{w} - g(\theta_\mathrm{w} - z))\right], \tag{4.34}$$

$$V_2(z) = \frac{i}{k_1}\left[q^{(j)}(\bar{\theta}_\mathrm{w} + g(\theta_\mathrm{w} - z)) + q^{(j)}(\bar{\theta}_\mathrm{w} - g(\theta_\mathrm{w} - z))\right]. \tag{4.35}$$

The Wiener-Hopf system (4.3) is therefore,

$$\begin{aligned} V(\cos(z),0) &= -\frac{1}{2}\sin(\theta_\mathrm{w} - z)\left[U(\cos(\theta_\mathrm{w} - z), -\theta_\mathrm{w}) - U(\cos(\theta_\mathrm{w} - z), \theta_\mathrm{w})\right] + \frac{1}{2}\left[V_1(z) + V_2(z)\right], \\ \sin(z)U(\cos(z),0) &= -\frac{1}{2}\sin(\theta_\mathrm{w} - z)\left[U(\cos(\theta_\mathrm{w} - z), -\theta_\mathrm{w}) + U(\cos(\theta_\mathrm{w} - z), \theta_\mathrm{w})\right] - \frac{1}{2}\left[V_1(z) - V_2(z)\right]. \end{aligned} \tag{4.36}$$

The method to solve the Wiener-Hopf system (4.36) is the same as the inhomogeneous Dirichlet problems except for a few key differences. This time we will need to reuse the mapping (4.13) with $\Theta = \theta_\mathrm{w}$ and we will also need to factorise both $\sin(z)$ and $\sin(\theta_\mathrm{w} - z)$ (see section 3.1 in Nethercote et al. (2019)). The end result is the following integral formula,

$$\begin{aligned} s^{(j+1)}(z) = \frac{1}{4\pi i}\int_{-i\infty}^{i\infty}\Bigg(&\frac{\delta\cos(\delta z)}{\cos(\delta\zeta) + \sin(\delta z)}\left[q^{(j)}(\bar{\theta}_\mathrm{w} + g(\zeta)) + q^{(j)}(\bar{\theta}_\mathrm{w} - g(\zeta))\right] \\ &+ \frac{\delta\cos(\delta z)}{\cos(\delta\zeta) - \sin(\delta z)}\left[q^{(j)}(-\bar{\theta}_\mathrm{w} + g(\zeta)) + q^{(j)}(-\bar{\theta}_\mathrm{w} - g(\zeta))\right]\Bigg)\mathrm{d}\zeta. \end{aligned} \tag{4.37}$$

The evaluation of this formula has shared difficulties with (4.30). The presence of $g(\zeta)$ will produce an infinite number of branch cuts, but the cut centred at the origin is cancelled out. The $q^{(j)}$ functions have an infinite number of simple poles contained on the real line (called the spectral poles). The rest of the integrand contributes one last set of simple poles located at $\zeta = (2n-1)\theta_\mathrm{w} \pm z$ where $n \in \mathbb{Z}$ (called the z-poles).

This integral formula for $s^{(j+1)}(z)$ is valid for $|\mathrm{Re}\{z\}| < \theta_\mathrm{w}$, however when z is outside this strip the contour must deform so that it passes in between the pair of poles at $\zeta = \pm\theta_\mathrm{w} - z$ and also in between the pair of poles at $\zeta = \pm\theta_\mathrm{w} + z$. This is demonstrated in Figure 7 with $\Theta = \theta_\mathrm{w}$.

Similarly to (4.30), it is not difficult to show that the formula (4.37) satisfies the boundary functional conditions (3.25). Also note that if $q^{(j)}(z^*) = (q^{(j)}(z))^*$ then $s^{(j+1)}(z^*) = (s^{(j+1)}(z))^*$, which alongside the last note of Section 4.1 and the conjugacy property (3.10) allows us to conclude that $q^{(j)}$ and $s^{(j)}$ satisfy the property $p(z^*) = (p(z))^*$ for all j.

Recall the alternate case in the edge conditions where $\delta > 2$. The above methodology does not change and the functions used in Liouville's theorem ($\mathcal{M}_1$ and $\mathcal{M}_2$) will still decay to zero as $|\alpha| \to \infty$ preserving the obtained solution in this case.

4.3 *Example: Penetrable half-space*

As an example to test (4.30) and (4.37), we will look at a simple case where the exact solution can be derived using conventional methods. In this example, we set $\bar{\theta}_\mathrm{w} = \theta_\mathrm{w} = \frac{\pi}{2}$ (corresponding to a half-space problem) so that the scattered part of the solution consists of a single reflected wave and a single

transmitted wave,

$$\Phi(r,\theta) = \Phi_{\rm I} + R\Phi_{\rm R}, \quad \Psi(r,\theta) = T\Phi_{\rm T}. \tag{4.38}$$

Here $\Phi_{\rm I}$, $\Phi_{\rm R}$ and $\Phi_{\rm T}$ represent the incident, reflected and transmitted waves respectively and are given by

$$\Phi_{\rm I} = e^{-ik_1 r\cos(\theta-\theta_{\rm I})}, \quad \Phi_{\rm R} = e^{ik_1 r\cos(\theta+\theta_{\rm I})}, \quad \Phi_{\rm T} = e^{-ik_2 r\cos(\theta-\theta_{\rm T})}. \tag{4.39}$$

The transmission angle $\theta_{\rm T}$ is found using Snell's Law,

$$\theta_{\rm T} = \sin^{-1}\left(\lambda_k \sin(\theta_{\rm I})\right) = \frac{\pi}{2} - g\left(\frac{\pi}{2} - \theta_{\rm I}\right). \tag{4.40}$$

The reflection and transmission coefficients (R and T respectively) are determined by the boundary conditions,

$$T = R+1, \quad R = \frac{\frac{\lambda_k\cos(\theta_{\rm I})}{\cos(\theta_{\rm T})} - \lambda}{\frac{\lambda_k\cos(\theta_{\rm I})}{\cos(\theta_{\rm T})} + \lambda} = 1 - \frac{2\lambda}{g'\left(\frac{\pi}{2}-\theta_{\rm I}\right)+\lambda}. \tag{4.41}$$

Figure 8 is a diagram illustrating the half-space and the components of the exact solution (4.38).

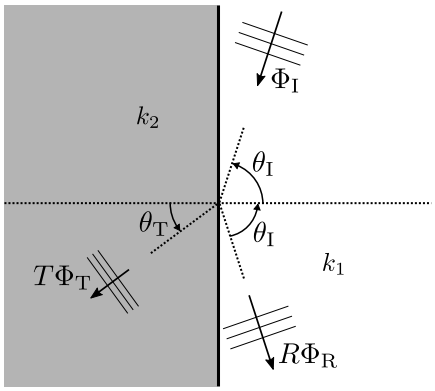

FIG. 8: Penetrable half-space geometry.

Finding the Taylor series expansion about $\lambda = 0$ of the exact solution (4.38) allows us to determine the expected solution of (4.30) and (4.37). Noting the expansions of the reflection and transmission coefficients,

$$R = 1 + 2\sum_{j=1}^{\infty}\left(\frac{-\lambda}{g'\left(\frac{\pi}{2}-\theta_{\rm I}\right)}\right)^j, \quad T = 2\sum_{j=0}^{\infty}\left(\frac{-\lambda}{g'\left(\frac{\pi}{2}-\theta_{\rm I}\right)}\right)^j, \tag{4.42}$$

each of the components in the high-contrast approximation are given as,

$$\Phi^{(0)} = \Phi_{\rm I} + \Phi_{\rm R}, \quad \Phi^{(j)} = 2\left(\frac{-1}{g'\left(\frac{\pi}{2}-\theta_{\rm I}\right)}\right)^j \Phi_{\rm R}, \quad j = 1,2...,$$

$$\Psi^{(j)} = 2\left(\frac{-1}{g'\left(\frac{\pi}{2}-\theta_{\rm I}\right)}\right)^j \Phi_{\rm T}, \quad j = 0,1,2.... \tag{4.43}$$

We already know the corresponding spectral function for $\Phi^{(0)}$,

$$s^{(0)}(z) = \frac{\cos(z)}{\sin(z) - \sin(\theta_{\mathrm{I}})}. \tag{4.44}$$

We use formulae adapted from (4.7) to derive what to expect for the other spectral functions. This means that for $s^{(j)}(z)$,

$$\begin{aligned} s^{(j)}(z) &= \frac{ik_1}{2}\int_0^{\infty}\left[\sin(z)\Phi^{(j)} - \frac{1}{ik_1 r}\frac{\partial \Phi^{(j)}}{\partial \theta}\right]_{\theta=0} e^{ik_1 r\cos(z)}\mathrm{d}r, \\ &= -\left(\frac{-1}{g'\left(\frac{\pi}{2}-\theta_{\mathrm{I}}\right)}\right)^j \frac{\sin(z)+\sin(\theta_{\mathrm{I}})}{\cos(z)+\cos(\theta_{\mathrm{I}})}. \end{aligned} \tag{4.45}$$

Other equivalent forms for $s^{(j)}(z)$ are,

$$s^{(j)}(z) = \left(\frac{-1}{g'\left(\frac{\pi}{2}-\theta_{\mathrm{I}}\right)}\right)^j \frac{\cos(z)-\cos(\theta_{\mathrm{I}})}{\sin(z)-\sin(\theta_{\mathrm{I}})} = -\left(\frac{-1}{g'\left(\frac{\pi}{2}-\theta_{\mathrm{I}}\right)}\right)^j \tan\left(\frac{z+\theta_{\mathrm{I}}}{2}\right). \tag{4.46}$$

Similarly for $q^{(j)}(z)$,

$$\begin{aligned} q^{(j)}(z) &= \frac{ik_2}{2}\int_0^{\infty}\left[\sin(z)\Psi^{(j)} - \frac{1}{ik_2 r}\frac{\partial \Psi^{(j)}}{\partial \theta}\right]_{\theta=\pi} e^{ik_2 r\cos(z)}\mathrm{d}r, \\ &= -\left(\frac{-1}{g'\left(\frac{\pi}{2}-\theta_{\mathrm{I}}\right)}\right)^j \frac{\sin(z)-\sin(\theta_{\mathrm{T}})}{\cos(z)+\cos(\theta_{\mathrm{T}})}, \end{aligned} \tag{4.47}$$

with the other equivalent forms,

$$q^{(j)}(z) = \left(\frac{-1}{g'\left(\frac{\pi}{2}-\theta_{\mathrm{I}}\right)}\right)^j \frac{\cos(z)-\cos(\theta_{\mathrm{T}})}{\sin(z)+\sin(\theta_{\mathrm{T}})} = -\left(\frac{-1}{g'\left(\frac{\pi}{2}-\theta_{\mathrm{I}}\right)}\right)^j \tan\left(\frac{z-\theta_{\mathrm{T}}}{2}\right). \tag{4.48}$$

We now rederive $q^{(j)}(z)$ and $s^{(j)}(z)$ via the integrals (4.30) and (4.37) as proof of validity in the half-space case. For $q^{(0)}(z)$, we use (4.31), noting that $\delta = \bar{\delta} = 1$,

$$q^{(0)}(z) = \frac{1}{2\pi i}\int_{-i\infty}^{i\infty}\left(\frac{\sin(\zeta)h'(\zeta)s^{(0)}\left(\frac{\pi}{2}+h(\zeta)\right)}{\cos(\zeta)+\sin(z)} - \frac{\sin(\zeta)h'(\zeta)s^{(0)}\left(-\frac{\pi}{2}+h(\zeta)\right)}{\cos(\zeta)-\sin(z)}\right)\mathrm{d}\zeta. \tag{4.49}$$

Using the formulae (2.18), (4.40) and (4.44), we find that,

$$h'(\zeta)s^{(0)}\left(\pm\frac{\pi}{2}+h(\zeta)\right) = -\frac{\sin(\zeta)}{\cos(\zeta)\mp\sin(\theta_{\mathrm{T}})},$$

hence,

$$q^{(0)}(z) = \frac{1}{2\pi i}\int_{-i\infty}^{i\infty}\left(\frac{\sin^2(\zeta)}{(\cos(\zeta)-\sin(z))(\cos(\zeta)+\sin(\theta_{\mathrm{T}}))} - \frac{\sin^2(\zeta)}{(\cos(\zeta)+\sin(z))(\cos(\zeta)-\sin(\theta_{\mathrm{T}}))}\right)\mathrm{d}\zeta. \tag{4.50}$$

This can be evaluated exactly by considering the box contour with the corner points $\zeta = \pm i\infty, -\frac{\pi}{2} \pm i\infty$,

$$\oint = \int_{-i\infty}^{i\infty} - \int_{-\frac{\pi}{2}+i\infty}^{i\infty} - \int_{-\frac{\pi}{2}-i\infty}^{-\frac{\pi}{2}+i\infty} + \int_{-\frac{\pi}{2}-i\infty}^{-i\infty}. \tag{4.51}$$

Obviously the first integral on the right hand side of (4.51) is $q^{(0)}(z)$. As $|\mathrm{Im}\{\zeta\}| \to \infty$, the integrand has the leading order behaviour, $O\left(e^{-|\mathrm{Im}\{\zeta\}|}\right)$. This implies that the integrals from $-\frac{\pi}{2} \pm i\infty$ to $\pm i\infty$ are 0. The integrand is antisymmetric about the point $\zeta = -\frac{\pi}{2}$, hence the integral from $-\frac{\pi}{2} - i\infty$ to $-\frac{\pi}{2} + i\infty$ is zero too. Lastly $\oint$ is equal to the sum of the anticlockwise residues from poles in the strip $\mathrm{Re}\{\zeta\} \in \left(-\frac{\pi}{2}, 0\right)$. The only poles in this strip are located at $\zeta = -\frac{\pi}{2} + z$ and $-\frac{\pi}{2} + \theta_\mathrm{T}$ and their respective residues are,

$$\begin{aligned} &\frac{1}{2\pi i}\frac{\cos(z)}{\sin(z)+\sin(\theta_\mathrm{T})}, \quad \text{at } \zeta = -\frac{\pi}{2} + z, \\ -&\frac{1}{2\pi i}\frac{\cos(\theta_\mathrm{T})}{\sin(z)+\sin(\theta_\mathrm{T})}, \quad \text{at } \zeta = -\frac{\pi}{2} + \theta_\mathrm{T}. \end{aligned}$$

Hence $q^{(0)}(z)$ is evaluated to,

$$q^{(0)}(z) = \frac{\cos(z) - \cos(\theta_\mathrm{T})}{\sin(z) + \sin(\theta_\mathrm{T})}, \tag{4.52}$$

which matches exactly with (4.48) with $j = 0$. Assuming that (4.48) is true, we find $s^{(j+1)}(z)$ for $j \geqslant 0$ by the integral (4.37),

$$\begin{aligned} s^{(j+1)}(z) = \frac{1}{4\pi i}\int_{-i\infty}^{i\infty} \Bigg(&\frac{\cos(z)}{\cos(\zeta)+\sin(z)} \left[q^{(j)}\left(\frac{\pi}{2} + g(\zeta)\right) + q^{(j)}\left(\frac{\pi}{2} - g(\zeta)\right)\right] \\ &+ \frac{\cos(z)}{\cos(\zeta)-\sin(z)} \left[q^{(j)}\left(-\frac{\pi}{2} + g(\zeta)\right) + q^{(j)}\left(-\frac{\pi}{2} - g(\zeta)\right)\right] \Bigg) \mathrm{d}\zeta, \end{aligned} \tag{4.53}$$

where,

$$\begin{aligned} q^{(j)}\left(\frac{\pi}{2} \pm g(\zeta)\right) &= -\left(\frac{-1}{g'\left(\frac{\pi}{2} - \theta_\mathrm{I}\right)}\right)^j \frac{\cos(\theta_\mathrm{T}) \pm \sin(g(\zeta))}{\cos(g(\zeta)) + \sin(\theta_\mathrm{T})}, \\ q^{(j)}\left(-\frac{\pi}{2} \pm g(\zeta)\right) &= \left(\frac{-1}{g'\left(\frac{\pi}{2} - \theta_\mathrm{I}\right)}\right)^j \frac{\cos(\theta_\mathrm{T}) \mp \sin(g(\zeta))}{\cos(g(\zeta)) - \sin(\theta_\mathrm{T})}. \end{aligned}$$

Applying the formulae (2.18) and (4.40) will simplify (4.53) to,

$$\begin{aligned} s^{(j+1)}(z) = \left(\frac{-1}{g'\left(\frac{\pi}{2} - \theta_\mathrm{I}\right)}\right)^{j+1} \frac{1}{2\pi i}\int_{-i\infty}^{i\infty} \Bigg(&\frac{\cos(z)\cos(\theta_\mathrm{I})}{(\cos(\zeta)+\sin(z))(\cos(\zeta)+\sin(\theta_\mathrm{I}))} \\ &- \frac{\cos(z)\cos(\theta_\mathrm{I})}{(\cos(\zeta)-\sin(z))(\cos(\zeta)-\sin(\theta_\mathrm{I}))} \Bigg) \mathrm{d}\zeta. \end{aligned} \tag{4.54}$$

Similarly to (4.50), this can be evaluated exactly by completing the contour via the points $\zeta = -\frac{\pi}{2} \pm i\infty$. As $|\mathrm{Im}\{\zeta\}| \to \infty$, the integrand has the leading order behaviour, $O\left(e^{-3|\mathrm{Im}\{\zeta\}|}\right)$, which implies that the integrals from $-\frac{\pi}{2} \pm i\infty$ to $\pm i\infty$ are 0. The integrand is also antisymmetric about the point $\zeta = -\frac{\pi}{2}$, hence the integral from $-\frac{\pi}{2} - i\infty$ to $-\frac{\pi}{2} + i\infty$ is zero too. Lastly $\oint$ is equal to the sum of the anticlockwise residues from poles in the strip $\mathrm{Re}\{\zeta\} \in \left(-\frac{\pi}{2}, 0\right)$ which are,

$$
\begin{aligned}
&-\left(\frac{-1}{g'\left(\frac{\pi}{2}-\theta_\mathrm{I}\right)}\right)^{j+1} \frac{1}{2\pi i} \frac{\cos(\theta_\mathrm{I})}{\sin(z)-\sin(\theta_\mathrm{I})}, \quad \text{at } \zeta = -\frac{\pi}{2} + z, \\
&\left(\frac{-1}{g'\left(\frac{\pi}{2}-\theta_\mathrm{I}\right)}\right)^{j+1} \frac{1}{2\pi i} \frac{\cos(z)}{\sin(z)-\sin(\theta_\mathrm{I})}, \quad \text{at } \zeta = -\frac{\pi}{2} + \theta_\mathrm{I}.
\end{aligned}
$$

Hence $s^{(j+1)}(z)$ is evaluated to,

$$
s^{(j+1)}(z) = \left(\frac{-1}{g'\left(\frac{\pi}{2}-\theta_\mathrm{I}\right)}\right)^{j+1} \frac{\cos(z)-\cos(\theta_\mathrm{I})}{\sin(z)-\sin(\theta_\mathrm{I})}, \tag{4.55}
$$

which matches perfectly with (4.46). Lastly, assuming that (4.46) is true, we find $q^{(j)}(z)$ for $j \geqslant 1$ by the integral (4.30),

$$
\begin{aligned}
q^{(j)}(z) = \frac{1}{4\pi i} \int_{-i\infty}^{i\infty} \Bigg(&\frac{\sin(\zeta)h'(\zeta)}{\cos(\zeta)+\sin(z)} \left[s^{(j)}\left(\frac{\pi}{2}+h(\zeta)\right) - s^{(j)}\left(\frac{\pi}{2}-h(\zeta)\right)\right] \\
&- \frac{\sin(\zeta)h'(\zeta)}{\cos(\zeta)-\sin(z)} \left[s^{(j)}\left(-\frac{\pi}{2}+h(\zeta)\right) - s^{(j)}\left(-\frac{\pi}{2}-h(\zeta)\right)\right] \Bigg) \mathrm{d}\zeta,
\end{aligned} \tag{4.56}
$$

where,

$$
\begin{aligned}
s^{(j)}\left(\frac{\pi}{2} \pm h(\zeta)\right) &= -\left(\frac{-1}{g'\left(\frac{\pi}{2}-\theta_\mathrm{I}\right)}\right)^{j} \frac{\cos(\theta_\mathrm{I}) \pm \sin(h(\zeta))}{\cos(h(\zeta))-\sin(\theta_\mathrm{I})}, \\
s^{(j)}\left(-\frac{\pi}{2} \pm h(\zeta)\right) &= -\left(\frac{-1}{g'\left(\frac{\pi}{2}-\theta_\mathrm{I}\right)}\right)^{j} \frac{\pm\sin(h(\zeta)) - \cos(\theta_\mathrm{I})}{\cos(h(\zeta))+\sin(\theta_\mathrm{I})}.
\end{aligned}
$$

After substitution and a little rearrangement we find that,

$$
\begin{aligned}
q^{(j)}(z) = \left(\frac{-1}{g'\left(\frac{\pi}{2}-\theta_\mathrm{I}\right)}\right)^{j} \frac{1}{2\pi i} \int_{-i\infty}^{i\infty} \Bigg(&\frac{\sin(\zeta)\sin(h(\zeta))h'(\zeta)}{(\cos(\zeta)-\sin(z))(\cos(h(\zeta))+\sin(\theta_\mathrm{I}))} \\
&- \frac{\sin(\zeta)\sin(h(\zeta))h'(\zeta)}{(\cos(\zeta)+\sin(z))(\cos(h(\zeta))-\sin(\theta_\mathrm{I}))} \Bigg) \mathrm{d}\zeta.
\end{aligned} \tag{4.57}
$$

Together with (2.18) and (4.40), we can simplify (4.57) to,

$$\begin{aligned} q^{(j)}(z) &= \left(\frac{-1}{g'\left(\frac{\pi}{2}-\theta_{\mathrm{I}}\right)}\right)^{j} \frac{1}{2\pi i}\int_{-i\infty}^{i\infty}\left(\frac{\sin^2(\zeta)}{(\cos(\zeta)-\sin(z))(\cos(\zeta)+\sin(\theta_{\mathrm{T}}))}\right. \\ &\quad \left. -\frac{\sin^2(\zeta)}{(\cos(\zeta)+\sin(z))(\cos(\zeta)-\sin(\theta_{\mathrm{T}}))}\right)\mathrm{d}\zeta, \\ &= \left(\frac{-1}{g'\left(\frac{\pi}{2}-\theta_{\mathrm{I}}\right)}\right)^{j} q^{(0)}(z), \end{aligned} \tag{4.58}$$

which matches exactly with (4.48). Equations (4.52), (4.55) and (4.58) prove that the high-contrast iterative scheme is valid for the penetrable half-space problem. Another important aspect to investigate is the convergence of the asymptotic series for this example.

Figure 9 is a set of MATLAB density plots of the exact solution (4.38) and the asymptotic solution (4.43) with an increasing number of components and the parameter values: $k_1 = 1$, $k_2 = 2$, $\lambda = 0.1$ and $\theta_{\mathrm{I}} = \pi/4$. These figures clearly show the convergence of the high-contrast approximation onto the exact solution.

One can show the nature of the convergence of the series more clearly by looking at the summations in (4.42) which clearly converge if $0 < \lambda < g'\left(\frac{\pi}{2}-\theta_{\mathrm{I}}\right)$. Figure 10 (left) shows the convergence of the reflection and transmission coefficients in series form (4.42) to the exact solution as the approximation order increases. Figure 10 (right) shows the absolute error of this convergence as the approximation order increases.

5. Strategies for numerical evaluation

So far, we have defined a high-contrast asymptotic approximation to the penetrable wedge problem and used the Wiener-Hopf technique to find the spectral components in integral form,

$$q^{(j)}(z) = \frac{1}{2\pi i}\int_{-i\infty}^{i\infty} q_{\mathrm{int}}^{(j)}(z,\zeta)\mathrm{d}\zeta, \quad s^{(j+1)}(z) = \frac{1}{2\pi i}\int_{-i\infty}^{i\infty} s_{\mathrm{int}}^{(j+1)}(z,\zeta)\mathrm{d}\zeta, \tag{5.1}$$

where,

$$\begin{aligned} q_{\mathrm{int}}^{(j)}(z,\zeta) &= \frac{\bar{\delta}\sin\left(\bar{\delta}\zeta\right)h'(\zeta)}{2\left(\cos\left(\bar{\delta}\zeta\right)+\sin\left(\bar{\delta}z\right)\right)}\left[s^{(j)}(\theta_{\mathrm{w}}+h(\zeta))-s^{(j)}(\theta_{\mathrm{w}}-h(\zeta))\right] \\ &\quad + \frac{\bar{\delta}\sin\left(\bar{\delta}\zeta\right)h'(\zeta)}{2\left(\cos\left(\bar{\delta}\zeta\right)-\sin\left(\bar{\delta}z\right)\right)}\left[s^{(j)}(-\theta_{\mathrm{w}}-h(\zeta))-s^{(j)}(-\theta_{\mathrm{w}}+h(\zeta))\right], \end{aligned} \tag{5.2}$$

$$\begin{aligned} s_{\mathrm{int}}^{(j+1)}(z,\zeta) &= \frac{\delta\cos\left(\delta z\right)}{2\left(\cos\left(\delta\zeta\right)+\sin\left(\delta z\right)\right)}\left[q^{(j)}(\bar{\theta}_{\mathrm{w}}+g(\zeta))+q^{(j)}(\bar{\theta}_{\mathrm{w}}-g(\zeta))\right] \\ &\quad + \frac{\delta\cos\left(\delta z\right)}{2\left(\cos\left(\delta\zeta\right)-\sin\left(\delta z\right)\right)}\left[q^{(j)}(-\bar{\theta}_{\mathrm{w}}-g(\zeta))+q^{(j)}(-\bar{\theta}_{\mathrm{w}}+g(\zeta))\right]. \end{aligned} \tag{5.3}$$

We have showed the validity of this representation for the half-space case, but now we wish to evaluate it for a more general wedge angle. This situation is much more difficult and the integrals will need to be evaluated numerically. While the integrals (5.1) are valid for any value $\theta_{\mathrm{w}} \in (0,\pi)$, in our examples we restrict $\theta_{\mathrm{w}} > \pi/2$ for convenience because the GO component is simpler to find in this configuration.

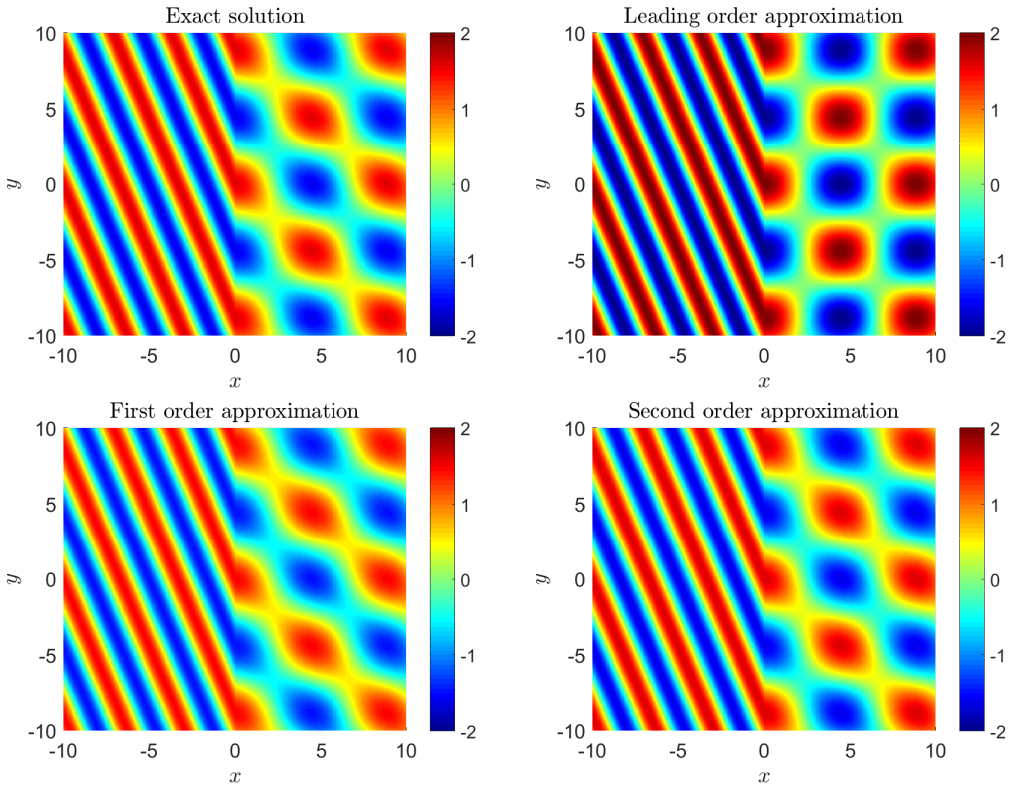

FIG. 9: A comparison of the exact solution (4.38) (upper left) and the asymptotic solution (4.43) including components up to $j = 0$ (upper right), $j = 1$ (lower left) and $j = 2$ (lower right). Here we have $k_1 = 1$, $k_2 = 2$, $\lambda = 0.1$ and $\theta_I = \pi/4$.

5.1 *Numerical evaluation of spectral integral*

In order to guarantee accuracy, one must ensure that the integration contour follows a path that does not approach any of the singularities too closely. One way to enforce this is to use an adaptive integration contour (a contour that depends on z) that steers itself around the poles (for example see Figure 7). In practice however, an integration contour that explicitly depends on z is obviously inefficient. We therefore fix the integration contour to be a straight line with endpoints $\pm i\infty$ but we must still be cautious about singularities.

The branch cuts will not be a concern if we do not consider contour paths going beyond $|\mathrm{Re}\{\zeta\}| = \pi$. This is because, in both (5.2) and (5.3), the cut centred at $\zeta = 0$ has been cancelled out which means that the nearest cuts to the contour are the ones centred at $\zeta = \pm\pi$.

In both integrands, the spectral poles are fixed in place (meaning that their locations are independent of z). The locations and residues of these spectral poles can be found through consideration of the poles of $s^{(0)}(z)$ and the boundary functional conditions (3.18) and (3.25), recalling that $q^{(j)}(z)$ and $s^{(j+1)}(z)$ have pole-free strips (see (3.15),(3.23)). In most cases these poles are far enough from the contour to not cause any issues. For this reason, we do not discuss these poles in detail here.

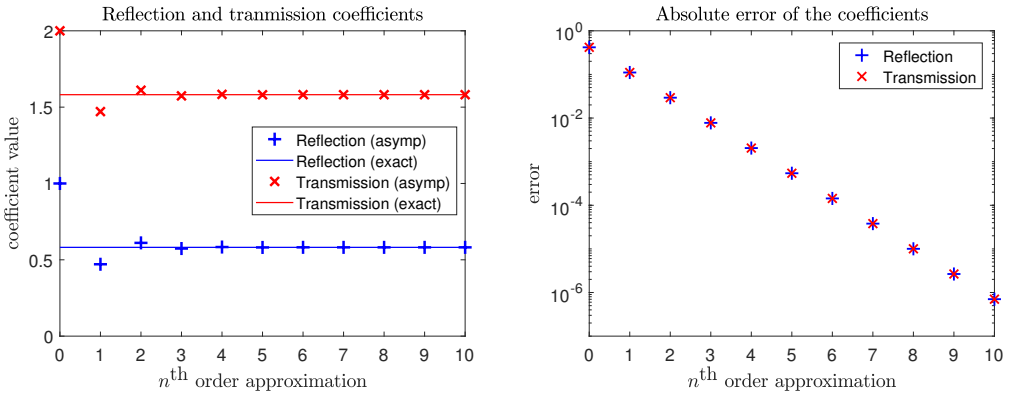

FIG. 10: A comparison between the exact and asymptotic forms of the reflection and transmission coefficients (left) and the absolute error (right) as the approximation order increases. Here we have $k_1 = 1$, $k_2 = 2$, $\lambda = 0.1$ and $\theta_I = \pi/4$.

The last set of poles (the z-poles) are located at $\zeta = (2n-1)\Theta \pm z$ where $\Theta = \bar{\theta}_w$ or θ_w (for $q^{(j)}(z)$ and $s^{(j+1)}(z)$ respectively) and $n \in \mathbb{Z}$. These poles approach the contour when $\mathrm{Re}\{z\} \to \mp(2n-1)\Theta$. After they cross the contour, their residues will need to be added to retain continuity. For $q^{(j)}_{\text{int}}$, the residues of the poles at $\zeta = (2n-1)\bar{\theta}_w \pm z$ are given by

$$\mathrm{Res}(q^{(j)}_{\text{int}}, (2n-1)\bar{\theta}_w \pm z) = \frac{1}{2}h'((2n-1)\bar{\theta}_w \pm z)\Big[s^{(j)}(\mp(-1)^n(\theta_w - h((2n-1)\bar{\theta}_w \pm z))) - s^{(j)}(\mp(-1)^n(\theta_w + h((2n-1)\bar{\theta}_w \pm z)))\Big], \tag{5.4}$$

while for $s^{(j+1)}_{\text{int}}$, the residues of the poles at $\zeta = (2n-1)\theta_w \pm z$ are

$$\mathrm{Res}(s^{(j+1)}_{\text{int}}, (2n-1)\theta_w \pm z) = \frac{(-1)^n}{2}\Big[q^{(j)}(\mp(-1)^n\bar{\theta}_w + g((2n-1)\theta_w \pm z)) + q^{(j)}(\mp(-1)^n\bar{\theta}_w - g((2n-1)\theta_w \pm z))\Big]. \tag{5.5}$$

Whenever such a crossing occurs, two poles will cross the contour at the same time in opposite directions due to the evenness of the integrands (see Figure 11). These poles will have residues that are equal but with opposite sign.

When one of these poles is getting too close to the contour, the numerical integration will begin to lose accuracy. To prevent this, we shall shift the entire integration contour a distance Θ to the right collecting the residues of any crossed poles. This means that we have two cases for evaluation.

Original contour: use $\displaystyle\int_{-i\infty}^{i\infty}$ when $\left(2n-\frac{1}{2}\right)\Theta < \mathrm{Re}\{z\} \leqslant \left(2n+\frac{1}{2}\right)\Theta$, (5.6)

Shifted contour: use $\displaystyle\int_{\Theta-i\infty}^{\Theta+i\infty}$ plus residues when $\left(2n+\frac{1}{2}\right)\Theta < \mathrm{Re}\{z\} \leqslant \left(2n+\frac{3}{2}\right)\Theta$, (5.7)

where $n \in \mathbb{Z}$. The strips in (5.6) are chosen because the local z-poles are closer to the shifted contour than the original (and vice versa for (5.7)). This is demonstrated in Figure 12 for when $\mathrm{Re}\{z\} \to \Theta^-$.

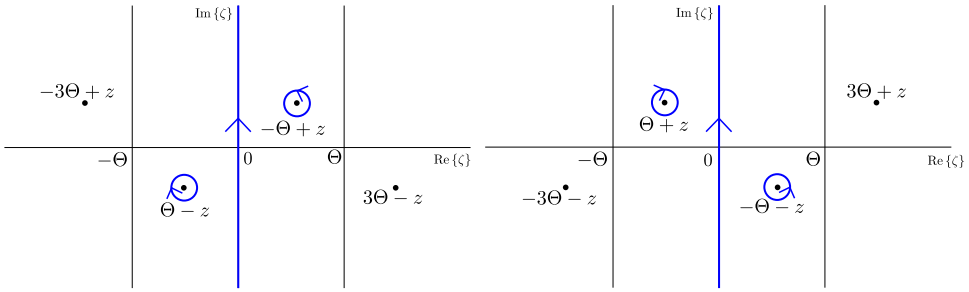

FIG. 11: Diagrams of the ζ-plane for when z-poles have crossed the integration contour. The relevant poles to include are circled for the cases where $\mathrm{Re}\{z\} > \Theta$ (left) and $\mathrm{Re}\{z\} < -\Theta$ (right).

Shifting the contour will cross a single z-pole and at most one spectral pole (likely more if we had $\theta_\mathrm{w} < \pi/2$). For $q_\mathrm{int}^{(j)}(z)$ the spectral pole is located at $\zeta = g(\theta_\mathrm{w} - \theta_\mathrm{I})$ (crossed only if $g(\theta_\mathrm{w} - \theta_\mathrm{I}) < \bar{\theta}_\mathrm{w}$) and the value of the residue is,

$$\mathrm{Res}(q_\mathrm{int}^{(j)}, g(\theta_\mathrm{w} - \theta_\mathrm{I})) = \left(\frac{-1}{g'(\theta_\mathrm{w} - \theta_\mathrm{I})}\right)^j \frac{\bar{\delta}\sin\left(\bar{\delta} g(\theta_\mathrm{w} - \theta_\mathrm{I})\right)}{\sin(\bar{\delta} z) + \cos\left(\bar{\delta} g(\theta_\mathrm{w} - \theta_\mathrm{I})\right)}. \tag{5.8}$$

For $s_\mathrm{int}^{(j+1)}(z)$ the spectral pole is located at $\zeta = \theta_\mathrm{w} - \theta_\mathrm{I}$ with the residue value,

$$\mathrm{Res}(s_\mathrm{int}^{(j+1)}, \theta_\mathrm{w} - \theta_\mathrm{I}) = -\left(\frac{-1}{g'(\theta_\mathrm{w} - \theta_\mathrm{I})}\right)^{j+1} \frac{\delta\cos(\delta z)}{\sin(\delta z) - \sin(\delta\theta_\mathrm{I})}. \tag{5.9}$$

For convenience, we define R_spec as the spectral pole contribution,

$$R_\mathrm{spec} = \begin{cases} \mathcal{H}(\bar{\theta}_\mathrm{w} - g(\theta_\mathrm{w} - \theta_\mathrm{I}))\mathrm{Res}(q_\mathrm{int}^{(j)}, g(\theta_\mathrm{w} - \theta_\mathrm{I})) & \text{for } q^{(j)}, \\ \mathrm{Res}(s_\mathrm{int}^{(j+1)}, \theta_\mathrm{w} - \theta_\mathrm{I}) & \text{for } s^{(j+1)}. \end{cases} \tag{5.10}$$

It is important to note that each time the contour is shifted or shifted back, a different z-pole is crossed.

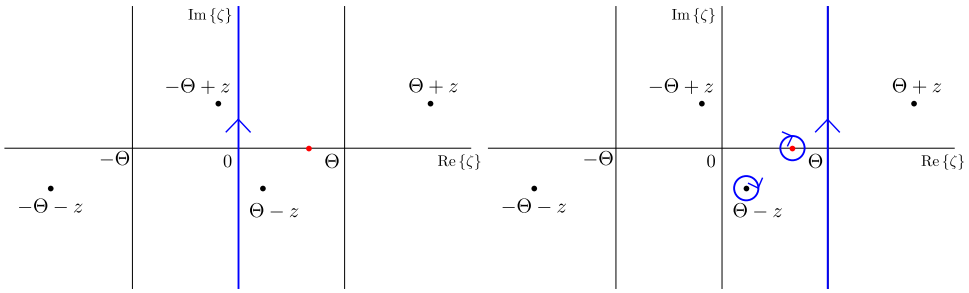

FIG. 12: ζ-plane diagrams of the original contour (left) versus the shifted contour (right) for when $\Theta/2 < \mathrm{Re}\{z\} < \Theta$. The red dot indicates a potentially crossed spectral pole.

As $|\mathrm{Re}\{z\}|$ becomes larger, identifying which contour to use and calculating the correct residues to add becomes quite tedious. However, one can form functional difference equations from the boundary

functional conditions (3.18) and (3.25). These functional equations are used as a method of analytic continuation and take the form,

$$q^{(j)}(z) = q^{(j)}(z\pm 4\bar{\theta}_{\rm w}) - h'(z\pm 3\bar{\theta}_{\rm w})\left[s^{(j)}(\mp\theta_{\rm w}+h(z\pm 3\bar{\theta}_{\rm w})) - s^{(j)}(\mp\theta_{\rm w}-h(z\pm 3\bar{\theta}_{\rm w}))\right] + h'(z\pm\bar{\theta}_{\rm w})\left[s^{(j)}(\pm\theta_{\rm w}+h(z\pm\bar{\theta}_{\rm w})) - s^{(j)}(\pm\theta_{\rm w}-h(z\pm\bar{\theta}_{\rm w}))\right], \tag{5.11}$$

$$s^{(j+1)}(z) = s^{(j+1)}(z\pm 4\theta_{\rm w}) - q^{(j)}(\mp\bar{\theta}_{\rm w}+g(z\pm 3\theta_{\rm w})) - q^{(j)}(\mp\bar{\theta}_{\rm w}-g(z\pm 3\theta_{\rm w})) + q^{(j)}(\pm\bar{\theta}_{\rm w}+g(z\pm\theta_{\rm w})) + q^{(j)}(\pm\bar{\theta}_{\rm w}-g(z\pm\theta_{\rm w})). \tag{5.12}$$

This allows us to extend a previously defined base strip (that has width $4\bar{\theta}_{\rm w}$ or $4\theta_{\rm w}$ for $q^{(j)}(z)$ and $s^{(j+1)}(z)$ respectively) to the entire complex plane (see Figure 13). These functional equations can be implemented in software such as MATLAB by defining a recursive function. We choose the following definition of the base strip for all spectral functions,

$$p(z) = \begin{cases} \dfrac{1}{2\pi i}\displaystyle\int_{\Theta-i\infty}^{\Theta+i\infty} p_{\rm int}(z,\zeta)\mathrm{d}\zeta - R_{\rm spec} - \mathrm{Res}(p_{\rm int},\Theta+z) & -\frac{3\Theta}{2} < \mathrm{Re}\{z\} \leqslant -\frac{\Theta}{2} \quad (5.13a)\\ \dfrac{1}{2\pi i}\displaystyle\int_{-i\infty}^{i\infty} p_{\rm int}(z,\zeta)\mathrm{d}\zeta & -\frac{\Theta}{2} < \mathrm{Re}\{z\} \leqslant \frac{\Theta}{2} \quad (5.13b)\\ \dfrac{1}{2\pi i}\displaystyle\int_{\Theta-i\infty}^{\Theta+i\infty} p_{\rm int}(z,\zeta)\mathrm{d}\zeta - R_{\rm spec} - \mathrm{Res}(p_{\rm int},\Theta-z) & \frac{\Theta}{2} < \mathrm{Re}\{z\} \leqslant \frac{3\Theta}{2} \quad (5.13c)\\ \dfrac{1}{2\pi i}\displaystyle\int_{-i\infty}^{i\infty} p_{\rm int}(z,\zeta)\mathrm{d}\zeta - 2\mathrm{Res}(p_{\rm int},\Theta-z) & \frac{3\Theta}{2} < \mathrm{Re}\{z\} \leqslant \frac{5\Theta}{2} \quad (5.13d) \end{cases}$$

where $\Theta = \bar{\theta}_{\rm w}$ (resp. $\theta_{\rm w}$) for $p = q^{(j)}$ (resp. $s^{(j+1)}$). Then (5.11) (resp. (5.12)) analytically continue this base strip to the entire z complex plane.

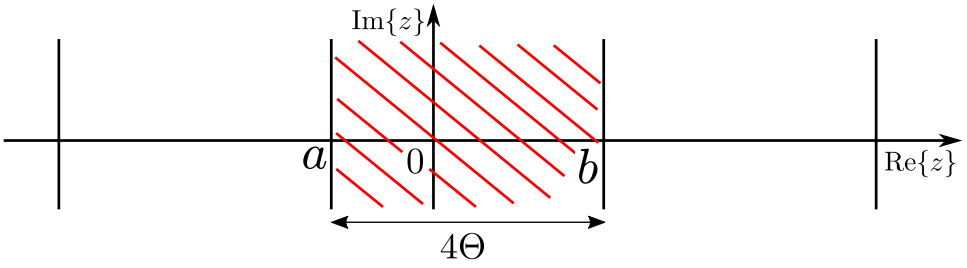

FIG. 13: Demonstration of the functional difference equations. The red region will be the base strip (5.13) with $a = -\frac{3\Theta}{2}$ and $b = \frac{5\Theta}{2}$. Then the adjacent strips will require the functional difference equations in the evaluation.

This strategy is complete for $q^{(0)}(z)$ but the higher order integrals are nested integrals because of the spectral functions inside the integrand. Numerical computations of nested integrals are notoriously difficult to evaluate numerically. However a sufficiently accurate approximation can give us a substantially quicker computation without sacrificing too much precision. We will use spline interpolation as detailed in the following steps.

Step 1 Take (5.13) and transform the integrals so that the range is from 0 to ∞, e.g.,

$$\frac{1}{2\pi i}\int_{-i\infty}^{i\infty} s_{\text{int}}^{(j)}(z,\zeta)\mathrm{d}\zeta = \frac{1}{\pi}\int_{0}^{\infty} s_{\text{int}}^{(j)}(z,it)\mathrm{d}t. \tag{5.14}$$

Step 2 Identify the spectral parts to interpolate, e.g. the following sections from $s_{\text{int}}^{(j)}(z,it)$,

$$\mathcal{Q}(t) = q^{(j)}(\pm\bar{\theta}_{\text{w}} + g(it)) + q^{(j)}(\pm\bar{\theta}_{\text{w}} - g(it)), \tag{5.15}$$

where $t \in [0,\infty)$.

Step 3 Interpolation is only possible on finite domains hence we map these spectral parts onto a unit-sized domain using functions such as,

$$t(\tau) = \frac{\tau}{1-\tau}, \quad \tau \in [0,1). \tag{5.16}$$

The ability to do this step is evidenced by knowing that the spectral parts are well-behaved at infinity because of the spectral functions asymptotic behaviour from (3.14) and (3.22).

Step 4 Use spline interpolation on a linearly spaced set of τ points to get an accurate numerical result that is continuously differentiable,

$$\widetilde{\mathcal{Q}}(t(\tau)) \approx \mathcal{Q}(t(\tau)). \tag{5.17}$$

Step 5 Invert the unit mapping to go back to the t domain by applying

$$\tau(t) = \frac{t}{1+t}. \tag{5.18}$$

Step 6 Integrate the approximated integrand with $\widetilde{\mathcal{Q}}(t)$ in place of $\mathcal{Q}(t)$.

On a side note, Appendix B can be used to further argue that the ideal unit mapping for $s^{(1)}(z)$ is,

$$t(\tau) = -(1/\delta)\ln(1-\tau), \quad \tau \in [0,1), \tag{5.19}$$

because it implies the following behaviour for $q^{(0)}(z)$ as $\tau \to 1^{-}$,

$$q^{(0)}(\text{Re}\{z\} - (i/\delta)\ln(1-\tau)) = -i\delta + O(1-\tau). \tag{5.20}$$

At the time of writing, ideal unit mappings in the general case have not been found so we will generally use (5.16) in later results.

Concluding this subsection, we have discussed our strategy to efficiently evaluate $q^{(j)}(z)$ and $s^{(j+1)}(z)$ by combining interpolation, two cases of fixed contours and functional difference equations. Figure 14 includes phase portraits of $s^{(0)}(z)$, $q^{(0)}(z)$, $s^{(1)}(z)$ and $q^{(1)}(z)$ with $\lambda_k = 1/2$, $\bar{\theta}_{\text{w}} = \pi/4$ and $\theta_{\text{I}} = \pi/8$ as well as indications of local poles, branch cuts and strips of analyticity.

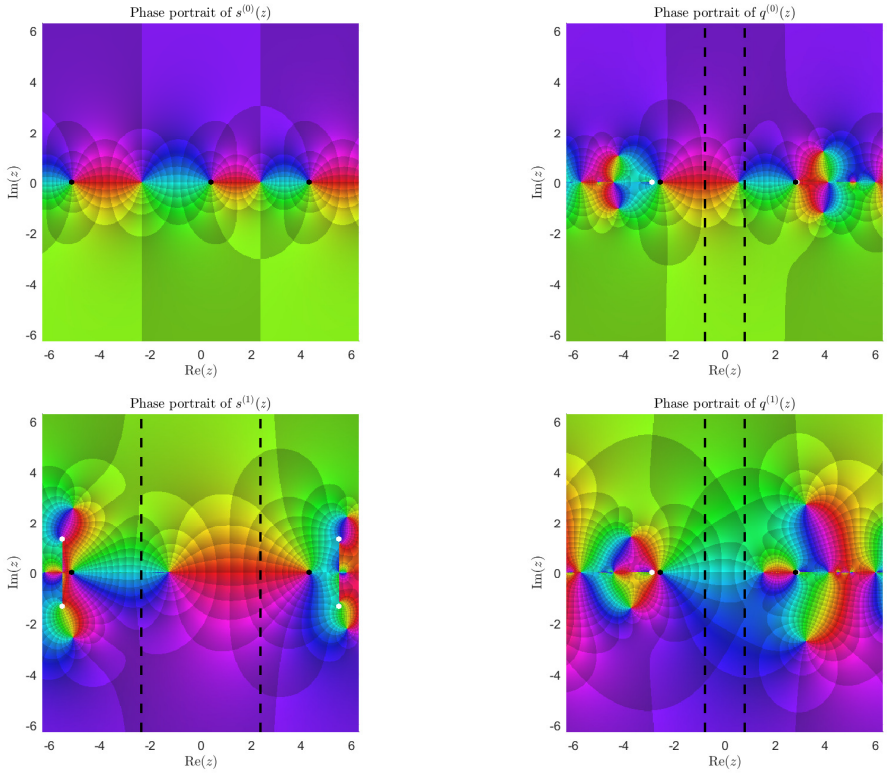

FIG. 14: Phase portraits of $s^{(0)}(z)$ (upper left), $q^{(0)}(z)$ (upper right), $s^{(1)}(z)$ (lower left) and $q^{(1)}(z)$ (lower right) with $\lambda_k = 1/2$, $\bar{\theta}_w = \pi/4$ and $\theta_I = \pi/8$. The black dots indicate the location of local poles and the white dots indicate the location of local branch points. For all portraits minus $s^{(0)}(z)$, the strips of analyticity, (3.15) and (3.23), are between the two dashed lines. See Figure 1 (right) for colour reference.

5.2 *Numerical evaluation of Sommerfeld integrals*

The tools developed for the evaluation of the spectral integrals can be adapted in order to evaluate the Sommerfeld integrals. Recall the two Sommerfeld integral forms of the exterior and interior total wave fields,

$$\Phi(r,\theta) = \frac{1}{2\pi i}\int_{\gamma_+ + \gamma_-} e^{-ik_1 r\cos(z)} s(\theta + z)\mathrm{d}z, \quad \Psi(r,\theta) = \frac{1}{2\pi i}\int_{\gamma_+ + \gamma_-} e^{-ik_2 r\cos(z)} q(\theta - \pi + z)\mathrm{d}z, \quad (5.21)$$

where the Sommerfeld contours $\gamma_\pm$ are displayed in Figure 3 and the spectral functions $s(z)$ and $q(z)$ have the high-contrast expansion of the form,

$$p(z) = p^{(0)}(z) + \lambda p^{(1)}(z) + \lambda^2 p^{(2)}(z) + O(\lambda^3). \quad (5.22)$$

All singularities in the two integrands are caused by the spectral functions and are confined to the real line and the local vicinity of branch cuts. The branch cuts for Φ are centred on and perpendicular

to the real line and the branch cuts for Ψ are on the real line. Using Sommerfeld contours for numerical integration is generally impractical because of the highly oscillatory nature of $\exp(-ik_{1,2}r\cos(z))$ when $k_{1,2}r$ is too large.

We deform the Sommerfeld contours to the steepest descent contours using similar methodology to section 5 in Nethercote et al. (2019). The deformation crosses all poles on the real line segment $z \in [-\pi,\pi]$ except for any poles situated on the branch cuts. These poles create the GO component (at least in part) leaving the steepest descent integral to represent the diffracted component. The deformation reduces the Sommerfeld integral to the form,

$$\Phi(r,\theta) = \Phi_{\text{GO}} + \frac{1}{2\pi i}\int_{\text{SDP}} e^{ik_1 r\cos(z)}\left[s(\theta+\pi+z) - s(\theta-\pi-z)\right]\mathrm{d}z, \tag{5.23}$$

$$\Psi(r,\theta) = \Psi_{\text{GO}} + \frac{1}{2\pi i}\int_{\text{SDP}} e^{ik_2 r\cos(z)}\left[q(\theta+z) - q(\theta-2\pi-z)\right]\mathrm{d}z, \tag{5.24}$$

where SDP is the steepest descent path shown in Figure 15 (left). The SDP is parametrised in terms of the Gudermannian function $\text{gd}(x)$,

$$z(t) = t - \text{gd}(it) = t - i\ln\left|\sec(t)+\tan(t)\right|, \quad t \in \left(-\frac{\pi}{2},\frac{\pi}{2}\right), \tag{5.25}$$

and has the properties,

$$\frac{\mathrm{d}z}{\mathrm{d}t} = 1 - i\sec(t), \quad \cos(z(t)) = 1 + i\sin(t)\tan(t), \tag{5.26}$$

the latter of which shows that along this path of steepest descent the exponential part $\exp(-ik_{1,2}r\cos(z))$ does not oscillate at all. GO discontinuities are produced when poles cross the steepest descent path, causing potential numerical issues.

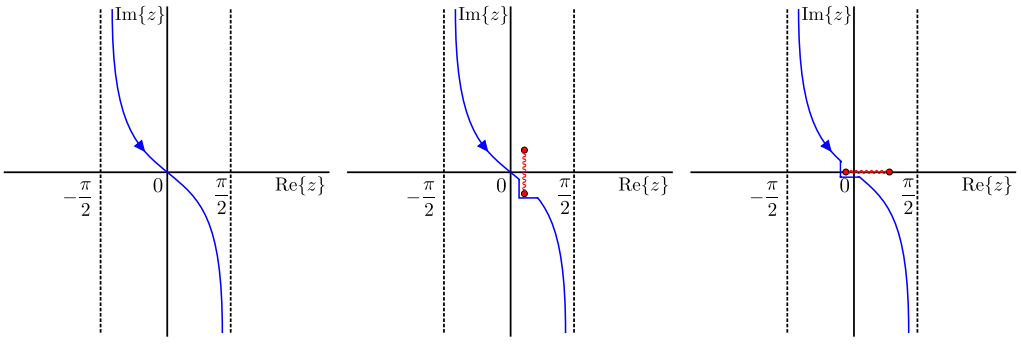

FIG. 15: Illustrations of the steepest descent path (in blue) normally (left) and around the branch cuts for Φ (middle) and Ψ (right).

The branch cuts in the spectral functions are another complication to consider. They will eventually intersect the SDP when θ is close to the wedge faces and we need to deform the SDP around the cuts to account for their contribution (see Figure 15 (middle) for the Φ Sommerfeld integral and Figure 15 (right) for the Ψ Sommerfeld integral). This contribution produces head/lateral waves that enforce continuity of the diffracted component across the wedge faces.

For Φ, one of the branch cuts is located at

$$z = \theta_{\mathrm{w}} - \theta + iy, \text{ where } y \in \left[-\cosh^{-1}\left(\frac{1}{\lambda_k}\right), \cosh^{-1}\left(\frac{1}{\lambda_k}\right) \right], \tag{5.27}$$

and intersects the contour when $\theta_{\mathrm{w}} - \cos^{-1}(\lambda_k) \leqslant \theta \leqslant \theta_{\mathrm{w}}$. There is also a second cut located at

$$z = \theta_{\mathrm{w}} + \theta + iy, \text{ where } y \in \left[-\cosh^{-1}\left(\frac{1}{\lambda_k}\right), \cosh^{-1}\left(\frac{1}{\lambda_k}\right) \right], \tag{5.28}$$

and intersects the contour when $-\theta_{\mathrm{w}} \leqslant \theta \leqslant -\theta_{\mathrm{w}} + \cos^{-1}(\lambda_k)$. (5.23) does have more branch cuts but these will not intersect the contour.

For Ψ, one of the branch cuts is located at

$$z = \theta - \theta_{\mathrm{w}} + x, \text{ where } x \in \left[-\cos^{-1}(\lambda_k), \cos^{-1}(\lambda_k) \right], \tag{5.29}$$

and intersects the contour when $\theta_{\mathrm{w}} \leqslant \theta \leqslant \theta_{\mathrm{w}} + \cos^{-1}(\lambda_k)$. A second cut is located at

$$z = \pi + \bar{\theta}_{\mathrm{w}} - \theta + x, \text{ where } x \in \left[-\cos^{-1}(\lambda_k), \cos^{-1}(\lambda_k) \right], \tag{5.30}$$

and intersects the contour when $\pi + \bar{\theta}_{\mathrm{w}} - \cos^{-1}(\lambda_k) \leqslant \theta \leqslant \pi + \bar{\theta}_{\mathrm{w}}$. (5.24) also has other inconsequential branch cuts that need not be considered. When numerically integrating, we should indent the contour so that the cuts are avoided.

Lastly, we reuse interpolation in the evaluation of Sommerfeld integrals, specifically on the spectral parts e.g. $s(\theta + \pi + z) - s(\theta - \pi - z)$. Similarly to the spectral integrals, we use a linearly spaced set of points and spline interpolation to create an accurate approximation that allows the integration to be substantially faster without sacrificing too much precision. Although this time, we will need some two-dimensional interpolations (e.g. θ and z parametrised by (5.25)).

5.3 *Numerical examples and comparisons*

Combining all the strategy components from the previous two subsections completes our method of evaluation for both the exterior and interior total wave fields. This works very well in most cases although one should be careful to include the correct GO poles. Because the integration is along the steepest descent contours, the value of $k_{1,2}r$ does not affect the computation speed much except for extreme cases. Before we conclude this article, we will define and evaluate four different test cases using the discussed strategies, discuss the convergence of the asymptotic series and compare with existing literature.

For all test cases, we will consider a right-angled wedge. The parameter values for the four test cases are defined in Table 1. The first two test cases will have both wedge faces illuminated by the incident wave creating a reflected and transmitted wave per face. The difference between these two test cases is the value of the contrast parameter. The other two test cases will have just the top face illuminated, creating a single reflection and transmission. For test case 3, this transmitted wave will also be totally reflected upon impact with the bottom face. For test case 4, the scatterer wavenumber is smaller, hence the transmitted wave will be internally reflected and retransmitted through the bottom face.

Figure 16 shows some polar plots of the total field's magnitude at $r = 5$ for all test cases using the asymptotic series with terms up to and including $j = 0,\ 1,\ 2$ and 3. All figures show converging behaviour as the order of the approximation increases. It is clear that test case 2 (with a smaller λ)

Test case	$\bar{\theta}_\mathrm{w}$	θ_I	k_1	k_2	λ
1	$\pi/4$	$\pi/8$	1	2	0.1
2	$\pi/4$	$\pi/8$	1	2	0.01
3	$\pi/4$	$\pi/2$	1	2	0.1
4	$\pi/4$	$\pi/2$	1	1.2	0.1

Table 1: Table of parameter values for the four different test cases.

converges much faster and one can see the extra retransmitted wave in test case 4 compared with test case 3. These plots also indicate the locations of the incident wave and GO discontinuities, where one can notice, when looking closely, small numerical inaccuracies. These are due to the fact that in this case the contour of integration is very near a pole. Automated deformation of the contour would solve this issue, but we do not do it here for brevity.

In the process of creating our numerical results, we analysed the accuracy by investigating the error of the individual interpolations and we checked that the boundary functional conditions (given by (3.18) and (3.25)) are satisfied by inputting the numerical data of the spectral functions. We can also check the convergence of the asymptotic series by considering the error in the interface conditions. Since we truncate both the exterior and interior asymptotic series at the same point, the Dirichlet interface conditions are automatically satisfied, hence we consider the error in the Neumann interface conditions. Applying the high-contrast approximation (truncated at j) and considering the boundary conditions of the individual components simplifies the Neumann interface conditions to

$$\left.\frac{\partial \Phi}{\partial \theta}\right|_{\theta=\pm\theta_\mathrm{w}} - \lambda \left.\frac{\partial \Psi}{\partial \theta}\right|_{\theta=\pi\mp\bar{\theta}_\mathrm{w}} = -\lambda^{j+1} \left.\frac{\partial \Psi^{(j)}}{\partial \theta}\right|_{\theta=\pi\mp\bar{\theta}_\mathrm{w}}. \tag{5.31}$$

We put the θ derivative in Sommerfeld integral form,

$$-\lambda^{j+1} \left.\frac{\partial \Psi^{(j)}}{\partial \theta}\right|_{\theta=\pi\mp\bar{\theta}_\mathrm{w}} = \frac{\lambda^{j+1} k_2 r}{2\pi} \int_{\gamma_+ + \gamma_-} \sin(z) e^{-ik_2 r\cos(z)} q^{(j)}(\mp\bar{\theta}_\mathrm{w} + z)\mathrm{d}z, \tag{5.32}$$

and use the same strategies outlined in Section 5.2 to evaluate these quantities. Figure 17 plots the absolute values of (5.31) with respect to r for test case 1. This figure clearly shows the error decreasing as the order of the approximation increases.

Finally we shall compare our solution with the uniform far-field formula stated in section 4.5 of Lyalinov (1999) because this paper features a similar high-contrast approximation to ours. Although this formula was stated to be uniform with respect to θ, there seems to be an invalid point at $\theta = \theta_\mathrm{I} - \pi$. It was also stated that this formula neglects the effect of the branch cuts in the spectral functions (which give rise to head/lateral waves) and because it is leading order, retransmitted waves do not appear either.

Figure 18 compares the third order approximation of test cases 3 and 4 with Lyalinov's far-field approximation. These figures show that there is clear agreement between the two solutions for most values of θ, the exceptions being at the singularity $\theta = \theta_\mathrm{I} - \pi$ and some approximation inaccuracies at the wedge faces. We mentioned earlier that Lyalinov does not include retransmitted waves in the final formula, hence there is disagreement in test case 4 by the bottom wedge face.

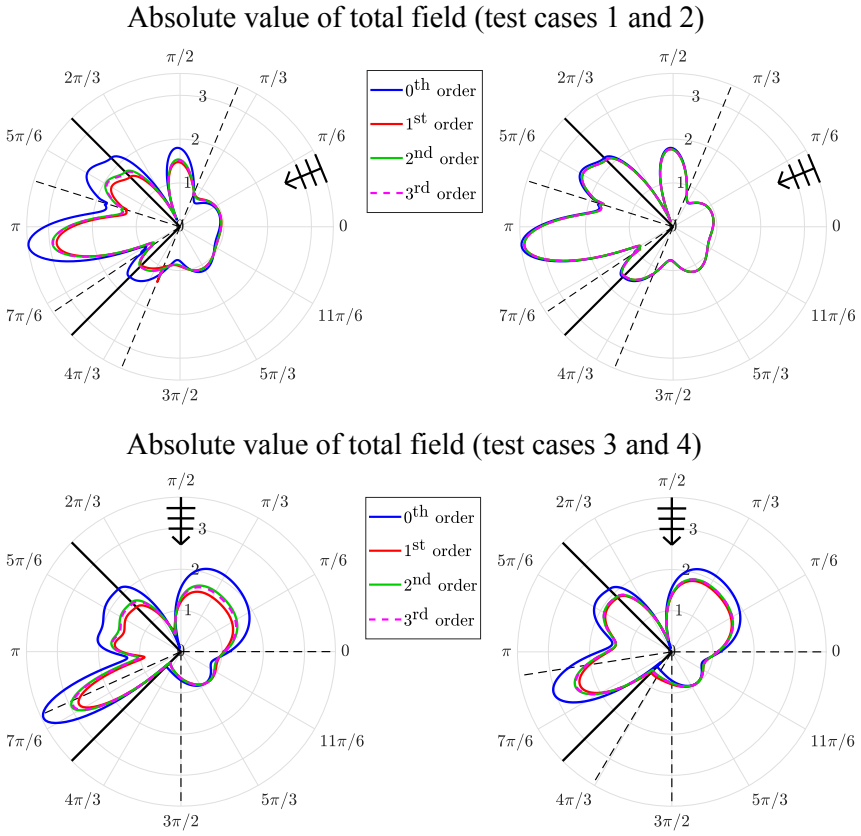

FIG. 16: Polar plots of the total field's magnitude at $r = 5$ where the approximation order goes up to and including $j = 3$. Each graph represents a different test case: 1 (upper left), 2 (upper right), 3 (lower left) and 4 (lower right).

5.4 *Concluding remarks*

To summarise this article, we created an asymptotic approximation to the penetrable wedge problem with the assumption of high-contrast between the host and the scatterer. This assumption split the problem into an infinite set of impenetrable wedge problems that were solved individually using a combination of the Sommerfeld-Malyuzhinets and Wiener-Hopf techniques. We also checked the solution analytically with the penetrable half-space problem and discussed our numerical evaluation strategy of the resulting integral solutions.

For our computations, we used MATLAB R2017a on a desktop with an Intel quad-core CPU @ 3.2 GHz 8 RAM. Table 2 illustrates the computation times to define the individual components of the high-contrast approximation. It is important to note that these times are approximate and only account for the definitions of the components and the interpolations required assuming that all previous ones have already been made.

Although the polar plots in Figure 16 show that our method can create an efficient and accurate

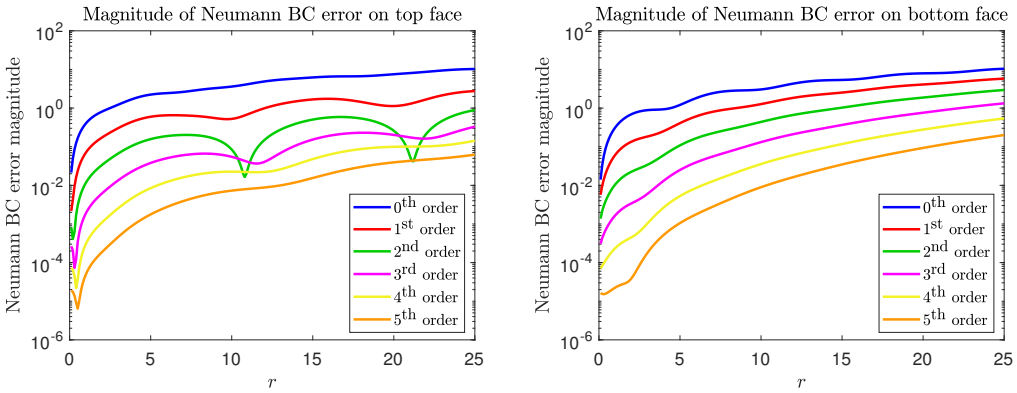

FIG. 17: Plots of the absolute values of (5.31) for test case 1 including the leading order to the fifth order approximations.

Approximation order	Spectral functions	Wave fields
0	$<$ 1 second	30 seconds
1	20 seconds	5 minutes
2	2 minutes	35 minutes
3	8 minutes	180 minutes

Table 2: Table of times to define the components and the interpolations required for test case 1. Note that these times are approximate.

solution, there are some drawbacks. Generally the strategies discussed in Section 5 work for a wide range of parameters provided λ is sufficiently small but will struggle for extreme cases such as grazing incidence ($\theta_{\mathrm{I}} \to \theta_{\mathrm{w}}$) and thin wedges ($\bar{\theta}_{\mathrm{w}} \to 0$). In the grazing incidence case, some of the spectral poles will approach the end points of the spectral integration contour causing potential numerical issues. The thin wedge case can be difficult because the z-poles become dense and approach the spectral integration contour on two sides.

Improvements could be made to the numerical strategies such as, defining the ideal unit mapping for the interpolations of the spectral functions by using the Lambert W function or using asymptotic approaches to account for branch cut contributions in the Sommerfeld integrals. It may also be worth investigating the convergence of the asymptotic scheme more rigorously because it could lead to a condition for convergence (e.g. recall $0 < \lambda < g'\left(\frac{\pi}{2} - \theta_{\mathrm{I}}\right)$ for the penetrable half-space) or finding an approximation for the error in case of convergence.

Because it is difficult to numerically compute Sommerfeld integrals when kr is too large, one future task is to create a simple high-frequency/far-field approximation that truly is uniform with respect to θ, which will allow us to efficiently predict the diffraction coefficient of the problem. This will require us to apply the method of steepest descent to Sommerfeld integrals however this case is more complicated due to the branch cuts. Obtaining this formula requires us to accurately approximate the branch cut integrals.

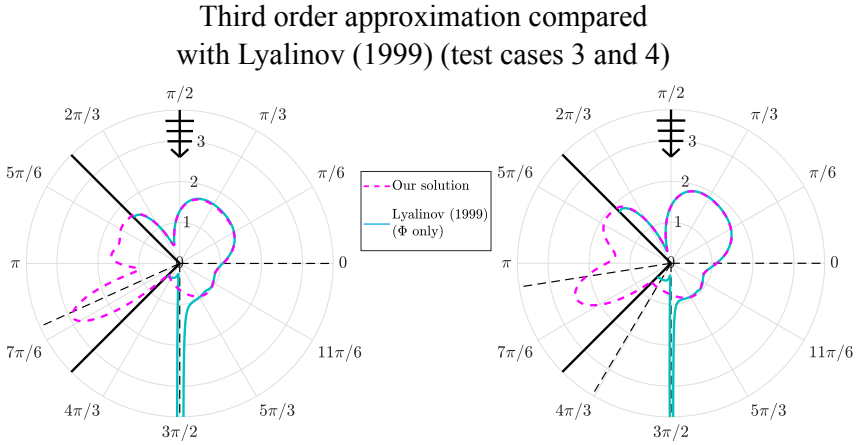

FIG. 18: Polar plot comparison of our third order approximation with the solution from Lyalinov (1999) at $r = 5$ for test case 3 (left) and 4 (right).

A high-frequency/far-field approximation will be useful in hybrid numerical-asymptotic approaches for convex polygon diffraction (see Groth et al. (2018)).

Recall that in this article, we assumed that the physical parameters are independent of each other. If we were to relax this particular assumption, then in both acoustic and electromagnetic settings we find that the refractive index and the contrast parameter could be connected by $\lambda_k \propto \sqrt{\lambda}$. We will explore how this can affect our method in future work.

Acknowledgements

Nethercote acknowledges the financial support from EPSRC (DTA studentship). Assier acknowledges that part of this work was supported by EPSRC (EP/N013719/1). Abrahams acknowledges the support by EPSRC/UKRI under grants no EP/K032208/1 and EP/R014604/1.

REFERENCES

Abramowitz, M. & Stegun, I. A. (1967) *Handbook of Mathematical Functions*. National Bureau of Standards, Washington D.C., 6th edition.

Assier, R. C. & Abrahams, I. D. (2019) A surprising observation in the quarter-plane problem. *arXiv:1905.03863*.

Assier, R. C. & Shanin, A. V. (2019) Diffraction by a quarter-plane. Analytical continuation of spectral functions. *Q. J. Mech. Appl. Math.*, **72**(1), 51–86.

Babich, V. M., Lyalinov, M. A. & Grikurov, V. E. (2007) *Diffraction Theory: The Sommerfeld-Malyuzhinets Technique (Alpha Science Series on Wave Phenomena)*. Alpha Science.

Babich, V. M. & Mokeeva, N. V. (2008) Scattering of the plane wave by a transparent wedge. *J. Math. Sci.*, **155**(3), 335–342.

Babich, V. M., Mokeeva, N. V. & Samokish, B. A. (2012) The Problem of Scattering of a Plane Wave by a Transparent Wedge: A Computional Approach. *J. Commun. Technol. Electron.*, **57**(9), 993–1000.

Bender, C. M. & Orszag, S. A. (1999) *Advanced Mathematical Methods for Scientists and Engineers I: Asymptotic Methods and Perturbation Theory*. Springer-Verlag, New York.

Bowman, J. J., Senior, T. B. A. & Uslenghi, P. L. E. (1987) *Electromagnetic and Acoustic Scattering by Simple Shapes*. Hemisphere Publishing Corporation.

Budaev, B. V. (1995) *Diffraction by Wedges*. CRC Press, 1st edition.

Budaev, B. V. & Bogy, D. B. (1995) Rayleigh wave scattering by a wedge. *Wave Motion*, **22**(1), 239–257.

Budaev, B. V. & Bogy, D. B. (1996) Rayleigh wave scattering by a wedge II. *Wave Motion*, **24**(3), 307–314.

Budaev, B. V. & Bogy, D. B. (1998) Rayleigh wave scattering by two adhering elastic wedges. *Proc. R. Soc. A Math. Phys. Eng. Sci.*, **454**, 2949–2996.

Budaev, B. V. & Bogy, D. B. (1999) Rigorous solutions of acoustic wave diffraction by penetrable wedges. *J. Acoust. Soc. Am.*, **105**(1), 74–83.

Chandler-Wilde, S. N., Graham, I. G., Langdon, S. & Spence, E. A. (2012) Numerical-asymptotic boundary integral methods in high-frequency acoustic scattering. *Acta Numer.*, **21**(2012), 89–305.

Croisille, J.-P. & Lebeau, G. (1999) *Diffraction by an Immersed Elastic Wedge*. Springer-Verlag.

Daniele, V. G. (2003a) Rotating Waves in the Laplace Domain for Angular Regions. *Electromagnetics*, **23**(3), 223–236.

Daniele, V. G. (2003b) The Wiener-Hopf Technique for Impenetrable Wedges having Arbitrary Aperture Angle. *SIAM J. Appl. Math.*, **63**(4), 1442–1460.

Daniele, V. G. (2010) The Wiener-Hopf Formulation of the Penetrable Wedge Problem: Part I. *Electromagnetics*, **30**(8), 625–643.

Daniele, V. G. (2011) The Wiener-Hopf Formulation of the Penetrable Wedge Problem: Part II. *Electromagnetics*, **31**(1), 1–17.

Daniele, V. G. & Lombardi, G. (2006) Wiener-Hopf Solution for Impenetrable Wedges at Skew Incidence. *IEEE Trans. Antennas Propag.*, **54**(9), 2472–2485.

Daniele, V. G. & Lombardi, G. (2007) Fredholm factorization of Wiener-Hopf scalar and matrix kernels. *Radio Sci.*, **42**(6), 1–19.

Daniele, V. G. & Lombardi, G. (2011) The Wiener-Hopf Solution of the Isotropic Penetrable Wedge Problem: Diffraction and Total Field. *IEEE Trans. Antennas Propag.*, **59**(10), 3797–3818.

Daniele, V. G., Lombardi, G. & Zich, R. S. (2017a) Network representations of angular regions for electromagnetic scattering. *PLoS One*, **12**(8), 1–53.

Daniele, V. G., Lombardi, G. & Zich, R. S. (2017b) The Electromagnetic Field for a PEC Wedge Over a Grounded Dielectric Slab: 1. Formulation and Validation. *Radio Sci.*, **52**(12), 1472–1491.

Daniele, V. G., Lombardi, G. & Zich, R. S. (2017c) The Electromagnetic Field for a PEC Wedge Over a Grounded Dielectric Slab: 2. Diffraction, Modal Field, Surface Waves, and Leaky Waves. *Radio Sci.*, **52**(12), 1492–1509.

Daniele, V. G., Lombardi, G. & Zich, R. S. (2018) The Double PEC Wedge Problem: Diffraction and Total Far Field. *IEEE Trans. Antennas Propag.*, **66**(12), 6482–6499.

Groth, S. P., Hewett, D. P. & Langdon, S. (2015) Hybrid numerical-asymptotic approximation for high-frequency scattering by penetrable convex polygons. *IMA J. Appl. Math.*, **80**(2), 324–353.

Groth, S. P., Hewett, D. P. & Langdon, S. (2018) A high frequency boundary element method for scattering by penetrable convex polygons. *Wave Motion*, **78**, 32–53.

Keller, J. B. (1962) Geometrical Theory of Diffraction. *J. Opt. Soc. Am.*, **52**(2), 116–130.

Knopoff, L. (1969) Elastic Wave Propagation in a Wedge. In Miklowitz, J., editor, *Wave Propag. Solids*, pages 3–43, Los Angeles. ASME.

Kontorovich, M. J. & Lebedev, N. N. (1939) On a method of solution of some problems of the diffraction theory. *J. Phys. (Academy Sci. U.S.S.R.)*, **1**(3), 229–241.

Kouyoumjian, R. G. & Pathak, P. H. (1974) A uniform GTD for an edge in a perfectly conducting surface. *Proc. IEEE*, **62**(11), 1448–1461.

Kraut, E. A. & Lehman, G. W. (1969) Diffraction of electromagnetic waves by a right-angle dielectric wedge. *J. Math. Phys.*, **10**(8), 1340–1348.

Larsen, J. (1981) Diffraction of elastic waves by a rigid wedge. *Proc. R. Soc. A Math. Phys. Eng. Sci.*, **376**(1767), 609–617.

Lawrie, J. B. & Abrahams, I. D. (2007) A brief historical perspective of the Wiener-Hopf technique. *J. Eng. Math.*, **59**(4), 351–358.

Lyalinov, M. A. (1999) Diffraction by a highly contrast transparent wedge. *J. Phys. A. Math. Gen.*, **32**(11), 2183–2206.

Macdonald, H. M. (1902) *Electric Waves*. University Press.

Malyuzhinets, G. D. (1958) Excitation, reflection and emission of surface waves from a wedge with given face impedances. *Sov. Phys. Dokl.*, **3**, 752–755.

Mokeeva, N. V. (2006) On the well-posedness of diffraction problems for angular domains. *J. Math. Sci.*, **138**(2), 5555–5564.

Mokeeva, N. V. (2007) The limiting absorption principle in the problem of a transparent wedge. *J. Math. Sci.*, **142**(6), 2597–2604.

Nethercote, M. A., Assier, R. C. & Abrahams, I. D. (2019) Analytical methods for perfect wedge diffraction: a review. *arXiv:1905.10562*.

Noble, B. (1958) *Methods based on the Wiener-Hopf Technique for the solution of partial differential equations*. Chelsea Publishing Company, New York, 2nd edition.

Radlow, J. (1964) Diffraction by a right-angled dielectric wedge. *Int. J. Eng. Sci.*, **2**(3), 275–290.

Rawlins, A. D. (1977) Diffraction by a dielectric wedge. *J. Inst. Math. its Appl.*, **19**(3), 261–279.

Rawlins, A. D. (1999) Diffraction by, or diffusion into, a penetrable wedge. *Proc. R. Soc. A Math. Phys. Eng. Sci.*, **455**(1987), 2655–2686.

Senior, T. B. A. (1959) Diffraction by an Imperfectly Conducting Wedge. *Commun. Pure Appl. Math.*, **12**(2), 337–372.

Shanin, A. V. (1996) On Wave Excitation in a Wedge-Shaped Region. *Acoust. Phys.*, **42**(5), 612–617.

Shanin, A. V. (1998) Excitation of Waves in a Wedge-Shaped Region. *Acoust. Phys.*, **44**(5), 592–597.

Smith, H. R., Webb, A., Connolly, P. & Baran, A. J. (2015) Cloud chamber laboratory investigations into the scattering properties of hollow ice particles. *J. Quant. Spectrosc. Radiat. Transf.*, **157**, 106–118.

Sommerfeld, A. (1896) Mathematische Theorie der Diffraction. *Math. Ann. (in Ger.*, **47**, 317–374.

Sommerfeld, A. (1901) Theoretisches über die Beugung der Röntgenstrahlen. *Zeitschrift für Math. und Phys. (in Ger.*, **46**, 11–97.

Sommerfeld, A. (1954) *Optics*. Academic Press, New York.

Sommerfeld, A. (2003) *Mathematical Theory of Diffraction*. Birkhauser, Boston.

Ufimtsev, P. Y. (2014) *Fundamentals of the Physical Theory of Diffraction*. John Wiley & Sons, 2nd edition.

Van Bladel, J. G. (2006) *Electromagnetic fields*. John Wiley & Sons, New Jersey, 2nd edition.

Wegert, E. (2012) *Visual Complex Functions*. Birkhauser Basel.

Wiener, N. & Hopf, E. (1931) Über eine klasse singulärer integralgleichungen. *Sitzungsberichte der Preuss. Akad. der Wissenschaften, Phys. Klasse (in Ger.*, **31**, 696–706.

Williams, W. E. (1959) Diffraction of an E-polarized plane wave by an imperfectly conducting wedge. *Proc. R. Soc. A Math. Phys. Eng. Sci.*, **252**(1270), 376–393.

A. An important mapping to connect two Sommerfeld integrals

In this section, we will define the mapping $g(z)$ and the associated inverse $h(z)$ to connect the two Sommerfeld integrals (2.16) and (2.17) by the identities (2.18). We need to be cautious so that software such as MATLAB/Mathematica can evaluate these mappings with the correct branch cut orientations.

Consider the following definitions,

$$g(z) = \cos^{-1}\left(\lambda_k \cos(z)\right), \quad h(z) = \cos^{-1}\left(\lambda_k^{-1} \cos(z)\right), \tag{A.1}$$

where $\lambda_k = k_1/k_2 \in (0,1)$. Both the mappings have an infinite number of branch points and branch cuts. For $g(z)$, the branch points are located at, $z = \pm i\cosh^{-1}\left(\lambda_k^{-1}\right) + n\pi$ and for $h(z)$, they are located at, $z = \pm\cos^{-1}\left(\lambda_k\right) + n\pi$ where $n \in \mathbb{Z}$. By default, MATLAB joins these branch points via complex infinity (shown as phase portraits in Figures A.19a and A.19b with $\lambda_k = 1/2$). As it stands these definitions are

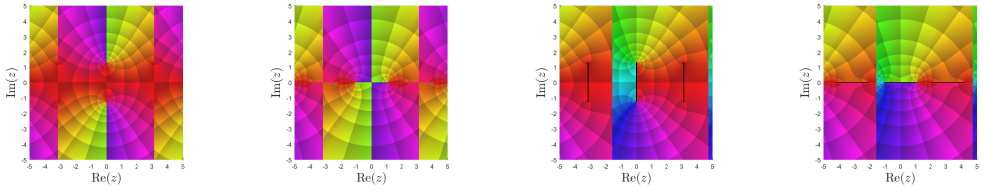

(a) Default definition of $g(z)$ (b) Default definition of $h(z)$ (c) Our definition of $g(z)$ (d) Our definition of $h(z)$

FIG. A.19: Phase plots of $g(z)$ and $h(z)$ with the default definition and our definition of the branch cuts (with $\lambda_k = 1/2$). In figure (c) and (d) the black lines indicate the branch cuts. See Figure 1 (right) for colour reference.

not useful since the branch cuts restrict much of the domain and limit the use of integration contours (e.g. Sommerfeld contours). Ideally, we want the mapping to be as similar to an identity map as possible. This will result in both mappings satisfying several different properties.

- $f(-z) = -f(z)$,
- $f(z^*) = (f(z))^*$ where z^* is the complex conjugate of z,
- $f(z + n\pi) = f(z) + n\pi$, for all $n \in \mathbb{Z}$,
- $f(z) \sim z$ as $\mathrm{Im}\{z\} \to \pm\infty$,

where f could be either g or h.

For $g(z)$, the branch cuts should be defined to join $z = i\cosh^{-1}\left(\lambda_k^{-1}\right) + n\pi$ and $z = -i\cosh^{-1}\left(\lambda_k^{-1}\right) + n\pi$ via $z = n\pi$ for all $n \in \mathbb{Z}$ and for $h(z)$, the branch cuts should be defined to join $z = \cos^{-1}\left(\lambda_k\right) + n\pi$ and $z = -\cos^{-1}\left(\lambda_k\right) + n\pi$ via $z = n\pi$ for all $n \in \mathbb{Z}$. We use the logarithmic formula for inverse cosine to manipulate the branch cuts,

$$g(z) = \frac{\pi}{2} + i\ln\left(i\lambda_k\cos(z) + \left(1 - \lambda_k^2\cos^2(z)\right)^{\frac{1}{2}}\right), \tag{A.2}$$

$$h(z) = \frac{\pi}{2} - i\ln(\lambda_k) + i\ln\left(i\cos(z) + \left(\lambda_k^2 - \cos^2(z)\right)^{\frac{1}{2}}\right). \tag{A.3}$$

The orientation of the branch cuts depends exclusively on how we define $\left(1 - \lambda_k^2\cos^2(z)\right)^{\frac{1}{2}}$ and $\left(\lambda_k^2 - \cos^2(z)\right)^{\frac{1}{2}}$. To obtain the correct branch, we rewrite these in terms of sine instead of cosine and define each square

root part separately. For $g(z)$, we define $\left(1-\lambda_k^2\cos^2(z)\right)^{\frac{1}{2}}$ as,

$$\left(1-\lambda_k^2\cos^2(z)\right)^{\frac{1}{2}} = -i\left(i\lambda_k\sin(z)-(1-\lambda_k^2)^{\frac{1}{2}}\right)^{\frac{1}{2}}\left(i\lambda_k\sin(z)+(1-\lambda_k^2)^{\frac{1}{2}}\right)^{\frac{1}{2}}, \tag{A.4}$$

such that,

$$\arg\left(i\lambda_k\sin(z)\pm(1-\lambda_k^2)^{\frac{1}{2}}\right)\in(-\pi,\pi], \text{ and } \left(1-\lambda_k^2\cos^2(z)\right)^{\frac{1}{2}}\Big|_{z=0} = (1-\lambda_k^2)^{\frac{1}{2}}. \tag{A.5}$$

This definition is compared with the default one by comparing Figures A.19a and A.19c. We can define $h(z)$ in a similar way,

$$\left(\lambda_k^2-\cos^2(z)\right)^{\frac{1}{2}} = \left(\sin(z)-(1-\lambda_k^2)^{\frac{1}{2}}\right)^{\frac{1}{2}}\left(\sin(z)+(1-\lambda_k^2)^{\frac{1}{2}}\right)^{\frac{1}{2}}, \tag{A.6}$$

where the two square roots are defined as follows,

$$\arg\left(\sin(z)\pm(1-\lambda_k^2)^{\frac{1}{2}}\right)\in(-\pi,\pi], \text{ and } \left(\lambda_k^2-\cos^2(z)\right)^{\frac{1}{2}}\Big|_{z=0} = i(1-\lambda_k^2)^{\frac{1}{2}}. \tag{A.7}$$

This definition is compared with the default one by comparing Figures A.19b and A.19d. However, Figures A.19c and A.19d show jumps across the infinite lines $\mathrm{Re}\{z\}=2\pi n-\pi/2$ where $n\in\mathbb{Z}$. These jumps are of size 2π and appear because the default branch of $\ln(z)$ in MATLAB (and similar software) limits the imaginary part to $(-\pi,\pi]$. Logically, we can correct this issue to make $g(z)$ or $h(z)$ satisfy the condition $f(z+n\pi)=f(z)+n\pi$ by adding the following,

$$z-\frac{\pi}{2}-i\ln(ie^{-iz}) = 2\pi\left\lfloor\frac{\mathrm{Re}\{z\}+\pi/2}{2\pi}\right\rfloor = \begin{cases} & \vdots \\ -2\pi & -5\pi/2\leqslant\mathrm{Re}\{z\}<-\pi/2 \\ 0 & -\pi/2\leqslant\mathrm{Re}\{z\}<3\pi/2 \\ 2\pi & 3\pi/2\leqslant\mathrm{Re}\{z\}<7\pi/2 \\ & \vdots \end{cases} \tag{A.8}$$

to $g(z)$ and $h(z)$ where $\lfloor z\rfloor$ indicates the integer part. In the principal logarithm branch $\mathrm{Re}\left\{i\ln(ie^{-iz})\right\}\in(-\pi,\pi]$. This means our final definitions of $g(z)$ and $h(z)$ are,

$$\begin{aligned} g(z) &= z-i\ln(ie^{-iz}) \\ &\quad +i\ln\left(i\lambda_k\cos(z)-i\left(i\lambda_k\sin(z)-(1-\lambda_k^2)^{\frac{1}{2}}\right)^{\frac{1}{2}}\left(i\lambda_k\sin(z)+(1-\lambda_k^2)^{\frac{1}{2}}\right)^{\frac{1}{2}}\right) \end{aligned} \tag{A.9}$$

$$\begin{aligned} h(z) &= z-i\ln(ie^{-iz})-i\ln(\lambda_k) \\ &\quad +i\ln\left(i\cos(z)+\left(\sin(z)-(1-\lambda_k^2)^{\frac{1}{2}}\right)^{\frac{1}{2}}\left(\sin(z)+(1-\lambda_k^2)^{\frac{1}{2}}\right)^{\frac{1}{2}}\right). \end{aligned} \tag{A.10}$$

Both these definitions satisfy all of the required conditions including the requirement that they are the inverse of each other. See Figure 4 for an example phase plot illustration of (A.9) and (A.10) where $\lambda_k=1/2$.

B. Asymptotic analysis of $q^{(0)}(z)$

In this appendix, we will discuss the asymptotic behaviour of the spectral function $q^{(0)}(z)$ as $|\mathrm{Im}\{z\}| \to \infty$. This could be useful because it can be pieced together with the asymptotic behaviour of the higher order spectral functions to find near-field approximations (as $kr \to 0$) or it can be used to improve the numerical methods present in Section 5.

It should be noted that the asymptotic expansion as $\mathrm{Im}\{z\} \to -\infty$ is the conjugate of the expansion as $\mathrm{Im}\{z\} \to \infty$ because $q^{(0)}(z^*) = \left(q^{(0)}(z)\right)^*$. For convenience we shall restrict the wedge angle such that $\bar{\theta}_\mathrm{w} \leqslant \theta_\mathrm{w}$ hence $\delta \leqslant \bar{\delta}$. We shall write $q^{(0)}(z)$ as a half range real integral,

$$q^{(0)}(z) = \frac{i}{\pi}\int_0^\infty \frac{\bar{\delta}\sinh(\bar{\delta}\zeta)h'(i\zeta)s^{(0)}\left(\theta_\mathrm{w}+h(i\zeta)\right)}{\cosh(\bar{\delta}\zeta)+\sin(\bar{\delta}z)} - \frac{\bar{\delta}\sinh(\bar{\delta}\zeta)h'(i\zeta)s^{(0)}\left(-\theta_\mathrm{w}+h(i\zeta)\right)}{\cosh(\bar{\delta}\zeta)-\sin(\bar{\delta}z)}\mathrm{d}\zeta. \quad \text{(A.1)}$$

To find the asymptotic expansion of $q^{(0)}(z)$, we shall relate it to the following function,

$$I(y;a,b) = \int_0^\infty \frac{a\sinh(ax)f_+(x)}{\cosh(ax)+i\sinh(ay)} - \frac{a\sinh(ax)f_-(x)}{\cosh(ax)-i\sinh(ay)}\mathrm{d}x, \quad \text{(A.2)}$$

where $b \leqslant a$ and $f_\pm(x)$ are complex functions that are well-defined on the real line and have the following asymptotic expansions as $x \to \infty$,

$$f_\pm(x) = -ib \mp Ae^{-bx} + O(e^{-2bx}). \quad \text{(A.3)}$$

It is easy to see that $q^{(0)}(z) = \frac{i}{\pi}I(-iz;\bar{\delta},\delta)$, $f_\pm(x) = h'(ix)s^{(0)}\left(\pm\theta_\mathrm{w}+h(ix)\right)$ and we want to find the asymptotic behaviour of (A.2) as $y \to \infty$. To do this, we need to split the integral as follows,

$$\int_0^\infty = \int_0^{\varepsilon(y)} + \int_{\varepsilon(y)}^\infty = I_1 + I_2,$$

where the midpoint $\varepsilon(y)$ is designed so that $\varepsilon(y) \to \infty$ and $\frac{\varepsilon(y)}{y} \to 0$ as $y \to \infty$. We shall choose $\varepsilon(y) = \frac{1}{a}\ln(y)$ and evaluate I_2 first. In this interval, x and y are considered to be very large and hence the integrand is approximated for large x and y,

$$\begin{aligned} I_2(y;a,b) &= \int_{\varepsilon(y)}^\infty \frac{a\sinh(ax)f_+(x)}{\cosh(ax)+i\sinh(ay)} - \frac{a\sinh(ax)f_-(x)}{\cosh(ax)-i\sinh(ay)}\mathrm{d}x, \\ &\underset{y\to\infty}{\sim} -ib\int_{\varepsilon(y)}^\infty \frac{ae^{ax}}{e^{ax}+ie^{ay}} - \frac{ae^{ax}}{e^{ax}-ie^{ay}}\mathrm{d}x - A\int_{\varepsilon(y)}^\infty \frac{ae^{ax-bx}}{e^{ax}+ie^{ay}} + \frac{ae^{ax-bx}}{e^{ax}-ie^{ay}}\mathrm{d}x. \end{aligned} \quad \text{(A.4)}$$

The first integral is trivial to integrate and the second can be integrated in terms of hypergeometric series (${}_2F_1$) by noting that,

$$\int \frac{x^{c-1}}{1-x}\mathrm{d}x = \sum_{n=0}^\infty \left(\int x^{c-1+n}\mathrm{d}x\right) = \frac{x^c}{c}\sum_{n=0}^\infty \left(\frac{cx^n}{c+n}\right) = \frac{x^c}{c}{}_2F_1(1,c;1+c;x). \quad \text{(A.5)}$$

Hence (A.4) is approximated as

$$\begin{aligned} I_2(y;a,b) &\underset{y\to\infty}{\sim} -ib\ln\left(\frac{-1-iye^{-ay}}{1-iye^{-ay}}\right), \\ &\quad -\frac{aA}{b}y^{-\frac{b}{a}}\left({}_2F_1\left(1,\frac{b}{a};1+\frac{b}{a};-\frac{ie^{ay}}{y}\right)+{}_2F_1\left(1,\frac{b}{a};1+\frac{b}{a};\frac{ie^{ay}}{y}\right)\right). \end{aligned} \quad \text{(A.6)}$$

We can find an asymptotic series for the hypergeometric function by using the following identity derived from equation 15.3.7 in Abramowitz & Stegun (1967),

$$ {}_2F_1(1,\sigma;1+\sigma;x) = \frac{\pi\sigma(-x)^{-\sigma}}{\sin(\pi\sigma)} - \frac{\sigma}{(\sigma-1)x}\,{}_2F_1(1,1-\sigma;2-\sigma;x^{-1}). \tag{A.7} $$

hence the asymptotic expansions that we require are,

$$ y^{-\frac{b}{a}}{}_2F_1\left(1,\frac{b}{a},1+\frac{b}{a},\mp\frac{ie^{ay}}{y}\right) = \frac{\pi b\,(\mp i)^{b/a}\,e^{-by}}{a\sin\left(\frac{\pi b}{a}\right)} \mp \frac{iby^{1-\frac{b}{a}}e^{-ay}}{(b-a)} + O(Y^{-2}). \tag{A.8} $$

After using the series expansions for hypergeometric series and for $\ln(1+z)$, we obtain the asymptotic approximation for I_2,

$$ I_2(y;a,b) \underset{y\to\infty}{\sim} -\pi b + 2bye^{-ay} - \frac{\pi Ae^{-by}}{\sin\left(\frac{\pi b}{2a}\right)}. \tag{A.9} $$

For the other integral I_1, y is considered much larger than x, hence,

$$ \begin{aligned} I_1(y;a,b) &= \int_0^{\varepsilon(y)} \frac{a\sinh(ax)f_+(x)}{\cosh(ax)+i\sinh(ay)} - \frac{a\sinh(ax)f_-(x)}{\cosh(ax)-i\sinh(ay)}\mathrm{d}x, \\ &\underset{y\to\infty}{\sim} \frac{-ia}{\sinh(ay)}\int_0^{\varepsilon(y)} \sinh(ax)(f_+(x)+f_-(x))\mathrm{d}x. \end{aligned} \tag{A.10} $$

We apply the following change of variables $x = \frac{1}{a}\ln(X)$,

$$ I_1(y;a,b) \underset{y\to\infty}{\sim} \frac{1}{\sinh(ay)}\int_1^y \frac{1-X^{-2}}{2i}\left(f_+\left(\frac{1}{a}\ln(X)\right)+f_-\left(\frac{1}{a}\ln(X)\right)\right)\mathrm{d}X. \tag{A.11} $$

Recall (A.3) which implies that as $X\to\infty$,

$$ f_+\left(\frac{1}{a}\ln(X)\right)+f_-\left(\frac{1}{a}\ln(X)\right) \underset{X\to\infty}{\sim} -2ib + O\left(X^{-\frac{2b}{a}}\right), \tag{A.12} $$

hence,

$$ \begin{aligned} I_1(y;a,b) \underset{y\to\infty}{\sim}& -2b\left(y-2+\frac{1}{y}\right)e^{-ay} \\ &+ \frac{1}{\sinh(ay)}\int_1^y \frac{1-X^{-2}}{2i}\left(f_+\left(\frac{1}{a}\ln(X)\right)+f_-\left(\frac{1}{a}\ln(X)\right)+2ib\right)\mathrm{d}X. \end{aligned} \tag{A.13} $$

The integral will be $o(y)$ as $y\to\infty$ because the integrand is well-defined and bounded on the interval and is $o(1)$ as $X\to\infty$. This means that the leading order behaviour of $I_1(y;a,b)$ is,

$$ I_1(y;a,b) = -2bye^{-ay} + o\left(ye^{-ay}\right). $$

So the asymptotic expansion for $I(y;a,b)$ as $y\to\infty$ is,

$$ I(y;a,b) \underset{y\to\infty}{\sim} -\pi b - \frac{\pi Ae^{-by}}{\sin\left(\frac{\pi b}{2a}\right)}. \tag{A.14} $$

Note that from the asymptotic expansions of $s^{(0)}(z)$, $h(z)$ and $h'(z)$, we can easily find that $A = 2i\delta\lambda_k^\delta \sin(\delta\theta_\mathrm{I})$, hence the asymptotic expansions for $q^{(0)}(z)$ as $\mathrm{Im}\{z\} \to \pm\infty$ are,

$$q^{(0)}(z) = \mp i\delta + \frac{2\delta\lambda_k^\delta \sin(\delta\theta_\mathrm{I})}{\sin(\delta\bar{\theta}_\mathrm{w})} e^{\pm i\delta z} + o(e^{\pm i\delta z}). \tag{A.15}$$

This same strategy can be applied to the higher order integrals as well but this is not discussed here for brevity.

5.3 Additional notes

The preceding article covered the general aspects of the high-contrast approximation, the derivation of the integral solutions and their practical use, however, some of the finer details were not thoroughly discussed for brevity. In these additional notes, we elaborate on why the edge conditions indicate the leading order behaviour of the spectral functions and prove that the integral solutions satisfy the boundary functional conditions. After this, there is also an alternate method to evaluate the Sommerfeld integrals than the one discussed in the article.

5.3.1 Edge conditions

We start the additional notes by looking more closely at how the edge conditions for the penetrable wedge problem (given by equation (2.15) in Nethercote et al. (2019a)) is split by the high-contrast approximation among the components. From the Frobenius method, the edge conditions take the following form for small r,

$$\Upsilon(r,\theta;\lambda) \sim \mathcal{A}(\lambda) + \mathcal{B}(\theta;\lambda) r^{\widehat{\delta}(\lambda)} - \frac{\mathcal{A}(\lambda)}{4}(kr)^2, \tag{5.1}$$

where Υ is one of the total wave fields (Φ or Ψ) with wavenumber $k = k_1$ and k_2 respectively. Say that $\widehat{\delta}$, $\mathcal{A}$ and $\mathcal{B}$ have the following asymptotic expansions as $\lambda \to 0$,

$$\widehat{\delta}(\lambda) = \delta + \sum_{j=1}^{\infty} C^{(j)}\lambda^j, \quad \mathcal{A}(\lambda) = \sum_{j=0}^{\infty} \mathcal{A}^{(j)}\lambda^j,$$
$$\mathcal{B}(\theta;\lambda) = \mathcal{B}(\theta;0) + \mathcal{B}_\lambda(\theta;0)\lambda + \mathcal{B}_{\lambda\lambda}(\theta;0)\frac{\lambda^2}{2} + O(\lambda^3). \tag{5.2}$$

We perform a Taylor expansion on Υ about $\lambda = 0$,

$$\Upsilon(r,\theta;\lambda) = \Upsilon(r,\theta;0) + \Upsilon_\lambda(r,\theta;0)\lambda + \Upsilon_{\lambda\lambda}(r,\theta;0)\frac{\lambda^2}{2} + O(\lambda^3), \tag{5.3}$$

where,

$$\begin{aligned}
\Upsilon(r,\theta;0) &\sim \mathcal{A}^{(0)} + \mathcal{B}(\theta;0)r^{\delta} - \frac{\mathcal{A}^{(0)}}{4}(kr)^2,\\
\Upsilon_{\lambda}(r,\theta;0) &\sim \mathcal{A}^{(1)} + \mathcal{B}_{\lambda}(\theta;0)r^{\delta} + \mathcal{B}(\theta;0)C^{(1)}r^{\delta}\ln(r) - \frac{\mathcal{A}^{(1)}}{4}(kr)^2,\\
\Upsilon_{\lambda\lambda}(r,\theta;0) &\sim 2\mathcal{A}^{(2)} + \mathcal{B}_{\lambda\lambda}(\theta;0)r^{\delta} + 2\mathcal{B}_{\lambda}(\theta;0)C^{(1)}r^{\delta}\ln(r) + 2\mathcal{B}(\theta;0)C^{(2)}r^{\delta}\ln(r)\\
&\quad + \mathcal{B}(\theta;0)\left(C^{(1)}\right)^2 r^{\delta}(\ln(r))^2 - \frac{\mathcal{A}^{(2)}}{4}(kr)^2. \qquad (5.4)
\end{aligned}$$

Substituting all of the definitions (5.4) into (5.3) will produce

$$\begin{aligned}
\Upsilon(r,\theta;\lambda) \sim &\left(\mathcal{A}^{(0)} + \mathcal{B}(\theta;0)r^{\delta} - \frac{\mathcal{A}^{(0)}}{4}(kr)^2\right)\\
&+ \left(\mathcal{A}^{(1)} + \mathcal{B}(\theta;0)C^{(1)}r^{\delta}\ln(r) + \mathcal{B}_{\lambda}(\theta;0)r^{\delta} - \frac{\mathcal{A}^{(1)}}{4}(kr)^2\right)\lambda\\
&+ \left(\mathcal{A}^{(2)} + \frac{\mathcal{B}(\theta;0)\left(C^{(1)}\right)^2}{2}r^{\delta}(\ln(r))^2 + \left(\mathcal{B}(\theta;0)C^{(2)} + \mathcal{B}_{\lambda}(\theta;0)C^{(1)}\right)r^{\delta}\ln(r)\right.\\
&\left.+ \frac{1}{2}\mathcal{B}_{\lambda\lambda}(\theta;0)r^{\delta} - \frac{\mathcal{A}^{(2)}}{4}(kr)^2\right)\lambda^2 + O(\lambda^3). \qquad (5.5)
\end{aligned}$$

Putting Υ as one of the total wave fields and applying the high-contrast approximation will obtain the edge conditions for the individual components,

$$\Phi^{(j)}, \Psi^{(j)} \sim \mathcal{A}^{(j)} - \frac{\mathcal{A}^{(j)}}{4}(k_{1,2}r)^2 + \sum_{n=0}^{j} B_n^{(j)}(\theta)r^{\delta}\left(\ln(r)\right)^{j-n} + \dots. \qquad (5.6)$$

Note that the definitions of $B_n^{(j)}$ differ between the wave fields but the $A^{(j)}$ values do not.

Now we look at how these individual edge conditions are transformed into the spectral space to determine the leading order behaviour for the spectral functions as $\mathrm{Im}\{z\} \to \pm\infty$. Take the following transforms of the total wave fields into the spectral functions,

$$\begin{aligned}
s(z) &= \frac{ik_1}{2}\int_0^{\infty}\left(\sin(z)\Phi - \frac{1}{ik_1 r}\frac{\partial\Phi}{\partial\theta}\right)\Big|_{\theta=0} e^{ik_1 r\cos(z)}\mathrm{d}r,\\
q(z) &= \frac{ik_2}{2}\int_0^{\infty}\left(\sin(z)\Psi - \frac{1}{ik_2 r}\frac{\partial\Psi}{\partial\theta}\right)\Big|_{\theta=\pi} e^{ik_2 r\cos(z)}\mathrm{d}r. \qquad (5.7)
\end{aligned}$$

We stick with the $s(z)$ case for now because the following procedure is exactly the same for $q(z)$. We transform the integral with the change of variables $R = -ik_1 r\cos(z)$, to get

$$s(z) = -\frac{1}{2}\int_0^\infty \left(\tan(z)\Phi\left(\frac{iR}{k_1\cos(z)}, 0\right) + \frac{1}{R}\frac{\partial\Phi}{\partial\theta}\left(\frac{iR}{k_1\cos(z)}, 0\right)\right)e^{-R}\mathrm{d}R, \quad (5.8)$$

where the physical limit $r \to 0$ is equivalent to $\mathrm{Im}\{z\} \to \pm\infty$ in the spectral space. For the leading order component, we have the approximation $\Phi^{(0)} \sim \mathcal{A}^{(0)} + B_0^{(0)}(\theta)r^\delta - \frac{\mathcal{A}^{(0)}}{4}(k_1 r)^2$ as $r \to 0$ which implies that,

$$\begin{aligned} s^{(0)}(z) \sim & -\frac{1}{2}\int_0^\infty \tan(z)\left(\mathcal{A}^{(0)} + B_0^{(0)}(0)\left(\frac{iR}{k_1\cos(z)}\right)^\delta + \frac{\mathcal{A}^{(0)}}{4}\left(\frac{R}{\cos(z)}\right)^2\right)e^{-R} \\ & + \frac{1}{R}\frac{\mathrm{d}B_0^{(0)}}{\mathrm{d}\theta}(0)\left(\frac{iR}{k_1\cos(z)}\right)^\delta e^{-R}\mathrm{d}R, \\ \sim & -\frac{\mathcal{A}^{(0)}}{2}\tan(z) + \frac{\mathcal{B}\delta\tan(z) + \mathcal{C}}{(\cos(z))^\delta}\Gamma(\delta) - \frac{\mathcal{A}^{(0)}\tan(z)}{4\cos^2(z)}. \end{aligned} \quad (5.9)$$

where $\Gamma(\delta)$ is the gamma function and the constants $\mathcal{B}$, $\mathcal{C}$ are absorbing $B_0^{(0)}$, δ and k_1. Noting that as $\mathrm{Im}\{z\} \to \pm\infty$,

$$\begin{aligned} \tan(z) &= \pm\, i(1 - 2e^{\pm 2iz}) + O\left(e^{\pm 4iz}\right), \\ (\sec(z))^\delta &= 2^\delta e^{\pm i\delta z}\left(1 - \delta e^{\pm 2iz} + O\left(e^{\pm 4iz}\right)\right), \end{aligned} \quad (5.10)$$

then we determine the leading order behaviour as $\mathrm{Im}\{z\} \to \pm\infty$ for the initial spectral functions $s^{(0)}(z)$ and $q^{(0)}(z)$,

$$s^{(0)}(z),\ q^{(0)}(z) \sim \pm A^{(0)} + O\left(e^{\pm i\delta z}, e^{\pm 4iz}\right), \quad (5.11)$$

where the notation $O(a, b)$ means,

$$O(a,b) = \begin{cases} O(a) & \text{if } \ b = o(a), \\ O(b) & \text{if } \ a = o(b), \end{cases}$$

and $A^{(0)} = -i\mathcal{A}^{(0)}/2$.

For the general components, we have the approximation (5.6) as $r \to 0$ which we substitute into (5.8) to obtain an approximation of the form,

$$s^{(j)}(z) \sim -\frac{\mathcal{A}^{(j)}}{2}\tan(z) - \frac{\mathcal{A}^{(j)}\tan(z)}{4\cos^2(z)} + (\sec(z))^{\delta}\sum_{n=0}^{j}\mathcal{B}_n\int_0^{\infty}(\tan(z)R+\mathcal{C}_n)\left(\ln\left(\frac{R}{\cos(z)}\right)\right)^n R^{\delta-1}e^{-R}\mathrm{d}R. \tag{5.12}$$

where $\mathcal{B}_n$ and $\mathcal{C}_n$ are constants absorbing k_1, δ and $B_n^{(j)}$. With the following expression,

$$\int_0^{\infty} R^{\delta-1}(\ln(R))^m e^{-R}\mathrm{d}R = \Gamma^{(m)}(\delta),$$

where $\Gamma^{(m)}$ is the m^{th} derivative of the Gamma function, we can evaluate each sum term of (5.12),

$$\begin{aligned}&\int_0^{\infty}(\tan(z)R+\mathcal{C}_n)\left(\ln\left(\frac{R}{\cos(z)}\right)\right)^n R^{\delta-1}e^{-R}\mathrm{d}R\\ &=\sum_{m=0}^{n}{}_nC_m\left(\Gamma^{(m)}(\delta+1)\tan(z)+\mathcal{C}_n\Gamma^{(m)}(\delta)\right)(\ln(\cos(z)))^{n-m},\end{aligned} \tag{5.13}$$

where ${}_nC_m$ is the binomial coefficient. Noting the following expansion as $\mathrm{Im}\{z\} \to \pm\infty$ for $N \geq 1$,

$$(\ln(\cos(z)))^N = (\mp iz)^N + \sum_{p=1}^{N}{}_NC_p(-\ln(2))^p(\mp iz)^{N-p} + O\left(z^{N-1}e^{\pm 2iz}\right) \tag{5.14}$$

and (5.10), then (5.13) can be asymptotically approximated as $\mathrm{Im}\{z\} \to \pm\infty$,

$$\int_0^{\infty}(\tan(z)R+\mathcal{C}_n)\left(\ln\left(\frac{R}{\cos(z)}\right)\right)^n R^{\delta-1}e^{-R}\mathrm{d}R = (\mathcal{C}_n \pm i\delta)\Gamma(\delta)(\mp iz)^n + O\left(z^{n-1}\right) \tag{5.15}$$

We can eventually conclude that the spectral functions $s^{(j)}(z)$ and $q^{(j)}(z)$ have the following asymptotic behaviour as $\mathrm{Im}\{z\} \to \pm\infty$,

$$s^{(j)}(z),\ q^{(j)}(z) \sim \pm A^{(j)} + O\left(z^j e^{\pm i\delta z}, e^{\pm 4iz}\right).$$

where $A^{(j)} = -i\mathcal{A}^{(j)}/2$.

5.3.2 Checking the boundary functional condition

In this section, we shall show that the spectral functions satisfy the boundary functional conditions,

$$q^{(j)}(\mp\bar{\theta}_{\mathrm{w}}+z)-q^{(j)}(\mp\bar{\theta}_{\mathrm{w}}-z)=h'(z)\left[s^{(j)}(\pm\theta_{\mathrm{w}}+h(z))-s^{(j)}(\pm\theta_{\mathrm{w}}-h(z))\right], \quad (5.16)$$

$$s^{(j+1)}(\pm\theta_{\mathrm{w}}+z)+s^{(j+1)}(\pm\theta_{\mathrm{w}}-z)=q^{(j)}(\mp\bar{\theta}_{\mathrm{w}}+g(z))+q^{(j)}(\mp\bar{\theta}_{\mathrm{w}}-g(z)). \quad (5.17)$$

First we take the integral formula for $q^{(j)}(z)$ and exploit the evenness of the integrand to half the integral range,

$$q^{(j)}(z)=\frac{1}{2\pi i}\int_0^{i\infty}\frac{\bar{\delta}\sin\left(\bar{\delta}\zeta\right)h'(\zeta)}{\cos\left(\bar{\delta}\zeta\right)+\sin\left(\bar{\delta}z\right)}\left[s^{(j)}(\theta_{\mathrm{w}}+h(\zeta))-s^{(j)}(\theta_{\mathrm{w}}-h(\zeta))\right]$$
$$-\frac{\bar{\delta}\sin\left(\bar{\delta}\zeta\right)h'(\zeta)}{\cos\left(\bar{\delta}\zeta\right)-\sin\left(\bar{\delta}z\right)}\left[s^{(j)}(-\theta_{\mathrm{w}}+h(\zeta))-s^{(j)}(-\theta_{\mathrm{w}}-h(\zeta))\right]\mathrm{d}\zeta.$$

Considering Figure 7 in Nethercote et al. (2019a), we shall deform the integration contour to $\mathcal{C}(z)$ which is defined as the path consisting of two straight lines joining the three points $\zeta=0$, $\mathrm{sign}(\mathrm{Im}\{z\})z$ and $i\infty$. This means that the formula for $q^{(j)}(z)$ is rewritten as,

$$q^{(j)}(z)=\frac{1}{2\pi i}\int_{\mathcal{C}(z)}\frac{\bar{\delta}\sin\left(\bar{\delta}\zeta\right)h'(\zeta)}{\cos\left(\bar{\delta}\zeta\right)+\sin\left(\bar{\delta}z\right)}\left[s^{(j)}(\theta_{\mathrm{w}}+h(\zeta))-s^{(j)}(\theta_{\mathrm{w}}-h(\zeta))\right]$$
$$-\frac{\bar{\delta}\sin\left(\bar{\delta}\zeta\right)h'(\zeta)}{\cos\left(\bar{\delta}\zeta\right)-\sin\left(\bar{\delta}z\right)}\left[s^{(j)}(-\theta_{\mathrm{w}}+h(\zeta))-s^{(j)}(-\theta_{\mathrm{w}}-h(\zeta))\right]\mathrm{d}\zeta.$$

For the first condition of (5.16), we must evaluate $q^{(j)}(-\bar{\theta}_{\mathrm{w}}+z)$ and $q^{(j)}(-\bar{\theta}_{\mathrm{w}}-z)$,

$$q^{(j)}(-\bar{\theta}_{\mathrm{w}}\pm z)=\frac{1}{2\pi i}\int_{\mathcal{C}(-\bar{\theta}_{\mathrm{w}}\pm z)}\frac{\bar{\delta}\sin\left(\bar{\delta}\zeta\right)h'(\zeta)}{\cos\left(\bar{\delta}\zeta\right)-\cos\left(\bar{\delta}z\right)}\left[s^{(j)}(\theta_{\mathrm{w}}+h(\zeta))-s^{(j)}(\theta_{\mathrm{w}}-h(\zeta))\right]$$
$$-\frac{\bar{\delta}\sin\left(\bar{\delta}\zeta\right)h'(\zeta)}{\cos\left(\bar{\delta}\zeta\right)+\cos\left(\bar{\delta}z\right)}\left[s^{(j)}(-\theta_{\mathrm{w}}+h(\zeta))-s^{(j)}(-\theta_{\mathrm{w}}-h(\zeta))\right]\mathrm{d}\zeta.$$

These two integrands are equivalent and the contour combination, $\mathcal{C}(-\bar{\theta}_{\mathrm{w}}+z)-\mathcal{C}(-\bar{\theta}_{\mathrm{w}}-z)$, will be closed. See Figure 5.1 for an illustration of the two contours $\mathcal{C}(-\bar{\theta}_{\mathrm{w}}+z)$ and $\mathcal{C}(-\bar{\theta}_{\mathrm{w}}-z)$ in the case where $\mathrm{Im}\{z\}>0$. If $\mathrm{Im}\{z\}>0$ then the

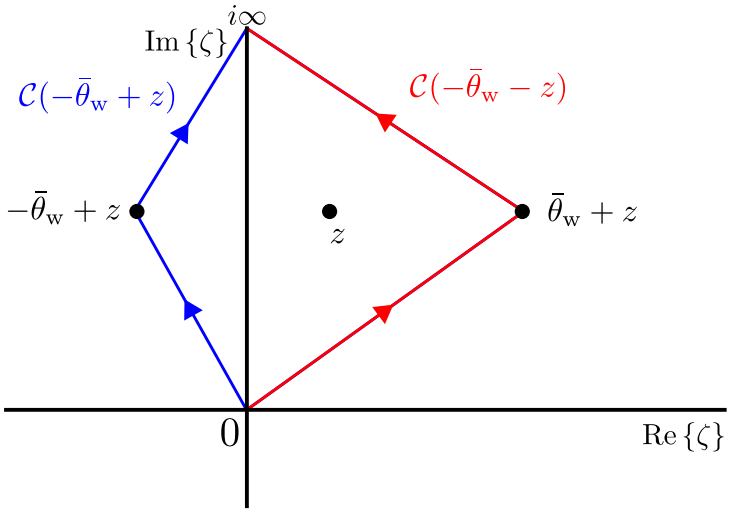

Figure 5.1: Illustration of the two contours $\mathcal{C}(-\bar{\theta}_{\mathrm{w}}+z)$ (shown in blue) and $\mathcal{C}(-\bar{\theta}_{\mathrm{w}}-z)$ (shown in red) when $\mathrm{Im}\{z\}>0$. This diagram includes one of the integrand's poles at $\zeta=z$.

closed contour joins the four points $\zeta=0$, $-\bar{\theta}_{\mathrm{w}}+z$, $i\infty$ and $\bar{\theta}_{\mathrm{w}}+z$ and encircles a pole at $\zeta=z$ in a clockwise direction. If $\mathrm{Im}\{z\}<0$ then the closed contour joins the four points $\zeta=0$, $\bar{\theta}_{\mathrm{w}}-z$, $i\infty$ and $-\bar{\theta}_{\mathrm{w}}-z$, encircling a pole at $\zeta=-z$ in an anti-clockwise direction. The application of Cauchy's Residue theorem in either case will imply that,

$$q^{(j)}(-\bar{\theta}_{\mathrm{w}}+z)-q^{(j)}(-\bar{\theta}_{\mathrm{w}}-z)=h'(z)\left[s^{(j)}(\theta_{\mathrm{w}}+h(z))-s^{(j)}(\theta_{\mathrm{w}}-h(z))\right].$$

Note that the case where $\mathrm{Im}\{z\}=0$ can also be proven in the limit $|\mathrm{Im}\{z\}|\to 0$.

For the second condition of (5.16), we must evaluate $q^{(j)}(\bar{\theta}_{\mathrm{w}}+z)$ and $q^{(j)}(\bar{\theta}_{\mathrm{w}}-z)$,

$$q^{(j)}(\bar{\theta}_{\mathrm{w}}\pm z)=\frac{1}{2\pi i}\int_{\mathcal{C}(\bar{\theta}_{\mathrm{w}}\pm z)}\frac{\bar{\delta}\sin\left(\bar{\delta}\zeta\right)h'(\zeta)}{\cos\left(\bar{\delta}\zeta\right)+\cos\left(\bar{\delta}z\right)}\left[s^{(j)}(\theta_{\mathrm{w}}+h(\zeta))-s^{(j)}(\theta_{\mathrm{w}}-h(\zeta))\right]$$
$$-\frac{\bar{\delta}\sin\left(\bar{\delta}\zeta\right)h'(\zeta)}{\cos\left(\bar{\delta}\zeta\right)-\cos\left(\bar{\delta}z\right)}\left[s^{(j)}(-\theta_{\mathrm{w}}+h(\zeta))-s^{(j)}(-\theta_{\mathrm{w}}-h(\zeta))\right]\mathrm{d}\zeta.$$

Both these integrands are equivalent and the combination, $\mathcal{C}(\bar{\theta}_\mathrm{w}+z)-\mathcal{C}(\bar{\theta}_\mathrm{w}-z)$, will also form a closed contour which joins the four points $\zeta=0$, $\mathrm{sign}(\mathrm{Im}\{z\})(\bar{\theta}_\mathrm{w}+z)$, $i\infty$ and $\mathrm{sign}(\mathrm{Im}\{z\})(-\bar{\theta}_\mathrm{w}+z)$ in that order. Cauchy's Residue theorem will evaluate the residue of a single pole at $\zeta=\mathrm{sign}(\mathrm{Im}\{z\})z$ with a winding number equal to $\mathrm{sign}(\mathrm{Im}\{z\})$ proving,

$$q^{(j)}(\bar{\theta}_\mathrm{w}+z)-q^{(j)}(\bar{\theta}_\mathrm{w}-z)=h'(z)\left[s^{(j)}(-\theta_\mathrm{w}+h(z))-s^{(j)}(-\theta_\mathrm{w}-h(z))\right].$$

As before, the case $\mathrm{Im}\{z\}=0$ is proven in the limit $|\mathrm{Im}\{z\}|\to 0$. Hence both conditions (5.16) are shown to be satisfied.

Showing that the integral formula for $s^{(j+1)}(z)$ satisfies the conditions (5.17) is done in a similar way. Firstly, we rewrite $s^{(j+1)}(z)$ as an integral along the path $\mathcal{C}(z)$.

$$\begin{aligned}s^{(j+1)}(z)=\frac{1}{2\pi i}\int_{\mathcal{C}(z)}&\frac{\delta\cos(\delta z)}{\cos(\delta\zeta)+\sin(\delta z)}\left[q^{(j)}(\bar{\theta}_\mathrm{w}+g(\zeta))+q^{(j)}(\bar{\theta}_\mathrm{w}-g(\zeta))\right]\\&+\frac{\delta\cos(\delta z)}{\cos(\delta\zeta)-\sin(\delta z)}\left[q^{(j)}(-\bar{\theta}_\mathrm{w}+g(\zeta))+q^{(j)}(-\bar{\theta}_\mathrm{w}-g(\zeta))\right]\mathrm{d}\zeta.\end{aligned}$$

For the first condition of (5.17), we must find $s^{(j+1)}(\theta_\mathrm{w}+z)$ and $s^{(j+1)}(\theta_\mathrm{w}-z)$.

$$\begin{aligned}s^{(j+1)}(\theta_\mathrm{w}\pm z)=\mp\frac{1}{2\pi i}\int_{\mathcal{C}(\theta_\mathrm{w}\pm z)}&\frac{\delta\sin(\delta z)}{\cos(\delta\zeta)+\cos(\delta z)}\left[q^{(j)}(\bar{\theta}_\mathrm{w}+g(\zeta))+q^{(j)}(\bar{\theta}_\mathrm{w}-g(\zeta))\right]\\&+\frac{\delta\sin(\delta z)}{\cos(\delta\zeta)-\cos(\delta z)}\left[q^{(j)}(-\bar{\theta}_\mathrm{w}+g(\zeta))+q^{(j)}(-\bar{\theta}_\mathrm{w}-g(\zeta))\right]\mathrm{d}\zeta.\end{aligned}$$

The addition of these two integrals will produce the closed contour $\mathcal{C}(\theta_\mathrm{w}+z)-\mathcal{C}(\theta_\mathrm{w}-z)$. This contour joins the four points $\zeta=0$, $\mathrm{sign}(\mathrm{Im}\{z\})(\theta_\mathrm{w}+z)$, $i\infty$ and $\mathrm{sign}(\mathrm{Im}\{z\})(-\theta_\mathrm{w}+z)$ (in that order) and encircles a pole at $\mathrm{sign}(\mathrm{Im}\{z\})z$ with a winding number equal to $\mathrm{sign}(\mathrm{Im}\{z\})$. Applying Cauchy's Residue theorem will therefore imply,

$$s^{(j+1)}(\theta_\mathrm{w}+z)+s^{(j+1)}(\theta_\mathrm{w}-z)=q^{(j)}(-\bar{\theta}_\mathrm{w}+g(z))+q^{(j)}(-\bar{\theta}_\mathrm{w}-g(z)).$$

For the second condition of (5.17), we must find $s^{(j+1)}(-\theta_\mathrm{w}+z)$ and $s^{(j+1)}(-\theta_\mathrm{w}-z)$.

$$s^{(j+1)}(-\theta_\mathrm{w}\pm z) = \pm\frac{1}{2\pi i}\int_{\mathcal{C}(\theta_\mathrm{w}\pm z)} \frac{\delta\sin(\delta z)}{\cos(\delta\zeta)-\cos(\delta z)}\left[q^{(j)}(\bar{\theta}_\mathrm{w}+g(\zeta))+q^{(j)}(\bar{\theta}_\mathrm{w}-g(\zeta))\right] + \frac{\delta\sin(\delta z)}{\cos(\delta\zeta)+\cos(\delta z)}\left[q^{(j)}(-\bar{\theta}_\mathrm{w}+g(\zeta))+q^{(j)}(-\bar{\theta}_\mathrm{w}-g(\zeta))\right]\mathrm{d}\zeta.$$

As before, adding together these two integrals will produce the contour $\mathcal{C}(-\theta_\mathrm{w}+z)-\mathcal{C}(-\theta_\mathrm{w}-z)$ joining the four points $\zeta=0$, $\mathrm{sign}(\mathrm{Im}\{z\})(-\theta_\mathrm{w}+z)$, $i\infty$ and $\mathrm{sign}(\mathrm{Im}\{z\})(\theta_\mathrm{w}+z)$ in a closed loop around a pole at $\mathrm{sign}(\mathrm{Im}\{z\})z$ with a winding number equal to $-\mathrm{sign}(\mathrm{Im}\{z\})$. Then Cauchy's Residue theorem implies

$$s^{(j+1)}(-\theta_\mathrm{w}+z)+s^{(j+1)}(-\theta_\mathrm{w}-z)=q^{(j)}(\bar{\theta}_\mathrm{w}+g(z))+q^{(j)}(\bar{\theta}_\mathrm{w}-g(z)),$$

as required, hence all the boundary functional conditions are satisfied.

5.3.3 Sommerfeld integral evaluation with hybrid contour

In this last subsection, we discuss an alternate method to evaluate the Sommerfeld integrals. Nethercote et al. (2019a) discusses a strategy that involves fully deforming the Sommerfeld contours to the local steepest descent contours (SDCs). This requires prior knowledge of the GO component and may require us to carefully navigate around branch cuts when appropriate. The following strategy is conceptually simpler because no poles are crossed and the branch cuts are avoided completely. Recall the two Sommerfeld integral forms of the total exterior and interior wave fields,

$$\Phi(r,\theta)=\frac{1}{2\pi i}\int_{\gamma_+}\Phi_\mathrm{int}(r,\theta,z)\mathrm{d}z, \tag{5.18}$$

$$\Psi(r,\theta)=\frac{1}{2\pi i}\int_{\gamma_+}\Psi_\mathrm{int}(r,\theta,z)\mathrm{d}z, \tag{5.19}$$

where the Sommerfeld contour γ_+ is displayed in Figure 5.2 and the integrands are given by,

$$\Phi_{\text{int}}(r,\theta,z) = e^{-ik_1 r\cos(z)}\left[s(\theta+z) - s(\theta-z)\right], \tag{5.20}$$

$$\Psi_{\text{int}}(r,\theta,z) = e^{-ik_2 r\cos(z)}\left[q(\theta-\pi+z) - q(\theta-\pi-z)\right]. \tag{5.21}$$

with the spectral functions $s(z)$ and $q(z)$.

It was stated in Nethercote et al. (2019a) that all singularities in the two integrands are caused by the spectral functions and are confined to the real line and the local vicinity of branch cuts. The branch cuts of Φ_{int} are centred on and perpendicular to the real line and the branch cuts of Ψ_{int} are entirely on the real line. There was also another statement saying that numerical integration on the Sommerfeld contour is impractical because the integrands will be highly oscillatory due to the presence of $\exp(-ik_{1,2}r\cos(z))$.

In this alternative method, we deform the left and right parts of the Sommerfeld contour to the tail ends of the SDCs and keep the bottom part high enough to be above the poles and branch cuts. This creates a special hybrid contour which we display in Figure 5.2.

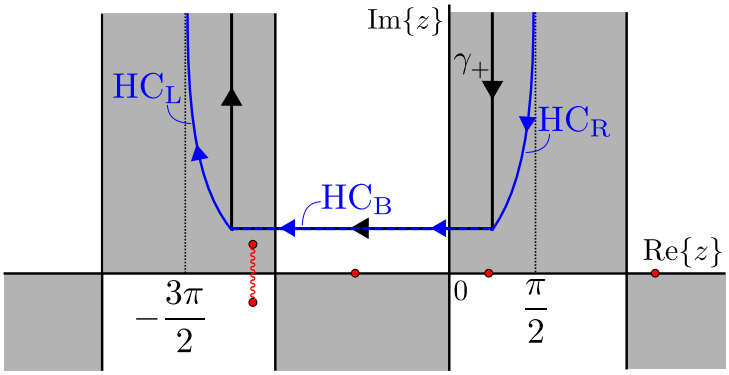

Figure 5.2: Illustration of the Sommerfeld contour γ_+ (black) alongside the hybrid contour parts, HC_L, HC_B and HC_R (blue). Pole locations and branch cuts are indicated in red.

This hybrid contour is defined in three segments with three different parametrisations,

$$\begin{aligned}
\mathrm{HC_R} &= \left\{ t : z = t + \mathrm{gd}(it),\ t_0 \le t < \frac{\pi}{2} \right\}, \\
\mathrm{HC_B} &= \left\{ t : z = t + \mathrm{gd}(it_0),\ -\pi - t_0 \le t \le t_0 \right\}, \\
\mathrm{HC_L} &= \left\{ t : z = -t - \pi + \mathrm{gd}(it),\ t_0 \le t < \frac{\pi}{2} \right\},
\end{aligned} \tag{5.22}$$

where the direction of each segment is indicated in Figure 5.2 and $\mathrm{gd}(it)$ is the Gudermannian function which takes the following definition in the interval $-\pi/2 < t < \pi/2$,

$$\mathrm{gd}(it) = i \ln\left(\sec(t) + \tan(t)\right) = i \ln\left(\tan\left(\frac{t}{2} + \frac{\pi}{4}\right)\right). \tag{5.23}$$

The parameter t_0 is chosen to keep $\mathrm{HC_B}$ above all poles and branch cuts. For Φ_{int}, we shall choose[1] $t_0 = \max\left(\pi/24, \cos^{-1}(\lambda_k)\right)$ so that $\mathrm{HC_B}$ has an appropriate minimum distance from the poles and does not intersect the branch cuts (which have the imaginary height given by $\mathrm{gd}(i\cos^{-1}(\lambda_k)) = i\cosh^{-1}(1/\lambda_k)$). Hence the integral (5.18) is rewritten as,

$$\begin{aligned}
\Phi(r,\theta) = &\frac{1}{2\pi i}\int_{\frac{\pi}{2}}^{t_0} \Phi_{\mathrm{int}}(r,\theta,t+\mathrm{gd}(it))(1+i\sec(t))\mathrm{d}t \\
&+ \frac{1}{2\pi i}\int_{t_0}^{-\pi-t_0} \Phi_{\mathrm{int}}(r,\theta,t+\mathrm{gd}(it_0))\mathrm{d}t \\
&+ \frac{1}{2\pi i}\int_{t_0}^{\frac{\pi}{2}} \Phi_{\mathrm{int}}(r,\theta,-\pi-t+\mathrm{gd}(it))(-1+i\sec(t))\mathrm{d}t.
\end{aligned} \tag{5.24}$$

For Ψ_{int}, the branch cuts are confined to the real line so we choose $t_0 = \pi/24$,

[1] Note that the value $\pi/24$ was obtained by trial and error and for convenience with the formula (5.23).

hence the integral (5.19) is rewritten as,

$$\begin{aligned}\Psi(r,\theta) = &\frac{1}{2\pi i}\int_{\frac{\pi}{2}}^{\frac{\pi}{24}} \Psi_{\text{int}}(r,\theta,t+\text{gd}(it))(1+i\sec(t))\text{d}t \\ &+ \frac{1}{2\pi i}\int_{\frac{\pi}{24}}^{-\frac{25\pi}{24}} \Psi_{\text{int}}(r,\theta,t+\text{gd}(i\pi/24))\text{d}t \\ &+ \frac{1}{2\pi i}\int_{\frac{\pi}{24}}^{\frac{\pi}{2}} \Psi_{\text{int}}(r,\theta,-\pi-t+\text{gd}(it))(-1+i\sec(t))\text{d}t. \end{aligned} \tag{5.25}$$

The numerical integration is also significantly quickened when we interpolate the spectral parts,

$$s(\theta+z)-s(\theta-z), \quad \text{or} \quad q(\theta-\pi+z)-q(\theta-\pi-z), \tag{5.26}$$

in a similar way to the method in Nethercote et al. (2019a). The integrals on the contour segments, $\text{HC}_{\text{L,R}}$, will need two-dimensional interpolations of (5.26) on θ and t. On HC_{B}, one could think that we need another two-dimensional interpolation but we could interpolate one of the spectral functions, $s(t+\text{gd}(it_0))$ (or $q(t+\text{gd}(it_0))$), on an extended t range instead. Then by utilising the property $s(z^*) = (s(z))^*$ (or $q(z^*) = (q(z))^*$), we can recreate the combination (5.26). This is significantly quicker to compute than a two-dimensional interpolation. In total, we create six spline interpolations which are listed in Table 5.1 with the respective intervals for θ and t.

This integration strategy with the hybrid contour is advantageous because it is much less complicated than fully deforming to the SDCs as discussed in Nethercote et al. (2019a). This is because it does not require prior knowledge of the GO component or the precise location of the branch cuts except for the branch point locations for the Φ case. Also because the contour stays clear of all singularities, they do not cause any numerical error (at GO discontinuities for example, the steepest descent contour intersects a simple pole but the hybrid contour does not).

However numerical integrations will be slower when $k_{1,2}r$ is large because of the highly oscillating exponential on HC_{B}. This same exponential will also require

Function to interpolate	t interval	
$s(t+\mathrm{gd}(it_0))$	$[-\pi-\theta_\mathrm{w}-t_0, \pi+\theta_\mathrm{w}+t_0]$	
$q(t+\mathrm{gd}(it_0))$	$\left[-\pi-\bar{\theta}_\mathrm{w}-t_0, \pi+\bar{\theta}_\mathrm{w}+t_0\right]$	
	θ interval	t interval
$s(\theta+t+\mathrm{gd}(it))-s(\theta-t-\mathrm{gd}(it))$	$[-\theta_\mathrm{w}, \theta_\mathrm{w}]$	$[t_0, \pi/2)$
$s(\theta-\pi-t+\mathrm{gd}(it))-s(\theta+\pi+t-\mathrm{gd}(it))$	$[-\theta_\mathrm{w}, \theta_\mathrm{w}]$	$[t_0, \pi/2)$
$q(\theta-\pi+t+\mathrm{gd}(it))-q(\theta-\pi-t-\mathrm{gd}(it))$	$\left[\pi-\bar{\theta}_\mathrm{w}, \pi+\bar{\theta}_\mathrm{w}\right]$	$[t_0, \pi/2)$
$q(\theta-2\pi-t+\mathrm{gd}(it))-q(\theta+t-\mathrm{gd}(it))$	$\left[\pi-\bar{\theta}_\mathrm{w}, \pi+\bar{\theta}_\mathrm{w}\right]$	$[t_0, \pi/2)$

Table 5.1: List of required interpolations and their respective θ and t intervals.

more accurate interpolations because its size (if $k_{1,2}r$ is large enough) can easily pick out any interpolation error.

For these reasons, we find that using the hybrid contour for Sommerfeld integrals is more appropriate for low-frequency/near-field evaluations (small $k_{1,2}r$) because the exponential is less troublesome which implies that the interpolations will require less accuracy and the integration is quicker to compute. The hybrid contour will also be more effective if the wavenumbers are of similar size (creating smaller branch cuts and allowing us to lower the height of $\mathrm{HC_B}$).

Chapter 6

Conclusions

6.1 Summary

In this thesis, we have investigated several analytic and asymptotic techniques that can be used for wave diffraction by wedges with perfect boundary conditions. We have also extended these techniques to create a new asymptotic approximation for penetrable wedge diffraction.

We started by defining the perfect and penetrable wedge diffraction problems in acoustic and electromagnetic physical settings (Chapter 1). Chapter 2 featured an introduction to one of the fundamental procedures for wave diffraction, the Wiener-Hopf technique, by applying it to the Sommerfeld half-plane problem. In doing so, we demonstrated the basic aspects of the procedure and showed its effectiveness for edge diffraction problems. Considering that the half-plane is a special case of a wedge, the solution provided a handy reference for the solution to perfect wedge diffraction.

In Chapter 3, we reviewed the existing literature on the subject of perfect wedge diffraction. We concluded that the Sommerfeld-Malyuzhinets (S-M) solution in the

form of a Sommerfeld integral should be considered as the 'gold standard' representation despite the apparent 'black magic' in its formulation. But this issue is addressed in appendix B of the inserted article using Green's integral operators. The review relayed the belief of many researchers, given in the references therein, that the Wiener-Hopf (W-H) technique can be applied to wedge diffraction problems despite not being directly designed for them. Alternative formulae were found using Macdonald's original separation of variables method and the Kontorovich-Lebedev (K-L) transform approach, which were proven to be equivalent to the S-M solution.

Three less well-known methods were also reviewed and all were shown to provide interesting mathematical formulations of the problem considered. For instance, the embedding formula was an efficient way to find the diffraction coefficient and is adaptable to many geometries. The random walk method is also adaptable and is very novel in its mathematical approach. The method of functionally-invariant solutions was concluded to be more useful for time-dependent problems (such as the tracking of wave fronts in time) as opposed to the time-harmonic problem it was applied to here.

The review article also assessed the various techniques to evaluate the 'gold standard' solution. This included integrating on steepest descent contours, a truncated series solution and geometrical theory of diffraction (GTD) asymptotic approximations. We determined that while the steepest descent integral was slower to evaluate, it provided the most accuracy for a wide range of parameters. We also determined that the truncated series is very accurate and fast as a low-frequency/near-field approximation. Similarly, the GTD approximations are very accurate and fast as high-frequency/far-field approximations.

We began studying the penetrable wedge diffraction problem in Chapter 4. Here we reviewed the literature on the topic but focused on four specific articles.

This included a low-contrast approximation (Rawlins, 1999), a high-contrast approximation (Lyalinov, 1999) as well as extensions of the W-H technique from Chapter 3 (Shanin, 1998; Daniele and Lombardi, 2011). While it was difficult to compare the methods directly, we believed that components of the methods described by Lyalinov (1999), Shanin (1998) and Daniele and Lombardi (2011) could be combined to create an effective high-contrast approximation.

With the knowledge of all of the techniques researched in previous chapters, we sought to solve the penetrable wedge diffraction problem in Chapter 5 by creating a high-contrast asymptotic approximation of the form,

$$\Phi = \sum_{j=0}^{\infty} \lambda^j \Phi^{(j)}, \quad \Psi = \sum_{j=0}^{\infty} \lambda^j \Psi^{(j)}. \tag{6.1}$$

Each of these wave field components, $\Phi^{(j)}$ and $\Psi^{(j)}$, were represented by a Sommerfeld integral,

$$\begin{aligned} \Phi^{(j)}(r,\theta) &= \frac{1}{2\pi i} \int_{\gamma_+ + \gamma_-} e^{-ik_1 r \cos(z)} s^{(j)}(\theta + z) \mathrm{d}z, \\ \Psi^{(j)}(r,\theta) &= \frac{1}{2\pi i} \int_{\gamma_+ + \gamma_-} e^{-ik_2 r \cos(z)} q^{(j)}(\theta - \pi + z) \mathrm{d}z, \end{aligned} \tag{6.2}$$

with $\gamma_\pm$ defined in Nethercote et al. (2019a), and each of the spectral functions were determined by an iterative scheme. The initial spectral function $s^{(0)}(z)$ was given by,

$$s^{(0)}(z) = \frac{\delta \cos(\delta z)}{\sin(\delta z) - \sin(\delta \theta_\mathrm{I})}. \tag{6.3}$$

For the interior spectral functions, $q^{(j)}(z)$ (with $j = 0, 1, 2, ...$), we integrate the known $s^{(j)}$ functions,

$$\begin{aligned} q^{(j)}(z) = \frac{1}{4\pi i} \int_{-i\infty}^{i\infty} \Bigg(& \frac{\bar{\delta} \sin\left(\bar{\delta}\zeta\right) h'(\zeta)}{\cos\left(\bar{\delta}\zeta\right) + \sin\left(\bar{\delta}z\right)} \left[s^{(j)}(\theta_\mathrm{w} + h(\zeta)) - s^{(j)}(\theta_\mathrm{w} - h(\zeta)) \right] \\ & - \frac{\bar{\delta} \sin\left(\bar{\delta}\zeta\right) h'(\zeta)}{\cos\left(\bar{\delta}\zeta\right) - \sin\left(\bar{\delta}z\right)} \left[s^{(j)}(-\theta_\mathrm{w} + h(\zeta)) - s^{(j)}(-\theta_\mathrm{w} - h(\zeta)) \right] \Bigg) \mathrm{d}\zeta, \end{aligned} \tag{6.4}$$

whereas the exterior spectral functions, $s^{(j+1)}(z)$ (with $j = 0, 1, 2, ...$), are determined by integrating the known $q^{(j)}$ functions,

$$s^{(j+1)}(z) = \frac{1}{4\pi i}\int_{-i\infty}^{i\infty}\left(\frac{\delta\cos(\delta z)}{\cos(\delta\zeta)+\sin(\delta z)}\left[q^{(j)}(\bar{\theta}_{\mathrm{w}}+g(\zeta))+q^{(j)}(\bar{\theta}_{\mathrm{w}}-g(\zeta))\right]\right.$$
$$\left.+\frac{\delta\cos(\delta z)}{\cos(\delta\zeta)-\sin(\delta z)}\left[q^{(j)}(-\bar{\theta}_{\mathrm{w}}+g(\zeta))+q^{(j)}(-\bar{\theta}_{\mathrm{w}}-g(\zeta))\right]\right)\mathrm{d}\zeta. \tag{6.5}$$

This procedure is illustrated in Figure 6.1, starting with parameter definitions and the initial spectral function to finish with the j^{th} order approximation.

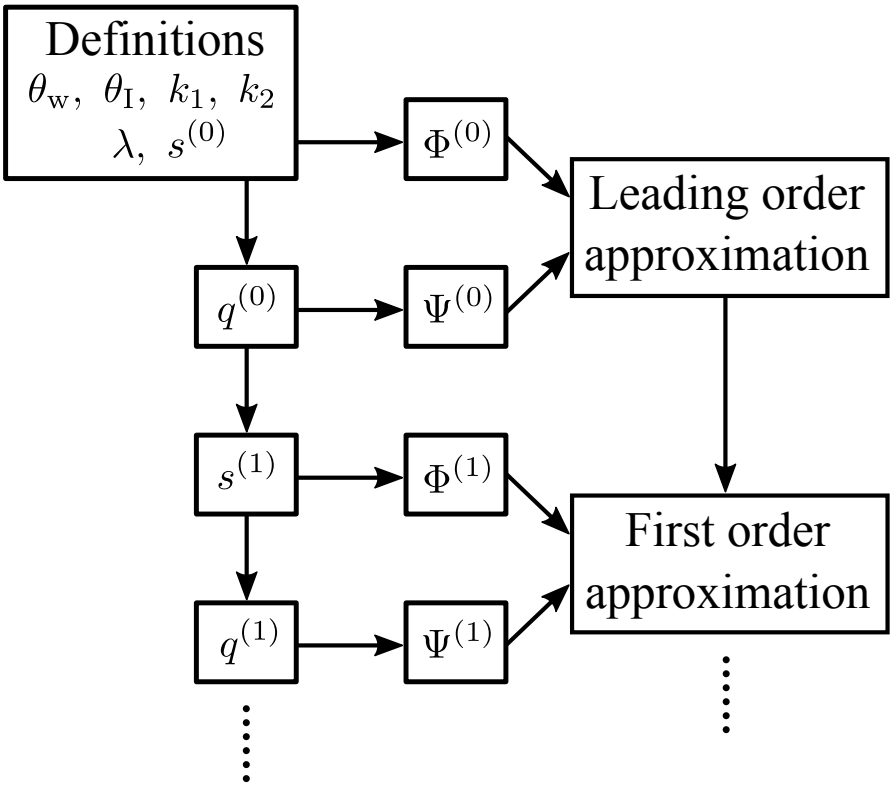

Figure 6.1: Flowchart to illustrate how to find the j^{th} order approximation. Start with the definitions in the top left and use (6.4) and (6.5) to work out the required spectral functions, use the Sommerfeld integrals (6.2) to determine the associated wave fields and then (6.1) gives the j^{th} order approximation.

This method proved to be efficient and accurate for a wide range of parameters provided that λ is sufficiently small. However, as highlighted in the conclusions of

the paper (Nethercote et al., 2019a), we found that the numerical strategies for the spectral integrals would need to be adapted in extreme cases such as thin wedges ($\bar{\theta}_{\mathrm{w}} \to 0$) and grazing incidence ($\theta_{\mathrm{I}} \to \theta_{\mathrm{w}}$). The former issue is because the z-poles become dense in this case and the spectral integration contour is squeezed between them. The latter case is because the spectral poles start approaching the spectral integration contour, and the code we have built at this time does not account for this.

6.2 Future extensions or formulations

The article (Nethercote et al., 2019a) also briefly mentioned a few improvements and extensions to the methodology, which we shall elaborate on in this section.

Interpolation. One of the suggested developments was aimed at improving the interpolation procedure for the spectral integrals. Recalling that as $\mathrm{Im}\{z\} \to \infty$,

$$p(z) = A^{(j)} + O(z^j e^{i\delta z}), \tag{6.6}$$

where $p = q^{(j)}$ or $s^{(j)}$, then we want a unit mapping $t(\tau) : [0,1) \to [0,\infty)$ such that

$$p\left(\mathrm{Re}\{z\} + it(\tau)\right) = A^{(j)} + O\left(1-\tau\right). \tag{6.7}$$

We suggested that this ideal unit mapping might involve the Lambert W (or product logarithm) function but this has not been fully investigated yet. Determining the constants $A^{(j)}$ explicitly will also be helpful to improve this interpolation procedure.

Error analysis It was also suggested in Nethercote et al. (2019a) that it is worthwhile to perform a rigorous analysis into the robustness of the asymptotic

scheme. Recall the end of section 4.3 of the article where we determined a condition for convergence $\left(0 < \lambda < g'\left(\frac{\pi}{2} - \theta_{\mathrm{I}}\right)\right)$ and illustrated the error of the asymptotic scheme (see figure 10 in Nethercote et al. (2019a)) for the special case with a penetrable half-space. In this case, it is simple to asymptotically approximate the error,

$$\left|\Phi - \sum_{n=0}^{j} \lambda^j \Phi^{(j)}\right| = \left|\Psi - \sum_{n=0}^{j} \lambda^j \Psi^{(j)}\right| \sim \frac{2\lambda^{j+1}}{\left(g'\left(\frac{\pi}{2} - \theta_{\mathrm{I}}\right)\right)^{j+1}}, \tag{6.8}$$

however, we wish to determine similar conditions and quantities for a more general value of wedge angle. With a more rigorous analysis, it is possible to do this, however, it will be much more difficult and there may be multiple convergence conditions and different error approximations to find.

GTD approximation. We could improve the numerical strategies discussed in the paper (Nethercote et al., 2019a) for the Sommerfeld integrals, by performing a rigorous asymptotic analysis of the spectral functions in the local regions around the branch cuts. This includes the local behaviour around branch points and determining the jump across the cuts. This asymptotic analysis is vital to create GTD approximations.

To explain this, we take the exterior total field using the steepest descent formula (see equation (5.23) in Nethercote et al. (2019a)) and apply the method of steepest descent as $k_1 r \to \infty$. Then we obtain the GTD approximation

$$\Phi \approx \Phi_{\mathrm{GO}} + \frac{e^{ik_1 r + i\frac{\pi}{4}}}{\sqrt{2\pi k_1 r}} \left[s(\theta - \pi) - s(\theta + \pi)\right]. \tag{6.9}$$

However, this approximation is only valid in the region $\theta \in (-\theta_{\mathrm{w}} + \cos^{-1}(\lambda_k), \theta_{\mathrm{w}} - \cos^{-1}(\lambda_k))$ (excluding GO discontinuities) because we have not considered the contribution from branch cuts here. The asymptotic analysis will allow us to accurately account for branch cut contributions (which physically represent head/lateral

waves) to create an accurate GTD approximation. This is also true for creating uniform GTD approximations (for example see Section 5.2 of Nethercote et al. (2019b) and references within).

Interior wedge example. In Nethercote et al. (2019a), all of the test cases in Table 1 had $\theta_w = 3\pi/4$. We explained that this choice was for convenience because the GO component is simpler to obtain. However, the solution is valid for all $\theta_w \in (0, \pi)$, but we have not as yet considered fully the case where $\theta_w < \pi/2$ in our MATLAB code. This is partly due to the more difficult GO component (as mentioned earlier) but also because the numerical strategies for the spectral integrals are affected by multiple spectral poles.

Take test case 2 in the aforementioned article with $\theta_w = \pi/4$ instead. Figure 6.2 (left) illustrates the GO component in this case by showing that the wedge faces have two reflections and two transmissions each. The red (resp. blue) lines trace the incident wave impacting the top (resp. bottom) face and then the bottom (resp. top) face.

We have not built the MATLAB code to account for all possibilities, but for a specific case, the ideas of the numerical strategies discussed in Nethercote et al. (2019a) are still valid. Figure 6.2 (right) is a polar plot of the total field's magnitude at $r = 5$ for this special test case including the leading and first order approximations.

Rational wedge case. So far, we have only suggested improvements to the numerical strategies. However, it is possible that the spectral integrals can be partly evaluated using analytical means. For instance, if $\theta_w = \frac{m\pi}{n}$ with coprime integers, m and n, then the spectral functions seem to display quasiperiodic behaviour (in $\mathrm{Re}\{z\}$) which has the potential to be exploitable.

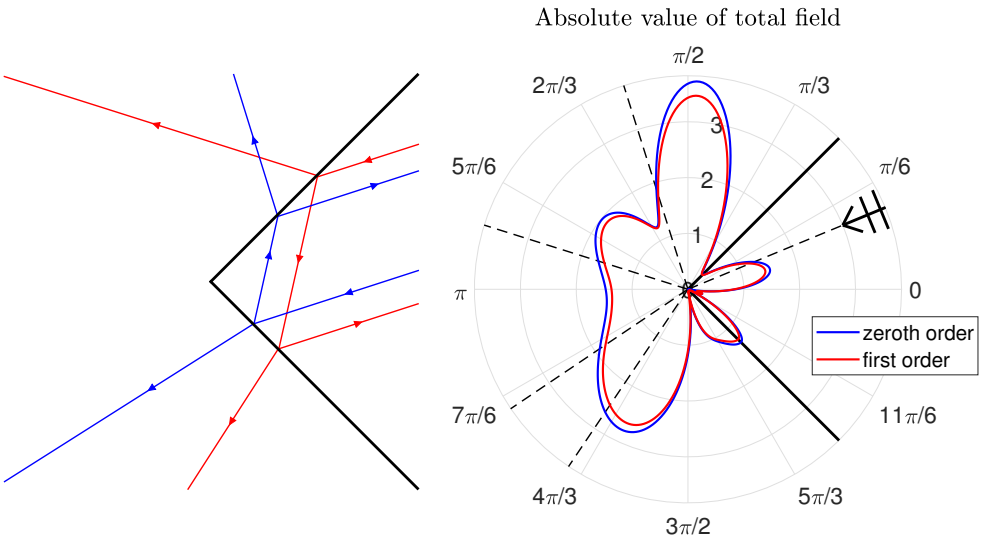

Figure 6.2: Ray interpretation of the GO component (left) and a polar plot of the total field's absolute value at $r = 5$ including the leading and first order approximation (right). Here we have the parameter values: $\theta_{\mathrm{w}} = \pi/4, \theta_{\mathrm{I}} = \pi/8, k_1 = 1, k_2 = 2, \lambda = 0.01$. Note that the dashed lines indicate GO discontinuities.

Integral combination. Another possibility is to combine the spectral integrals. The idea is to switch the order of the integrals and evaluate the inner one so that the spectral function $s^{(j+1)}(z)$ (resp. $q^{(j+1)}(z)$) is written as an integral of $s^{(j)}(z)$ (resp. $q^{(j)}(z)$) only. However, these inner integrals are likely to be very complicated so will require significant analysis before they can be evaluated correctly and accurately.

Alternative formulation. We stated in Nethercote et al. (2019a) that λ_k and λ are assumed to be independent of each other. Now let us remove this assumption. In an acoustic setting, recalling that we are in an adiabatic process (see Section 1.1.1), we have

$$\lambda_k = \frac{c_2}{c_1} = \sqrt{\frac{\gamma_{c2} p_2 \rho_1}{\gamma_{c1} p_1 \rho_2}}, \tag{6.10}$$

where p_1 and p_2 are the resting pressures in the host and scatterer regions respectively. In an electromagnetic setting (see Section 1.1.2), we have a similar

relationship,

$$\lambda_k = \frac{c_2}{c_1} = \sqrt{\frac{\mu_1 \epsilon_1}{\mu_2 \epsilon_2}}. \tag{6.11}$$

In both cases, the wavenumber is proportional to the square root of the contrast parameter, $\lambda_k \propto \sqrt{\lambda}$. We can use this to reformulate the asymptotic approximation to be ascending powers of λ_k instead. For example, assume that $\lambda_k = \sqrt{\lambda}$ and take the problem of the penetrable half-space with the solution,

$$\Phi = e^{-ik_1 r\cos(\theta-\theta_\mathrm{I})} + Re^{ik_1 r\cos(\theta+\theta_\mathrm{I})}, \quad \Psi = Te^{-ik_2 r\cos(\theta-\theta_\mathrm{T})}, \tag{6.12}$$

where,

$$T = R + 1, \quad R = \frac{\frac{\lambda_k \cos(\theta_\mathrm{I})}{\cos(\theta_\mathrm{T})} - \lambda}{\frac{\lambda_k \cos(\theta_\mathrm{I})}{\cos(\theta_\mathrm{T})} + \lambda} \quad \text{and} \quad \theta_\mathrm{T} = \frac{\pi}{2} - g\left(\frac{\pi}{2} - \theta_\mathrm{I}\right). \tag{6.13}$$

Taylor expanding the coefficients as $\lambda_k \to 0$ will obtain,

$$R = 1 + 2\sum_{j=1}^{\infty}\left(\frac{-\lambda_k \cos(\theta_\mathrm{T})}{\cos(\theta_\mathrm{I})}\right)^j, \quad T = 2\sum_{j=0}^{\infty}\left(\frac{-\lambda_k \cos(\theta_\mathrm{T})}{\cos(\theta_\mathrm{I})}\right)^j. \tag{6.14}$$

This indicates that a similar high-contrast expansion could be made as $\lambda_k \to 0$ and this will be explored in future work.

6.3 Concluding remarks

Upon reflection of the work presented in this thesis, it is important to see the pedagogical value in the review article (Nethercote et al., 2019b) and the literature review in Chapter 4, especially for one who is new to the mathematical theory of diffraction. In presenting (Nethercote et al., 2019a), we wanted to convey the novelty of the high-contrast asymptotic scheme, the versatility of the Wiener-Hopf technique and the capability of the numerical strategies employed for integral evaluation. This last chapter was aimed to summarise the thesis as well as to

show the extendibility of the procedure with various improvements and alternative formulations.

Recall that we briefly discussed our motivations in Chapter 1 and the research area of hybrid numerical-asymptotic schemes in Chapter 4. Earlier in Section 6.2, we stated that the GTD approximation was missing the head/lateral wave component. Head waves are a key missing component needed for the improvement of the hybrid numerical-asymptotic methods featured in (Groth et al., 2018). Being able to approximate this head wave component will improve this methodology for convex polygon diffraction which can be extended to diffraction by an random ensemble of ice crystals (such as an ice cloud). We can then attempt to support the ensuing results by designing a reliable experiment to measure wave scattering by ice clouds.

Bibliography

M. Ablowitz and A. Fokas. *Complex Variables: Introduction and Applications.* Cambridge University Press, 2nd edition, 2003.

M. Abramowitz and I. A. Stegun. *Handbook of Mathematical Functions: With Formulas, Graphs and Mathematical Tables.* National Bureau of Standards, Washington D.C., 6th edition, 1967.

V. Andrew. *Efficient numerical evaluation of the scattering of acoustics waves by arrays of cylinders and bodies of revolution of arbitrary cross section.* Phd thesis, University of Manchester, 2014.

V. M. Babich and N. V. Mokeeva. Scattering of the plane wave by a transparent wedge. *J. Math. Sci.*, 155(3):335–342, 2008.

V. M. Babich, M. A. Lyalinov, and V. E. Grikurov. *Diffraction Theory: The Sommerfeld-Malyuzhinets Technique (Alpha Science Series on Wave Phenomena).* Alpha Science, 2007.

V. M. Babich, N. V. Mokeeva, and B. A. Samokish. The Problem of Scattering of a Plane Wave by a Transparent Wedge: A Computational Approach. *J. Commun. Technol. Electron.*, 57(9):993–1000, 2012.

C. M. Bender and S. A. Orszag. *Advanced Mathematical Methods for Scientists*

and Engineers I: Asymptotic Methods and Perturbation Theory. Springer-Verlag, New York, 1999.

J. Billingham and A. King. *Wave Motion*. Cambridge University Press, 2001.

B. V. Budaev. *Diffraction by Wedges*. CRC Press, 1st edition, 1995.

B. V. Budaev and D. B. Bogy. Rayleigh wave scattering by two adhering elastic wedges. *Proc. R. Soc. A Math. Phys. Eng. Sci.*, 454(1979):2949–2996, 1998.

B. V. Budaev and D. B. Bogy. Rigorous solutions of acoustic wave diffraction by penetrable wedges. *J. Acoust. Soc. Am.*, 105(1):74–83, 1999.

F. Cajori. *A history of physics in its elementary branches: including the evolution of physical boundaries*. Macmillan Company, New York, 1899.

G. F. Carrier, M. Krook, and C. E. Pearson. *Functions of a Complex Variable: Theory and Technique*. McGraw-Hill, 1966.

S. N. Chandler-Wilde, I. G. Graham, S. Langdon, and E. A. Spence. Numerical-asymptotic boundary integral methods in high-frequency acoustic scattering. *Acta Numer.*, 21:89–305, 2012.

R. Craster and A. V. Shanin. Embedding formulae for diffraction by rational wedge and angular geometries. *Proc. R. Soc. A Math. Phys. Eng. Sci.*, 461 (2059):2227–2242, 2005.

D. G. Crighton, A. P. Dowling, J. E. Ffowcs Williams, M. A. Heckl, and F. G. Leppington. *Modern Methods in Analytical Acoustics*. Springer-Verlag, 1992.

J.-P. Croisille and G. Lebeau. *Diffraction by an Immersed Elastic Wedge*. Springer-Verlag, 1999.

V. G. Daniele. The Wiener-Hopf Technique for Impenetrable Wedges having Arbitrary Aperture Angle. *SIAM J. Appl. Math.*, 63(4):1442–1460, 2003a.

V. G. Daniele. Rotating Waves in the Laplace Domain for Angular Regions. *Electromagnetics*, 23(3):223–236, 2003b.

V. G. Daniele. The Wiener-Hopf Formulation of the Penetrable Wedge Problem: Part I. *Electromagnetics*, 30(8):625–643, 2010.

V. G. Daniele. The Wiener-Hopf Formulation of the Penetrable Wedge Problem: Part II. *Electromagnetics*, 31(1):1–17, 2011.

V. G. Daniele and G. Lombardi. Wiener-Hopf Solution for Impenetrable Wedges at Skew Incidence. *IEEE Trans. Antennas Propag.*, 54(9):2472–2485, 2006.

V. G. Daniele and G. Lombardi. Fredholm factorization of Wiener-Hopf scalar and matrix kernels. *Radio Sci.*, 42(6):1–19, 2007.

V. G. Daniele and G. Lombardi. The Wiener-Hopf Solution of the Isotropic Penetrable Wedge Problem: Diffraction and Total Field. *IEEE Trans. Antennas Propag.*, 59(10):3797–3818, 2011.

V. G. Daniele and R. S. Zich. *The Wiener-Hopf Method in Electromagnetics*. Scitech, Edison, New Jersey, 2014.

V. G. Daniele, G. Lombardi, and R. S. Zich. The Electromagnetic Field for a PEC Wedge Over a Grounded Dielectric Slab: 1. Formulation and Validation. *Radio Sci.*, 52(12):1472–1491, 2017a.

V. G. Daniele, G. Lombardi, and R. S. Zich. The Electromagnetic Field for a PEC Wedge Over a Grounded Dielectric Slab: 2. Diffraction, Modal Field, Surface Waves, and Leaky Waves. *Radio Sci.*, 52(12):1492–1509, 2017b.

V. G. Daniele, G. Lombardi, and R. S. Zich. Network representations of angular regions for electromagnetic scattering. *PLoS One*, 12(8):1–53, 2017c.

V. G. Daniele, G. Lombardi, and R. S. Zich. The Double PEC Wedge Problem: Diffraction and Total Far Field. *IEEE Trans. Antennas Propag.*, 66(12):6482–6499, 2018.

A. M. Davis. Two-dimensional acoustical diffraction by a penetrable wedge. *J. Acoust. Soc. Am.*, 100(3):1316–1324, 1996.

A. Einstein and N. Rosen. On gravitational waves. *J. Franklin Inst.*, 223(I):43–54, 1937.

L. B. Felsen and N. Marcuvitz. *Radiation and scattering of waves*. John Wiley & Sons, Hoboken, N.J., 2nd edition, 1994.

A. L. Gower, I. D. Abrahams, and W. J. Parnell. A Proof that Multiple Waves Propagate in Ensemble-Averaged Particulate Materials. *arXiv:1905.06996*, 2019.

S. P. Groth, D. P. Hewett, and S. Langdon. Hybrid numerical-asymptotic approximation for high-frequency scattering by penetrable convex polygons. *IMA J. Appl. Math.*, 80(2):324–353, 2015.

S. P. Groth, D. P. Hewett, and S. Langdon. A high frequency boundary element method for scattering by penetrable convex polygons. *Wave Motion*, 78:32–53, 2018.

D. S. Jones. *Acoustic and Electromagnetic Waves*. Oxford University Press, Oxford, 1986.

J. B. Keller. Geometrical Theory of Diffraction. *J. Opt. Soc. Am.*, 52(2):116–130, 1962.

L. Knopoff. Elastic Wave Propagation in a Wedge. In J. Miklowitz, editor, *Wave Propag. Solids*, pages 3–43, Los Angeles, 1969. ASME.

E. A. Kraut and G. W. Lehman. Diffraction of electromagnetic waves by a right-angle dielectric wedge. *J. Math. Phys.*, 10(8):1340–1348, 1969.

J. Larsen. Diffraction of elastic waves by a rigid wedge. *Proc. R. Soc. A Math. Phys. Eng. Sci.*, 376(1767):609–617, 1981.

J. B. Lawrie and I. D. Abrahams. A brief historical perspective of the Wiener-Hopf technique. *J. Eng. Math.*, 59(4):351–358, 2007.

M. A. Lyalinov. Diffraction by a highly contrast transparent wedge. *J. Phys. A. Math. Gen.*, 32(11):2183–2206, 1999.

M. A. Lyalinov. Acoustic scattering of a plane wave by a circular penetrable cone. *Wave Motion*, 48(1):62–82, 2011.

M. A. Lyalinov. The far field asymptotics in diffraction by a plane sector. In *2013 Int. Symp. Electromagn. Theory*, pages 893–896, Hiroshima, Japan, 2013a.

M. A. Lyalinov. Scattering of acoustic waves by a sector. *Wave Motion*, 50(4): 739–762, 2013b.

M. A. Lyalinov. Electromagnetic scattering by a plane angular sector : I . Diffraction coefficients of the spherical wave from the vertex. *Wave Motion*, 55:10–34, 2015.

M. A. Lyalinov and N. Y. Zhu. Diffraction of a skew incident plane electromagnetic wave by an impedance wedge. *Wave Motion*, 44(1):21–43, 2006.

M. A. Lyalinov and N. Y. Zhu. *Scattering of Waves by Wedges and Cones with Impedance Boundary Conditions*. Scitech, Edison, New Jersey, 2013.

H. M. Macdonald. *Electric Waves*. University Press, 1902.

G. D. Malyuzhinets. Excitation, reflection and emission of surface waves from a wedge with given face impedances. *Sov. Phys. Dokl.*, 3:752–755, 1958.

P. A. Martin. *Multiple Scattering: Interaction of Time-Harmonic Waves with N obstacles*. Cambridge University Press, Cambridge, 2006.

N. V. Mokeeva. On the well-posedness of diffraction problems for angular domains. *J. Math. Sci.*, 138(2):5555–5564, 2006.

N. V. Mokeeva. The limiting absorption principle in the problem of a transparent wedge. *J. Math. Sci.*, 142(6):2597–2604, 2007.

M. A. Nethercote, R. C. Assier, and I. D. Abrahams. High-contrast approximation for penetrable wedge diffraction. 2019a.

M. A. Nethercote, R. C. Assier, and I. D. Abrahams. Analytical methods for perfect wedge diffraction: a review. *arXiv:1905.10562*, 2019b.

B. Noble. *Methods based on the Wiener-Hopf Technique for the solution of partial differential equations (1988 reprint)*. Chelsea Publishing Company, New York, 1958.

A. N. Norris, F. A. Amirkulova, and W. J. Parnell. Source amplitudes for active exterior cloaking. *Inverse Probl.*, 28(10):105002, 2012.

A. V. Osipov and A. N. Norris. The Malyuzhinets theory for scattering from wedge boundaries: a review. *Wave Motion*, 29:313–340, 1999.

J. Radlow. Diffraction by a right-angled dielectric wedge. *Int. J. Eng. Sci.*, 2(3): 275–290, 1964.

A. D. Rawlins. Diffraction by a dielectric wedge. *J. Inst. Math. its Appl.*, 19(3): 261–279, 1977.

A. D. Rawlins. Plane-wave diffraction by a rational wedge. *Proc. R. Soc. A Math. Phys. Eng. Sci.*, 411(1841):265–283, 1987.

A. D. Rawlins. A green's function for diffraction by a rational wedge. *Math. Proc. Cambridge Philos. Soc.*, 105(1):185–192, 1989.

A. D. Rawlins. Diffraction by, or diffusion into, a penetrable wedge. *Proc. R. Soc. A Math. Phys. Eng. Sci.*, 455(1987):2655–2686, 1999.

W. D. Rowley. *Mathematical Modelling of Novel Metamaterials for Noise Reduction Applications*. Phd thesis, University of Manchester, 2018.

M. A. Salem, A. H. Kamel, and A. V. Osipov. Electromagnetic fields in the presence of an infinite dielectric wedge. *Proc. R. Soc. A Math. Phys. Eng. Sci.*, 462(2072):2503–2522, 2006.

S. H. Schot. Eighty years of Sommerfeld's radiation condition. *Hist. Math.*, 19(4): 385–401, 1992.

A. V. Shanin. On Wave Excitation in a Wedge-Shaped Region. *Acoust. Phys.*, 42 (5):612–617, 1996.

A. V. Shanin. Excitation of Waves in a Wedge-Shaped Region. *Acoust. Phys.*, 44 (5):592–597, 1998.

A. Sommerfeld. Mathematische Theorie der Diffraction. *Math. Ann. (in Ger.)*, 47:317–374, 1896.

A. Sommerfeld. Theoretisches über die Beugung der Röntgenstrahlen. *Zeitschrift für Math. und Phys. (in Ger.)*, 46:11–97, 1901.

A. Sommerfeld. *Mathematical Theory of Diffraction*. Birkhauser, Boston, 2003.

A. A. Tuzhilin. On the theory of inhomogeneous functional Malyuzhinets equations. *Differ. nye Uravn. (in Russ.)*, 9(11):2058–2064, 1973.

J. G. Van Bladel. *Electromagnetic fields*. John Wiley & Sons, New Jersey, 2nd edition, 2006.

E. Wegert. *Visual Complex Functions*. Birkhauser Basel, 2012.

N. Wiener and E. Hopf. Über eine klasse singulärer integralgleichungen. *Sitzungsberichte der Preuss. Akad. der Wissenschaften, Phys. Klasse (in Ger.)*, 31: 696–706, 1931.